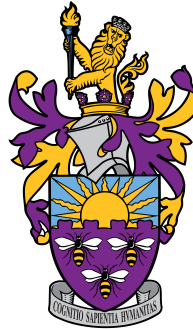


CHARACTERISATION AND BEAM TEST DATA  
ANALYSIS OF 3D SILICON PIXEL DETECTORS FOR  
THE ATLAS UPGRADE



A THESIS SUBMITTED TO  
THE UNIVERSITY OF MANCHESTER  
FOR THE DEGREE OF DOCTOR OF PHILOSOPHY (PhD)  
IN THE FACULTY OF  
ENGINEERING AND PHYSICAL SCIENCES

CLARA NELLIST

PARTICLE PHYSICS GROUP  
SCHOOL OF PHYSICS AND ASTRONOMY

2013





# Contents

<b>List of Figures</b>	<b>11</b>
<b>List of Tables</b>	<b>13</b>
<b>Abstract</b>	<b>15</b>
<b>Declaration</b>	<b>17</b>
<b>Copyright</b>	<b>19</b>
<b>Acknowledgements</b>	<b>21</b>
<b>1 Introduction</b>	<b>27</b>
<b>2 Theoretical Background</b>	<b>29</b>
2.1 Properties of semiconductors . . . . .	29
2.1.1 Doping . . . . .	30
2.1.2 The pn-junction . . . . .	31
2.2 Radiation detection . . . . .	32
2.2.1 Interactions of heavy charged particles . . . . .	32
2.2.2 Photon interactions . . . . .	34
2.2.3 Interactions of heavy neutral particles . . . . .	35
2.2.4 Signal collection . . . . .	35
2.3 Radiation damage in silicon semiconductors . . . . .	36
2.3.1 Type inversion . . . . .	38
2.3.2 Radiation hardness of other materials . . . . .	38
2.4 Pixel detectors . . . . .	39
2.4.1 Detector layout . . . . .	39
2.4.2 Hybrid detectors . . . . .	40
<b>3 The LHC and ATLAS</b>	<b>41</b>
3.1 The CERN accelerator complex . . . . .	41
3.1.1 The LHC . . . . .	41
3.2 The ATLAS Detector . . . . .	44
3.2.1 The Inner Detector . . . . .	48
3.2.2 The Calorimeters . . . . .	52
3.2.3 The Muon Spectrometer . . . . .	54

<b>4</b>	<b>ATLAS Pixel Upgrade</b>	<b>55</b>
4.1	Insertable B-Layer . . . . .	55
4.1.1	Readout electronics . . . . .	61
4.2	Further upgrade projects . . . . .	64
4.2.1	ATLAS Forward Physics . . . . .	64
4.2.2	High luminosity LHC . . . . .	65
<b>5</b>	<b>3D Silicon Detectors</b>	<b>67</b>
5.1	Fabrication . . . . .	67
5.2	3D Silicon Layouts . . . . .	69
5.2.1	Electrode configuration . . . . .	70
5.2.2	Active and slim edges . . . . .	72
5.2.3	Magnetic field . . . . .	73
5.3	Design for the IBL . . . . .	74
5.4	Summary . . . . .	76
<b>6</b>	<b>Laboratory Characterisation</b>	<b>77</b>
6.1	The laboratory setup . . . . .	77
6.2	USBPix . . . . .	77
6.3	STControl . . . . .	78
6.3.1	Tuning the front-end . . . . .	79
6.4	Results . . . . .	80
6.4.1	IV . . . . .	80
6.4.2	Testing the front-end . . . . .	80
6.4.3	Threshold and noise scans . . . . .	82
6.4.4	Source scans . . . . .	82
6.5	Summary . . . . .	83
<b>7</b>	<b>Beam Tests</b>	<b>85</b>
7.1	Beam test facilities . . . . .	85
7.1.1	DESY . . . . .	85
7.1.2	Super Proton Synchrotron, CERN . . . . .	87
7.2	Beam test setup . . . . .	87
7.2.1	Telescope . . . . .	88
7.2.2	Cooling . . . . .	89
7.2.3	Mounting devices . . . . .	89
7.2.4	Data acquisition software . . . . .	91
7.2.5	Online data monitoring . . . . .	93
7.3	Tested devices . . . . .	93
7.4	Track reconstruction . . . . .	93
7.4.1	GEAR file . . . . .	96
7.4.2	EUTelescope . . . . .	96
7.4.3	CED . . . . .	99
7.5	Data analysis . . . . .	99
7.5.1	Clusters . . . . .	101
7.5.2	Residuals . . . . .	102
7.6	Results . . . . .	104

7.6.1	Tracking efficiency . . . . .	104
7.6.2	Edge efficiency . . . . .	111
7.6.3	Charge sharing . . . . .	117
7.6.4	High eta studies . . . . .	117
<b>8</b>	<b>Antiproton Beam Test</b>	<b>129</b>
8.1	Theoretical background . . . . .	130
8.2	Experimental setup . . . . .	130
8.3	Initial results . . . . .	132
8.4	Simulation . . . . .	132
8.4.1	Geant4 framework . . . . .	133
8.4.2	Simulation setup . . . . .	133
8.5	Simulation results . . . . .	143
8.5.1	Two dimensional hitmaps . . . . .	143
8.5.2	Annihilation depth . . . . .	148
8.5.3	Secondaries produced . . . . .	155
8.5.4	Energy deposit . . . . .	158
8.5.5	Charge collected . . . . .	161
8.6	Summary . . . . .	163
<b>9</b>	<b>Summary and Conclusions</b>	<b>165</b>
	<b>References</b>	<b>167</b>



# List of Figures

2.1	Diagram showing the occupancy of electrons within the energy bands for conductors, semiconductors and insulators. . . . .	30
2.2	Representation of an impurity occupying the site of a silicon atom in the lattice producing an n-type and p-type semiconductor. . . . .	31
2.3	Representation of the relative depletion regions . . . . .	32
2.4	The stopping power for positive muons in copper as a function of the muon momentum . . . . .	33
2.5	Illustrations of major photon interactions . . . . .	34
2.6	Simulation of the development of clustered damage within a silicon wafer . . .	36
2.7	Relationship between the depletion voltage and effective doping as a function of the fluence . . . . .	38
2.8	Sketches of two hits on a single-sided strip detector, a double-sided strip detector and a pixel detector. . . . .	39
2.9	Illustration of a single cell of a pixel, bump-bonded to the readout electronics.	40
3.1	The CERN accelerator complex . . . . .	42
3.2	Total integrated luminosity. . . . .	43
3.3	The LHC experiments . . . . .	44
3.4	The ATLAS detector. . . . .	45
3.5	Detection of particles in the ATLAS detector. . . . .	46
3.6	The ATLAS coordinate system. . . . .	47
3.7	The ATLAS inner detector. . . . .	48
3.8	The ATLAS pixel detector. . . . .	49
3.9	An ATLAS Barrel Pixel Module. . . . .	50
3.10	Distribution of material by radiation length and interaction length within the ATLAS Inner Detector as a function of $ \eta $ . . . . .	51
3.11	The ATLAS calorimeters. . . . .	53
3.12	The ATLAS muon subsystem. . . . .	54
4.1	Comparison of pile up in the current ATLAS inner detector and simulated pile up in the base line design for an upgraded ATLAS inner detector. . . . .	56
4.2	The fluence received by the ATLAS Inner Detector per year as a function of distance from the interaction point. . . . .	57
4.3	Comparison of pile up in the current ATLAS inner detector and simulated pile up in the base line design for an upgraded ATLAS inner detector. . . . .	57

4.4	A rendered image of the ATLAS Insertable B-Layer inside of the current pixel layer . . . . .	58
4.5	Diagram of the IBL stave layout for case with mixed sensor types. . . . .	58
4.6	Drawing of the cross-section of the IBL staves in the ATLAS detector . . . .	60
4.7	Comparison of double-chip planar module and single chip 3D silicon module for the IBL . . . . .	60
4.8	Comparison of the current ATLAS planar pixel edge with the newer slim-edge design used for the IBL. . . . .	61
4.9	Size comparison between the current pixel detector readout chip (FE-I3) and the new readout chip designed for the IBL (FE-I4) . . . . .	62
4.10	A sketch of the ATLAS FE-I4a readout chip. . . . .	63
4.11	Comparison of the relationship between the preamplifier signal and the discriminator output signal for changes in the injected charge, threshold and feedback current . . . . .	64
4.12	Feynman diagram of Higgs production by CEP. . . . .	65
4.13	The irradiation dose distribution over CNM 57 and the corresponding efficiencies from AFP beam test studies . . . . .	65
5.1	Holes in the silicon wafer etched using the DRIE process at SINTEF . . . . .	68
5.2	Comparison between a 3D silicon sensor and a planar sensor. . . . .	69
5.3	Sketch of a 3D silicon pixel cell. . . . .	70
5.4	3D sensors with FE-I3 pixel pitch with two, three and four electrodes per pixel	71
5.5	The signal efficiency for 2E, 3E and 4E 3D silicon devices as a function of the fluence. . . . .	71
5.6	Edge efficiency of an FE-I4 CNM 3D pixel detector irradiated with neutrons to a fluence of $1 \times 10^{15} \text{ n}_{eq} \text{ cm}^{-2}$ . . . . .	73
5.7	Sketch of the effect of the magnetic field on the charge distribution within the pixels of a planar detector and 3D silicon detector. . . . .	74
5.8	Comparison of cluster size for track incidence angles between $-30^\circ$ and $+30^\circ$ for a planar detector and two 3D silicon detectors manufactured at Stanford (STA) and FBK . . . . .	74
5.9	Common IBL wafer floor plan for CNM and FBK . . . . .	75
5.10	Double-sided 3D silicon designs for the fabrication facilities FBK with full-through electrodes and CNM with partial-through electrodes . . . . .	76
6.1	The laboratory setup at CERN . . . . .	78
6.2	Photograph of the USBPix system . . . . .	79
6.3	Measured current in $\mu\text{A}$ as a function of reverse bias voltage (V) for a non-irradiated FE-I3 3D silicon sensor, SINTEF 105, at temperatures of $-15^\circ\text{C}$ (blue), $0^\circ\text{C}$ (red) and $20^\circ\text{C}$ (green). . . . .	81
6.4	Analogue and digital scans . . . . .	81
6.5	Threshold and noise scans . . . . .	82
6.6	Noise readings as a function of the reverse bias voltage . . . . .	83
6.7	A two dimensional hitmap taken during a source scan with internal triggers. .	84
6.8	Charge distribution as a function of cluster size . . . . .	84
7.1	The DESY beam test complex . . . . .	86

7.2	The DESY beam hall. . . . .	86
7.3	The CERN beam hall. . . . .	87
7.4	Illustration of a standard beam test setup . . . . .	88
7.5	Dortmund box . . . . .	90
7.6	Photograph of the Dortmund cooling box in the beam test setup. . . . .	91
7.7	Photograph of two FE-I4 devices on <i>L</i> -shaped aluminium mounts . . . . .	91
7.8	Schematic for rotation plate indicating the positions the plate should be screwed into the base plate to obtain selected rotations in $\eta$ . . . . .	92
7.9	The EUDAQ control panel . . . . .	92
7.10	Example of EUDET Online Monitoring plots. . . . .	94
7.11	Example of EUDET Online Monitoring correlation plots . . . . .	95
7.12	Flow diagram illustrating the five stages to reconstruct .lcio data from a beam test experiment and output a .root file. . . . .	97
7.13	Visual output produced by CED . . . . .	101
7.14	Example of the output from the clustersvsrun analysis class . . . . .	103
7.15	Residual for the y-direction for cluster size of 2. . . . .	104
7.16	Sensor efficiency maps for FBK 11 and FBK 13. . . . .	106
7.17	Comparison of efficiency against reverse bias voltage for 3D silicon pixel de- tectors (a) FBK 11 and (b) FBK 13 in Batch 2 of the IBL beam test at DESY. . . . .	107
7.18	Comparison of inefficiency maps for non-irradiated 3D silicon pixel detector FBK 13 with a threshold of 1800 e <sup>-</sup> in Batch 2 of the IBL beam test at DESY. . . . .	107
7.19	Two dimensional efficiency maps for an FBK non-irradiated IBL sensor. . . . .	108
7.20	Three dimension efficiency maps for non-irradiated FBK device in the IBL CERN beam test from October 2012. . . . .	109
7.21	Two dimensional efficiency maps for a non-irradiated CNM IBL sensor. . . . .	110
7.22	Comparison of the raw hitmaps for the three devices under test in Batch 4 of the CERN beam test, May 2012. . . . .	113
7.23	Comparison of combined efficiency pixel hitmaps for all the left edge pixels, folded into a single pixel cell. . . . .	113
7.24	Edge efficiency pixels for SINTEF 98. The red line is a fit to the data. The black lines at 200 $\mu\text{m}$ and 780 $\mu\text{m}$ define the edges of the pixel. . . . .	114
7.25	Edge efficiency pixels for SINTEF 115. The red line is a fit to the data. The black lines at 200 $\mu\text{m}$ and 780 $\mu\text{m}$ define the edges of the pixel. . . . .	115
7.26	Efficiency for the edge pixels and whole sensor for SINTEF 98 and SINTEF 115. . . . .	116
7.27	Two dimensional probability of charge sharing maps for an FBK non-irradiated IBL sensor . . . . .	117
7.28	Sketch of the setup of Batch 1a of the June 2012 beam test at CERN. . . . .	119
7.29	Photograph of setup of Batch 1a, June beam test, CERN 2012 from above and the side. . . . .	120
7.30	Enable mask for FBK 11 on an FE-I4 read out chip, irradiated to $6 \times 10^{15} n_{eq}\text{cm}^{-2}$ . . . . .	121
7.31	Comparison of two dimensional hitmaps for non-irradiated FBK 13 and irra- diated FBK 11 . . . . .	122
7.32	Simulated cluster size for a tilted sensor . . . . .	122
7.33	Comparison of the lvl1 distributions for FBK 13 and FBK 11 . . . . .	123

7.34	Comparison of cluster size distributions for CNM 55 for each set of tilt angles in the setup. . . . .	124
7.35	Comparison of the cluster size distributions at different angles for FBK 13 in the June IBL beam test, 2012. . . . .	125
7.36	Comparison of the cluster size distributions at different angles for FBK 11 in the June IBL beam test, 2012. . . . .	126
7.37	Cluster size distributions for $\eta$ angles of $80^\circ$ and $85^\circ$ . . . . .	127
7.38	Mean cluster size recorded for 3D silicon pixel detectors, FBK 13 (non-irradiated), and FBK 11 (proton irradiated to $6 \times 10^{15} \text{ n}_{eq} \text{ cm}^{-2}$ ) . . . . .	127
8.1	Sketch of the Moire deflectometer illustrating the use of two gratings to produce a fringe pattern on the position sensitive detector. . . . .	129
8.2	A schematic of the Antiproton Decelerator (AD) at CERN. The AD provides antiprotons to the four fixed-target experiments. . . . .	131
8.3	A schematic of the AEGIS experimental setup at CERN . . . . .	131
8.4	Photographs from the antiproton beam test setup. . . . .	133
8.5	Photograph from the antiproton beam test setup. . . . .	134
8.6	Simulated antiproton initial kinetic energy distribution for beam tests in December 2012 . . . . .	135
8.7	Raw 2D hitmaps for two events using the 3D silicon detector, CNM 55, from the antiproton beam test. . . . .	136
8.8	Sketch of the layout of the layers on the backside of the simulated 3D silicon detector . . . . .	137
8.9	Two dimensional hitmap of the distribution of the initial antiproton position in the x-y plane. . . . .	138
8.10	Simulated initial kinetic energy spectrum for antiprotons. . . . .	139
8.11	Simulated two dimensional efficiency map for a single 3D silicon non-irradiated pixel cell biased to -30 V . . . . .	139
8.12	Simulated charge collection position for hits originating within a pixel using the digitiser. . . . .	140
8.13	Visual representations of antiproton annihilations within the 3D silicon sensor for one event, ten events and one hundred events. . . . .	141
8.14	An extract of information displayed after a single antiproton annihilation event. . . . .	142
8.15	Comparison of the visual output from a single antiproton annihilation event with the charge hitmap. . . . .	144
8.16	Two dimensional charge hitmap from 20 simulated antiproton events. . . . .	145
8.17	Comparison of two dimensional charge hitmaps from 200 simulated $\pi^+$ and $\pi^-$ events on the 3D silicon pixel detector. . . . .	146
8.18	Comparison of the charge collected for $\sim 50$ events where the antiproton annihilated in the (a) aluminium and (b) silicon layer. . . . .	147
8.19	A pie chart to illustrate the percentage of annihilations that occur in each layer of the simulated detector for the spectrum of initial kinetic energy . . . . .	148
8.20	Simulated distribution of the antiproton annihilation depth in the 3D silicon pixel detector. . . . .	149
8.21	Annihilation depth of the simulated antiproton as a function of the initial kinetic energy. . . . .	150



8.22	Simulated distribution of the antiproton annihilation depth for a fixed initial kinetic energy . . . . .	150
8.23	Comparison of final depth of antiprotons or protons in a 230 $\mu\text{m}$ thick wafer of silicon, copper or lead for initial kinetic energies between 0 and 2 MeV . . .	151
8.24	Comparison of final depth of antiprotons or protons in a 230 $\mu\text{m}$ thick wafer of silicon, copper or lead for initial kinetic energies between 0 and 2 MeV. . .	152
8.25	Comparison of secondary particles produced for three initial kinetic energies 0.05 MeV, 0.20 MeV and 0.60 MeV. . . . .	153
8.26	Distribution of the simulated antiproton annihilation depth in lead for changes in the SetDefaultCut parameter for Geant4. . . . .	154
8.27	Annihilation depth of simulated antiprotons in a lead wafer as a function of the initial kinetic energy after a SetDefaultCut of $10^{-6}$ has been applied. . . .	154
8.28	Distribution of the simulated antiproton annihilation depth in silicon for changes in the SetDefaultCut parameter for Geant4. . . . .	155
8.29	Multiplicity of annihilation products for each simulated antiproton annihilation.	156
8.30	Simulated track length in the sensitive region of a 3D silicon pixel detector for charged pions created as a result of an antiproton annihilation. . . . .	157
8.31	Simulated initial kinetic energy deposited in the sensitive region of a 3D silicon pixel detector for charged pions created as a result of an antiproton annihilation.	158
8.32	Distribution of the total energy deposited in the sensitive silicon wafer per simulated antiproton annihilation. . . . .	159
8.33	Distribution of the fraction of total energy deposited within the pixel cell with the greatest energy deposit (E1) per simulated antiproton annihilation. . . . .	159
8.34	Distribution of the fraction of total energy deposited within the pixel cell with the greatest energy deposit (E1) per simulated antiproton annihilation as a function of the initial kinetic energy of the antiproton. . . . .	160
8.35	Comparison of the total energy deposited in the sensitive silicon wafer for simulated antiprotons in the aluminium layer or the silicon bulk. . . . .	160
8.36	Distribution of the total energy deposited by selected annihilation products for a simulated antiproton annihilation in a 3D silicon pixel detector. Heavy nuclei are selected as: helium-3, deuteron and tritium. Other encompasses all further annihilation products produced. . . . .	161
8.37	Fraction of total cluster energy for selected annihilation products from reference	161
8.38	Distribution of the total charge deposited in the sensitive silicon wafer per simulated antiproton annihilation. . . . .	162
8.39	Distribution of the total charge deposited in the sensitive silicon wafer per simulated antiproton annihilation as a function of the initial kinetic energy of the antiproton. . . . .	162
8.40	Distribution of the fraction of total charge deposited within the pixel cell with the greatest charge deposit (C1) per simulated antiproton annihilation. . . . .	163
8.41	Comparison of the total charge deposited in the sensitive silicon wafer for simulated antiprotons in the aluminium layer or the silicon bulk. . . . .	163
8.42	Comparison of simulated and experiment output of a 3D silicon pixel detector in an antiproton beam test. . . . .	164



# List of Tables

2.1	Variables used in the Bethe equation . . . . .	33
3.1	Details for each barrel layer of the ATLAS pixel detector . . . . .	51
3.2	Details for each endcap layer for the ATLAS pixel detector . . . . .	51
4.1	Specifications for technologies to be included in the IBL. . . . .	59
4.2	Sensor requirements for IBL devices . . . . .	59
4.3	Comparison of specifications for FE-I3 and FE-I4 readout cards. . . . .	62
5.1	Comparison of 3D and planar pixel sensors . . . . .	70
7.1	A list of some of the 3D silicon pixel devices tested in beam tests during 2011 and 2012. . . . .	96
7.2	The structure of the reconstructed beam test data file in .root format . . . . .	100
7.3	Efficiency measured for bias voltage scans of FBK devices in Batch 2 of the IBL beam test at DESY, 2012. . . . .	105
7.4	Breakdown of bias voltages for Batch 4 data from CERN beam test, May 2012. . . . .	111
7.5	Comparison of the efficient pixel width and total sensor efficiency for the 3D silicon pixel detectors SINTEF 98 and SINTEF 115, both on FE-I3 readout cards. . . . .	112
7.6	Information about the devices in Batch 1 of the IBL beam test at CERN in 2012. . . . .	118
7.7	Breakdown of tilt angles for Batch 1a data from CERN beam test, June 2012. . . . .	118
7.8	Comparison of the mean cluster size in the x-direction at different angles for the 3D silicon pixel detectors, FBK 11 and FBK 13, in the June IBL beam test, 2012, biased to -160 V and -20 V respectively. Both detectors were tuned to a threshold of 1600 e <sup>-</sup> . . . . .	123
8.1	Multiplicity of annihilation products for each simulated antiproton annihilation. . . . .	156



# Abstract

3D silicon pixel detectors are a novel technology where the electrodes penetrate the silicon bulk perpendicularly to the wafer surface. As a consequence the collection distance is decoupled from the wafer thickness resulting in a radiation hard pixel detector by design. Between 2010 and 2012, 3D silicon pixel detectors have undergone an intensive programme of beam test experiments. As a result, 3D silicon has successfully qualified for the ATLAS upgrade project, the Insertable B-Layer (IBL), which will be installed in the long-shutdown in 2013-14. This thesis presents selected results from these beam test studies with 3D sensors bonded to both current ATLAS readout cards (FE-I3) and newly developed readout cards for the IBL (FE-I4). 3D devices were studied using 4 GeV positrons at DESY and 120 GeV pions at the SPS at CERN. Measurements presented include tracking efficiency (of the whole sensor, the pixel and the area around the electrodes), studies of the active edge pixels of SINTEF devices and also cluster size distributions as a function of incident angle for IBL 3D design sensors. A simulation of 3D silicon sensors in an antiproton beam test for the AEGIS experiment, with comparison to experimental results and a previous simulation, are also presented.



# Declaration

No portion of the work referred to in the thesis has been submitted in support of an application for another degree or qualification of this or any other university or other institute of learning.





# Copyright

1. The author of this thesis (including any appendices and/or schedules to this thesis) owns certain copyright or related rights in it (the “Copyright”) and she has given The University of Manchester certain rights to use such Copyright, including for administrative purposes.
2. Copies of this thesis, either in full or in extracts and whether in hard or electronic copy, may be made **only** in accordance with the Copyright, Designs and Patents Act 1988 (as amended) and regulations issued under it or, where appropriate, in accordance with licensing agreements which the University has from time to time. This page must form part of any such copies made.
3. The ownership of certain Copyright, patents, designs, trade marks and other intellectual property (the “Intellectual Property”) and any reproductions of copyright works in the thesis, for example graphs and tables (“Reproductions”), which may be described in this thesis, may not be owned by the author and may be owned by third parties. Such Intellectual Property and Reproductions cannot and must not be made available for use without the prior written permission of the owner(s) of the relevant Intellectual Property and/or Reproductions.
4. Further information on the conditions under which disclosure, publication and commercialisation of this thesis, the Copyright and any Intellectual Property and/or Reproductions described in it may take place is available in the University IP Policy (see <sup>1</sup>), in any relevant Thesis restriction declarations deposited in the University Library, The University Library’s regulations (see <sup>2</sup>) and in The University’s policy on Presentation of Theses

---

<sup>1</sup><http://documents.manchester.ac.uk/DocuInfo.aspx?DocID=487>

<sup>2</sup><http://www.manchester.ac.uk/library/aboutus/regulations>



# Acknowledgements

I would like to thank everyone who has supported me academically and otherwise during this period of my life. There are too many names to mention all of them here, so I apologise to anyone not listed, please know your support was greatly appreciated!

Firstly I would like to thank my supervisor, Cinzia Da Via, for sharing her wisdom and enthusiasm. I especially value the motivational talk on the Jura with ice-cream. Thanks also go to my advisor, Stephen Watts, for the tireless proofreading of this thesis in the evenings after a long day of Head of School responsibilities.

Thank you to the ATLAS IBL, 3D, PPS and Diamond communities. It has been a pleasure working with all of you! Thank you to Philippe Grenier, Jens Weingarten, Sebastian Grinstein and Marco Bomben for additional support and guidance. To the other test beam shifters, thank you for making the long test beam days (and nights!) endurable, even fun! Thank you to the EUTelescope group and users for the advice and discussions, especially Igor Rubinskiy, Matthias George and Phillip Hamnett for answering my endless questions. Thank you to Christian Gallrapp for all of the assistance in the CERN laboratory. My PhD *older brothers*, Marcello Borri and Ching-Hung (Jack) Lai for the many discussions. I wish to thank Terry Wyatt and Christian Schwanenberger for the supervision of my masters project which lead me directly to a PhD in Particle Physics.

To everyone in the AEGIS community for the collaboration on the antiproton experiment. It has been truly fascinating!

Manchester has been my second home for eight years and I would like to thank everyone at the university and the HEP group in particular for making it such a rewarding time. I will miss the coffee breaks and clockwords. A special mention to Fred Loebinger for his endless enthusiasm for Manchester and for convincing me this was the best university to study at - you were right! To Anne Morrow and Sabah Salih, thank you for the invaluable administrative and computational support. To stranger-on-the-train Neil Gaspov for discussing my thesis with me from Manchester to Oxford.

To everyone at CERN during my two LTAs (Long Term Attachments). For the poker nights, skiing, water-skiing, girls' nights, Mario Kart, Wine with Kat, zombies in the tunnels and compulsory coffee at 4pm. It was a blast! Also, this thesis would have been completed far sooner without your distractions, but I've been told it's very important to network during your PhD.

Personally, I would like to thank my parents, Jane and Dave Nellist, for fostering my curiosity in science and encouraging it to thrive. To my siblings, Bethan, Charlotte and Joseph for their constant friendship. A special thank you is given to my grandmother, Norma Warner, for sharing her home with me during a very nomadic time.

To Ewen. Thank you for your love, support and companionship, and for ensuring I ate properly in these final thesis-writing weeks. I look forward to Venice!

Finally, to anyone I offered beer to in exchange for their assistance or advice, you should probably claim it now.

Clara.

To my parents.



*“Mercy!” cried Gandalf. “If the giving of knowledge is to be the cure of your inquisitiveness, I shall spend all the rest of my days in answering you. What more should you like to know?”*

*“The names of all the stars, and of all living things, and the whole history of Middle-Earth and Over-heave and of the Sundering Seas,” laughed Pippin. “Of course! What less?”*

— J.R.R. Tolkien, *The Two Towers*





# 1 | Introduction

The study of the fundamental particles and interactions in the Universe requires the development of sophisticated detectors. In the absence of the substantial advances in detector technology utilised in the ATLAS detector, and the significant efforts expended in their development, discovery of new fundamental particles, such as the recently identified Higgs boson at 126 GeV [1], would not have been feasible in the time scale achieved. This thesis describes studies made by the 3D silicon collaboration working on the development of improved particle detectors for future upgrades of the ATLAS detector at the Large Hadron Collider (LHC) at CERN.

Theoretical background on the basics of semiconductor properties, detection of radiation and the damage caused by it, which is required for the understanding of later chapters is presented in Chapter 2. The current LHC and ATLAS detector are described, with a focus on the pixel sub-detector, in Chapter 3. The Inner Detector of the ATLAS experiment will be upgraded in the first long-shutdown period in 2013–2014 with the insertion of an additional layer between the current first pixel layer and a smaller beam pipe. This is known as the Insertable B-Layer project and is presented in Chapter 4. For this project, a new pixel detector was required and consequently an intense programme of beam tests to decide between competing technologies took place. The process of characterising a detector in a laboratory is described in Chapter 5, and selected results from beam tests are presented in Chapter 6. From this qualification programme, 3D silicon sensors were chosen to make up 25% of the new pixel layer.

A 3D silicon module, developed for ATLAS, was used in an antiproton beam test for the AEGIS experiment. The motivation was to evaluate whether this technology was useful for this experiment. A simulation of the detector in the antiproton beam was created in Geant4 and the results are discussed in Chapter 8. Chapter 9 summarises the thesis.



## 2 | Theoretical Background

Solid-state detectors have a high material density, fast readout and produce large numbers of charge carriers which allows for good position resolution. This makes them preferable to other detector types, such as gaseous detectors, for high rate environments. However in this high rate environment, solid-state detectors are susceptible to radiation damage, so research and development is required to improve the radiation hardness of these detectors.

In this chapter, the properties of semiconductors are introduced in Section 2.1. Methods of radiation detection are discussed in Section 2.2 and how this radiation damages silicon semiconductors is described in Section 2.3. Finally, Section 2.4 describes silicon detectors in further detail.

The theoretical background of the Standard Model of particle physics will not be presented here, since the author assumes a basic knowledge from the reader. However, for a comprehensive discussion of the subject, the reader is recommended to consult one of the many published works on the subject, such as [2].

### 2.1 Properties of semiconductors

Generally speaking, there are three types of solid-state materials, conductors, insulators and semiconductors [3]; each results from the manner in which the energy bands are filled by electrons. The occupancy of electrons in the energy bands for each of these three types is illustrated in Fig. 2.1 as described in [4]. Conductors, as the name suggests, are highly conductive due to either overlapping energy levels or a partially filled conduction band. Metals, such as silver and copper, fall within this category. Insulators, glass for example, have a large region (greater than  $\sim 9$  eV) between the two energy levels known as a band gap, thus reducing the movement of electrons due to the high excitation energy required to release an electron from its bonds. However, just as in the story of *goldilocks and the three bears*, for semiconductors the band gap region is small enough to be ‘just right’, allowing for some very interesting properties (described below).

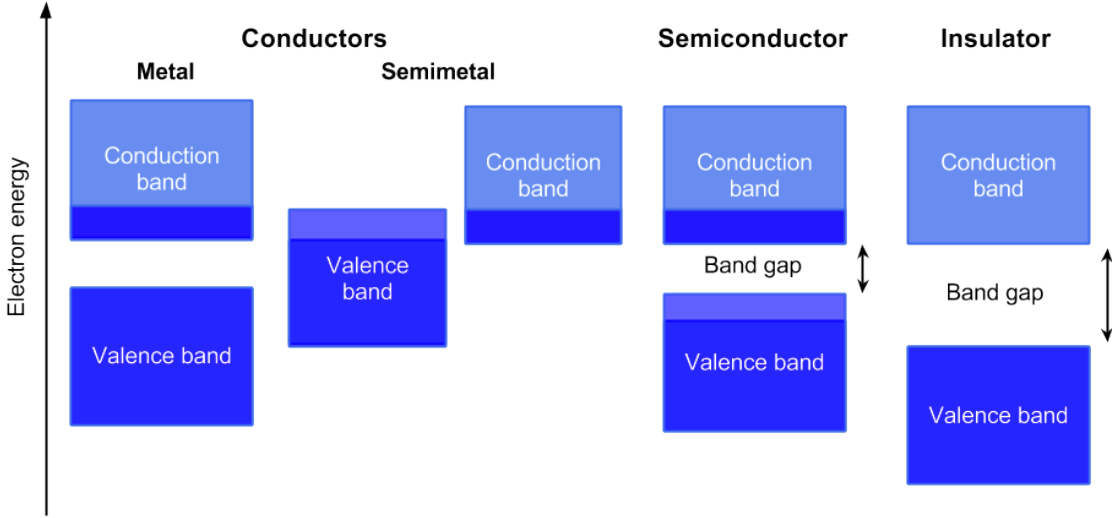


Figure 2.1: Diagram showing the occupancy of electrons within the energy bands for conductors (metals and semimetals), semiconductors and insulators. Adapted from [4].

The probability as a function of time, that an electron-hole pair is generated due to thermal excitation alone is,

$$p(T) = CT^{\frac{3}{2}} \exp\left(-\frac{E_g}{2kT}\right) \quad (2.1)$$

where  $k$  is Boltzmann's constant,  $T$  is the absolute temperature,  $E_g$  is the energy of the band gap and  $C$  is the material proportionality constant [5]. With a band gap energy of  $\sim 1$  eV<sup>1</sup>, it is likely that some electrons will be excited from the valence band to the conduction band simply due to the thermal energy in the semiconductor. As the temperature of the semiconductor is reduced, the number of thermally excited electrons decreases until, at absolute zero, the solid becomes an insulator. The empty regions of positive charge left behind by an absence of an electron can be thought of as a virtual particle called a *hole*. When the concentration of electrons in the conduction band exactly equals the concentration of holes in the valence band, this type of semiconductor is known as *intrinsic*. The number of thermally excited charge carriers determines how conductive the semiconductor is. By introducing impurities into the lattice of the semiconductor a greater density of electrons or holes can be produced – this is *doping* and the resulting semiconductor is called extrinsic.

### 2.1.1 Doping

The lattice of a certain type of semiconductor has a specific density of electrons per unit area. Taking an intrinsic group IV semiconductor such as silicon as an example and adding

<sup>1</sup>1 eV is the energy required to move an electron across an electric potential difference of one volt.

an impurity from group V such as phosphorus, an excess of electrons are produced due to the extra electron provided by the dopant. This results in a lower proportion of holes. These are denoted as majority carriers and minority carriers respectively. The resulting semiconductor is known as *n-type*, shown in Fig. 2.2a. This type of dopant is called a donor. An excess of holes due to an impurity from a group III atom results in a *p-type* semiconductor, shown in Fig. 2.2b. An extremely large concentration of the impurity is denoted with a '+', thus a semiconductor with a very high density of group V impurities is called  $p^+$ -type. This dopant type is called an acceptor and a common acceptor for silicon is boron.

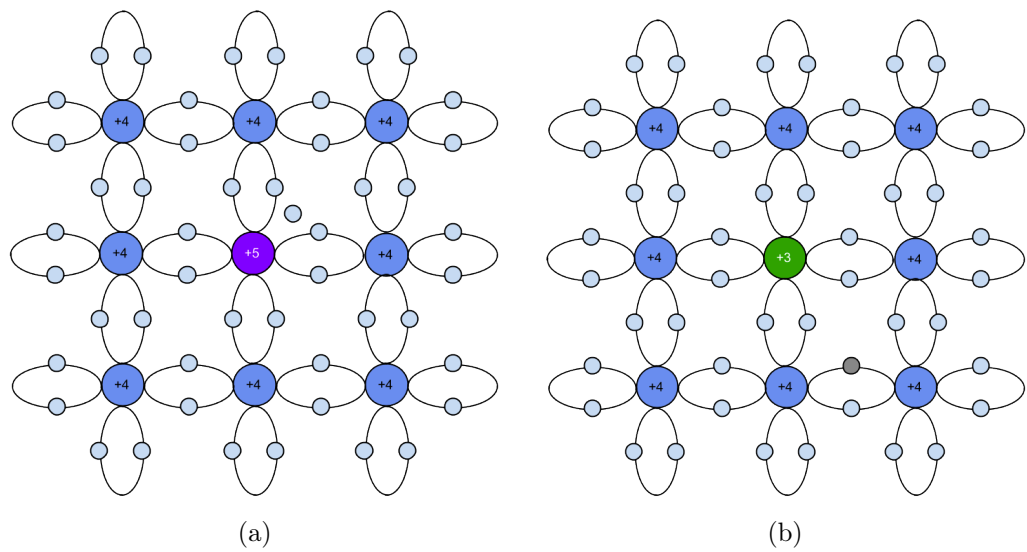


Figure 2.2: Representation of an impurity occupying the site of a silicon atom in the lattice. The light grey circles represent the electrons. The donor in (a) donates an extra electron, creating an n-type semiconductor. The acceptor in (b) reduces the density of electrons creating a p-type semiconductor. The missing electron is illustrated in (b) by a darker grey circle.

### 2.1.2 The pn-junction

A junction is formed when doped semiconductors of p-type and n-type are brought into contact with each other. Diffusion of carriers across the junction exposes fixed ionic charge, which results in an electric field (built-in) which prevents further diffusion. The density of free carriers is greatly reduced in the region close to the junction and this is known as the *depletion zone*, illustrated in Fig. 2.3a.

When an electric potential is applied, a small current is produced due to the net migration of the electrons and holes. If the positive terminal is connected to the p-type (and hence the

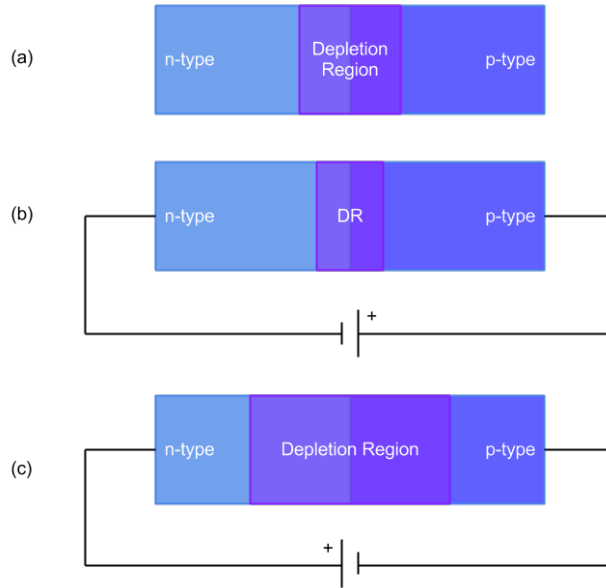


Figure 2.3: Representation of the relative depletion regions for (a) an unbiased pn-junction, (b) a forward biased semiconductor and (c) a reverse biased semiconductor.

negative is connected to the n-type) this is known as *forward bias* and results in a smaller depletion zone (Fig. 2.3b). The opposite, where the positive terminal is connected to the n-type, is known as *reverse bias* (Fig. 2.3c). In this case the depletion zone is extended. If the reverse bias voltage is great enough, the depletion zone extends all the way to the edge of the semiconductor. This is called full depletion. If the voltage continues to increase, avalanche breakdown will eventually occur.

## 2.2 Radiation detection

There are various methods in which particles interact within matter depending on their mass, charge and momentum. Brief descriptions of interactions of heavy charged particles, photons and heavy neutral particles with matter will be presented in this section.

### 2.2.1 Interactions of heavy charged particles

The primary method of interaction of heavy charged particles is via the electromagnetic interaction. In this case, heavy charged particles are defined as particles with a rest mass greater than the rest mass of an electron. An example of a heavy charged particle is an alpha particle, which is the nucleus of a helium atom, consisting of two protons and two neutrons.

Table 2.1: Variables used in equation 2.2 [6].

Symbol	Definition	Units or Value
E	Incident partle energy $\gamma M c^2$	MeV
T	Kinetic energy	MeV
$m_e c^2$	Electron mass x $c^2$	0.510 998 918(44) MeV
$r_e$	Classical electron radius $e^2/4\pi\epsilon_0 m_e c^2$	2.817 940 325(28) fm
$N_A$	Avogadro's number	6.0221415(10)x10 <sup>23</sup> mol <sup>-1</sup>
Z	Atomic number of absorber	
A	Atomic mass of absorber	g mol <sup>-1</sup>
K/A	$4\pi N_A r_e^2 m_e^2 / A$	0.307075 MeV g <sup>-1</sup> cm <sup>2</sup> for A = 1 g mol <sup>-1</sup>
I	Mean excitation energy	eV
$\delta(\beta\gamma)$	Density effect correction to ionization energy loss	

The Bethe formula (eq. 2.2) describes the energy loss as a function of distance for heavy charged particles. It can also be thought of as the stopping distance for a particle travelling with a relativistic velocity,  $\beta$ , in a particular material with an atomic number, Z.

$$-\left\langle \frac{dE}{dx} \right\rangle = K z^2 \frac{Z}{A} \frac{1}{\beta^2} \left[ \frac{1}{2} \ln \frac{2m_e c^2 \beta^2 \gamma^2 T_{max}}{I^2} - \beta^2 - \frac{\delta(\beta\gamma)}{2} \right] [6] \quad (2.2)$$

The Bethe formula above is only valid for the range  $0.1 < \beta\gamma < 10^4$  [6] and the definitions of the variables are in Table 2.1. Figure 2.4 shows the stopping power for positive muons in copper as a function of the muon momentum.

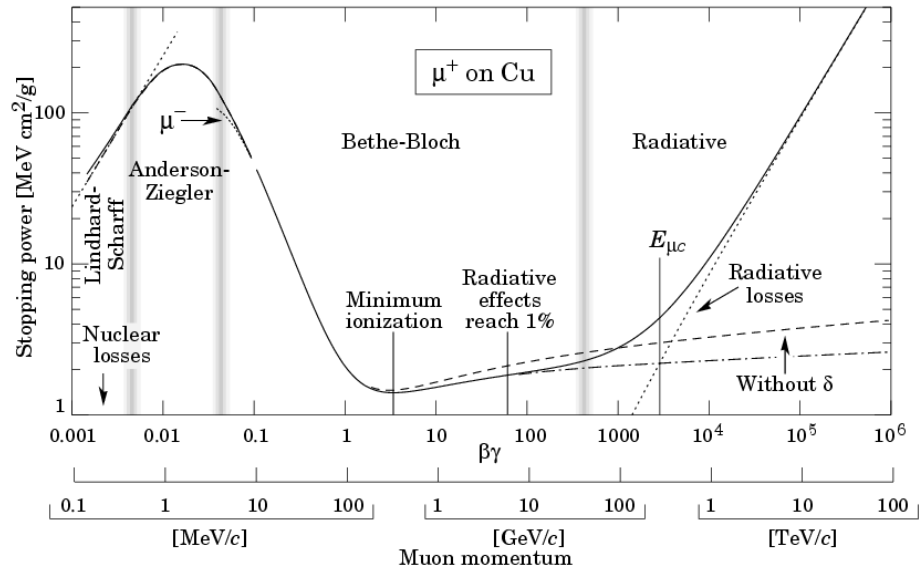


Figure 2.4: The stopping power for positive muons in copper as a function of the muon momentum [6]. The solid line is the total stopping power of the muon.

### 2.2.2 Photon interactions

The three main processes for interactions of photons with matter are via the photoelectric effect, Compton scattering and pair production, each illustrated in Fig. 2.5a, b and c respectively and described below.

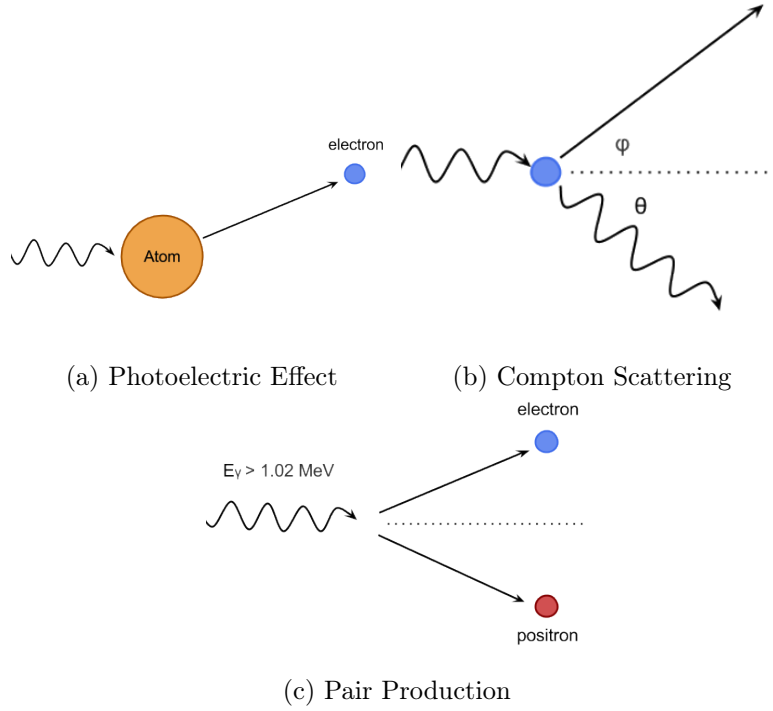


Figure 2.5: Illustrations of the three major photon interactions with matter.

#### Photoelectric effect

When the energy of a photon is greater than the binding energy of an electron to an atom, the photon can be absorbed by the atom causing the release of the electron. The remaining atom is ionised until a free electron is captured. The energy of the emitted electron,  $E_{e^-}$ , is given by

$$E_{e^-} = h\nu - E_b \quad (2.3)$$

where  $h\nu$  is the energy of the photon and  $E_b$  is the binding energy of the electron to the atom.

#### Compton Scattering

Compton scattering occurs when a photon hits an atomic electron, transferring some of its energy and causing the electron to move off at an angle  $\phi$ . The photon is scattered at an



angle  $\theta$  with a reduced energy. This effect was first observed by Arthur H. Compton in 1923 [7].

### Pair production

The creation of an electron-positron pair can occur when a photon has an energy of greater than the combined rest mass of the two new particles. Any extra photon energy is equally divided between the two particles as kinetic energy. After a short period of time, the positron will annihilate with an electron in the bulk of the material producing two photons with energy of 511 keV.

### 2.2.3 Interactions of heavy neutral particles

Heavy neutral particles, as the name suggests, carry no charge and therefore do not interact via the electromagnetic interaction. Neutrons interact with the nucleus of an atom within matter and can travel centimetres before such an interaction occurs. During an interaction, the neutron can lose all of its energy, or some energy with a large change in direction. Secondary particles from an interaction are either those displaced from the atomic nuclei, or products of neutron-induced nuclear reaction [8].

### 2.2.4 Signal collection

When a charged particle traverses the material, electrons are excited from the valence band and an electron-hole pair is formed. The energy required to create an electron-hole pair in silicon at 300K is 3.62 eV [5].

Charge carriers diffuse due to their thermal energy. If an electric field is applied, then the charge carriers will drift towards the electrodes. The time it takes for them to reach the electrodes depends on the mobility,  $\mu$ , of the charge carriers in an electric field of strength,  $E$ ,

$$\mu(E) = \mu_0 \left( \frac{1}{1 + \left( \frac{\mu_0 E}{\nu_{sat}} \right) \beta} \right)^{-\beta} \quad (2.4)$$

The signal collection will also be affected by the presence of a magnetic field. This will not only affect the charged particles traversing the detector, but also charge carriers within. The Lorentz force for a particle with charge  $q$  and a velocity  $\mathbf{v}$  in a magnetic field  $\mathbf{B}$  is,

$$\mathbf{F} = q(\mathbf{E} + \mathbf{v} \times \mathbf{B}) \quad (2.5)$$

where  $\mathbf{E}$  is the electric field vector. The angle of deflection of charge carriers is known as the Lorentz angle.

## 2.3 Radiation damage in silicon semiconductors

Radiation damage to silicon detectors occurs due to two processes: non-ionising and ionising energy loss [9]. It is important to understand these processes and the effect they have on the silicon detector in order to design sensors that are able to function efficiently after a high dose of radiation. The following is a brief description of radiation damage. For further information see [10] and the references within.

Non-Ionising Energy Loss, or NIEL, occurs when a particle traverses the silicon causing lattice displacement of atoms through energy transfer. This damage is caused by hadrons, and leptons if they have high enough energy. If the energy from the initial particle is great enough, the displaced atom can itself cause further displacements. These further displacements are known as defect clusters and are illustrated in the simulated data in Fig. 2.6 [11]. The amount of NIEL depends on the momentum and the type of the incident particle, however, it is normally described as the equivalent of the damage caused by the fluence of 1 MeV neutron, denoted as  $n_{eq}$  for a given area  $\text{cm}^{-2}$ .

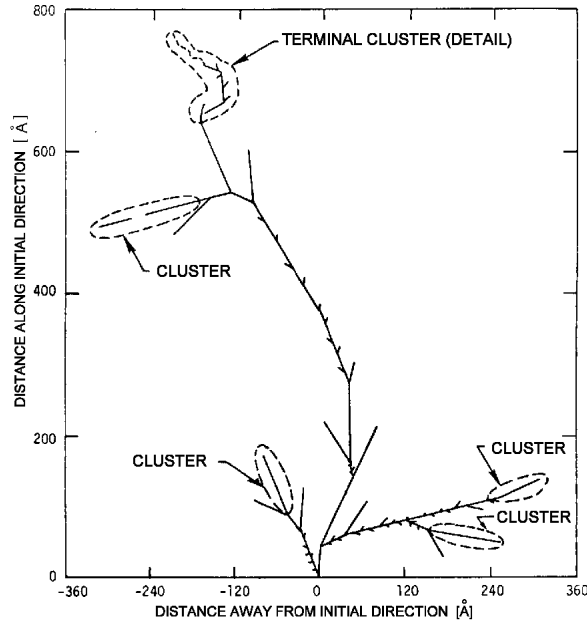


Figure 2.6: Simulation of the development of clustered damage within a silicon wafer [11].

The damage caused by NIEL can result in energy levels forming in the band gap region which contributes to an increase of leakage current and a loss of collected charge. This is due to the trapping of charge carriers at these sites and then a subsequent release of the charge after a delay. Furthermore, the increase in the number of acceptor sites results in a change of the effective doping concentration, requiring higher voltages to reach full depletion, or in the case that these voltages cannot be provided, the detector is under-depleted. The increase in leakage current is material type independent and is generally proportional to the radiation dose,  $\Phi_{eq}$ , and the total depleted sensor volume,  $V$  as shown in the following,

$$\Delta I = \alpha \Phi_{eq} V \quad (2.6)$$

where  $\alpha$  is the current related damage constant. Ionisation loss within the wafer does not cause significant damage to the lattice structure. Loss of collected charge occurs due to charge trapping within the defects in the silicon lattice sites. This lost charge does not contribute to the total collected charge from the particle and results in a reduction of the charge collection efficiency (CCE). The length a particle can drift before being trapped,  $L_{drift}$ , is equal to the effective trapping time,  $\tau_{eff}$  multiplied by the drift velocity,  $\nu_{drift}$  as follows,

$$L_{drift} = \tau_{eff} \nu_{drift} \quad (2.7)$$

The total trapping probability is the inverse of the effective trapping time and is proportional to the effective radiation dose by,

$$\frac{1}{\tau_{eff}} = \beta(t, T) \Phi_{eq} \quad (2.8)$$

where  $\beta$  is the trapping constant for a pair of negative and positive charges. [12]

Ionising Energy Loss (IEL) causes surface damage to a device as positive charge collects at the oxide layer. This is due to charged particles crossing the surface layer creating electron-hole pairs. The electrons diffuse more rapidly. The holes become trapped, creating an increase in positive surface charge. This is most serious in MOS devices and is not normally a problem in bulk silicon detectors.

Reversal of some of the effects of radiation damage has been observed when the sensor is left at room temperature. This is called *reverse annealing* [13]. Radiation effects can anneal after the sensor is no longer being irradiated. In reverse annealing the acceptor density continues to increase at room temperature. This is why silicon sensors are kept cold. Operating devices at low temperatures also reduces radiation induced leakage current.

### 2.3.1 Type inversion

The effective doping concentration,  $|N_{eff}|$ , of the silicon wafer can be described by the concentration of the donor ( $N_d$ ) and acceptor ( $N_a$ ) sites by the following equation:

$$|N_{eff}| = |N_d - N_a| \quad (2.9)$$

For a detector of depth,  $d$ , the depletion voltage,  $V_{dep}$ , is related to the effective doping concentration by,

$$|V_{dep}| = \left( \frac{q_0}{2\epsilon\epsilon_0} \right) |N_{eff}| d^2 \quad (2.10)$$

As a semiconductor is damaged by radiation over time, the number of acceptor sites increases. Consequently, for a semiconductor that was originally doped as n-type, the doping concentration will decrease until a point is reached where the number of acceptor sites cancels out the donors in the semiconductor. After this point, further radiation damage continues to increase the concentration of acceptor sites and the semiconductor is subsequently p-type [11]. This effect is illustrated in Fig. 2.7 for a 300  $\mu\text{m}$  silicon detector at various fluence levels. For a material which was originally n-type, the junction will move from one side of the sensor to the other after the detector has undergone type inversion.

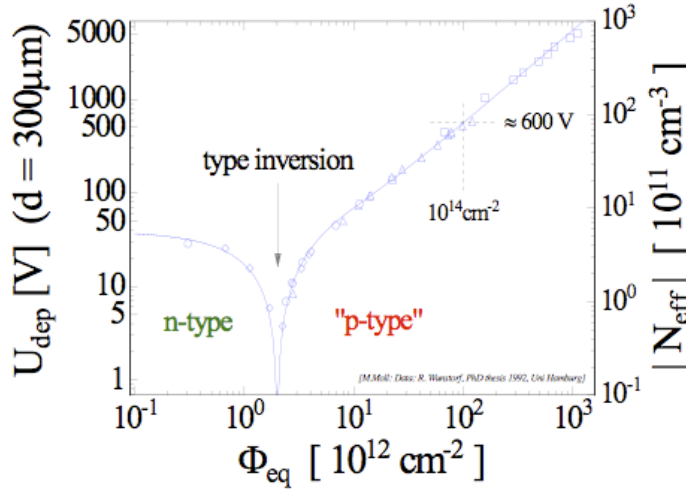


Figure 2.7: Relationship between the depletion voltage,  $U_{dep}$ , (left) and effective doping,  $N_{eff}$ , (right) as a function of the fluence for a 300  $\mu\text{m}$  silicon detector [11].

### 2.3.2 Radiation hardness of other materials

Other materials can be used for semiconductor detectors, so why is silicon still a popular choice? A novel detector technology currently undergoing research within the detector com-

munity is pixel detectors manufactured from diamond [14]. Diamond has a greater band gap region than silicon (5.5 eV) and a higher displacement energy of 42 eV/atom which makes it intrinsically more radiation hard than silicon. The leakage current of a diamond detector is lower than silicon due to the higher band gap and therefore it is possible to run the device at room temperature. However, diamond also requires higher energy to create an electron-hole pair (13 eV compared to 3.6 eV) which results in a lower charge production and a lower overall signal size. Diamond is a promising material for detector development, however more time is required for prototypes to be studied.

## 2.4 Pixel detectors

### 2.4.1 Detector layout

A single layer of strip detectors provides one-dimensional hit information in the direction of the strip, illustrated in the sketch in Fig. 2.8a. Two-dimensional positional information can be determined by creating double-sided strip detectors. In this case the position in  $x$  from one side is combined with the position in  $y$  from the other to provide an  $xy$  point. However, as illustrated in Fig. 2.8b, if there are two or more hits on the sensor, there is an ambiguity in the reconstruction of the two-dimensional positions, known as *ghost-hits*. Figure 2.8c, shows how this ambiguity can be resolved whilst maintaining the two-dimensional information by replacing the readout strips with pixels.

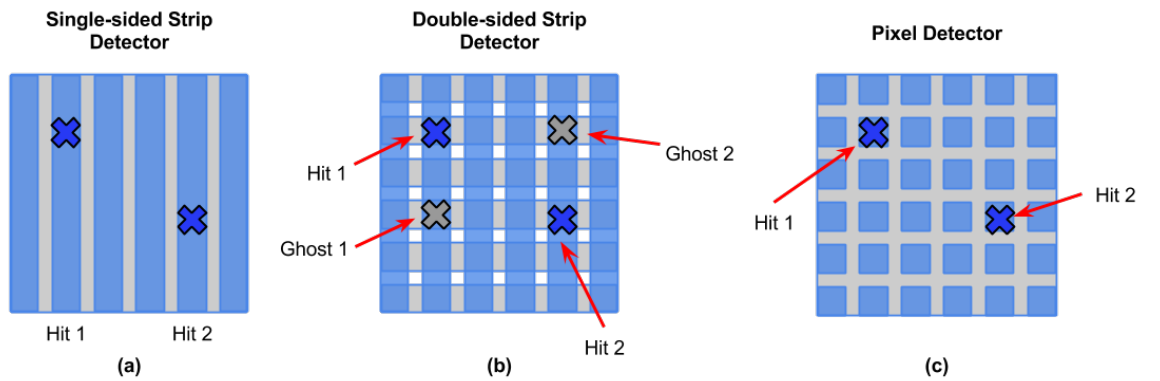


Figure 2.8: Sketches of two hits on (a) a single-sided strip detector, (b) a double-sided strip detector and (c) a pixel detector. Ghost hits are illustrated in (b) due to the ambiguity of reconstructing multiple hits.

### 2.4.2 Hybrid detectors

Charge collected at each pixel needs to be read out to be processed. One method to do this is to connect every pixel of the sensitive detector to a matrix of readout elements. The connection is made via a bump-bond and due to the close proximity, the readout is fast. The combination of the sensitive detector and the front-end readout chip is known as a *hybrid detector*, and is illustrated in Fig. 2.9. Hybrid detectors offer an advantage over integrated methods of readout electronics in that the pixels can be readout simultaneously which is ideal for a high hit-rate environment.

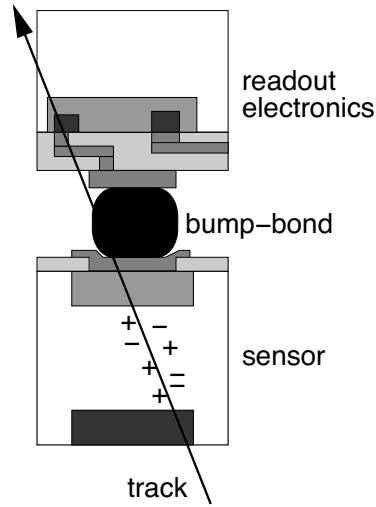


Figure 2.9: Illustration of a single cell of a pixel, bump-bonded to the readout electronics [15]. The arrow shows the track of a charged particle passing through the cell, resulting in a release of electron-hole pairs. The electrical signal is passed to the readout electronics through the bump-bond.

## 3 | The LHC and ATLAS

The European Organisation for Nuclear Research (CERN) is located near the Franco-Swiss border near Geneva. CERN was established in 1954 and aims to study the fundamental properties of particles to better understand the universe and its structure. There are approximately 2,400 people employed by CERN, with over 10,000 visiting scientists from all over the world. This huge organisation designs and builds complex and advanced accelerators and detectors to push the limits of scientific knowledge [16]. The Large Hadron Collider (LHC) [17], is the largest and most powerful particle accelerator to date.

This chapter will describe the accelerator complex at CERN in Section 3.1. The ATLAS detector, with a focus on the Pixel Detector, is described in Section 3.2.

### 3.1 The CERN accelerator complex

The CERN accelerator complex, illustrated in Fig. 3.1 [18], consists of a series of linear accelerators (LINACs) and synchrotrons which aim to accelerate protons from rest to a design energy of 7 TeV. Studies are also performed with ion – ion collisions. The accelerator injection chain for protons is as follows: LINAC2  $\rightarrow$  Booster  $\rightarrow$  Proton Synchrotron (PS)  $\rightarrow$  Super Proton Synchrotron (SPS). The LHC, with a circumference of 27 km, is the final accelerator in this chain and takes the protons from an energy of 450 GeV to operational energy.

#### 3.1.1 The LHC

The LHC was built in the existing tunnel for the Large Electron Positron (LEP) collider, which collided electrons and positrons together with a final centre of mass energy of 209 GeV. Synchrotron radiation is the radiation emitted in the form of photons when a particle is bent in a circular orbit. This was first observed in the General Electric 70 MeV Synchrotron in 1947 [19]. The power emitted due to synchrotron radiation is related to the rest mass of the particle by the following,

### CERN's accelerator complex

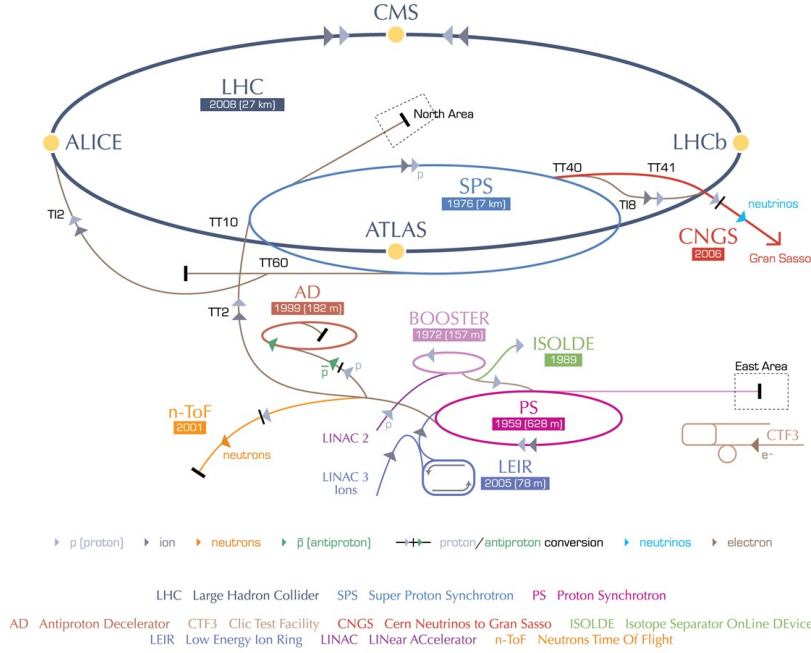


Figure 3.1: The CERN accelerator complex. Figure by Christiane Lefèvre [18]

$$P_\gamma \propto \frac{1}{m^4} \quad (3.1)$$

Although electrons are fundamental particles and produce cleaner collisions [20], they also emit more synchrotron radiation for an accelerator of a given radius compared to hadrons [2].

Since the LHC collides protons, composed of three valence quarks bound together by gluons, the collisions are dominated by the strong force and it is not clear which particles have interacted, or at what energy. Consequently there are many background events in which interesting events can be hidden. High precision detectors are required to identify and track the numerous particles produced in each collision in order to separate signal from background.

Before shutting down in 2013, the LHC had reached beam energies of 4 TeV, resulting in a centre of mass energy of 8 TeV. The two beams of protons are accelerated in separate beam pipes in opposite directions around the LHC tunnel, not as a continuous stream, but nominally in 2,808 bunches of particles [21]. The protons are accelerated by precisely timed radio-frequency (RF) pulses. Super-conducting dipole magnets are used to direct the beams around the tunnel and quadrupole magnets focus the beam at the collision point for each



detector.

The instantaneous luminosity,  $\mathcal{L}_o$ , of an accelerator is defined as the number of collisions per  $\text{cm}^2$  per second. For a specific number of bunches,  $N_b$ , and particles per bunch in each beam,  $n_i$ , the instantaneous luminosity can be written as:

$$\mathcal{L}_o = \frac{r}{4\pi} \frac{N_b f n_1 n_2}{\sigma_x \sigma_y} \quad (3.2)$$

where  $f$  is the revolution frequency, and  $\sigma_i$  are the transverse beam dimensions in the x- and y-axis. The reduction factor,  $r$ , accounts for a non-zero crossing angle and the length of the bunch which is assumed to be equal in each beam. It is also assumed that the beams have a gaussian profile and equal velocities. For the LHC, the reduction factor is  $\sim 0.8$ . The interaction rate,  $R$ , for a given physics process can be determined from the instantaneous luminosity and the cross-section for that process,  $\sigma$  by,

$$R = \mathcal{L}_o \sigma \quad (3.3)$$

If we integrate the instantaneous luminosity with respect to time, we get the integrated luminosity, below, which is given in units of  $\text{cm}^{-2}$ .

$$L = \int \mathcal{L}_o dt \quad (3.4)$$

The total integrated luminosity recorded by the ATLAS detector in 2011 and 2012 (for beam energies of 7 TeV and 8 TeV respectively) is shown in Fig. 3.2.

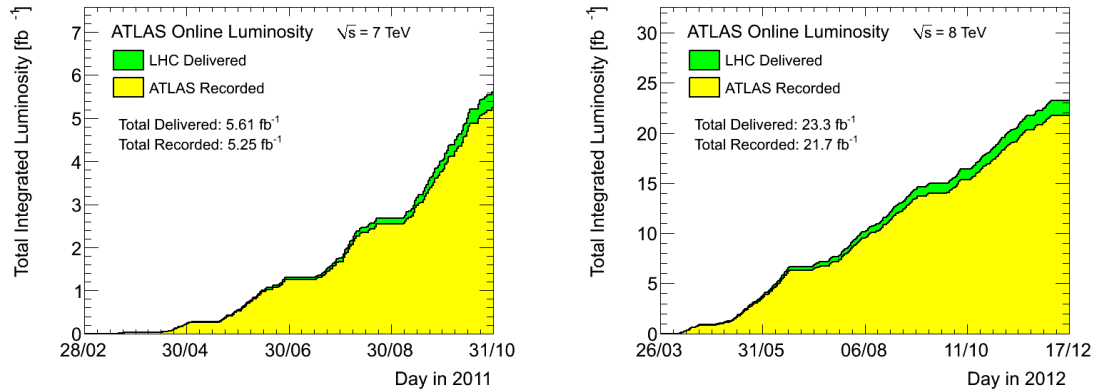


Figure 3.2: Total integrated luminosity delivered by the LHC (shown in green) and recorded by the ATLAS detector (shown in yellow) over time for 2011 (left) and 2012 (right). For beam energies of 7 TeV and 8 TeV respectively.

There are four main points on the LHC ring where the two beams are brought to collide each within a detector, shown in Fig. 3.3. These are A Toroidal LHC ApparatuS (ATLAS) [22] at

point 1, A Large Ion Collider Experiment (ALICE) [23] at point 2, Compact Muon Solenoid (CMS) [24] at point 5 and Large Hadron Collider Beauty (LHCb) [25] at point 8.

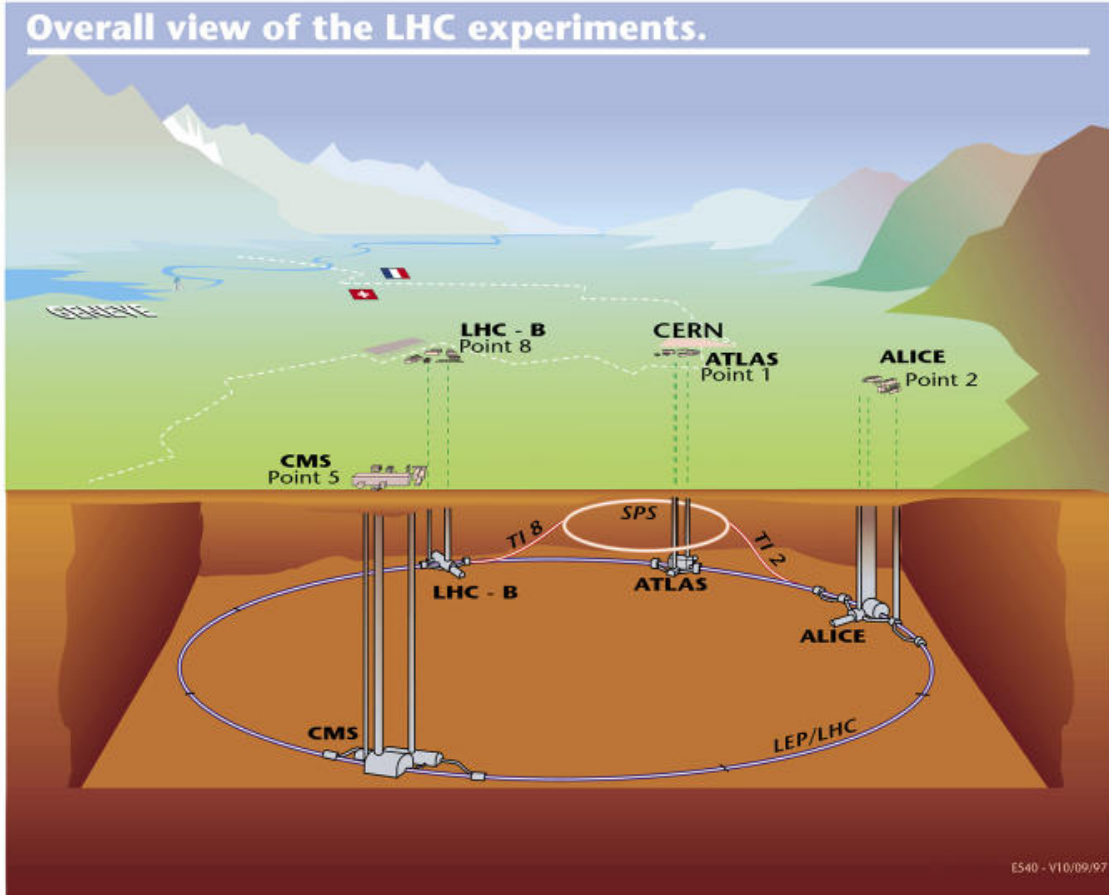


Figure 3.3: Image showing the Large Hadron Collider ring with the locations of the four experiments.

## 3.2 The ATLAS Detector

The ATLAS [22] detector is located at Point 1 on the LHC ring, roughly 100 m underground and is approximately 44 m long and 25 m tall, filling most of the cavern excavated for it. One of the two general-purpose detectors at the LHC, ATLAS consists of many sub-detector layers each designed to measure the various properties of particles produced from proton-proton (or ion-ion) collisions with the aim of recording as much information as possible from collisions of interest. These layers are structured as barrels which fit inside each other like a Matryoshka doll and end-caps which complete the regions at the edge to ensure continuous data coverage. The ATLAS sub-detectors are shown in Fig. 3.4, each one having a specific role in the identification of particles. The primary purpose of the Inner Detector is to track

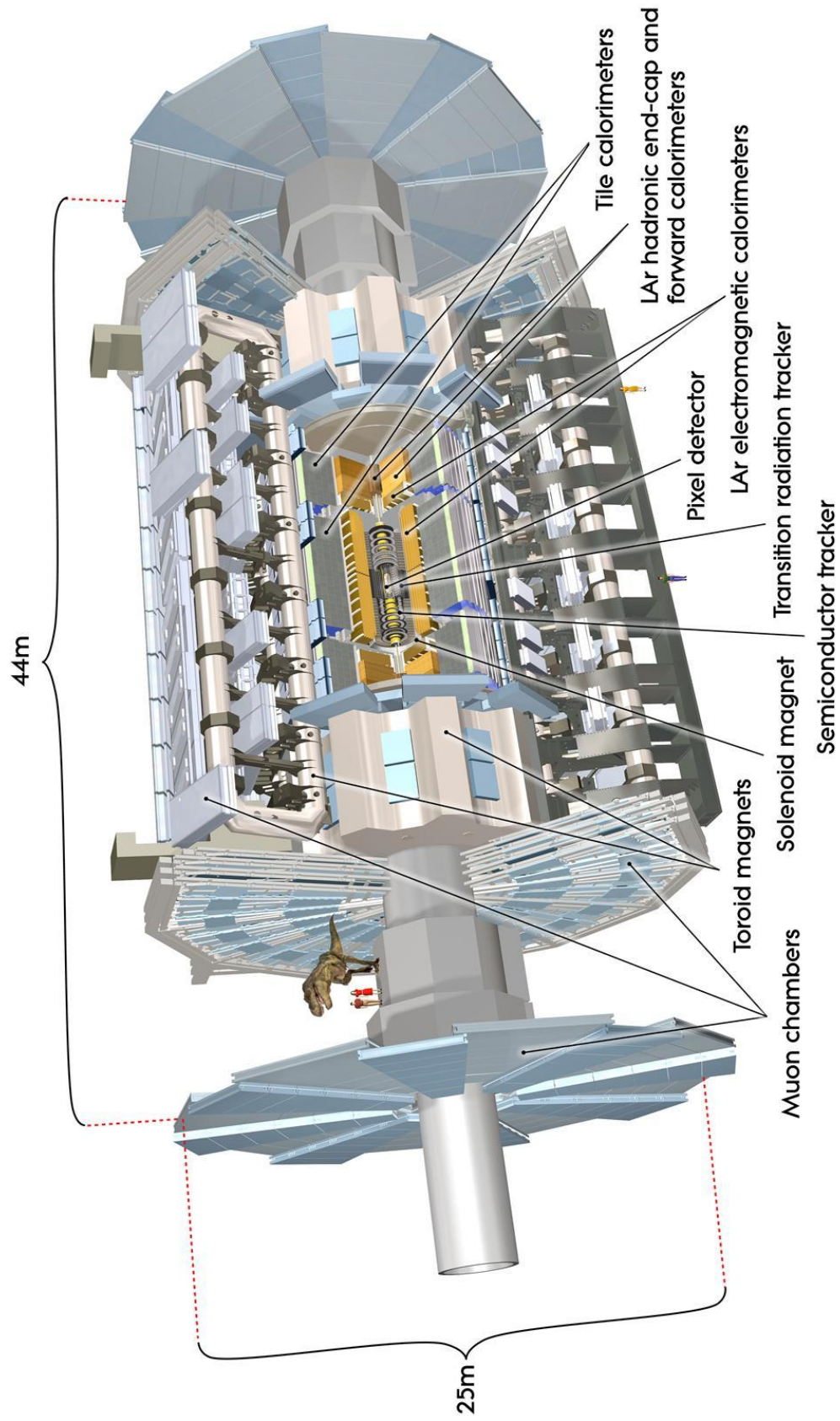


Figure 3.4: The ATLAS detector. The dimensions of the detector are given and the sub-detectors are labelled. Image courtesy of the ATLAS Experiment at CERN, <http://atlas.ch>. For scale, the Tyrannosaurus rex in the diagram is 4 m high at the hip [26].

charged particles. The energy of particles are recorded in the Calorimeters and the Muon Spectrometer measures the properties of muons which traverse the entire ATLAS detector. Figure 3.5 illustrates which particles are measured in each sub-detector. Note that neutrinos are not detected by any of the sub-detectors and are inferred from the ‘missing energy’ in the reconstruction of events. This method requires that all other particles and their properties are measured with the greatest efficiency possible.

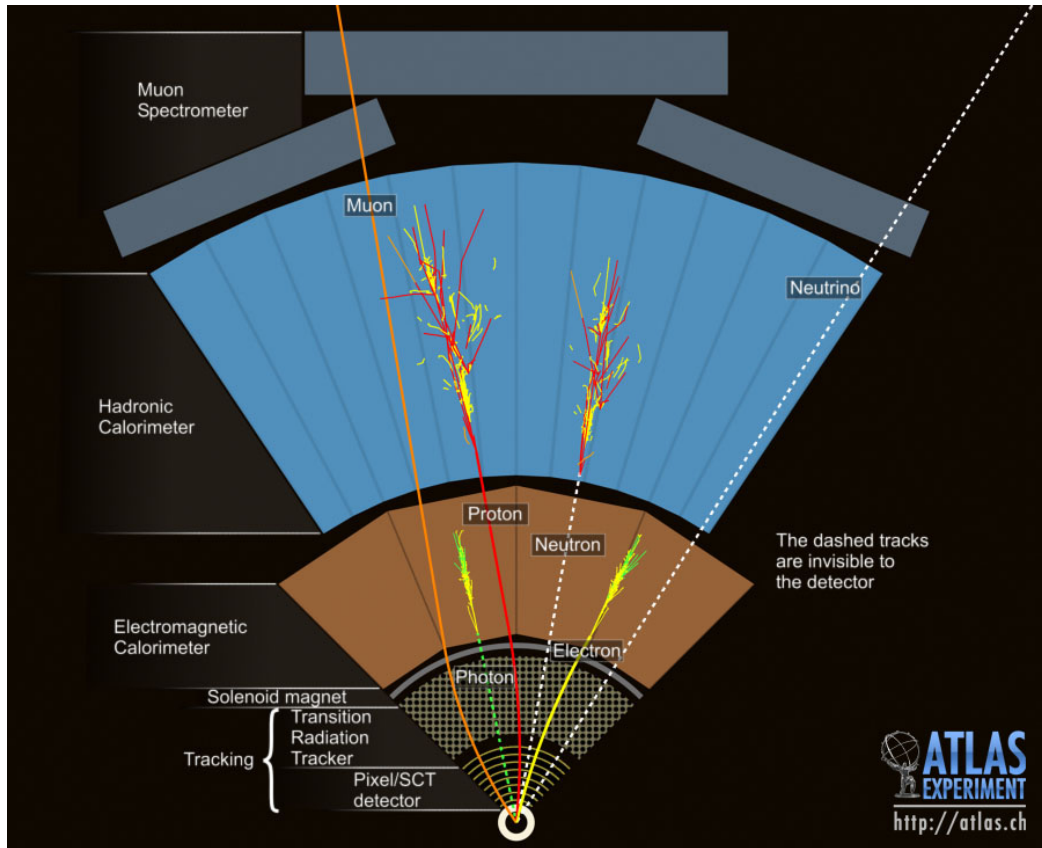


Figure 3.5: Illustration showing the detection of particles in each section of the ATLAS detector. Image courtesy of the ATLAS Experiment at CERN, <http://atlas.ch>.

Further details of the ATLAS detector design and expected physics performance can be found in the Technical Design Report in Ref. [27].

The ATLAS coordinate system is a right-handed system centred on the nominal interaction point at the centre of the detector. As shown in Fig. 3.6, the  $z$ -axis is parallel to the beam pipe, with the positive direction towards point 8 or the LHCb detector. The  $x$ -axis points towards the centre of the LHC ring and the  $y$ -axis points upwards. The angles  $\phi$  and  $\theta$  are the azimuthal (beam axis) and polar (from the  $z$ -axis to the  $x$ - $y$  plane) angles respectively. Pseudorapidity,  $\eta$ , as a function of the polar angle can be defined as:

$$\eta = -\ln \tan \left( \frac{\theta}{2} \right) \quad (3.5)$$

This term is generally used in particle physics to describe the angle of a particle within the detector since it can also be approximately defined as a function of the momentum of the particle,  $p$ :

$$y = \frac{1}{2} \ln \left( \frac{|\mathbf{p}| + p_z}{|\mathbf{p}| - p_z} \right) \quad (3.6)$$

Values of the momentum and energy in the x-y plane are described as transverse.

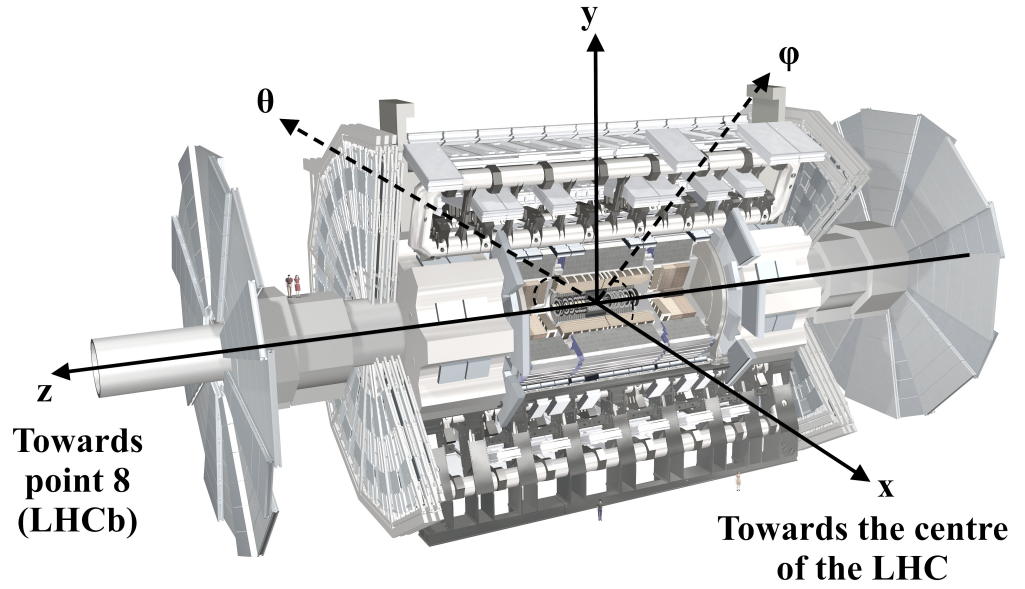


Figure 3.6: Illustration showing the ATLAS coordinate system. Background image courtesy of the ATLAS Experiment at CERN, <http://atlas.ch>.



### 3.2.1 The Inner Detector

The ATLAS Inner Detector (ID) [28, 29] is the closest sub-detector to the interaction point. It has an inner radius of 0.05 m, reaches an outer radius of 1.15 m and is 6.2 m wide. From the centre out, the ID is composed of the Pixel Detector, the Semi-Conductor Tracket (SCT) and the Transition Radiation Tracker (TRT), shown collectively in Fig. 3.7. In each sub-detector, the barrel regions lie parallel to the beam pipe with the end-caps perpendicular. The pseudorapidity region covered by the ID is  $|\eta| \leq 2.5$ . The material budget of the ID is required to be as low as possible to reduce the number of particles showering before reaching the calorimeters. This also reduces multiple scattering in the detector.

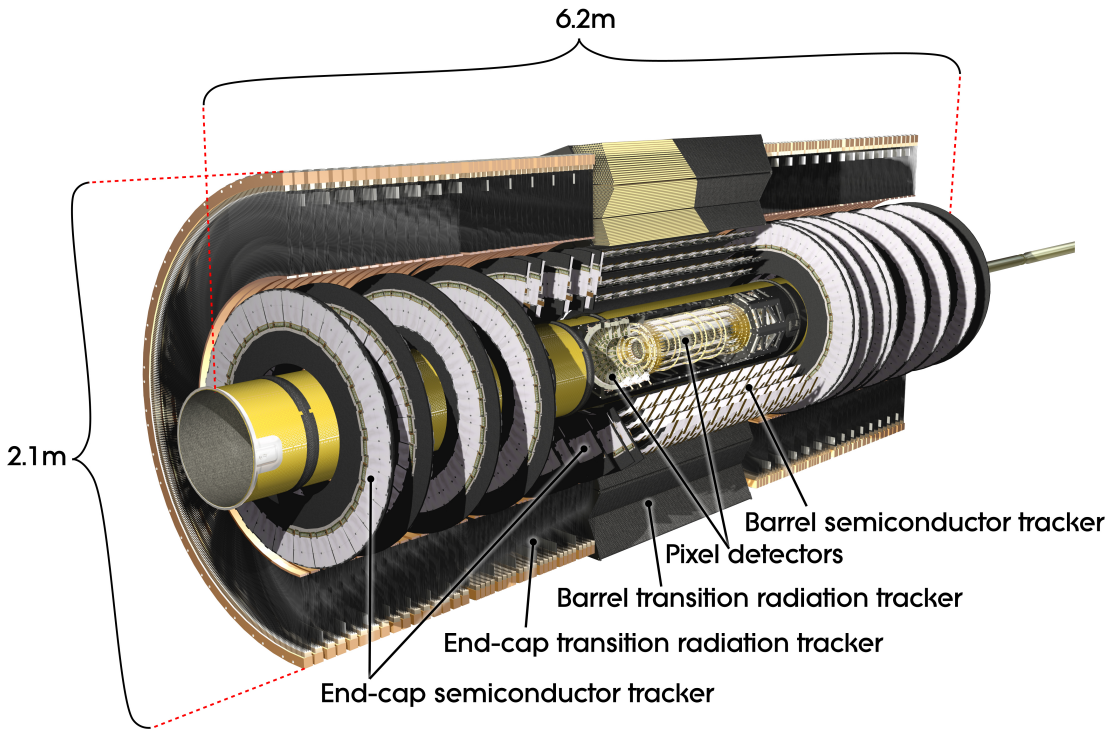


Figure 3.7: The ATLAS inner detector. Image courtesy of the ATLAS Experiment at CERN, <http://atlas.ch>.

Before the Inner Detector there is the 0.0008 m thick beryllium beam pipe, starting at a radius of 0.058 m. The beam pipe contains the vacuum environment required for the Large Hadron Collider and separates it from the ATLAS detector. The material choice was similarly to reduce particle showering and multiple scattering.

The solenoid magnet, located between the inner detector and the electromagnetic calorimeter, produces a magnetic field of 2 T which bends charged particles, allowing a measurement of their momentum.

### The Pixel Detector

At the very heart of ATLAS, the pixel detector is constructed from three barrel layers and six end-cap discs, three on either side, shown in Fig. 3.8. The barrel layers, from inside out, are layer 0 (also known as the b-layer), layer 1 and layer 2 at 50.5 mm, 88.5 mm and 122.5 mm from the interaction point respectively.

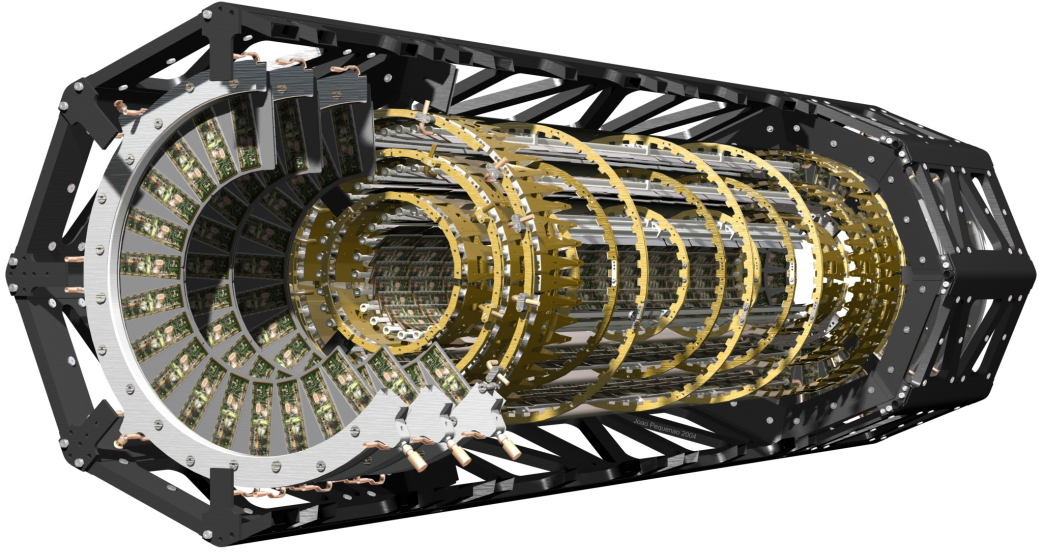


Figure 3.8: The ATLAS pixel sub-detector. Image courtesy of the ATLAS Experiment at CERN, <http://atlas.ch>.

The primary function of the pixel detector is to provide high granularity track points in order to allow reconstruction of particle positions as accurately as possible. By extending a particle track back towards the interaction point, it can be determined if the particle originated from close to the primary vertex of the interaction, or if it was the product of a ‘long-lived’ particle such as a bottom quark or  $\tau$ -lepton. In this case ‘long-lived’ is on the order of  $10^{-12}$  seconds, which is enough time for a particle to travel  $\sim 3$  mm. To be able to distinguish these vertices, the resolution of the pixel detector should be as small as possible. Calculated from the root mean squared of the residuals, from test beam the spacial resolution is  $12 \mu\text{m}$  in  $R\phi$  [15].

A Barrel Pixel Module is shown in Fig. 3.9 and consists of a hybrid structure of multiple parts (described in Section 2.4.2). The sensor for the pixel detector is a semiconductor planar  $n^+ - n$  silicon pixel sensor with a bulk thickness of  $256 \pm 3 \mu\text{m}$ . Each sensor is bump-bonded to a set of ATLAS FE-I3 front-end readout chips, discussed further in Section 4.1.1. There are sixteen FE chips in each module, arranged in two rows of eight. For each sensor tile there are 47232 pixels arranged as 144 columns by 328 rows. They have a standard pixel

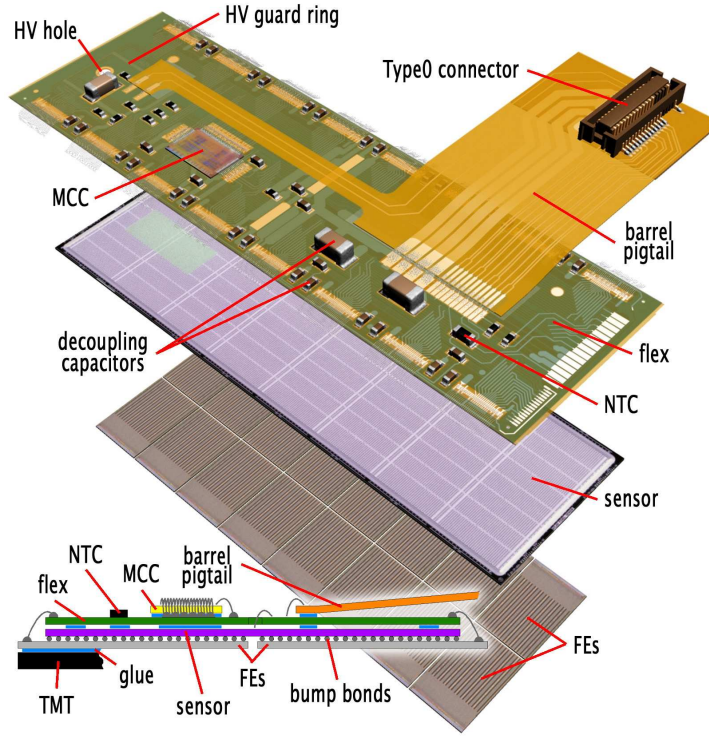


Figure 3.9: An ATLAS Barrel Pixel Module. The hybrid structure consists of sixteen front-end (FE) chips, the silicon sensor tile, the flex and the barrel pigtail [15].

pitch of  $400\text{ }\mu\text{m} \times 50\text{ }\mu\text{m}$ , which corresponds to the  $z$ - and  $\phi$ -directions respectively when installed in the ATLAS barrel. However, 11% of pixels have a pitch of  $600\text{ }\mu\text{m} \times 50\text{ }\mu\text{m}$ ; the extra length is to ensure complete coverage between neighbouring front-end chips and hence are located at the edge of the sensor. Pixels in the  $\phi$ -direction are connected (*ganged*) together between neighbouring FE chips, resulting in a total of 46080 readout channels per module. The MCC is the Module Control Chip [30] which controls the front end readout card.

The number of modules in each barrel and further information per layer is shown in Table 3.1. Table 3.2 shows the same information for the three end-cap layers (note that they are symmetrical on either side of the barrel) [15].

Due to the proximity to the interaction point, the pixel detector should be radiation hard and was intended to operate for ten years with an expected fluence of  $5 \times 10^{14}\text{ n}_{eq}\text{cm}^{-2}$  during the initial run of the LHC. To supplement the performance of the pixel detector, the addition of an extra layer was planned for the first shutdown (2013 – 2014). Called the Insertable B-Layer (IBL) project, this upgrade to the ATLAS ID is discussed in Section 4.1.

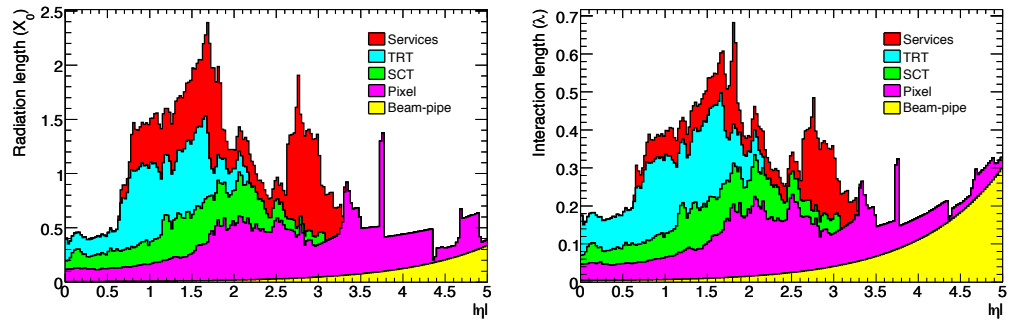


Table 3.1: Details for each barrel layer of the ATLAS pixel detector [15].

Layer Number	Mean Radius [mm]	Number of Staves	Number of Modules	Number of Channels	Active Area [m <sup>2</sup> ]
0	50.5	22	286	13,178,880	0.28
1	88.5	38	494	22,763,520	0.49
2	122.5	52	676	31,150,080	0.67
Total		112	1456	67,092,480	1.45

Table 3.2: Details for each endcap layer for the ATLAS pixel detector [15].

Disk Number	Mean z [mm]	Number of Sectors	Number of Modules	Number of Channels	Active Area [m <sup>2</sup> ]
0	495	8	48	2,211,840	0.0475
1	580	8	48	2,211,840	0.0475
2	650	8	48	2,211,840	0.0475
Total one endcap		24	144	6,635,520	0.14
Total both endcaps		48	288	13,271,040	0.28

Figure 3.10: Distribution of material by radiation length (left) and interaction length (right) within the ATLAS Inner Detector as a function of  $|\eta|$  [22].

For a detector close to the interaction point, the material budget of each barrel is an important factor to consider. If the material budget is too high, this will cause showering which will reduce the accuracy of the positional resolution of the tracking layers and result in lower energy measurements in the calorimeters. Figure 3.10 shows the distribution of the material described by the radiation length ( $X_0$ ) and the interaction length ( $\lambda$ ) as a function of  $|\eta|$ . The pixel layers (coloured in purple) have a greater contribution to this after 1.5  $|\eta|$ .

### The Semi-Conductor Tracker (SCT)

After the pixel detector is the Semi-Conductor Tracker (SCT), which is made from double-sided silicon strip detectors. Each side has 768 active strips which are mounted back-to-back and rotated to an angle of 40 mrad with respect to each-other, consequently providing a 3-dimensional space position for tracks within ATLAS. There are four barrel layers with 18 discs, nine in each end-cap, providing a minimum of four space points for tracking. The SCT has a spatial resolution of  $16\text{ }\mu\text{m}$  and  $580\text{ }\mu\text{m}$  in  $R\phi$  and  $z$  respectively.

### The Transition Radiation Tracker (TRT)

The Transition Radiation Tracker (TRT) is the final section of the Inner Detector and it continues the tracking of the particles with a greatly reduced material budget and at lower financial cost when compared to the semi-conductor layers.

The TRT is composed of multiple layers of straws, which lie parallel to the beam pipe in the barrel section and are arranged radially in the end caps. Each straw is 4 mm in diameter, with a maximum length of 150 cm. On average a charged particle crossing the TRT will produce 36 position points. Inside, the straws are filled with the intrinsically radiation hard xenon gas and a  $31\text{ }\mu\text{m}$  diameter gold-plated tungsten anode wire.

The resolution is  $130\text{ }\mu\text{m}$  per straw in the  $R\phi$  plane due to the drift-time measurements made for each straw. Two thresholds (a minimum and a maximum) are applied for electron identification due to transition radiation. Transition radiation occurs when a charged particle passes through a material boundary with different dielectric properties [31]. In this case the material is polypropylene which is arranged in fibres around the TRT straws. The resulting photons create larger ionisation signals in the Xenon gas than the crossing of a charged particle within the straw.

### 3.2.2 The Calorimeters

The ATLAS Calorimeters subsystem [32], as illustrated in Fig. 3.11, consists of the Electro-Magnetic (EM) and the Hadronic Calorimeter barrels and end-caps. The primary function of the calorimeter is to provide measurements of the energy and position of EM and hadronic showers as they develop. Both sections are known as ‘sampling calorimeters’ and consist of an absorbent layer to cause showering followed by a material for readout; these layers alternate until there has been sufficient material to measure the total energy of the particle shower. The shape of the shower reconstructed from energy deposit data gives an indication of the identity of the particle that produced it. Compared to a homogeneous design,

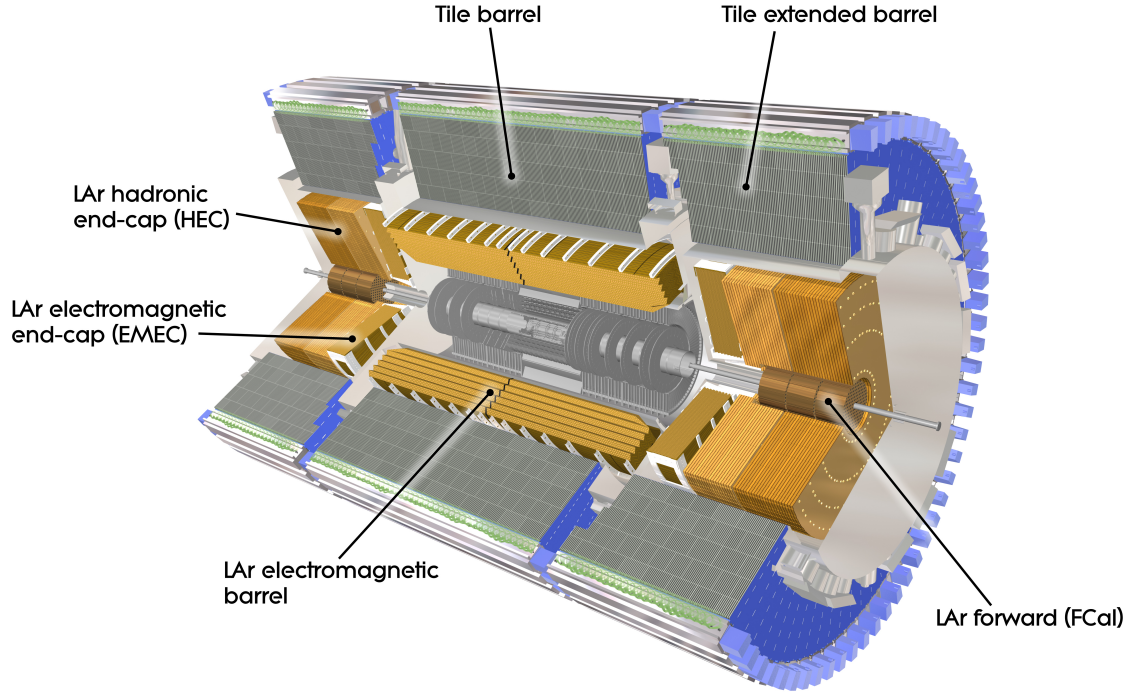


Figure 3.11: The ATLAS calorimeters. Image courtesy of the ATLAS Experiment at CERN, <http://atlas.ch>.

a sampling calorimeter has a better spacial resolution, but this is at the cost of the energy resolution.

### The Electromagnetic Calorimeter

The ElectroMagnetic (EM) calorimeter is built from layers of lead and liquid argon (LAr) and measures the energy of particles that interact via electromagnetic processes. The barrel section covers the region of  $|\eta| < 1.48$ , while the end cap is from  $1.38 < |\eta| < 3.2$ . Prior to the EM calorimeter, there is a pre-sampler layer of liquid argon to allow for corrections of energy lost in the inner layers.

### The Hadronic Calorimeter

The Hadronic Calorimeter consists of alternating layers of steel to absorb and scintillators to sample. The interaction processes in this subdetector are hadronic, such as interactions with the nucleus, which produce charged particles. The charged particles create ultraviolet (UV) light when they pass through the scintillators. This UV light is shifted in wavelength to visible light by a fibre and then collected and measured in photomultiplier tubes. The barrel covers the region  $|\eta| < 1.7$ , and the end caps cover  $1.5 < |\eta| < 3.2$ .

### 3.2.3 The Muon Spectrometer

As shown in Fig. 3.12, the ATLAS Muon Spectrometer (MS) system [33] is the outer most detector system of ATLAS and is designed to measure the momentum and charge of muons. As shown previously in Fig. 3.5, muons travel through the whole ATLAS detector so far without being stopped. Due to the high rate of collisions within ATLAS, a further use of the muon spectrometer is for level one triggering which reduces the volume of data read out.

The final layer of ATLAS is a toroidal magnet system. The system is inhomogeneous and provides a magnetic field in the range of 0.5 T in the barrel and 1 T in the end cap. The magnet bends the muons to allow momentum measurements within the MS.

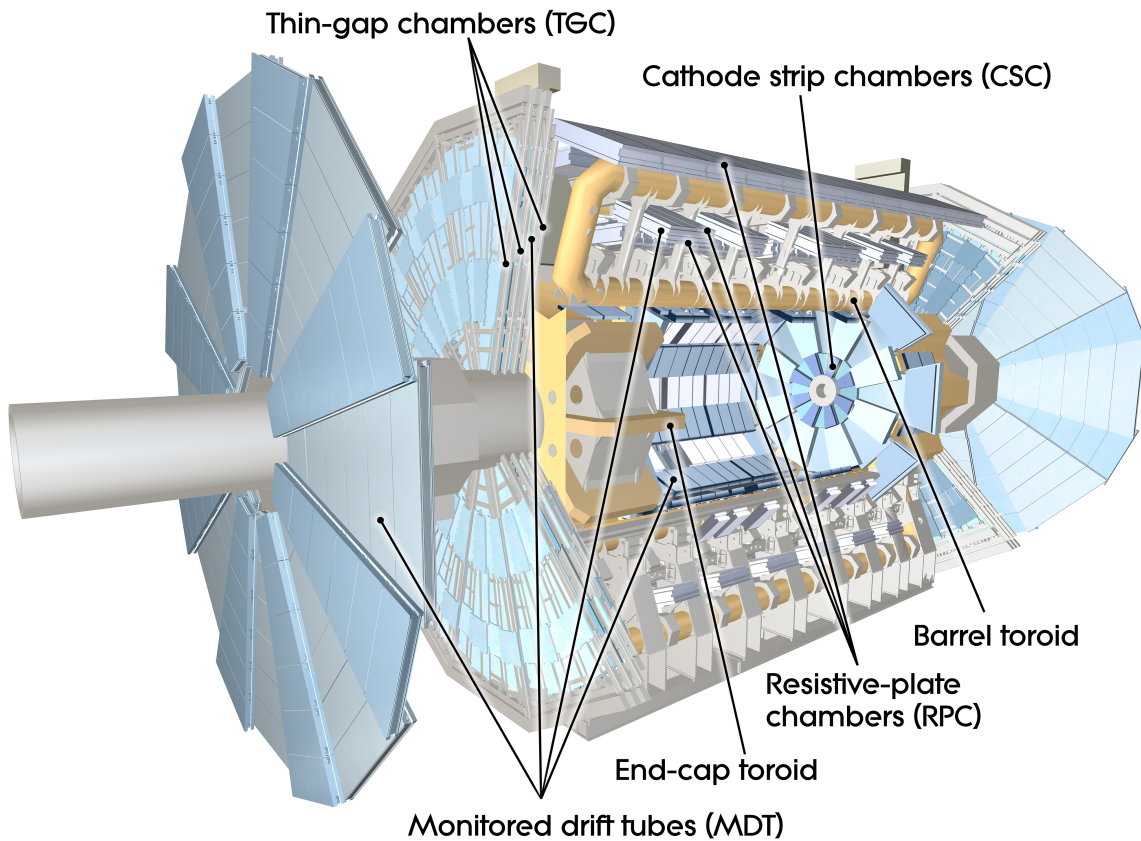


Figure 3.12: The ATLAS muon subsystem. Image courtesy of the ATLAS Experiment at CERN, <http://atlas.ch>.

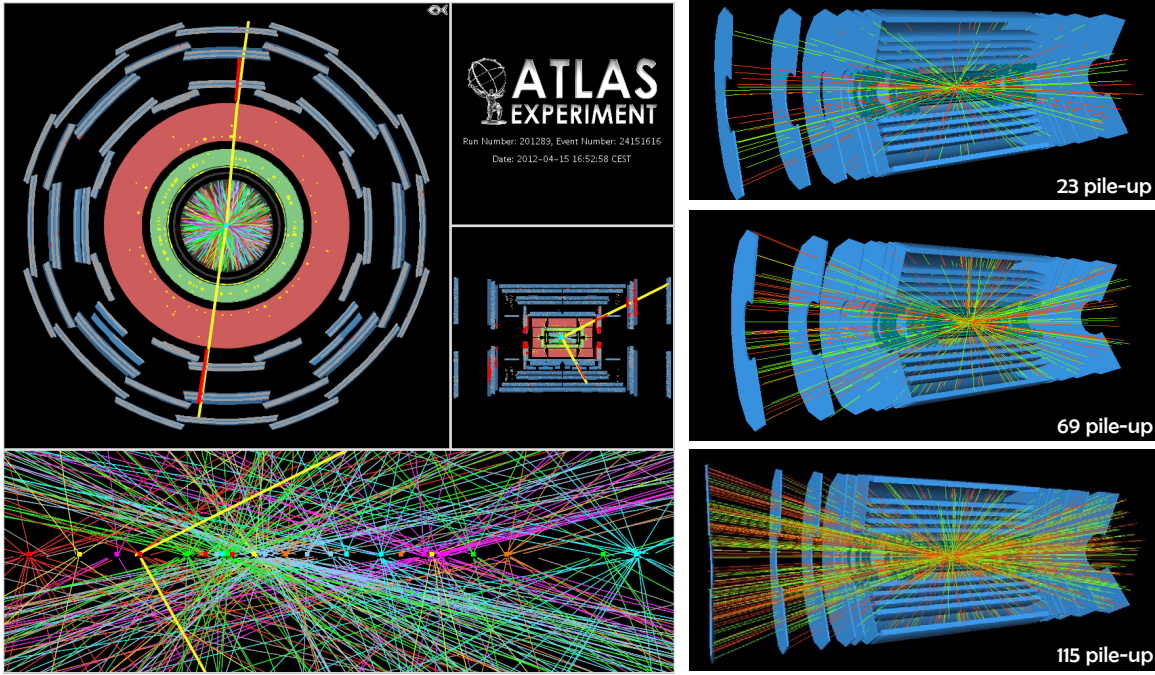
## 4 | ATLAS Pixel Upgrade

The Large Hadron Collider (LHC) has scheduled upgrades to increase the energy and luminosity of the beam. As a result, greater pile up is expected in the ATLAS detector, which will cause higher occupancy within modules. The pile up within ATLAS for a candidate Z boson event is presented in the event display in Fig. 4.1a. The lower part of the figure shows 25 reconstructed vertices and the multitude of tracks reconstructed. Figure. 4.1b shows the expected pile up in the baseline design of a new all-silicon inner detector, known as ITk, for an upgraded ATLAS. The pile up goes from 23 to 69 and eventually 115 [34]. The ATLAS detector, and especially the inner detector, must be upgraded to cope with these changes. The modules were designed for a fluency of  $1 \times 10^{34} \text{ cm}^{-2}\text{s}^{-1}$  and radiation damage that exceeds this will result in module failures.

Two upgrades to the ATLAS pixel tracker are planned: a supplementary layer closest to the beam pipe, known as the Insertable B-Layer (IBL) will be installed during the first long shut-down in 2013-2014. Details of the IBL are presented in Section 4.1. A new detector to be installed down the beam pipe 210 m from the centre of the ATLAS detector, which will be built using 3D silicon modules is also briefly discussed in Section 4.2.1. During the long shut-down in  $\sim 2022$ , the replacement of the entire pixel sub-detector for the High Luminosity LHC is foreseen, this is described in Section 4.2.2.

### 4.1 Insertable B-Layer

The proximity to the interaction point means that the ATLAS pixel sub-detector layer will receive the highest radiation dose of all ATLAS detectors. The fluence received within the inner detector as a function of distance in  $z$  (along the beam pipe) and  $R$  from the interaction point is shown in Fig. 4.2. As discussed in Section 2.3, radiation causes damage to the silicon sensors and also the readout electronics, which degrades the performance of the detector. In the long shutdown in  $\sim 2022$ , the whole inner detector will need to be replaced. However, instead of removing the current b-layer, due to timing and feasibility issues it was decided that another layer would be inserted. The ATLAS Insertable B-Layer (IBL) [35] project was set up to build and install a new pixel detector layer between the current ATLAS pixel b-



(a) A candidate Z boson event with 25 reconstructed vertices. (ATLAS Experiment © 2013 CERN)

(b) Pile up of 23 (top), 69 (middle) and 115 (bottom) in the base line design for an upgraded ATLAS inner detector [34].

Figure 4.1: Comparison of pile up in the current ATLAS inner detector (a) and simulated pile up in the base line design for an upgraded ATLAS inner detector (b).

layer and a new, narrower beam pipe of radius  $\sim 3.2$  cm. The photograph in Fig. 4.3a, shows the current ATLAS beam pipe and the pixel detector during the installation in building SR1 [28]. The rendered image in Fig. 4.3b illustrates the location of the new layer between the current pixel detector and a smaller beam pipe. The installation of the IBL is currently taking place (at the time of writing) during the long shut-down of the LHC in 2013-14. A further rendered image of the IBL in-situ can be found in Fig. 4.4

As discussed in Section 3.2.1, accurate tagging of secondary vertices is vital for many physics analyses, such as those containing a b-quark. This new inner pixel layer will improve the tagging efficiency in the ATLAS detector and assist in a higher pile-up environment. Due to the increased proximity to the interaction point and the smaller pixel size, the impact parameter resolution will improve with the addition of the IBL, resulting in improved tracking precision [35]. Furthermore, in the case of hardware failure in the other pixel layers, additional redundancy will be provided, with the inclusion of an extra space point.

The major specifications for technologies chosen for the IBL are written in Table. 4.1, with the sensor requirements written in Table. 4.2. Due to these requirements, novel pixel detec-



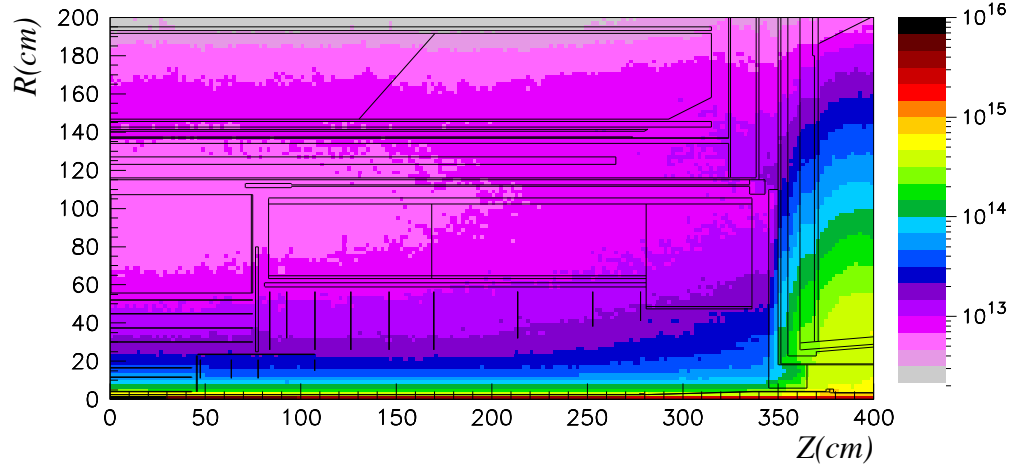
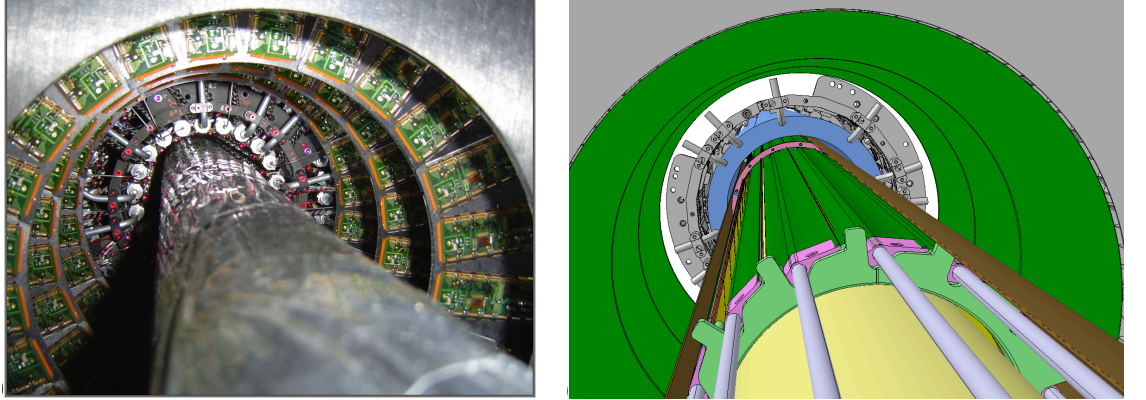


Figure 4.2: The fluence for the ATLAS Inner Detector as a function of distance from the interaction point (in R, outwards and Z, along the beam pipe). The fluence is given in units of  $1 \text{ MeV } n_{eq} \text{ cm}^2$  [28].



(a) Photograph of the current ATLAS pixel layers and the beam pipe. (b) Rendered image showing the location of the ATLAS insertable b-layer.

Figure 4.3: Comparison between the current pixel layer and the location of the insertable b-layer [35].

tor technologies were needed to cope with the demands. Three technologies were originally competing for inclusion within the IBL: planar silicon sensors (PPS), 3D silicon and diamond. In 2011, the planned installation of the IBL was brought forward two years from 2015-2016 to 2013-2014. Due to incompatibilities with the production schedule of diamond and the installation of the IBL, diamond was withdrawn from the selection process of potential technologies. The prototype diamond modules produced were selected to be used for the later named Diamond Beam Monitor (DBM) [36].

The IBL will be constructed of 14 staves; each staff consisting of 12 modules (75%) of pla-

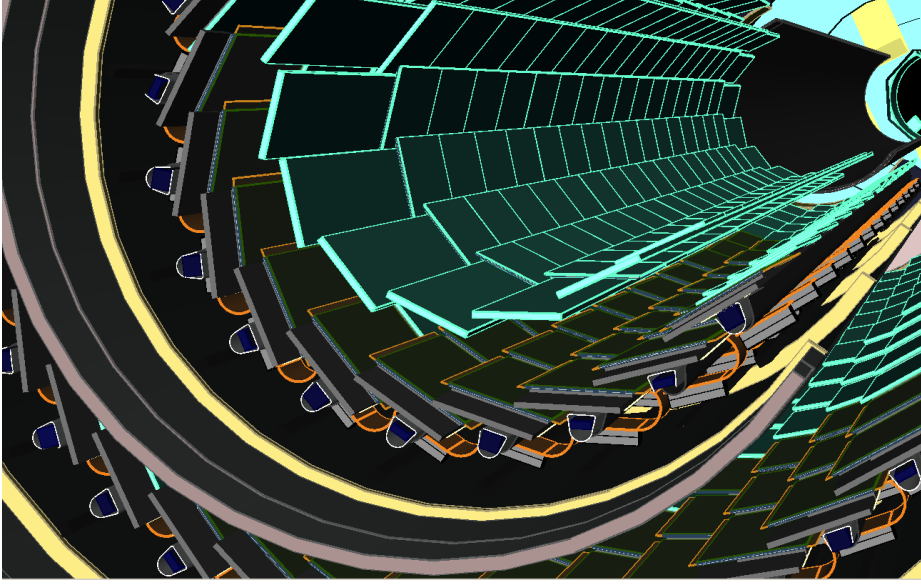


Figure 4.4: A rendered image of the ATLAS Insertable B-Layer inside of the current pixel layer [35]. The new, smaller beam pipe is not shown. Note that the IBL modules are tilted in  $\phi$  and overlap, but there is no overlap in  $z$ .

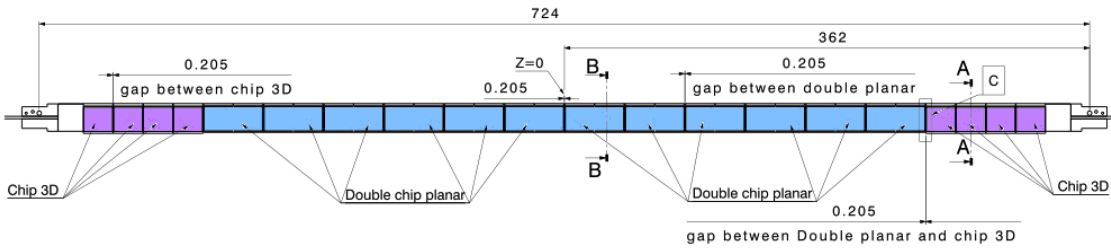


Figure 4.5: Diagram of the IBL stave layout for case with mixed sensor types. The 3D silicon modules (purple) are located in the high  $\eta$  regions at either edge of the stave, with the planar double chip sensors in the centre (blue). Original (black & white) image from [37]

nar n-in-n sensors and eight modules (25%) of 3D silicon sensors. The latter will be located symmetrically in the high  $\eta$  regions, four either side as illustrated in Fig. 4.5. The arrangement is to make the most of the charge collection capability at the highest angles. The IBL staves will be made of carbon fibre with a titanium cooling pipe and  $\text{CO}_2$  will be used as the method of cooling. A schematic of the cross-section of the IBL [35], indicating the tilt of the staves with respect to the interaction point, and the overlap between neighbouring staves, is shown in Fig. 4.6. Each stave will be tilted in the radial direction by  $14^\circ$ , which will compensate for the reduced efficiency of normal incident tracks that pass through the electrodes of 3D silicon devices (see Section 5.2).



Table 4.1: Specifications for technologies to be included in the IBL.

	Value	Unit
Number of staves	14	
Number of modules per stave (single/double FE-I4)	32 / 16	
Pixel size ( $\phi, z$ )	50, 250	$\mu\text{m}$
Module active size WxL (single/double FE-I4)	16.8 x 20.4 / 40.8	$\text{mm}^2$
Coverage in $\eta$ , no vertex spread	$ \eta  < 3.0$	
Coverage in $\eta$ , $2\sigma$ (=112 mm) vertex spread	$ \eta  < 2.58$	
Active z extent	330.15	mm
Geometrical acceptance in z (min,max)	97.4, 98.8	%
Stave tilt angle in $\phi$ (center of sensor, min, max)	14.00, -0.23, 27.77	degree
Overlap in $\phi$	1.82	degree
Center of the sensor radius	33.25	mm
Sensor thickness:		
Planar silicon	200	$\mu\text{m}$
3D silicon	$230 \pm 15$	$\mu\text{m}$
Radiation length at $z=0$	1.54	% of $X_0$

Table 4.2: Sensor requirements for IBL devices [35].

Requirement	Value	Conditions
NIEL dose tolerance	$5 \times 10^{15} \text{ n}_{eq}\text{cm}^{-2}$	–
Ionizing dose tolerance	250 Mrad	–
Hit efficiency in active area* r- $\phi$	>97%	Single MIP
MIP resolution*	<10 $\mu\text{m}$	2T B-field, 15° incidence
Z MIP resolution*	72 $\mu\text{m}$	Digital resolution for 250 $\mu\text{m}$ pixel
Maximum bias voltage	1000 V	–
Radiation thickness	<500 $\mu\text{m}$ Si equiv.	–

There are two versions of the FE-I4b module for the IBL known as the single-chip and the double-chip, holding one and two sensors respectively. Planar modules will be constructed with the double-chip front end, while 3D silicon sensors will solely use single chips, with two single 3D silicon chips making a module. This is due to the differences in the fabrication processes between planar and 3D silicon sensors.

The design for the 3D silicon pixel sensor will be discussed in Section 5.3, but the photograph in Fig. 4.7 illustrates the difference in size between the two types of modules, the double-chip width being twice as long as the single-chip.

The planar silicon sensor design is a 200  $\mu\text{m}$  thick n-in-n with electrodes implanted on the surface and is manufactured by CiS, Germany. They have a slim edge design utilising a

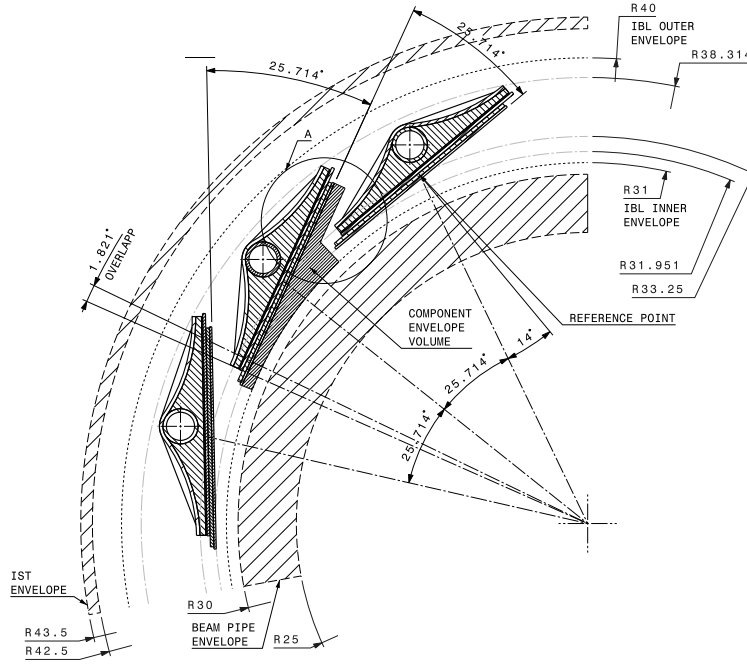


Figure 4.6: Drawing of the cross-section of the IBL staves in the ATLAS detector [35]

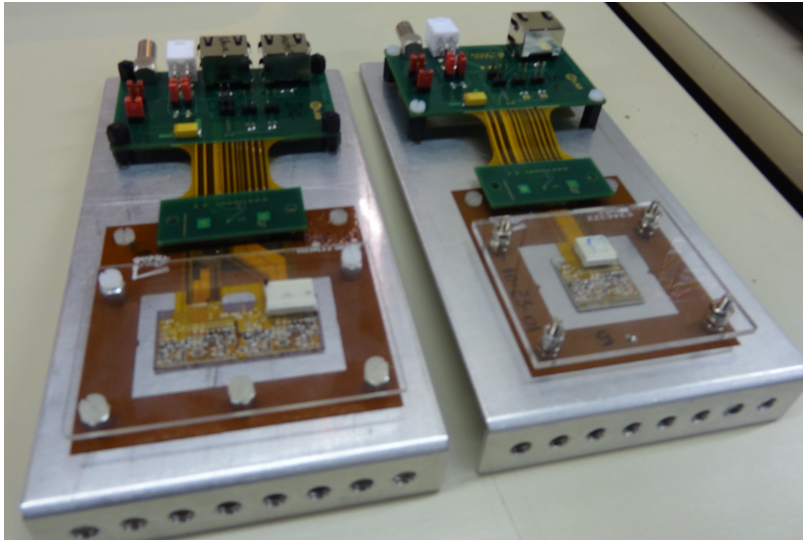


Figure 4.7: Comparison of double-chip planar module and single chip 3D silicon module for the IBL both bonded to FE-I4 flex readout chips and mounted onto aluminium L-plates in preparation for a beam test. Note the difference in size; the double chip planar sensor has a width twice as long when compared to the single-chip sensor.

guard ring structure that reduces the dead area at the edge of the sensor to  $\sim 200 \mu\text{m}$ , as illustrated in Fig. 4.8 [35].

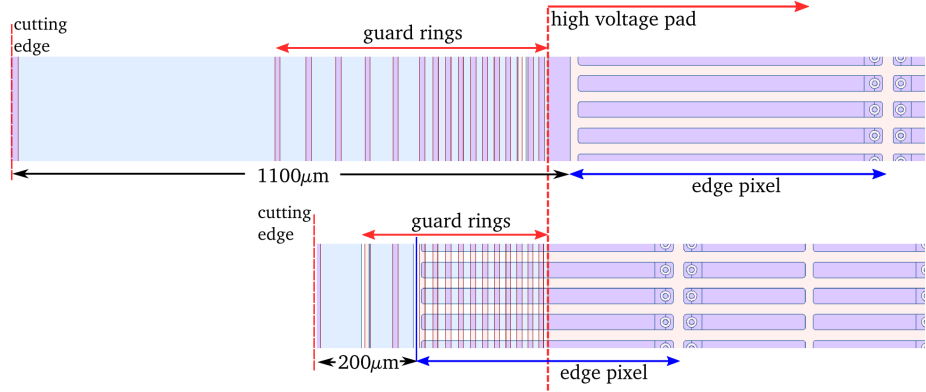


Figure 4.8: Comparison of the current ATLAS planar pixel edge (above) with the newer slim-edge design used for the IBL. The inactive region is reduced from 1100  $\mu\text{m}$  to 200  $\mu\text{m}$  [35].

#### 4.1.1 Readout electronics

Due to the small space available for the IBL, it was decided that it would not be possible to tilt the sensors in the  $z$ -direction. Therefore, to compensate for loss of efficiency from gaps between modules, larger sensors with a greater active area were desirable. Furthermore, to improve the impact resolution, a design with smaller pixels was selected. This meant that new readout electronics were required to be compatible with this new design. For comparison, the size of the new pixel readout card and the current ATLAS version are shown in the superimposed photographs in Fig. 4.9. Numerical values for the specification for the new readout chip are displayed in Table. 4.3. The new readout card designed for the IBL is called FE-I4 [38]. The chip size is 20.0 by 18.6  $\text{mm}^2$  compared to the smaller FE-I3 readout card which is 7.6 by 10.8  $\text{mm}^2$ . The increase in size will reduce the material budget of the IBL (since less overlap for the devices will be required) and the total cost of bump-bonding will also be reduced. The pixel size is smaller in FE-I4, with the long edge reduced from 400  $\mu\text{m}$  to 250  $\mu\text{m}$ . This results in a greater number of total pixels in the array. The short pixel edge is maintained at 50  $\mu\text{m}$  as this is limited by the bump-bonding pitch. As a consequence of the larger size of the readout chip, the total inactive fraction of the chip is reduced.

The increase in the data rate from 40  $\text{Mb s}^{-1}$  for FE-I3 modules to 160  $\text{Mb s}^{-1}$  for FE-I4 modules will greatly increase the capabilities of the module in a higher hit-rate environment.

There is an independent analogue component for every individual pixel. At this stage, the threshold, which discriminates the hits, and the conversion from charge to a time over threshold (TOT) value are both applied. Both values are tuned by the user (see Section 6.3.1). Figure 4.10 illustrates the organisation of the FE-I4 readout chip. The pixels in the readout

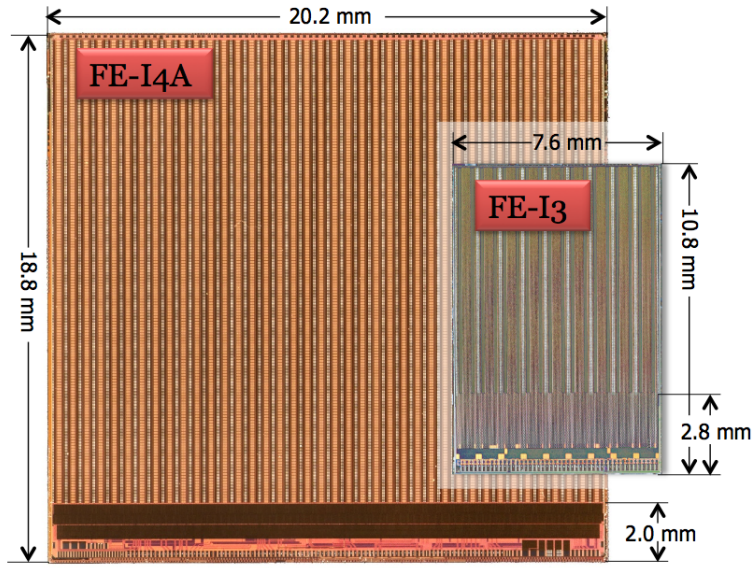


Figure 4.9: Size comparison between the current pixel detector readout chip (FE-I3) and the new readout chip designed for the IBL (FE-I4) [39].

Table 4.3: Comparison of specifications for FE-I3 and FE-I4 readout cards.

	FE-I3	FE-I4
Pixel Size	$50 \times 400 \mu m^2$	$50 \times 250 \mu m^2$
Pixel Array	$18 \times 160$	$80 \times 336$
Chip Size	$7.6 \times 10.8 mm^2$	$20.0 \times 18.6 mm^2$
Active Fraction	74%	89%
Analogue Current	$16 \mu A/\text{pixel}$	$10 \mu A/\text{pixel}$
Digital Current	$10 \mu A/\text{pixel}$	$10 \mu A/\text{pixel}$
Analogue Supply Voltage	1.6V	1.5V
Digital Supply Voltage	2.0V	1.2V
Data Rate	40Mb/s	160Mb/s

chip are divided into double columns. A four-pixel digital region, also known as 4-PDR, groups a pair of pixels either side of this double column structure [39]. Information is then sent from the 4-PDR to the peripheral logic in the 2.0 mm at the edge of the chip. Figure 4.11 illustrates the output of the discriminator after the preamplifier.

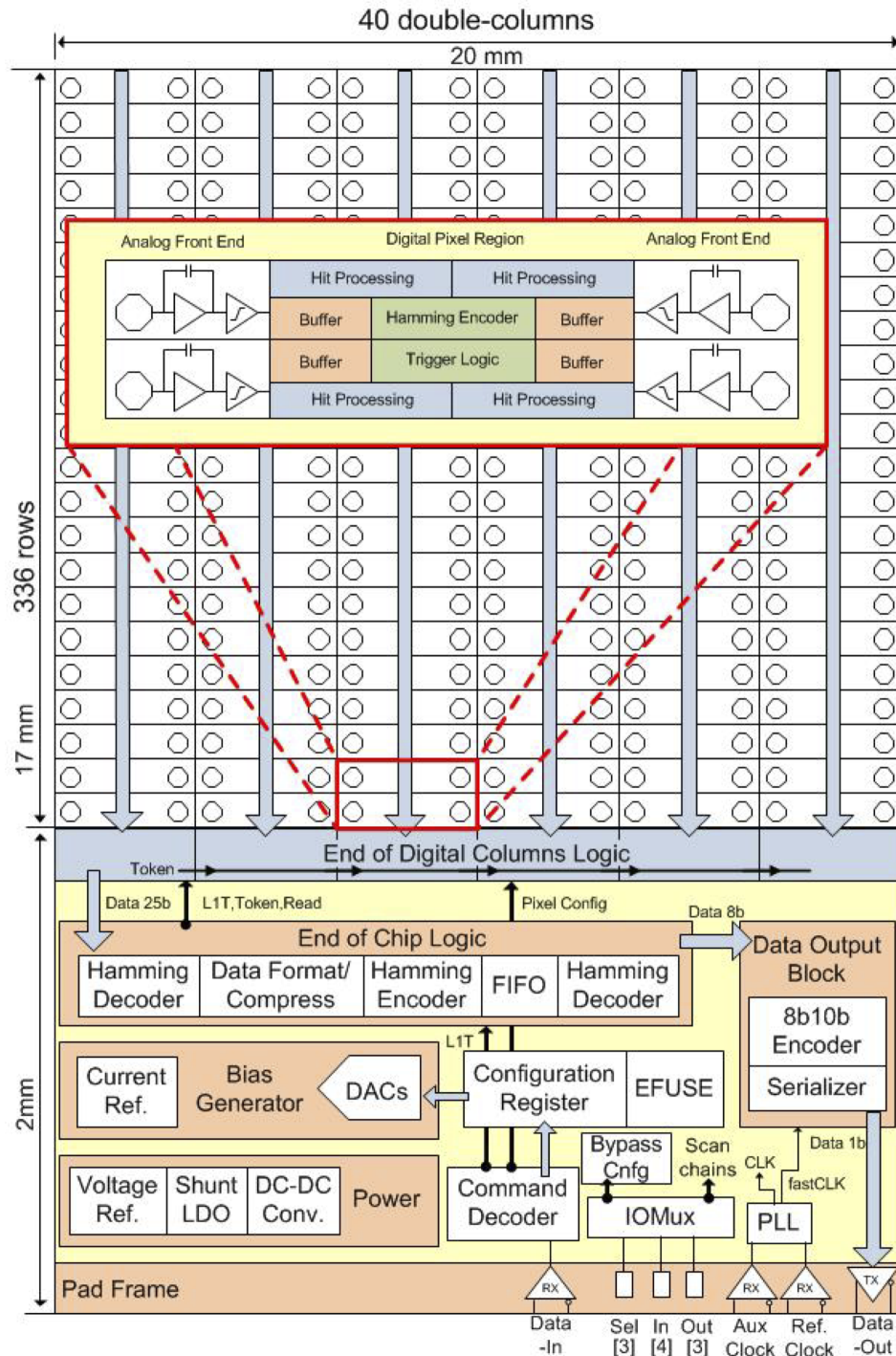


Figure 4.10: A sketch of the ATLAS FE-I4a readout chip, illustrating the organisation of the integrated circuit [39].

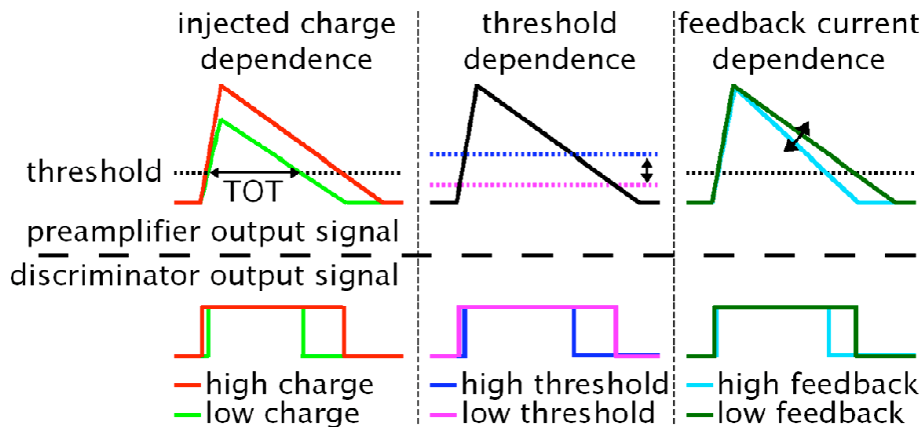


Figure 4.11: Comparison of the relationship between the preamplifier signal and the discriminator output signal for changes in the injected charge, threshold and feedback current [40].

## 4.2 Further upgrade projects

The applications for 3D silicon detectors in addition to the IBL are manyfold. Those relating to ATLAS upgrade are presented below.

### 4.2.1 ATLAS Forward Physics

The process [41] shown in Fig. 4.12 is known as Central Exclusive Production (CEP). Compared to a collision, in which the protons are destroyed and all of their energy goes into the creation of new particles, in this process the protons remain intact and continue to travel down the beam pipe. These protons will have less energy than the other protons in the beam and so will bend differently in the magnetic fields, essentially using the LHC as a spectrometer. The central system produced could be a Higgs boson (or another new particle), which would decay and be detected in the ATLAS detector.

A detector placed 220 m down the beam pipe would be able to detect the spacial position of protons undergoing CEP and determine their missing energy. This detector would need to be as close to the beam pipe as possible, without interfering with the beam. Therefore sensors used would be required to have as little dead area as possible. The detector would also need to be movable transversely to the beam pipe so that it does not effect the beam during injections and ramping [41] Beam test studies<sup>1</sup> show promising results for 3D silicon sensors that have good initial electrical performance before inhomogeneous irradiation [42].

<sup>1</sup>The author assisted in the acquisition of data for these studies, but not in the analysis of results.



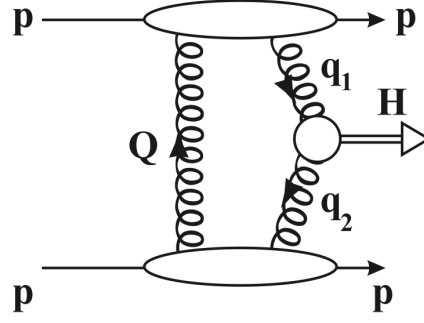


Figure 4.12: Feynman diagram showing a Higgs boson particle produced from two protons which remain intact and continue to travel down the beam pipe [41].

The inhomogeneous irradiation level for CNM 57, an FE-I4 device, is shown in Fig. 4.13a. The efficiency sensor map in the top of Fig. 4.13b, shows the efficiency for the whole sensor. Higher pixel rows received the greater irradiation dose. The bottom hitmap is a combination of the pixel efficiency for all pixels (after the exclusion of dead and noisy pixels) in the lower irradiated region. 3D silicon devices with IBL design have been selected as the technology of choice for the ATLAS forward physics detector due to slim edges and radiation hardness.

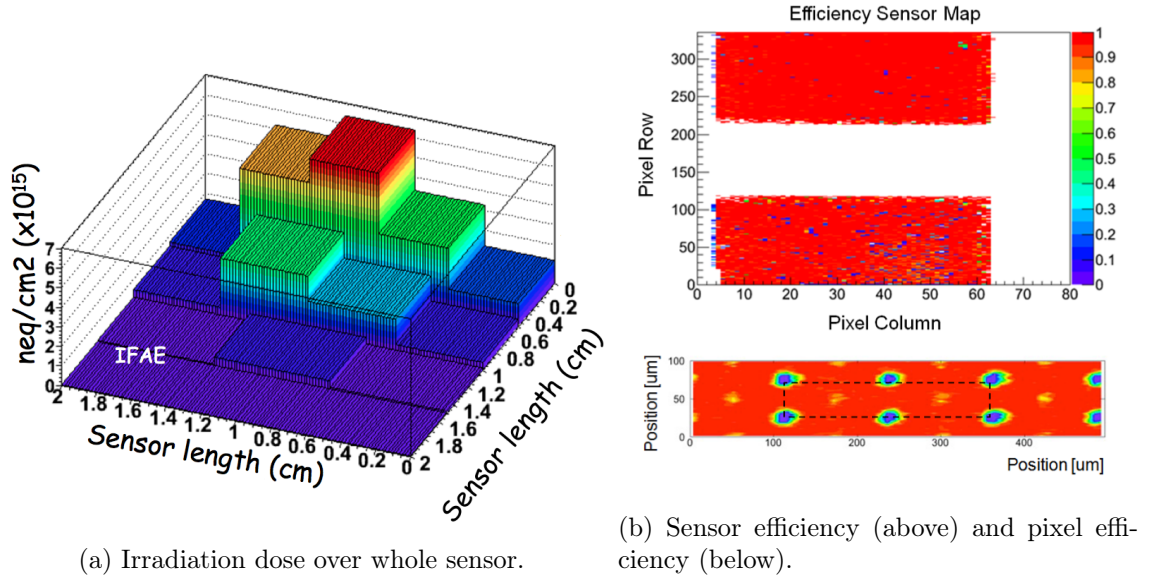


Figure 4.13: The irradiation dose distribution over CNM 57 (a) and the corresponding sensor efficiency and pixel efficiency maps from AFP beam test studies [42].

#### 4.2.2 High luminosity LHC

The phase 2 shutdown period, planned for 2021 – 2022, will see major upgrades to the accelerator facility at CERN. The LHC will become the High-Luminosity LHC (HL-LHC)

as the instantaneous luminosity is increased to  $5 \times 10^{34} \text{ cm}^{-2} \text{ s}^{-1}$ . As the luminosity of the LHC increases to an expected  $10^{35} \text{ cm}^{-2} \text{ s}^{-1}$  and the bunch crossing decreases, the high radiation environment will extend further out from the ATLAS interaction point, requiring radiation hard pixel layers at higher radii. Pixel detector technology for the HL-LHC will therefore be required to be of low radiation length and minimal cost for the production of many sensors. A total dose of  $2 \times 10^{16} \text{ n}_{eq} \text{ cm}^{-2}$  is expected for the closest layers.



## 5 | 3D Silicon Detectors

Three-dimensional (3D) silicon pixels sensors, introduced in 1995 [43] as an alternative to planar silicon detectors, are so-named because the electrodes, of one or both doping types, penetrate the bulk of the silicon wafer perpendicular to the surface. This 3D structure is dissimilar to the planar silicon pixel sensors currently in the ATLAS inner detector, where the electrodes are implanted on the surface of the device. Due to the collaborative nature of the working relationship between the 3D ATLAS R&D Collaboration, consisting of 18 institutions, and the four processing facilities where 3D silicon sensors are manufactured, the time scale between design conception and manufacturing was accelerated [44].

This chapter presents a description of 3D silicon detectors, including the fabrication process in Section 5.1. The various design layouts are discussed in Section 5.2 and Section 5.3 describes the layout chosen for the IBL upgrade project.

### 5.1 Fabrication

The four processing facilities where 3D silicon devices are produced are:

- CNM (Centro Nacional de Microelectrónica) in Barcelona, Spain
- FBK (Fondazione Bruno Kessler) in Trento, Italy
- SINTEF (Stiftelsen for Industriell og TEknisk Forskning) in Oslo, Norway
- Stanford Nanofabrication Facility, Stanford University, CA, USA

There are a number of fabrication steps required to manufacture 3D silicon detectors. Firstly, the silicon wafer must be grown. A 4-inch sized wafer is produced using the Float Zone (FZ) technique. The selection of doping type for the readout electrodes is decided by the speed of the charge carriers. In this case electrons are the charge carriers and therefore n-type readout electrodes are used. The bulk doping type is chosen primarily for radiation hardness (see Section 2.3). Consequently, the wafer is doped to be p-type, since n-type silicon is found to suffer from type inversion due to irradiation damage and the junction moves to the opposite

side.

Creating electrodes within the silicon bulk is possible due to a technology known as Deep Reactive-Ion Etching (DRIE) [45], developed for Micro-Electro-Mechanical Systems (MEMS). A method of DRIE, known as the Bosch process, uses a repetitive alteration of plasma etching and the application of a passivation layer. The plasma etching *drills* into the silicon wafer and the passivation layer prevents the etching from occurring parallel to the wafer surface. This process produces long columns with an aspect ratio as low as 20. For example, 400  $\mu\text{m}$  long columns with a radius of 50  $\mu\text{m}$  etched at SINTEF can be seen in Fig. 5.1. These columns can subsequently be doped with poly-silicon to form electrodes.

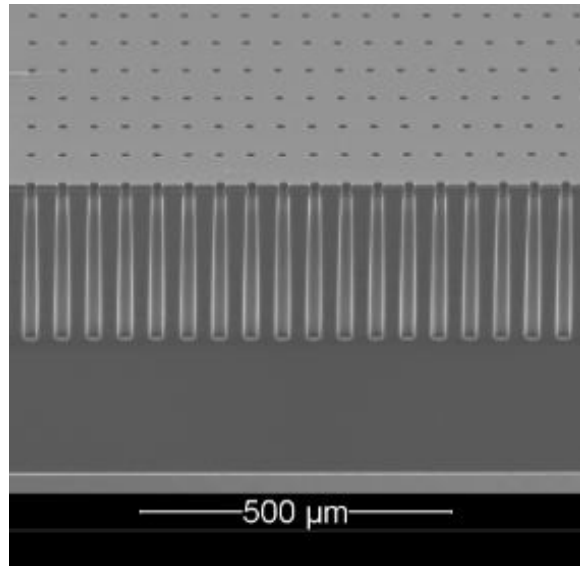


Figure 5.1: Holes in the silicon wafer etched using the DRIE process at SINTEF [46]. The holes are 400  $\mu\text{m}$  long with a radius of 50  $\mu\text{m}$ .

The final stage is the removal of the support wafer required for mechanical strength during the fabrication process.

This complicated fabrication process can be simplified by manufacturing the 3D sensor with a double-sided design. These sensors are produced at CNM and FBK with the electrodes penetrating from both sides of the wafer. The major manufacturing benefit is that this does not require a support wafer. However, it is not feasible to include an active edge, so a slim edge design is implemented instead (see Section 5.2.2).

Further details of the fabrication process of 3D sensors can be found in the following references [47, 48].

## 5.2 3D Silicon Layouts

As described in Section 2.1, the electron-hole pairs, produced when a charged particle passes through the silicon sensor, drift due to the electric field towards the  $n^+$  and  $p^+$  electrodes respectively. Due to the layout of the electrodes, this path is parallel to the wafer surface in 3D silicon devices instead of perpendicular as in planar pixel sensors. A sketch illustrating a charged particle traversing a 3D silicon sensor (left) and a planar sensor (right) with the relative paths of the charge carriers to the electrodes is shown in Fig. 5.2.

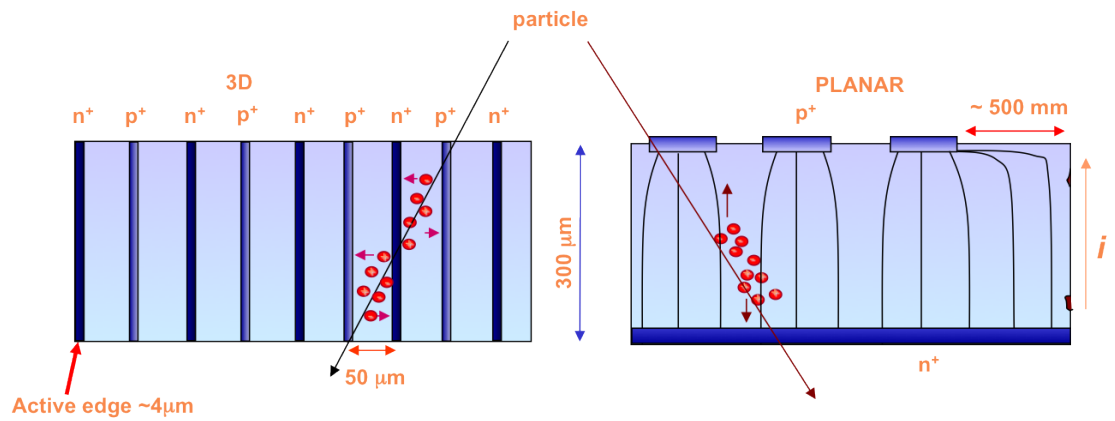


Figure 5.2: Comparison between a 3D silicon sensor (left) and a planar sensor (right). The difference between the position of the electrodes and consequently the inter-electrode distance can clearly be seen. Figure taken from [49].

The layout of 3D silicon sensors plays a key role in the success of this technology. The collection distance between electrodes, which can be as low as 50  $\mu\text{m}$ , is decoupled from the wafer thickness, responsible for charge generation. The charge generated for an identical minimum ionising particle traversing each sensor technology would be the same if the wafer material and thickness do not differ. The main benefits intrinsic to 3D detector technology when compared with standard planar silicon pixel devices are:

- Faster response time, providing the pixel pitch is less than the thickness of the bulk. This is due to the shorter distances the electrons have to travel before they are picked up by an electrode, as illustrated in Fig. 5.2.
- Greater radiation hardness [50]. The short distance between electrodes reduces the path required for charge carriers to travel before the signal is collected. This results in a reduced likelihood that the charge will encounter a defect during its path.
- Lower bias voltage required to fully deplete the sensor [51].

Table 5.1: Comparison of 3D and planar pixel sensors [52].

Sensor geometry	3D	Planar
Collection path	$\sim 50 \mu\text{m}$	200–300 $\mu\text{m}$
Depletion voltage	$< 10 \text{ V}$	30–100 V
Charge collection time	$\sim \text{ns}$	Tens of ns

The differences between 3D and planar pixel sensors for major parameters are in Table 5.1 [52]. Many methods of readout are possible for 3D silicon devices since the electrodes are accessible from both above and below the detector.

A sketch of a pixel cell is shown in Fig. 5.3. The cell is centred with half a pixel extended in the horizontal and vertical directions. The bias electrodes are doped p-type and are shown in blue. The readout electrodes are shown in red and are doped n-type.

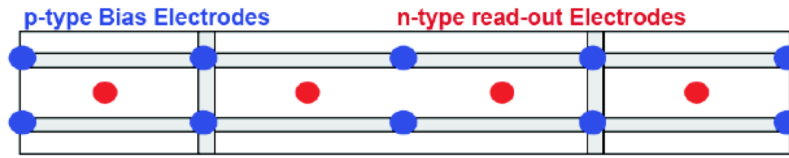


Figure 5.3: A sketch of a 3D silicon pixel cell with two electrodes per pixel. The cell is centred in the figure, with half a cell extending in each direction. The bias electrodes are doped p-type and are shown in blue. The readout electrodes are shown in red and are doped n-type.

### 5.2.1 Electrode configuration

There are different possibilities for the arrangement of electrodes within a 3D sensor pixel depending on the number of electrodes in each. Figure 5.4 shows the layouts for FE-I3 sized pixels with pitch of 400 by 50  $\mu\text{m}$  with two (left), three (middle) and four (right) electrodes per pixel, referred to as 2E, 3E and 4E respectively. The p-n inter-electrode spacing for each design is 103  $\mu\text{m}$ , 71  $\mu\text{m}$  and 56  $\mu\text{m}$ . Note that the pixels at the edges of an FE-I3 sensor are  $\sim 100 \mu\text{m}$  longer and so an extra electrode is included to fill the gap and maintain the inter-electrode spacing. Pixel cells are arranged in a tessellated formation to reduce the amount of dead space.

There are advantages to having a higher number of electrodes per pixel. For example, the p-to-n inter-electrode distance decreases as the number of electrodes per pixel increases. This results in an increase in the response time of the sensor, a lower bias voltage and better radiation hardness. As shown in Fig. 5.5, the signal efficiency of the sensor with two electrodes

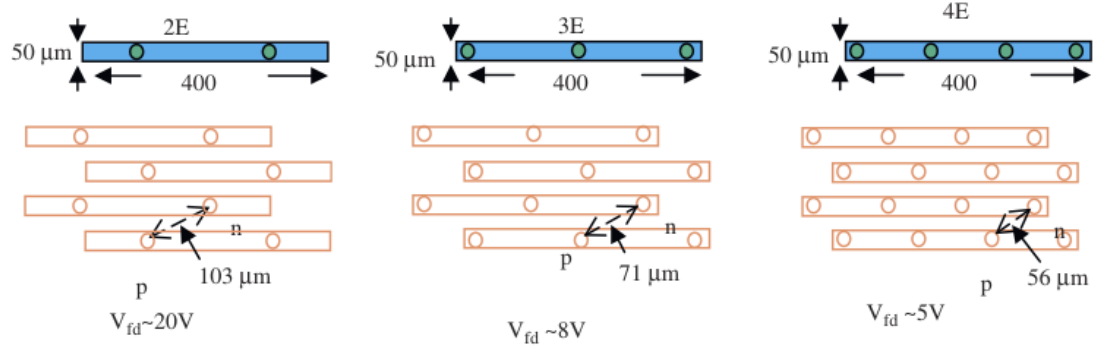


Figure 5.4: 3D sensors with FE-I3 pixel pitch ( $400 \times 50 \mu\text{m}$ ) with two (left), three (middle) and four (right) electrodes per pixel [53]. The inter-electrode distance, and as a result the bias voltage required, varies for the different layouts.

per pixel (2E) and hence a larger inter-electrode distance is lower than for four electrodes per pixel (4E) (smaller inter-electrode distance) for the same fluence [53].

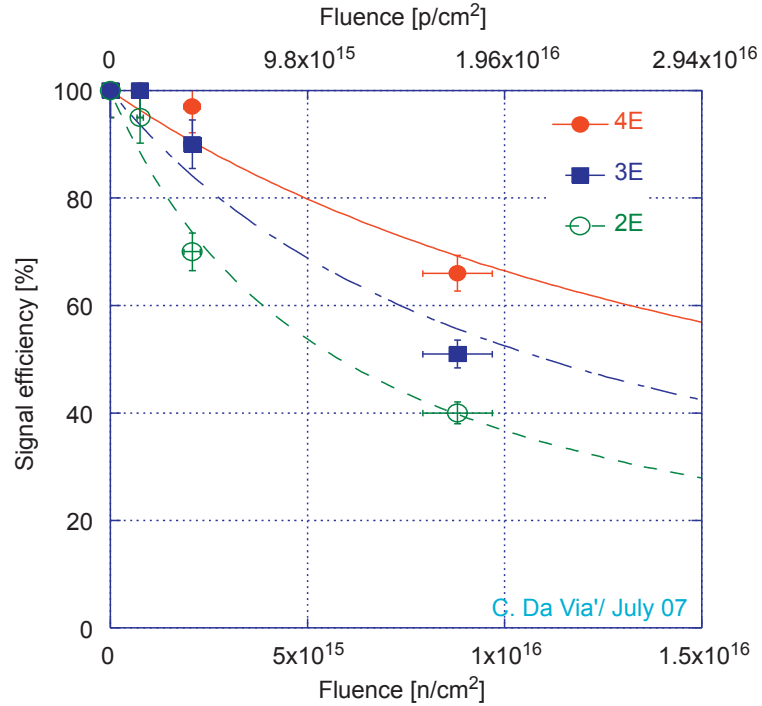


Figure 5.5: The signal efficiency for 2E, 3E and 4E 3D silicon devices as a function of the fluence [53].

However, it is known that there is a lower charge collection efficiency when a particle track

passes through an electrode (such as when the sensor is perpendicular to a particle beam) [54]. Consequently, an increase in the density of electrodes in the entire sensor will negatively effect the overall efficiency of the device when placed perpendicular to a particle beam [53]. However, the probability that the signal will be trapped due to a defect increases with the inter-electrode distance.

### 5.2.2 Active and slim edges

An important requirement for a new pixel detector technology is that the sensors are active as close to their physical edge as possible to reduce the amount of ‘dead area’ on the sensor. This reduces the need to overlap sensors to ensure full coverage and hence there will be less total material in the detector, minimising multiple scattering and energy loss close to the interaction point. In previous detectors, guard ring structures were required to gradually lower the voltage and to terminate electric field lines [55] resulting in a large inactive region at the edge of the detector. In 3D silicon devices, a smaller inactive region is achieved through etching a trench into the edge of the silicon wafer using the same process used to create the electrodes. The trench is doped to produce a final electrode at the wafer edge which completes the electric field lines, thereby reducing the dead area to no more than a few microns [56]. This process requires a support wafer and is therefore only suitable for the original full 3D design.

For the manufacture of a double-sided 3D structure, creating an active edge is not possible, so a slim edge design is produced via additional electrodes after the edge pixel - a 3D version of the guard ring design [58]. A one dimensional hit efficiency map projected in the long pixel direction at the edge region of an irradiated FE-I4 CNM detector is displayed in Fig. 5.6, along with a sketch of the layout of the edge pixel. The edge pixel has the same dimensions as the other pixels in the device and is  $250\text{ }\mu\text{m}$  long. The CNM device was irradiated with neutrons to a fluence of  $1 \times 10^{15}\text{ n}_{eq}\text{ cm}^{-2}$  and was biased at 160 V (slightly below full depletion resulting in a higher efficiency drop at the electrodes, although this did not affect the edge efficiency result). Due to the slim edge design, the inactive region is a modest  $200\text{ }\mu\text{m}$  [57].

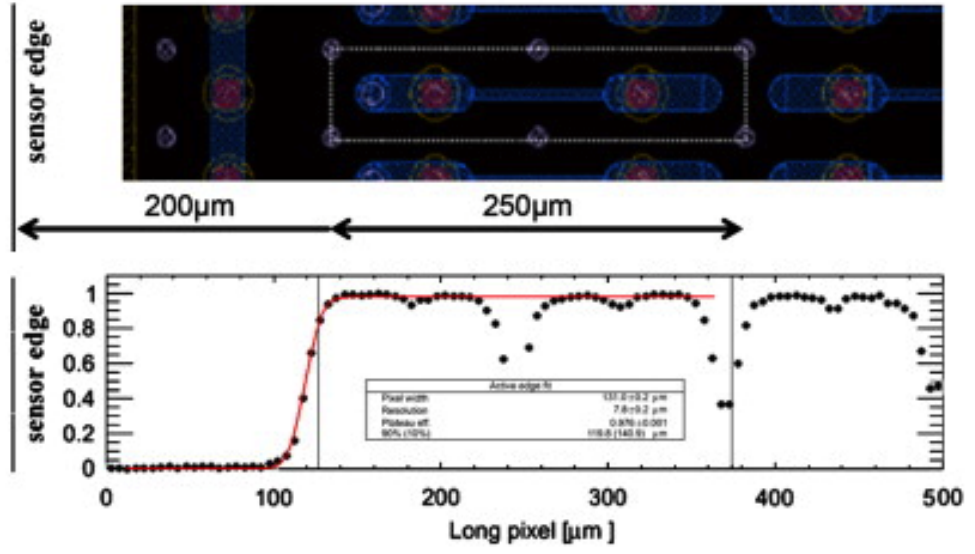


Figure 5.6: Edge efficiency of an FE-I4 CNM 3D pixel detector irradiated with neutrons to a fluence of  $1 \times 10^{15} \text{ n}_{eq} \text{ cm}^{-2}$  [57]. A sketch of the layout of the edge pixel is shown above for reference. The black line to the left, demonstrates the cut edge of the sensor. The two black lines (one at  $\sim 125 \mu\text{m}$  and one at  $\sim 375 \mu\text{m}$ ) show the width of the edge pixel.

### 5.2.3 Magnetic field

It has been shown in beam tests at CERN in 2009, that a magnetic field of 2 T has little effect on the charge distribution within 3D silicon sensors [59]. The sketch in Fig. 5.7 diagrammatically compares the effect of a magnetic field on a planar silicon device and a 3D silicon detector. It can be seen that, due to the long distance charge carriers must travel in a planar device, the deflection in the location of charge collected in the electrodes due to the magnetic field is greater [59]. The distribution of the average cluster size as a function of the incident angle of a particle track is symmetrical around  $0^\circ$  for 3D silicon detectors manufactured at two different facilities (Stanford and FBK) as shown in Fig. 5.8. In comparison, the cluster size is a minimum at the Lorentz angle for planar silicon detectors which is around  $7^\circ$  [60].

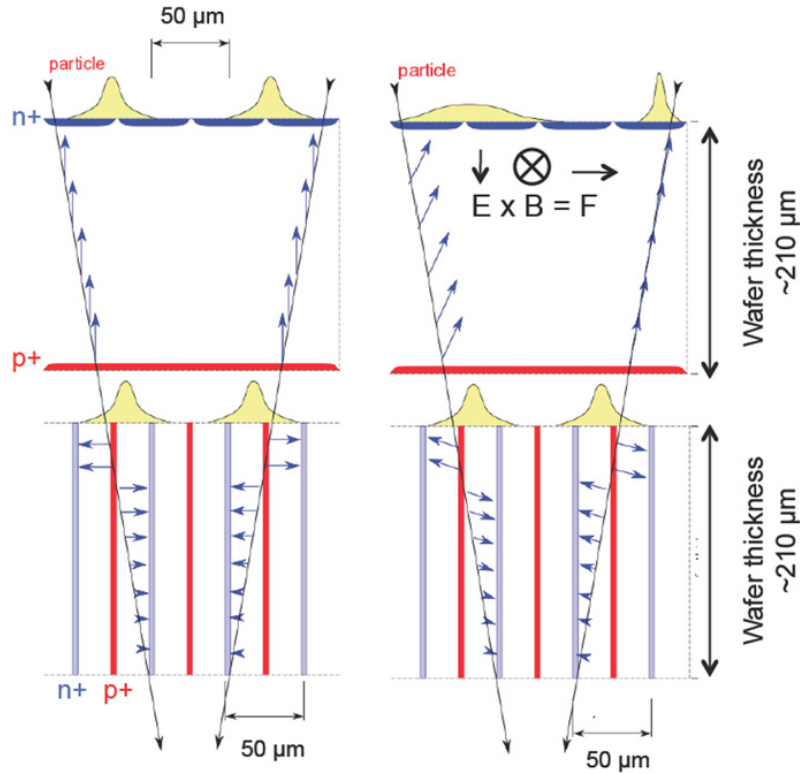


Figure 5.7: Sketch of the effect of the magnetic field on the charge distribution within the pixels of a planar detector (top) and 3D silicon detector (bottom). The magnetic field is off (left) and on (right). [59]

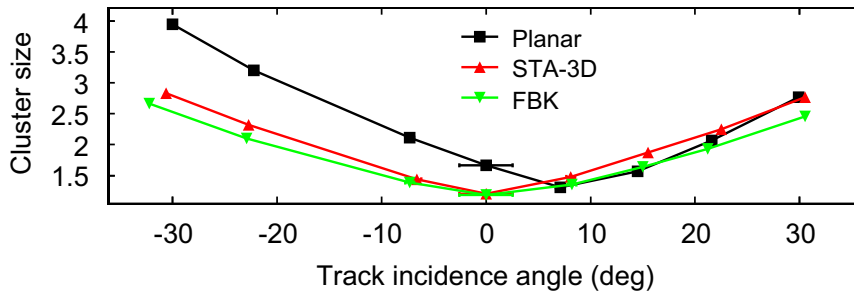


Figure 5.8: Comparison of cluster size for track incidence angles between  $-30^\circ$  and  $+30^\circ$  for a planar detector and two 3D silicon detectors manufactured at Stanford (STA) and FBK. All three are bonded to FE-I3 readout chips. [60]

### 5.3 Design for the IBL

3D silicon sensors for the IBL were manufactured at CNM and FBK using the double-sided fabrication process described in Section 5.1. They have a standard thickness of  $230 \mu\text{m}$  and an inter-electrode distance of  $71 \mu\text{m}$  [52]. Both designs have a standard FE-I4 pixel array of



80 rows by 336 columns, compared to 18 by 160 for the FE-I3 devices in the ATLAS pixel detector. The sensors were produced on a similar wafer floor plan, shown in Fig. 5.9 for CNM (left) and FBK (right). The devices labelled 1–8 are  $\sim 2 \times 2$  cm, IBL design 3D silicon sensors compatible with an FE-I4 readout chip. The structures around the edge of these devices are FE-I3 compatible sensors and test structures, such as diodes. The latter can be used to test various design parameters with the aim of developing and improving simulations of pixel sensors.

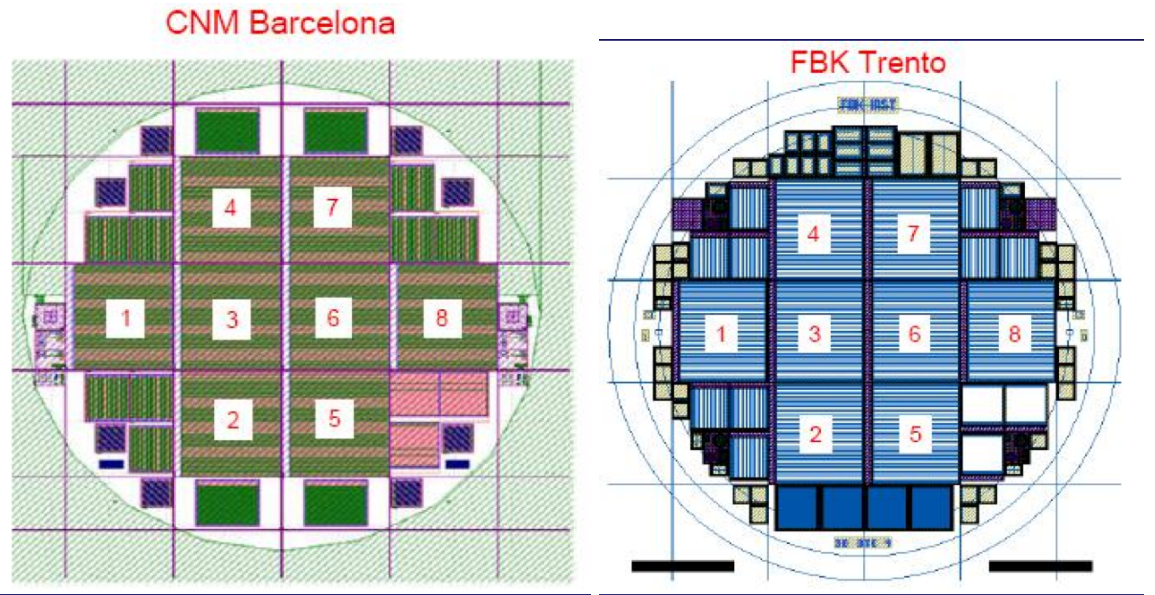


Figure 5.9: Common IBL wafer floor plan for CNM (left) and FBK (right). Sensor sections labelled 1–8 are  $\sim 2 \times 2$  cm and of IBL design [39].

However, there are some differences between the two layouts. The electrodes in sensors manufactured at FBK penetrate fully through the silicon; juxtaposed to this, the electrodes in CNM sensors stop  $\sim 20 \mu\text{m}$  from the wafer surface. Known as full-through and partial-through designs respectively, a comparison of FBK and CNM is shown in Fig. 5.10 [39]. The differences in electrode depth has an effect on the comparative charge collection of the two sensors. It is expected that charge sharing will be slightly lower for FBK sensors, which have electrodes that fully penetrate the silicon bulk, than for CNM. This is a result of the electric field component at the tip of the CNM electrode which is perpendicular to the magnetic field [59].

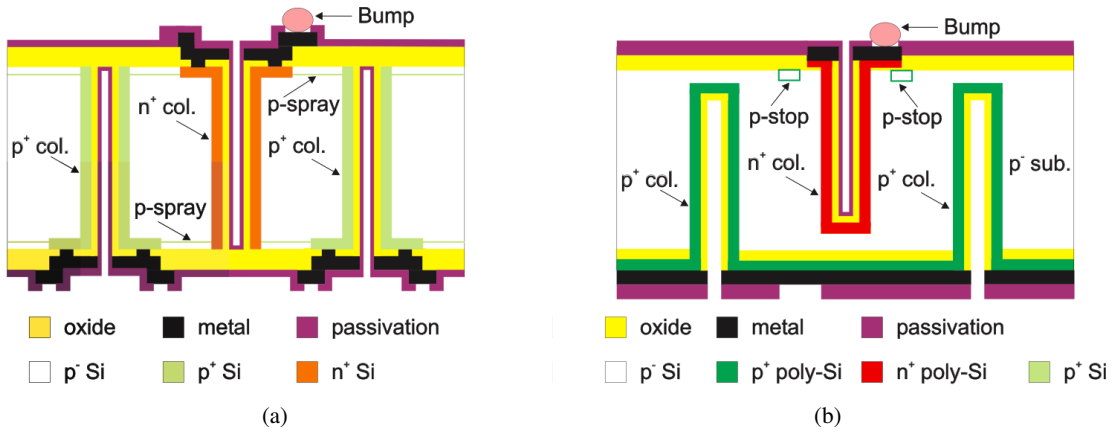


Figure 5.10: Double-sided 3D silicon designs for the fabrication facilities (a) FBK with full-through electrodes and (b) CNM with partial-through electrodes [39].

## 5.4 Summary

In 2009 3D silicon sensors were a promising choice for the Insertable B-Layer, but being a novel detector technology still in the research and development stage, an intensive laboratory and beam test qualification process was required before they could be selected for inclusion in the upgraded ATLAS detector and in other experimental projects.

## 6 | Laboratory Characterisation

Before the devices can be irradiated, or tested in a beam test, they need to be characterised to determine how well they function. Due to the intrinsic differences in the electronics of each pixel, characterisation of the sensors is also required to make the output as uniform as possible.

In this chapter the setup required for characterisation of a module in a laboratory is described in Section 6.1. The main equipment used, USBPix, is presented in Section 6.2 with Section 6.3 detailing the corresponding software STControl. Standard results from this testing procedure are presented in Section 6.4.

### 6.1 The laboratory setup

Devices are characterised in a clean room to control the level of dust and airborne particles that could damage the sensors and testing equipment. Figure 6.1 shows some of the equipment used to characterise the sensors from the clean room laboratory at CERN. The climate chamber shown in the left of the photograph is used to control the temperature and humidity levels of the environment to allow testing of the devices at various temperatures. It also provides a dark environment to tune the devices as external photons increase the noise (unwanted excess charge) within the sensor. Controlling the temperature is especially important for irradiated devices which can exhibit higher leakage current at increased temperatures.

### 6.2 USBPix

USBPix [61, 62] is a modular device used as an interface between the ATLAS pixel front-end readout card and the data acquisition software on a local computer. Developed as a alternative to TurboDAQ [63], the previous ATLAS pixel detector testing system, USBPix was designed to have a minimum amount of hardware components and its small size makes it portable. In addition to USBPix and the computer, the only further hardware required are two voltage supplies, one for low voltage and one for high. The two components that make up USBPix are the Multi-IO board, which was developed at the University of Bonn, Germany,



Figure 6.1: Photograph of the laboratory setup at CERN. The USBPix system, the climate chamber, the computer and the power supplies are all labelled as shown.

and a front-end adapter card. Two adapter cards are available depending on which type of readout card is being tested; one for the current ATLAS front-end readout card, FE-I3, and one for the new readout card designed for the IBL, FE-I4. Figure 6.2 shows a photograph of the USBPix system with the cables that connect it to the front-end readout card. In this example the USBPix Multi-IO board is attached to an FE-I4 adapter card.

On the Multi-IO board is a Field Programmable Gate Array (FPGA), which deals with all signals to the front-end. There is also 2Mb of onboard memory. It is possible to operate the USBPix system with an external trigger through either a LEMO connector or an ethernet cable to the RJ45 (USB) connector. The ethernet cable is required for operation with a telescope during a beam test (see Section 7).

### 6.3 STControl

The software to communicate with the USBPix hardware is called System Test Control, or STControl for short [64]. STControl utilises the libraries of ROOT, QT and ATLAS PixLib. A configuration file is required to set the digital to analogue converter (DAC) settings on the front-end card. Tuning scans are performed to determine the initial global settings for the front-end card, these can later be tuned further to select pixel data acquisition (DAQ) settings with the aim of producing a uniform output for each pixel.

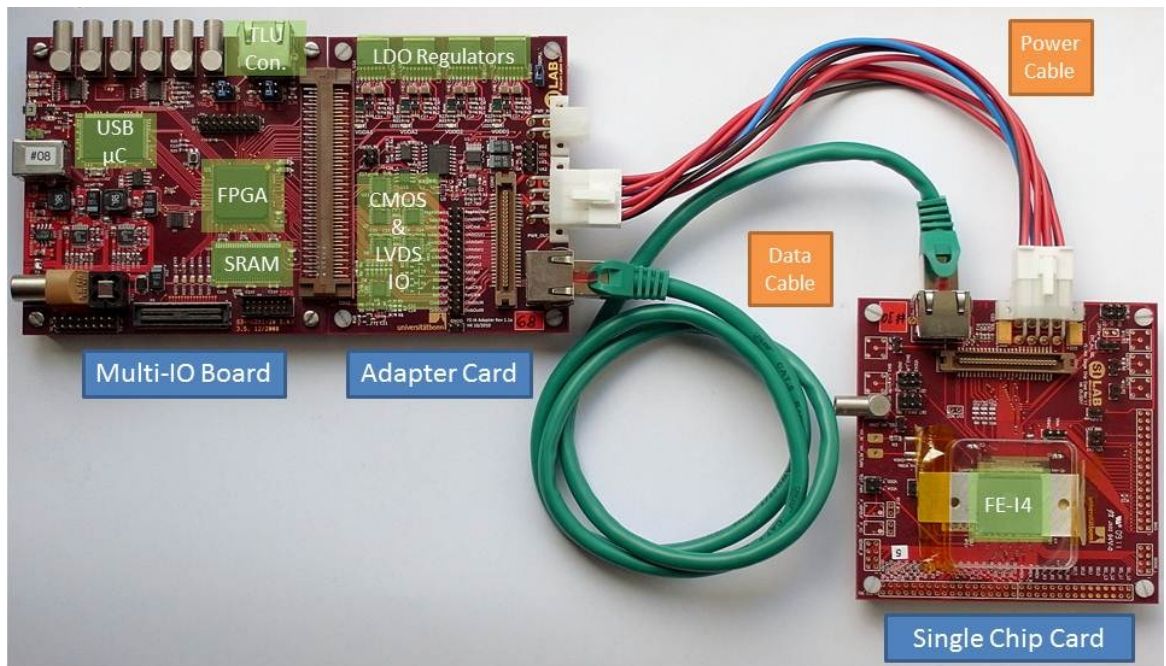


Figure 6.2: Photograph of the USBPix system [62]. The Multi-IO board and the FE-I4 adapter card are shown on the left and the single chip readout card, connected to the adapter card via a data cable and power cables, is to the right.

### 6.3.1 Tuning the front-end

The process for tuning the front-end after the global parameters have been set is as follows:

- A current-voltage (IV) scan
- RXDelay scan (FE-I4 only)
- Analogue and digital scans
  - For the analogue scan, charge is injected into the analogue component of the readout card 200 times for every pixel and measurements are taken after the digital discriminator. In an ideal case, the number of measurements would equal the number of injections.
  - A similar process of injecting hits into the discriminator of the readout card to test the digital only component are performed.
  - Through deduction, this allows the user to determine if there is a problem with either component.
- Threshold and TOT scans

- To judge the quality of the initial global parameters. These should be close to the required threshold and TOT for the following tune to provide the best results.
- TDAC
  - The TDAC parameter determines the local threshold for each pixel, by comparing the threshold for an injected charge with the threshold set. The TDAC value is varied until the two match.
- FDAC
  - The FDAC parameter alters the feedback current in the preamplifier and as a consequence the TOT is altered for a specific charge (See Fig. 4.11 in Section 4.1.1).
- TDAC
  - The threshold will be altered by the change in TOT, so this scan is run for a second time.
- Threshold and TOT scans again to confirm required results.
  - If needed, the TDAC and FDAC tunes can be performed until results are satisfactory.

## 6.4 Results

### 6.4.1 IV

It is important to know at what voltage to run the detector at for optimal performance. If the supplied bias voltage is too low, the device will be under-depleted. However, if the voltage is excessive, an avalanche break-down can occur possibly damaging the device. The optimum voltage can be determined by recording the current as a function of the input voltage, known as an IV curve. Figure 6.3 shows the IV curve for a non-irradiated SINTEF device bonded to an FE-I4 readout card. The IV curve is dominated by a short circuit in the device which causes the rise in current at 12 V and it is therefore consistent for different temperatures. However, the device is fully depleted between 5–10 V and can be operated without issues in this range.

### 6.4.2 Testing the front-end

To test that the front-end is performing as expected, scans of the analogue and digital response are carried out. A charge is injected into each pixel 200 times and the response recorded. The result should equal 200 and each plot should have a uniform output, as



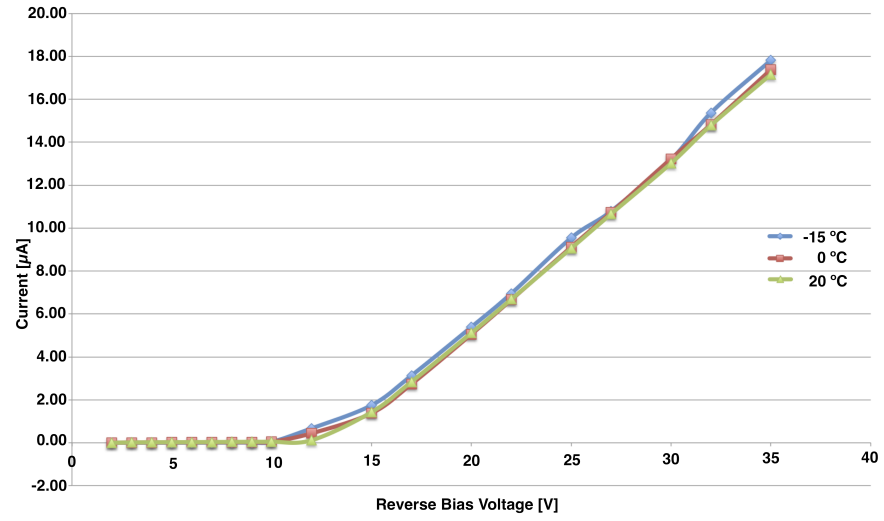


Figure 6.3: Measured current in  $\mu\text{A}$  as a function of reverse bias voltage (V) for a non-irradiated FE-I3 3D silicon sensor, SINTEF 105, at temperatures of  $-15\text{ }^{\circ}\text{C}$  (blue),  $0\text{ }^{\circ}\text{C}$  (red) and  $20\text{ }^{\circ}\text{C}$  (green).

illustrated in the examples in Fig. 6.4 for a non-irradiated 3D silicon sensor on an FE-I3 readout card. Note the black pixel in the analogue scan to the left. This is due to a problem in the analogue component for that pixel since the corresponding pixel in the digital scan does not show any problems.

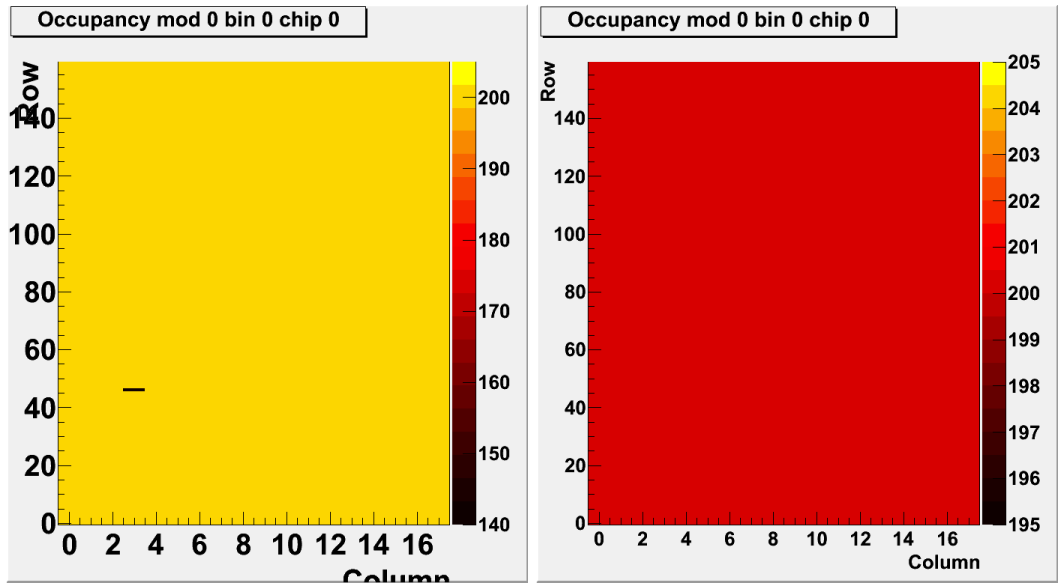


Figure 6.4: Analogue scan (left) and digital scan (right) for a non-irradiated 3D silicon sensor on an FE-I3 front-end card (SINTEF 105) tuned to a threshold of  $3200\text{ e}^-$ .

### 6.4.3 Threshold and noise scans

A threshold setting is required for the front-end card to limit the noise recorded from the module. The output from a threshold scan for an FE-I3 3D device tuned to 3200 e is in the left of Fig. 6.5, with the measured noise to the right. As mentioned in Section 3.2.1, the edge pixels of FE-I3 pixel detectors are longer, with a pixel pitch of  $600\text{ }\mu\text{m} \times 50\text{ }\mu\text{m}$ , compared to  $400\text{ }\mu\text{m} \times 50\text{ }\mu\text{m}$  for the pixels in the centre. This results in greater noise from the long pixels, evident in the second, higher peak in the noise scan in Fig. 6.5. The increase in noise for the longer pixels is of the order 100 e. Figure 6.6 shows results for a non-irradiated SINTEF sensor bonded to an FE-I3 readout card. It can be seen that for a lower threshold tuning, there is a higher level of noise.

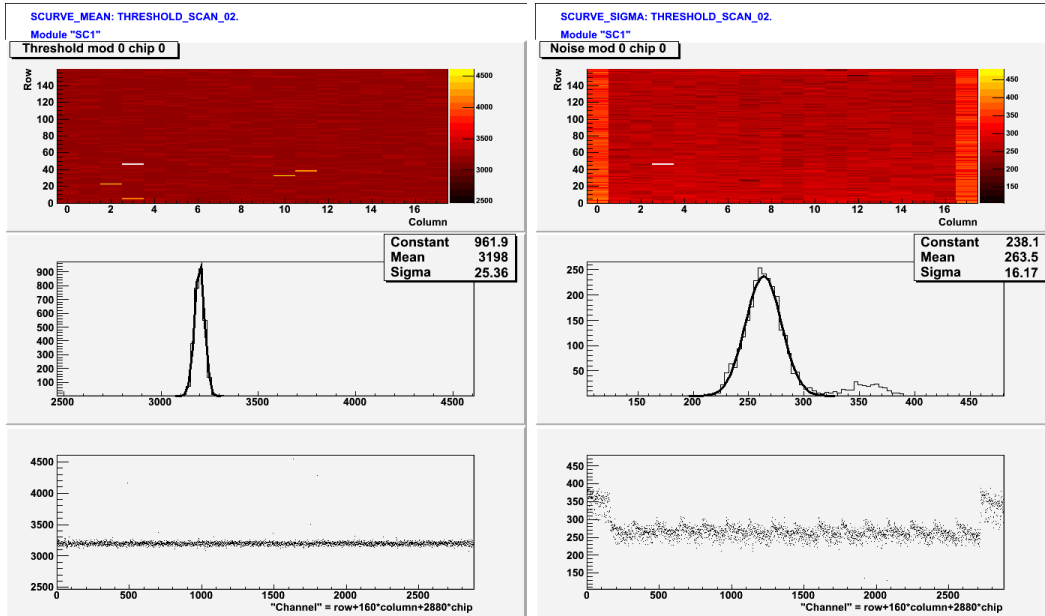


Figure 6.5: Threshold scan (left) and noise scan (right) for a non-irradiated 3D silicon sensor on an FE-I3 front-end card. These scans were taken after the module had been tuned. The second peak in the noise scan at  $\sim 305\text{ e}^-$  is due to the longer pixels at the edge of the device.

### 6.4.4 Source scans

A scan with a radioactive source allows measurements of the module with an external charge. The scan can be taken with internal triggers, or with an external trigger from a scintillator. The two dimensional hitmap in Fig. 6.7 was taken with a strontium-90 source with internal triggering. Strontium-90 is an isotope of the element strontium and undergoes  $\beta^-$  decay, whereby it emits an electron, known in this case as a beta particle. Internal triggers were required due to a copper plate located on the reverse of the module, which prevented exter-



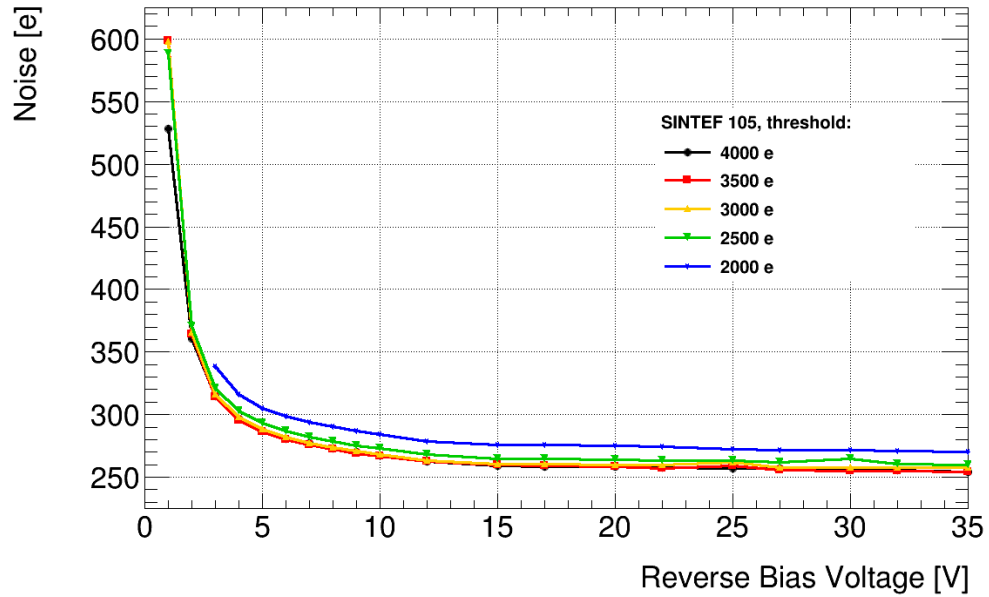


Figure 6.6: Noise readings (in electrons) as a function of the reverse bias voltage applied to the module for five different threshold tunings. For a non-irradiated 3D sensor on FE-I3 (SINTEF 105)

nal triggering with a scintillator. The green oval of greater hits is the centre of the beam profile from the source and can clearly be seen. There is a group of white pixels around column 3 and row 45. This is due to *stuck* pixels at that location which fired excessively and consequently were required to be switched off.

Charge distributions for various cluster sizes are shown in Fig. 6.8. Clusters are selected by taking all pixel hits within one trigger window and combining those that have a neighbour in rows or columns, or with a coinciding lvl1 value. The combined charge distribution for all cluster sizes is in the top left of the figure. The top right shows cluster sizes of one which has the greatest fraction of events. The distribution is dominated by noise which has a lower charge. The distributions on the bottom are for cluster sizes of two and three, in the left and right respectively. There are fewer total events for these cluster sizes (with peaks of  $\sim 2500$  and  $\sim 1200$  events). The thick black line in each quarter is a fit to a Landau distribution.

## 6.5 Summary

After the devices have been characterised in the laboratory, they can be tested further if required at a beam test facility. The process described here was performed for every device in the following chapter.

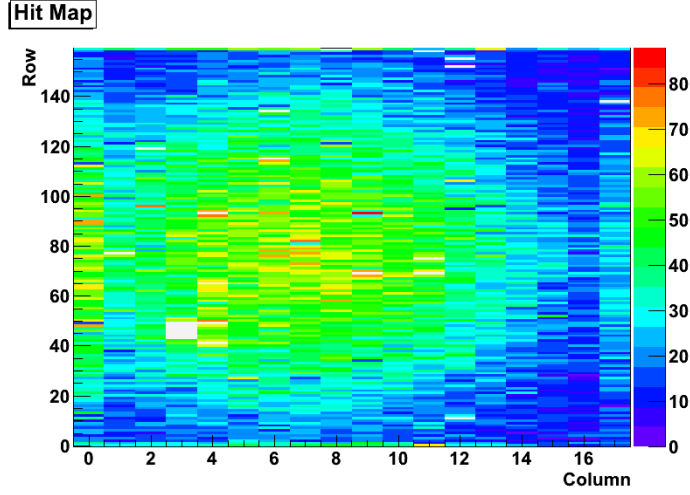


Figure 6.7: A two dimensional hitmap taken during a source scan with internal triggers. The shape of the source (the oval of green) can clearly be seen. The group of white pixels around the location of (3, 45) have been switched off. The scan was performed for a non-irradiated 3D silicon sensor on an FE-I3 front-end card (SINTEF 105) tuned to a threshold of  $3200\text{ e}^-$ . The device was biased to -20V and the temperature was  $20\text{ }^{\circ}\text{C}$ .

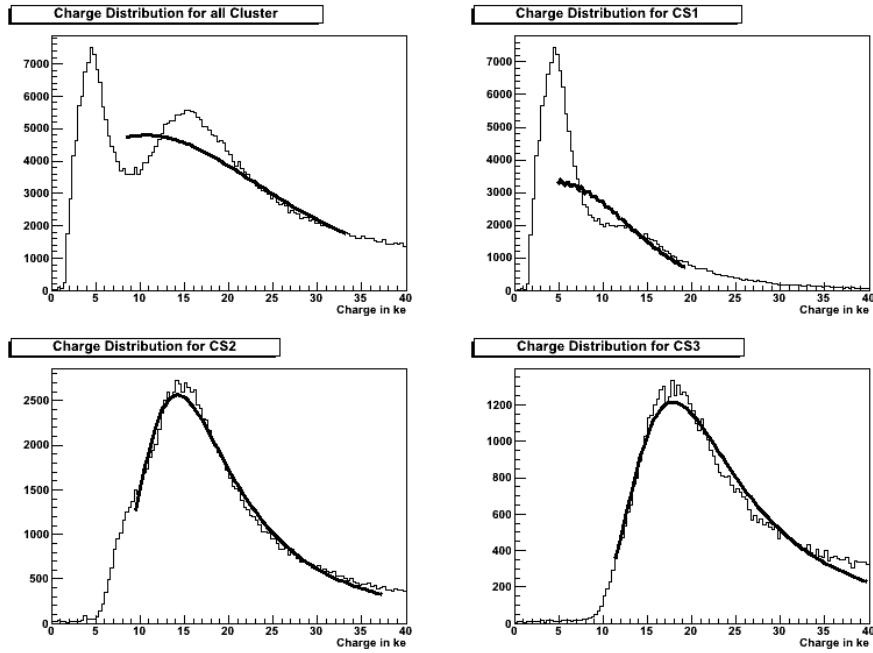


Figure 6.8: Charge distribution as a function of cluster size for all clusters (top left), cluster size = 1 (top right), cluster size = 2 (bottom left), cluster size = 3 (bottom right). The thick black line is a Landau fit to the data. The scan was performed for a non-irradiated 3D silicon sensor on an FE-I3 front-end card (SINTEF 105) tuned to a threshold of  $3200\text{ e}^-$ . The device was biased to -20V and the temperature was  $20\text{ }^{\circ}\text{C}$ .

## 7 | Beam Tests

New detectors are required to be tested in an environment similar to that which they will be exposed to within ATLAS to determine how well they function. A beam test, where the device is read out within a beam of particles, is preferable to using a radioactive source in a lab since the statistics will be much higher. The particle type and energy is usually well known within a beam test, however the exact position of a particle at any one time is difficult to determine. Therefore, a set of well understood detectors known as a *telescope* is used in beam test experiments to track the charged particles. These tracks can be reconstructed offline to evaluate the efficiency and charge sharing performance of the devices under test for various parameters such as the tilt angle, threshold or bias voltage.

Beam tests studying various 3D silicon devices have been performed with positrons at DESY in Hamburg, Germany and with muons at CERN in Geneva, Switzerland.

In this chapter, the beam test facilities at DESY and CERN are presented in Section 7.1. The general setup of a beam test at DESY and CERN is described in Section 7.2. The various 3D pixel devices tested in ATLAS 3D and IBL beam test periods over the previous three years will be presented in Section 7.3. The offline reconstruction and data analysis process is discussed in Sections 7.4 and 7.5 respectively. Finally Section 7.6 contains the results obtained from combining all of the previous stages.

### 7.1 Beam test facilities

#### 7.1.1 DESY

Deutsches Elektronen-Synchrotron (DESY) is the German accelerator research centre located in Hamburg. The facility was the location of the Hadron-Elektron-Ring-Anlage (HERA) accelerator, which collided electrons or positrons with protons primarily to investigate the properties of the quarks within via deep inelastic scattering. These collisions took place in two main detectors, H1 and ZEUS, both built in 1997 and run until shutdown in 2007.

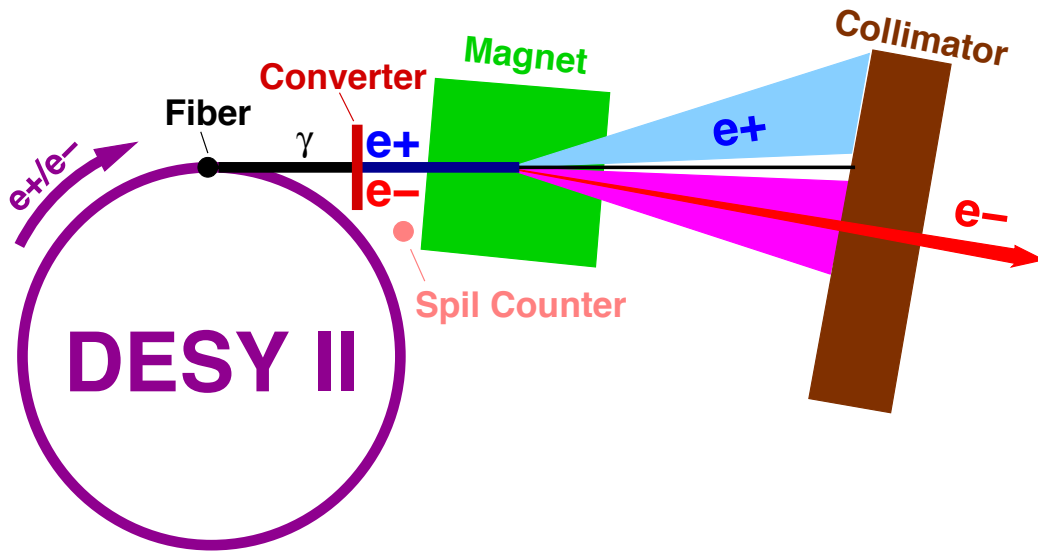


Figure 7.1: A diagram illustrating the process of producing an electron or positron beam for tests at DESY [65].

An illustration of the process of producing electrons ( $e^-$ ) or positrons ( $e^+$ ) at a specific energy for beam tests at DESY is shown in Fig. 7.1 [65]. The DESY II synchrotron accelerates positrons or electrons and then a carbon fibre placed in the  $e^+$  or  $e^-$  beam produces photons through bremsstrahlung radiation. These photons impact a metal plate which converts them to pairs of  $e^+/e^-$ . A dipole magnet spreads the beam out as a function of the sign and energy. The desired beam energy within the range of 1–6 GeV/c is chosen with a collimator. The beam is subsequently directed into one of three beam areas. The rate of electrons or positrons is  $1000 \text{ s}^{-1} \text{ cm}^{-2}$ . A photograph of beam area 21 at DESY is shown in Fig. 7.2; the telescope and tested devices are to the left of centre and the beam direction is from right to left.

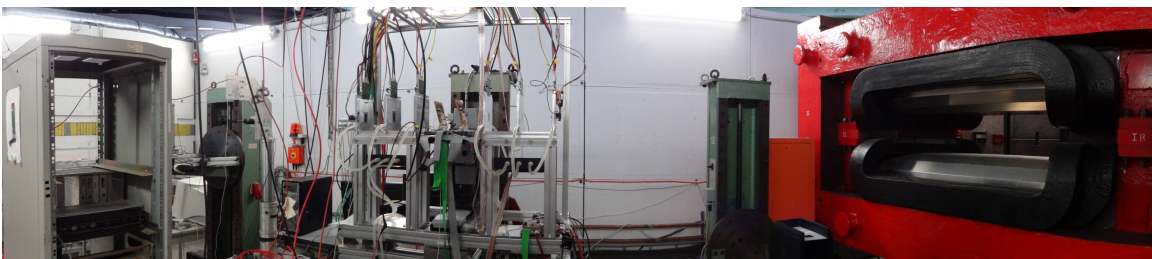


Figure 7.2: Photograph of the DESY beam hall. The beam direction is from right to left.

### 7.1.2 Super Proton Synchrotron, CERN

The Super Proton Synchrotron (SPS) at CERN is the final accelerator in the injection chain for the LHC and is primarily required to accelerate protons to 450 GeV as described in Section 3.1. However, the proton beam is also extracted from the SPS before injection and directed towards three targets (T2, T4 and T6), producing beams of muons for the CERN North Area for testing. The main user for each beam line has control over the momentum of the muons from 10–400 GeV/ $c^2$ . Due to the multiple extractions of particles from the SPS, the beam arrives in spills with around 4500 triggers provided per spill. The spill length and frequency depend on how many users require beam extraction. Generally each spill is of the order of 5–10 seconds, with a new spill every  $\sim 30$ –40 seconds. The 3D silicon and IBL beam tests used both beam lines H6 and H8; the latter is shown in the photograph in Fig. 7.3 in which the beam direction is from left to right.



Figure 7.3: Photograph of the CERN beam hall. The beam direction is from left to right. Photograph credit B. DeWilde.

There is a preference of having beam tests located at the SPS at CERN instead of at DESY. This is due to the higher level of multiple scattering of the positrons from DESY, which produces reconstructed results with a lower resolution.

## 7.2 Beam test setup

The common beam test setup for 3D silicon devices consists of a telescope, which is split into two arms with a central testing area in the middle. Two pairs of scintillators ( $1 \times 2 \text{ cm}^2$ ), each pair at  $90^\circ$  to each other, are located in coincidence either side of the telescope to trigger on incident particles. Data are recorded during a window of 16 level 1 (lvl1) trigger counts, this is known as an *event*. These triggers are passed to a Trigger Logic Unit (TLU). This setup is illustrated in Fig. 7.4. After a specific number of events, the data set is saved as a *run*. Runs are required to be big enough that sufficient statistics are collected, but low enough

that the setup has not changed significantly over the time taken to record it. Furthermore, it is desirable to keep file sizes small and to save data frequently enough to safeguard against possible software crashes.

The Devices Under Test (DUTs) are located in the central area and each are readout via a USBPix system (described in Section 6.2), or in later beam tests, the RCE system [66], a new readout based on National Instruments. Several USBPix devices can be run simultaneously from a single computer running the data acquisition software, EUDAQ. At DESY, due to the increased amount of multiple scattering, normally only two devices are tested; at CERN up to four devices can be run at once and generally this number is limited by the size of the box described in Section 7.2.2. For various reasons it is required to have a device that is well understood as part of the testing setup, known as a reference sensor. Since the telescope is read out at a rate of  $112 \mu\text{s}$  in a rolling shutter mode and the DUTs are read out every  $400 \text{ ns}$ , the reference sensor is primarily there to determine if a hit on the DUT is registered as ‘in time’. Another reason to have a reference sensor is to check that the data are sensible by comparing established plots, such as cluster size and TOT histograms, for the reference with previous results.

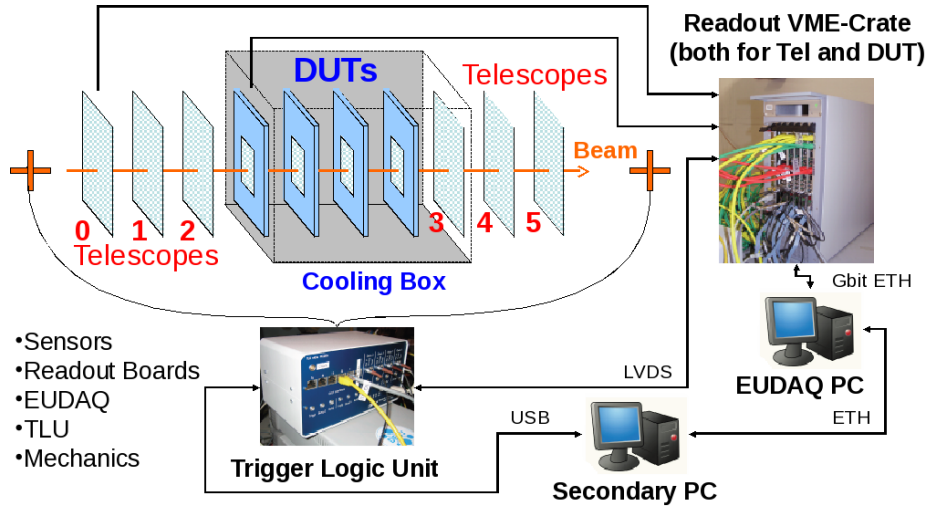


Figure 7.4: Illustration of a standard beam test setup [67].

### 7.2.1 Telescope

The purpose of a telescope is to use mature detectors that are well understood with a resolution better than the pixel pitch of the devices under test, to record hits from a particle track in a beam test environment. Using offline software to reconstruct the tracks from the telescope planes, studies of new detectors can be performed to understand various features

such as efficiency and the sharing of charge between strips or pixels.

### EUDET telescope

The EUDET telescope is made from six identical planes of Mimosa-26 [68] pixel detectors, three up- and three down-stream from the central testing area. The active sensor area is 21.2 mm by 10.6 mm. The pixel pitch is 18.4  $\mu\text{m}$ , with the pixels arranged in a 1152 x 576 matrix.

Further telescopes copied from the EUDET design have been built by the DESY group, all of which are subsequently named after poisonous flowers<sup>1</sup>. The other telescope used for data presented in this thesis is the ACONITE telescope. However, since the designs are identical, the name EUDET will be used to refer to either telescope.

#### 7.2.2 Cooling

Due to the increase in leakage current from radiation damage, irradiated sensors should be operated in the dark and at low temperatures. A polystyrene box was designed and built at the University of Dortmund to reduce the amount of light impacting on the sensors during data taking, to have a low material budget and provide insulation from external temperature changes.

To cool devices during a beam test, blocks of dry ice were placed in a second compartment in the box on top of an aluminium plate, shown in Fig. 7.5. Underneath the aluminium plate, a copper strip connected to the *L*-shaped mount (see Section 7.2.3) of each device is placed to facilitate the cooling process. A photograph of the cooling box in the centre of the two telescope arms in the beam test setup is in Fig. 7.6. Complications arise when the dry ice sublimates, reducing the weight on the end of the platform and moving the box (and therefore the sensors) during data taking. This can cause issues for the alignment and a compromise is required when choosing the length of a data-taking run since runs with high statistics are desired. Nitrogen gas is piped into the box to reduce condensation and ice forming on the sensors which could cause damage through short-circuiting or possibly through the expansion of ice on the delicate wire-bonding.

#### 7.2.3 Mounting devices

Devices being tested are mounted onto a *L*-shaped aluminium mount which, when screwed into the aluminium plate in the Dortmund cooling box, places the sensors normal to the beam and ideally overlapping in the x-y plane, such as in Fig. 7.7. The material choice

---

<sup>1</sup>Aconite, anemone, caladium and datura.



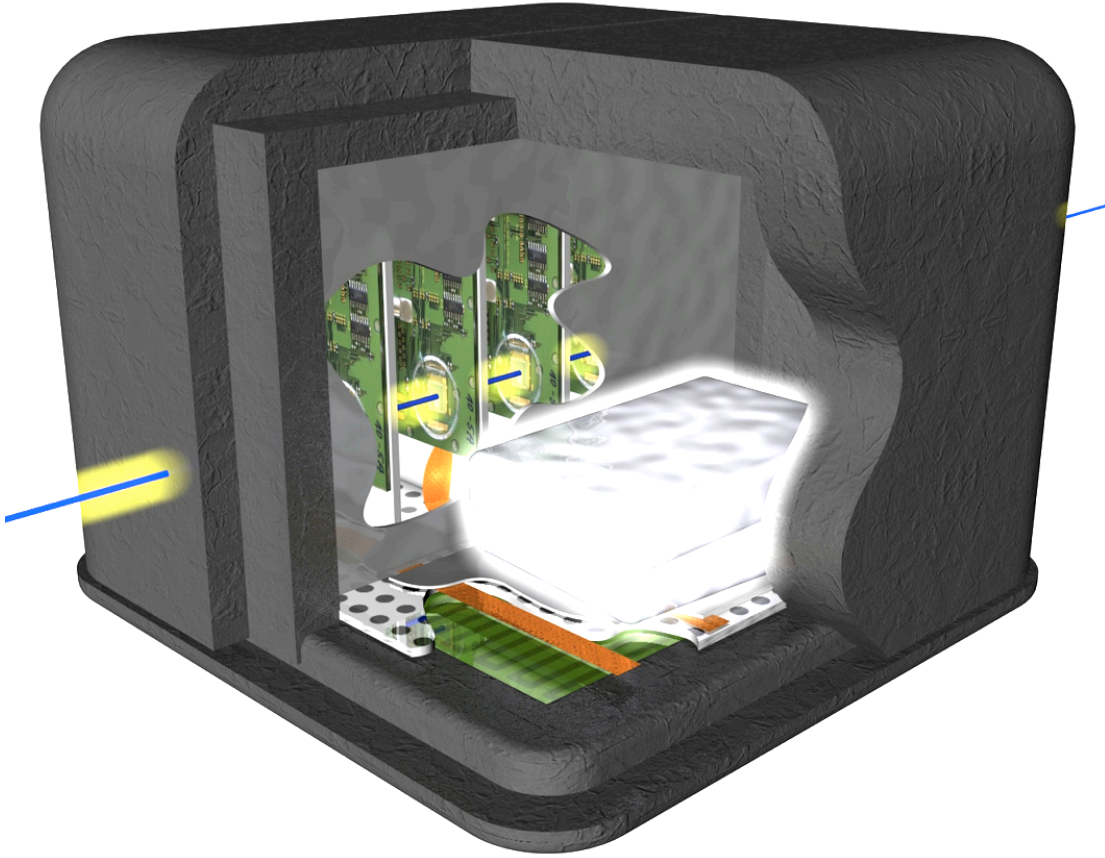


Figure 7.5: Computer aided design of the polystyrene box provided by the University of Dortmund [69]. The devices are in the first compartment to the back of the image and the blocks of dry-ice can be located in the second compartment on top of an aluminium plate. The orange strips are copper which is connected to the L-mount of each device and then placed under the aluminium plate to facilitate the cooling process. The blue line illustrates a particle traversing the devices inside the box.

allows for a transfer of heat away from the sensors since the aluminium plate is also in contact with the dry ice. Kapton tape [70], which is electrically insulating and stable at low temperatures, is used to cover the *L*-shaped mounts to prevent short-circuiting. The Kapton tape is visible in Fig. 7.7.

To tilt the sensors in the beam test, aluminium wedges with specific tilt angles are used to tilt in  $\phi$  (See Fig. 7.7). For rotations in the  $\eta$ -direction, a block with holes drilled for selected angles, as illustrated in Fig. 7.8, was used. The holes correspond with the holes drilled into the base plate allowing the desired angle to be obtained.



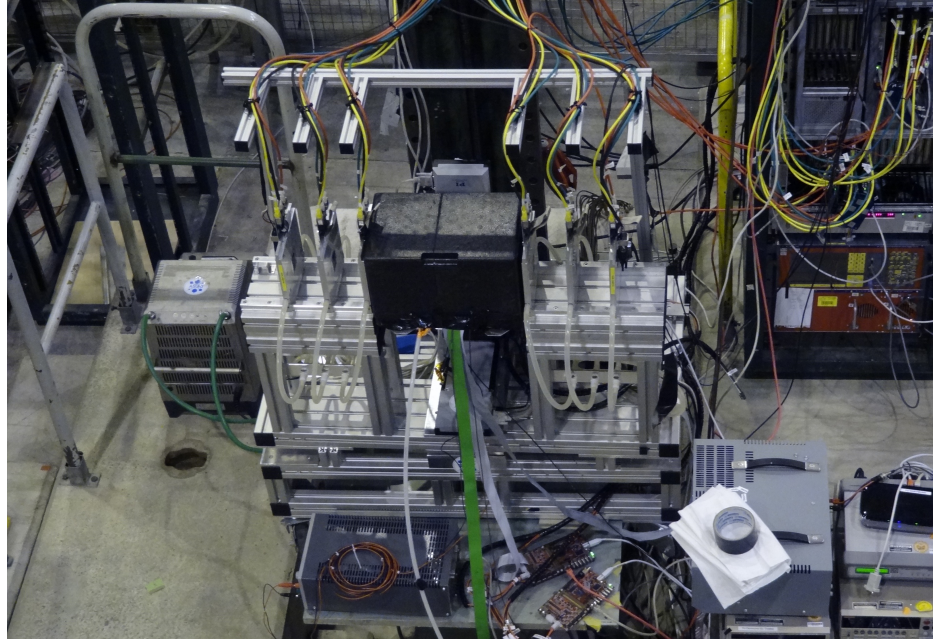


Figure 7.6: Photograph of the Dortmund cooling box fixed between the two arms of the EUDET telescope in the beam test setup.

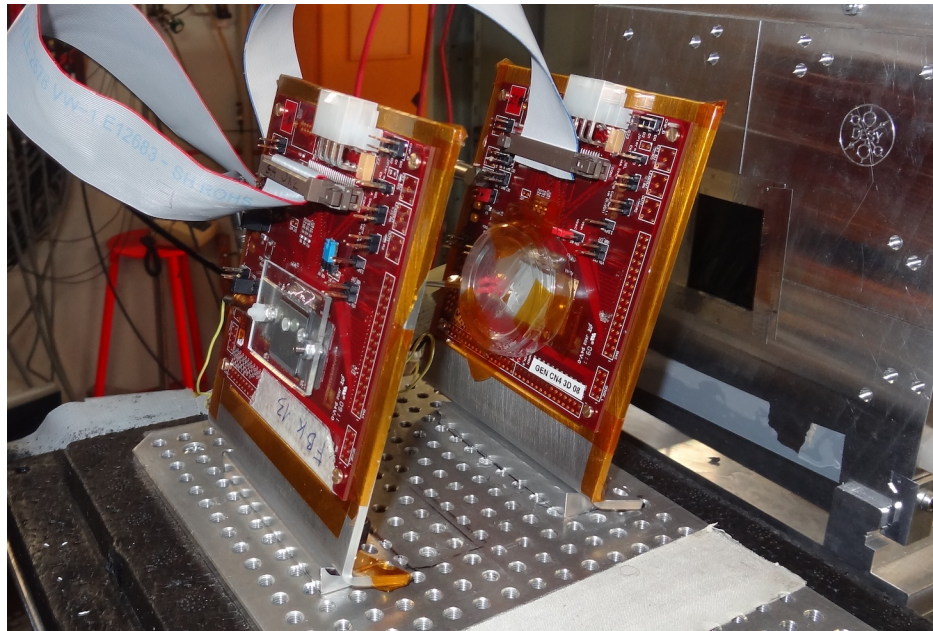


Figure 7.7: Photograph of two FE-I4 devices on *L*-shaped aluminium mounts screwed into the aluminium plate of the Dortmund box.

#### 7.2.4 Data acquisition software

The software used for data acquisition is called EUDAQ [71], which is an operating system independent framework that uses processors to communicate between the various hardware

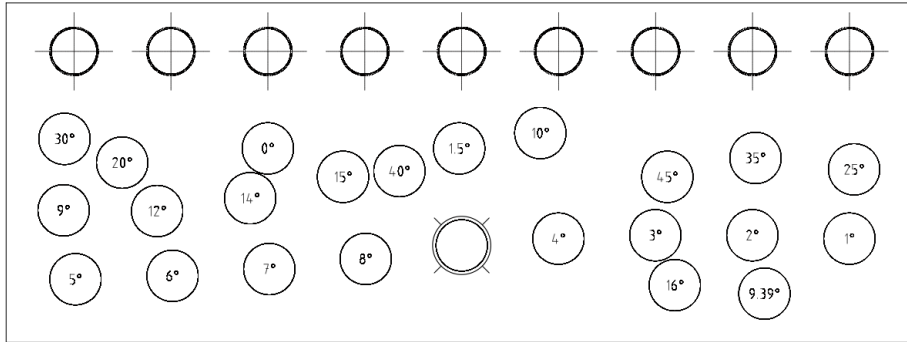


Figure 7.8: Schematic for rotation plate indicating the positions the plate should be screwed into the base plate to obtain selected rotations in  $\eta$ .

devices. The graphical interface called Run Control, shown in Fig. 7.9 allows the user on shift to interact with these processors. Data are output as a single RAW file and contains all of the information from each telescope plane and DUT such as hit positions and time over threshold for individual events.

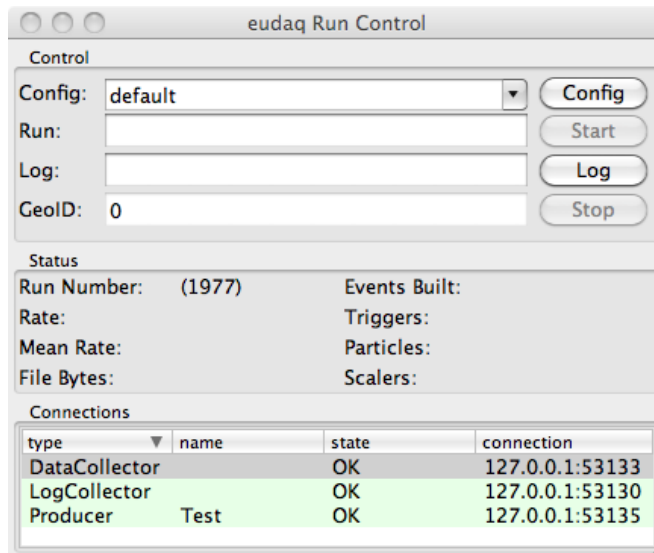


Figure 7.9: The EUDAQ control panel [71].

A new GeoID is set from the control panel when the setup has changed. This is important to group runs from the same angle or configuration together.

### 7.2.5 Online data monitoring

During data taking, it is useful to monitor certain plots in real time using a Data Quality Monitoring (DQM) programme. This is to ensure that the data for each run are not corrupted. Figure 7.10 shows an example of online data monitoring plots provided by the EUDET Telescope Online Monitor. For each DUT and telescope plane the two dimensional hitmaps for the raw and clustered data are available as well as the TOT and cluster size. A histogram of hot pixels gives an indication of how noisy the sensor is; masking noisy pixels or increasing the threshold could reduce problems with data analysis later. The Online Monitor also provides correlation plots.

### Correlations

A two-dimensional plot of the position of a hit in x or y for one device compared to the hit position on the same axis for another is known as a correlation plot. These are provided in the Online Monitor (see Fig. 7.11) – they indicate whether two sensors overlap in the beam and allow the shifter to check that one device has not fallen out of sync with the other. Ideally for two well aligned sensors of the same dimensions and rotation, the hits on the correlation plots will start at the bottom left corner at zero, and extend at a  $45^\circ$  angle to the top right. Hits due multiple scattering or those that are out of time will not be on this line. Straight lines in the horizontal or vertical direction are generally due to noisy or ‘stuck’ pixels.

Note that in the example in Fig. 7.11 the correlations in window eight indicate that the sensor was flipped in the y-direction which would need to be taken into account during reconstruction. Furthermore, windows nine and ten show no correlations, indicating that there is a problem with data acquisition for that sensor, it is useful to find this out early so it can be resolved.

## 7.3 Tested devices

A (non-exhaustive) list of 3D devices tested in test beams between 2011 and 2012 is presented in Table 7.1, with those used for results in this thesis clearly marked. Irradiation values are quoted for each irradiated sensor including the type of particle used for irradiation (proton or neutron).

## 7.4 Track reconstruction

Before the data from the beam test can be analysed, particle tracks through the setup must be reconstructed; this is performed with the software *EUTelescope*. The software requires a

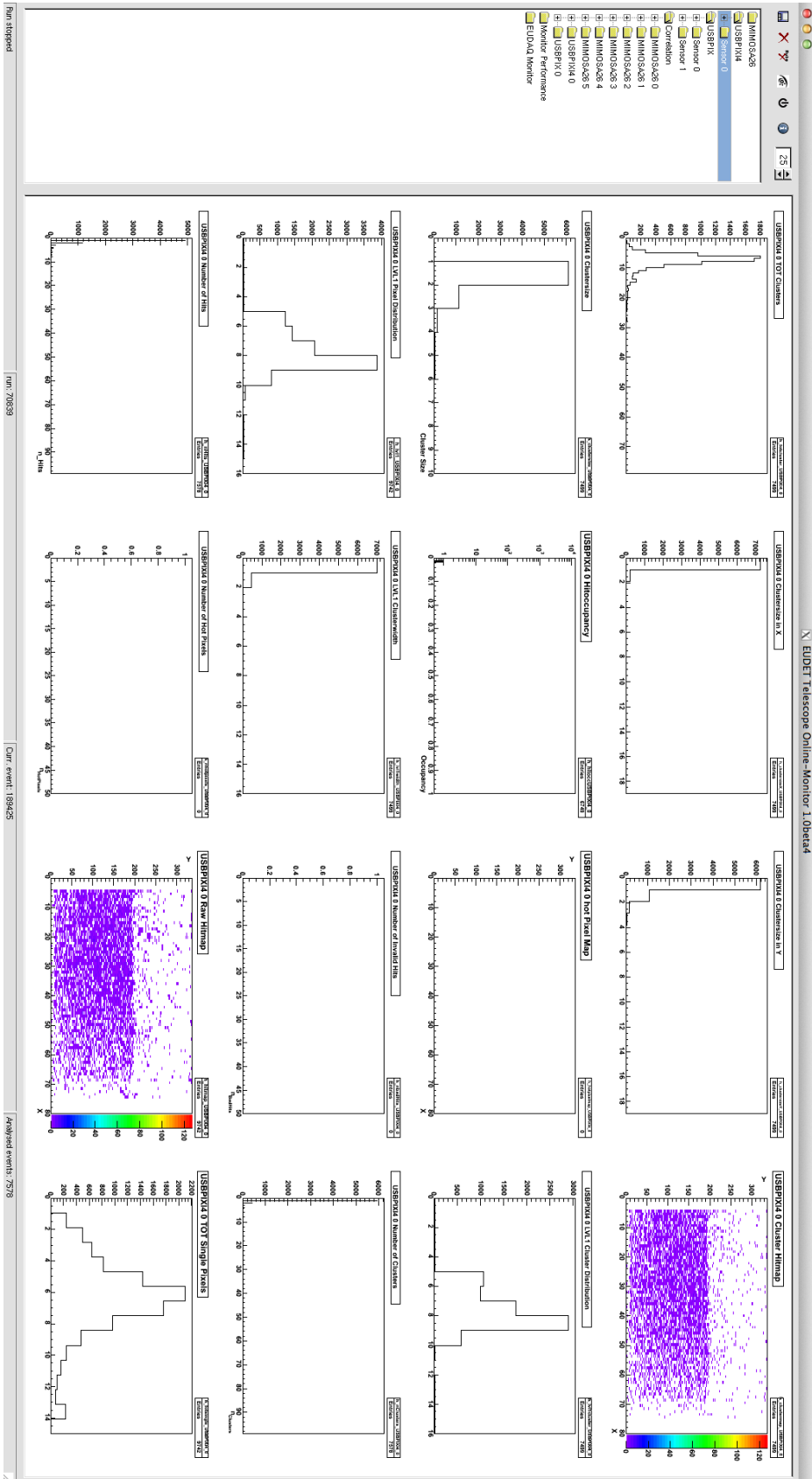


Figure 7.10: Example of EUTET Online Monitoring plots for a non-irradiated 3D silicon sensor bonded to FE-14.



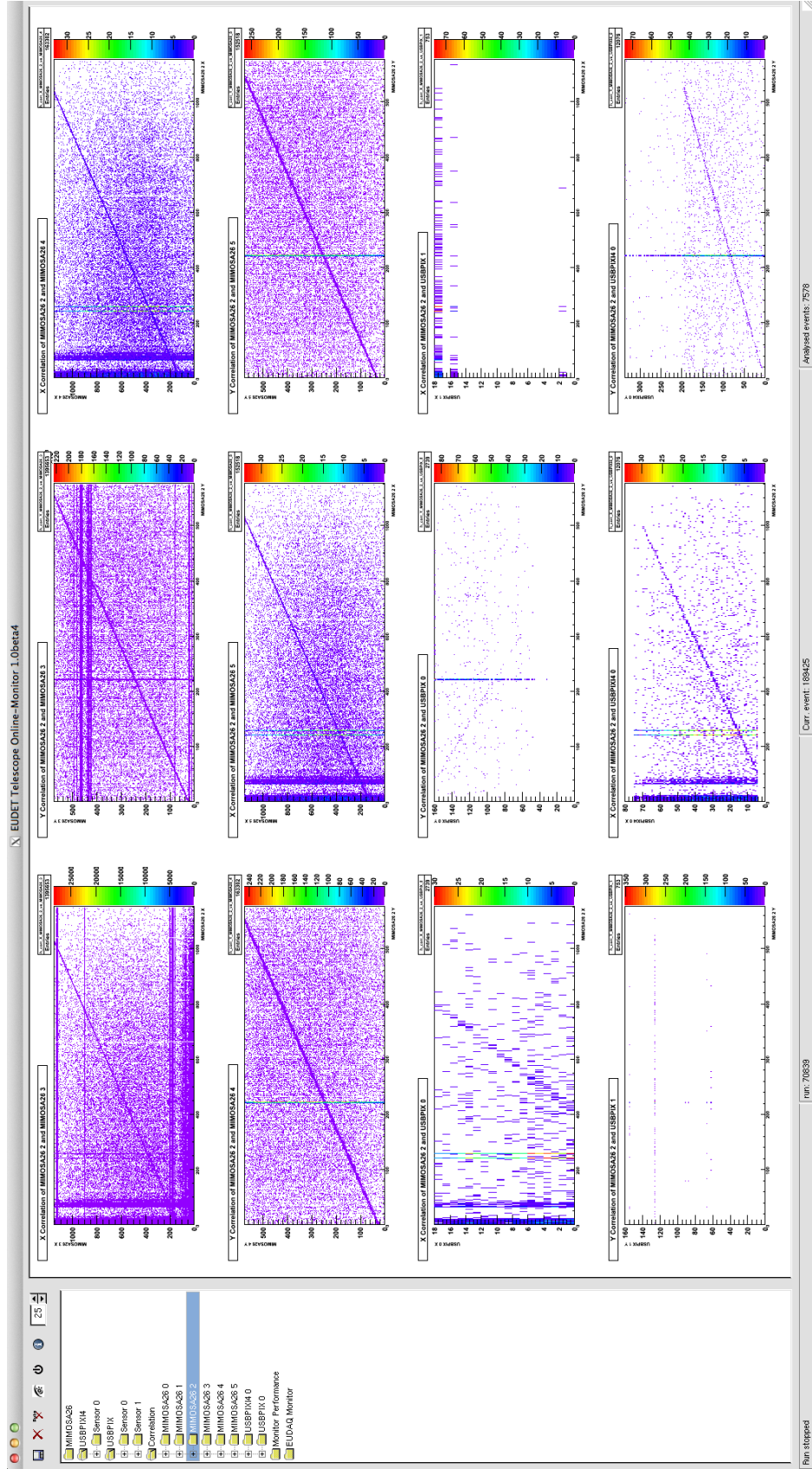


Figure 7.11: Example of EUEDET Online Monitoring correlation plots. Correlations are for a EUEDET plane and either another telescope plane (1-6), a non-irradiated 3D silicon sensor bonded to FE-I3 (7-8), an irradiated 3D silicon sensor bonded to FE-I3 (9-10) and a non-irradiated 3D silicon sensor bonded to FE-I4 (11-12).

Table 7.1: A list of some of the 3D silicon pixel devices tested in beam tests during 2011 and 2012.

Device Name	FE	Inter-electrode spacing ( $\mu\text{m}$ )	Thickness ( $\mu\text{m}$ )	Irradiation ( $n_{eq} \text{ cm}^{-2}$ )	Particle	Reported
CNM 34	I4a	71 (2E)	230	$5 \times 10^{15}$	Proton	–
CNM 55	I4a	71 (2E)	230	0	–	Yes
CNM 57	I4a	71 (2E)	230	$0 \text{ \& } 5 \times 10^{15}$	Proton	–
CNM 81	I4a	71 (2E)	230	$5 \times 10^{15}$	Neutron	–
FBK 11	I4a	71 (2E)	230	$6 \times 10^{15}$	Proton	Yes
FBK 13	I4a	71 (2E)	230	0	–	Yes
F10-23-01	I4b	71 (2E)	230	0	–	Yes
SINTEF 98	I3	56 (4E)	200	0	–	Yes
SINTEF 105	I3	71 (2E)	200	0	–	–
SINTEF 115	I3	103 (2E)	200	$3 \times 10^{15}$	Proton	Yes

description of the position of each device in the telescope frame of reference, this is recorded in a *GEAR file*.

#### 7.4.1 GEAR file

The layout of the experiment is described in a GEAR file, which details the positions and sizes of each telescope and tested device in the setup. Further information such as pixel pitch, rotations using Euler angles, thickness and radiation length of each device is also entered by the user. A unique device ID is assigned to distinguish detectors. Traditionally, telescopes are given an ID number between zero and nine, FE-I3 detectors between 10 and 19, and FE-I4 detectors between 20 and 29. For example, in a beam test with the EUDET telescope, two FE-I3 devices and an FE-I4 reference device, the ID numbers used would be 0-2 (telescope arm one), 10 (DUT 1), 11 (DUT 2), 20 (reference) and 3-5 (telescope arm two). This is the setup for Batch 4 of the 3D beam test at CERN in May, 2012 presented in Section 7.6.2.

#### 7.4.2 EUTelescope

EUTelescope [72] is an offline reconstruction and data analysis programme using Marlin processors. The software takes the RAW data output from a beam test and, after a number of stages, produces fitted tracks in a three dimensional global reference frame as a .root file. These stages are conversion, clustering, hitmaker, alignment and tracking, and are illustrated in the diagram in Fig. 7.12 [73]. Each stage is described in detail below.

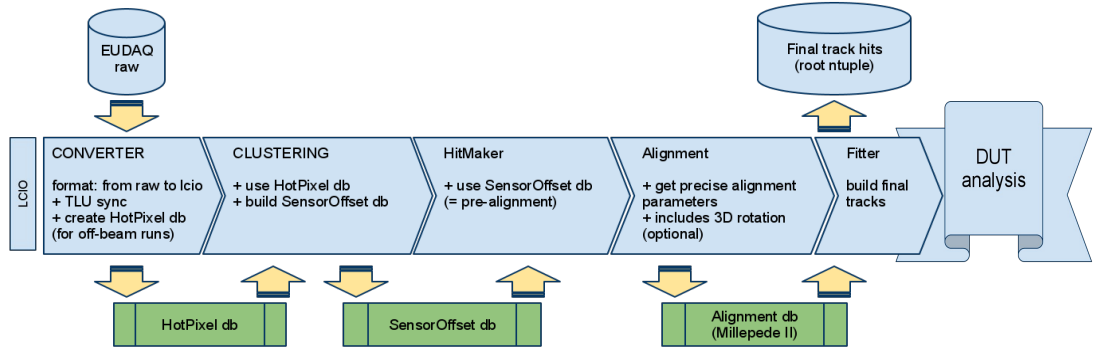


Figure 7.12: Flow diagram illustrating the five stages to reconstruct .lcio data from a beam test experiment and output a .root file. The blue arrows represent each stage of the reconstruction. The green boxes are external data produced from one stage and read into another. [73]

### Converter

Before reconstruction can be performed, the data must be converted from the RAW data format to the Linear Collider In/Out (LCIO) data format required. In the latter format all information from a single trigger is stored as one *event*.

- Column
  - The column number of the recorded hit pixel. For FE-I4 this is from 0 → 79.
- Row
  - The row number of the recorded hit pixel. For FE-I4 this is from 0 → 335.
- Time Over Threshold
  - The TOT value is between 0 → 15 (for FE-I4) for FE-I4.
- Level 1 Trigger
  - The time the hit was registered within the lvl1 trigger window. The value is between 0 → 16.
- Readout Identification number
  - The origin of the identified readout board.

An optional process called *Hotpixelkiller* can be implemented to find noisy pixels which otherwise would confuse alignment later. The setting is usually selected to define pixels as noisy when the frequency is greater than 0.01. The result of this cut is that if a pixel fires more often than once per 100 events in a run, it is added to a mask of noisy pixels. For

irradiated sensors the decision made for the frequency threshold is more relevant as a balance must be made between masking too many and allowing some noisy pixels through.

## Clustering

The charge collected from a single particle track may be registered in multiple cells within one device. This is due to charge sharing between neighbouring pixels or tilting of the sensor. These hits from multiple pixels must be grouped together into a *cluster*. There are many algorithms designed for clustering data, the two main ones used for track reconstruction are *Cluster Weighted Centre* and *Cluster Charge Weighted Centre*.

### *Cluster Weighted Centre*

The X and Y coordinates are averaged separately to give a value for the cluster centre. This algorithm is used for the telescope planes since only the location of the hit for each position in the cluster is known, therefore each hit has an equal weighting in determining the centre of the cluster position.

### *Cluster Charge Weighted Centre*

Using the Time Over Threshold (TOT) information from the DUT as a weight, the ‘centre of mass’ for the cluster can be calculated.

## Hitmaker

The local coordinates of the sensor, in terms of column and row number, are translated into the global coordinate system of the telescope. This is a right-handed cartesian coordinate system, with positions in the x-, y- and z-axes. The z-axis is the beam direction which is always perpendicular to the telescope planes for beam tests described here, and is ideally centred close to  $x = y = 0$ . This stage requires a steering file created by the user called a GEAR file. The GEAR file contains information about the beam test setup, such as the dimensions of the sensors, the pixel pitch in each direction and the sensitive and non-sensitive thicknesses of every device. The positions of each detector, along with any shifts or rotations are also provided.

The global coordinates determined in *hitmaker* are used to provide pre-alignment values in the X- and Y-directions.

## Alignment

There are two stages to the alignment procedure. The first stage performed in *hitmaker* is the pre-alignment. This is used as input for the second stage which utilises the software



MillepedeII [74] to determine the alignment constants. For a rigid body, six parameters are required for describing translations and rotations in space; three shift coordinates  $dX$ ,  $dY$ ,  $dZ$ , and three rotation angles, these are defined in the GEAR file (see Section 7.4.1).

The track fitting process uses a Kalman like fitting algorithm [75] called Deterministic Annealing Fitter (DAF) to calculate tracks from the hit positions. The actual path of the particle through the setup is not a straight line, but kinked due to multiple scattering. The fitting algorithm takes these kinks into account when deciding upon the fitted track. The following assumptions [76] are made when fitting tracks:

- The telescope planes are parallel, and at normal incidence to the particle beam.
- The angular spread of the particle beam is small and scattering angles are also minimal.
- Material thicknesses are much less than the separation between planes.
- There is a negligible beam energy loss as the beam crosses each telescope plane.

### Track finder

After alignment, the final stage is to reconstruct the particle track through the setup. The location that the track traverses each DUT plane is taken as the fitter hit coordinate. The final output file is in a .root format, with the structure shown in Table 7.2 [69].

#### 7.4.3 CED

The C Event Display (CED) [77] is a graphical programme which displays the detector planes along with the hit positions and reconstructed track from each run visually. The detector planes are drawn from information in the GEAR file used in the reconstruction and the hits and tracks are provided from the run-track.slcio file produced after the tracking stage. The programme is very useful for allowing comparisons between hit positions and reconstructed tracks ‘by eye’. Figure 7.13 shows the visual output of a typical event produced in CED. The first and last three planes are from the telescope, while the three in the middle are the DUTs. The green line is the reconstructed track. The green dots on the planes are a second set of hits from a particle which did not pass the cuts required to reconstruct the track.

## 7.5 Data analysis

The offline analysis software developed by the ATLAS pixel collaboration to study beam test data is called *TBMon* [78]. Written in C++ [79] and including ROOT [80] classes, TBMon reads in the .root file produced after the tracking stage of EUTelescope and allows the user to cluster the DUT data, fine-tune alignment and analyse the efficiency, charge sharing

Table 7.2: The structure of the reconstructed beam test data file in .root format [69].

Tree/Branch		
<b>euhits</b>		
nHits	int	Number of hits in this event
xPos	std::vector<double>	Global x coordinate [mm]
yPos	std::vector<double>	Global y coordinate [mm]
zPos	std::vector<double>	Global z coordinate [mm]
clusterId	std::vector<int>	ID of the corresponding cluster
sensorId	std::vector<int>	ID of the corresponding sensor
<b>zspix</b>		
nPixHits	int	Number of raw hits in this event
euEvt	int	Current event number
col	std::vector<int>	column of raw data hit
row	std::vector<int>	row of the raw data hit
tot	std::vector<int>	TOT of the raw data hit
lv1	std::vector<int>	LVL1 value of the raw data hit
iden	std::vector<int>	ID of the sensor
chip	std::vector<int>	ID of the sensor in the MCC board
clusterId	std::vector<int>	ID of corresponding cluster
<b>eutracks</b>		
nTrackParams	int	Number of parameters for estimation
euEvt	int	Event number
xPos	std::vector<double>	The fitted x position [mm]
yPos	std::vector<double>	The fitted y position [mm]
dxdz	std::vector<double>	The fitted derivate $\partial x / \partial z$
dydz	std::vector<double>	The fitted derivate $\partial y / \partial z$
trackNum	std::vector<int>	The track ID
iden	std::vector<int>	ID of the corresponding sensor
chi2	std::vector<double>	$\chi^2$ of the track
ndof	std::vector<double>	tracks's degrees of freedom
<b>euclusters</b>		
euEvt	int	Event number
size	std::vector<int>	Number of pixels in a cluster
sizeX	std::vector<int>	Cluster width in x [pixels]
sizeY	std::vector<int>	Cluster width in y [pixels]
posX	std::vector<int>	Position of the cluster in x [pixels]
posY	std::vector<int>	Position of the cluster in y [pixels]
charge	std::vector<int>	Sum charge of the cluster [TOT]
iden	std::vector<int>	ID of the corresponding sensor
ID	std::vector<int>	ID of the cluster
<b>timings</b>		
NTimings	int	Number of timings in this event
SensorId	int	ID of the corresponding sensor
ThId	std::vector<int>	TLU ID of this event
TpId	std::vector<int>	TPLL ID of this event
RealtimeSec	std::vector<int>	Realtime since clock reset [s]
RealtimeNs	std::vector<int>	Realtime since clock reset [ns]
RunNumber	std::vector<int>	Number of the run

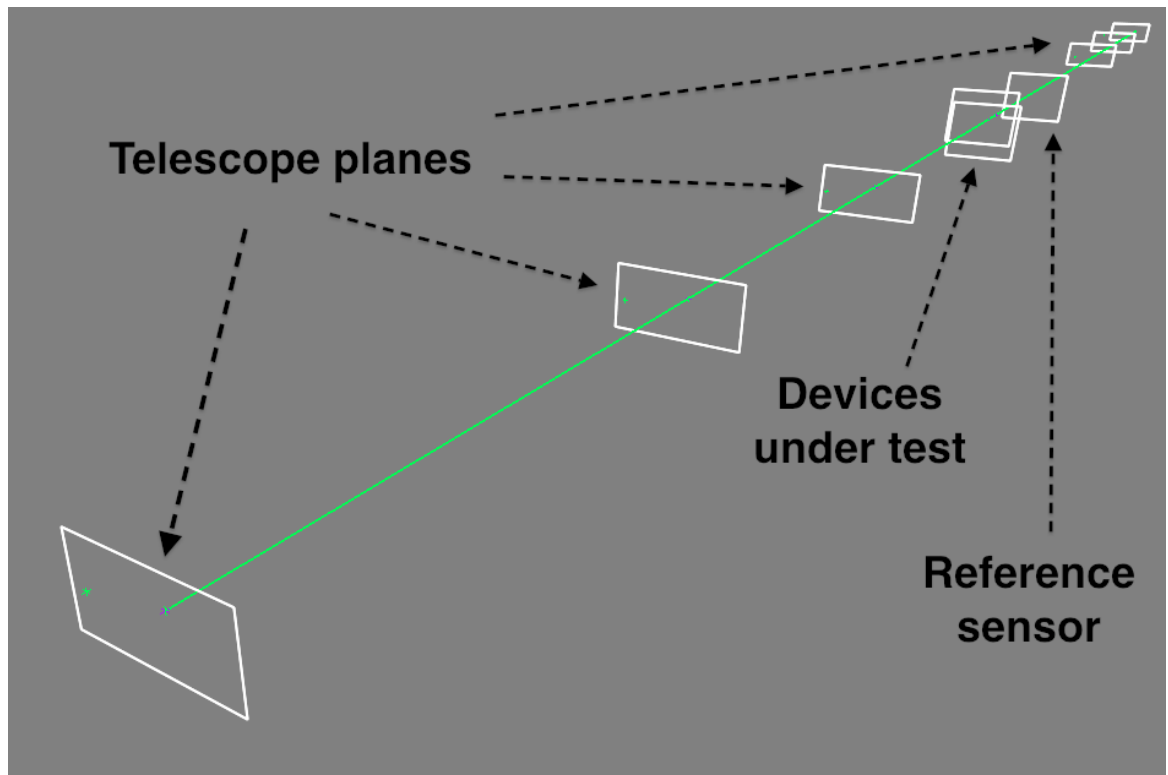


Figure 7.13: Visual output produced by CED.

and other features of the sensor depending on the analysis class selected. The standard pre-analysis steps are as follows:

- Hotpixel finder
- Check alignment
- Eta correction
- Check alignment

The check alignment analysis class is run a second time, with the results from the eta correction class applied and the results from the first iteration of alignment corrections removed.

### 7.5.1 Clusters

Charge is collected in multiple, neighbouring pixels when the particle track is at an inclination or when charge sharing occurs. These multiple hits must be grouped together as a cluster. Although clustering is already performed in the reconstruction stage, this information is not stored in the .root file and so clustering must be performed again.

### Clusters vs run

A new analysis class for TBMon was created to study the sizes of clusters per run over a given period of time. This was in part a response to the problem of the dry ice sublimating as mentioned in Section 7.2.2. Since the size of a cluster is a function of the tilt angle of the sensors, these plots indicate to the user if the box has moved significantly during data taking. Figure 7.14 is an example of the output from this class. The figure in the top shows a steady cluster size over time, indicating that the sensor has not tilted significantly during these runs. The error bars are present, but the errors are too small to be seen. The missing points are bad runs from the reconstruction that have been excluded from the analysis. Bad runs can be caused by desynchronisation of the data or, less often, physical changes in the environment such as the crane moving overhead of the experimental area causing vibrations which affect data taking. The lower figure in Fig. 7.14 is an example of poorer set of runs. The statistics are lower and the alignment not perfect. This results in a greater spread in cluster sizes.

The errors calculated are the standard error. Equation (7.1) describes the standard deviation of the data. The standard error, shown in Eq. (7.2), is the resolution of the mean of the data [81].

$$\sigma = \sqrt{\frac{1}{N-1} \sum_i (x_i - \bar{x})^2} \quad (7.1)$$

$$\sigma_{err} = \frac{\sigma}{\sqrt{N}} \quad (7.2)$$

### 7.5.2 Residuals

The residuals are calculated separately for x and y and are the difference between the position of the reconstructed track and the position of the cluster centre. If the reconstruction has gone well, the residual is a Gaussian distribution centred at zero with a base width approximately equal to the pixel pitch. However, this would be wider for results from DESY where there is increased multiple scattering. The Gaussian shape is due to charge sharing at the edge of the pixels. There are various algorithms for calculating the centre of a cluster with size greater than two<sup>2</sup>, these are listed below.

- Analog
- Digital
- MaxToT

---

<sup>2</sup>For a cluster size of one, all algorithms will give the same result.

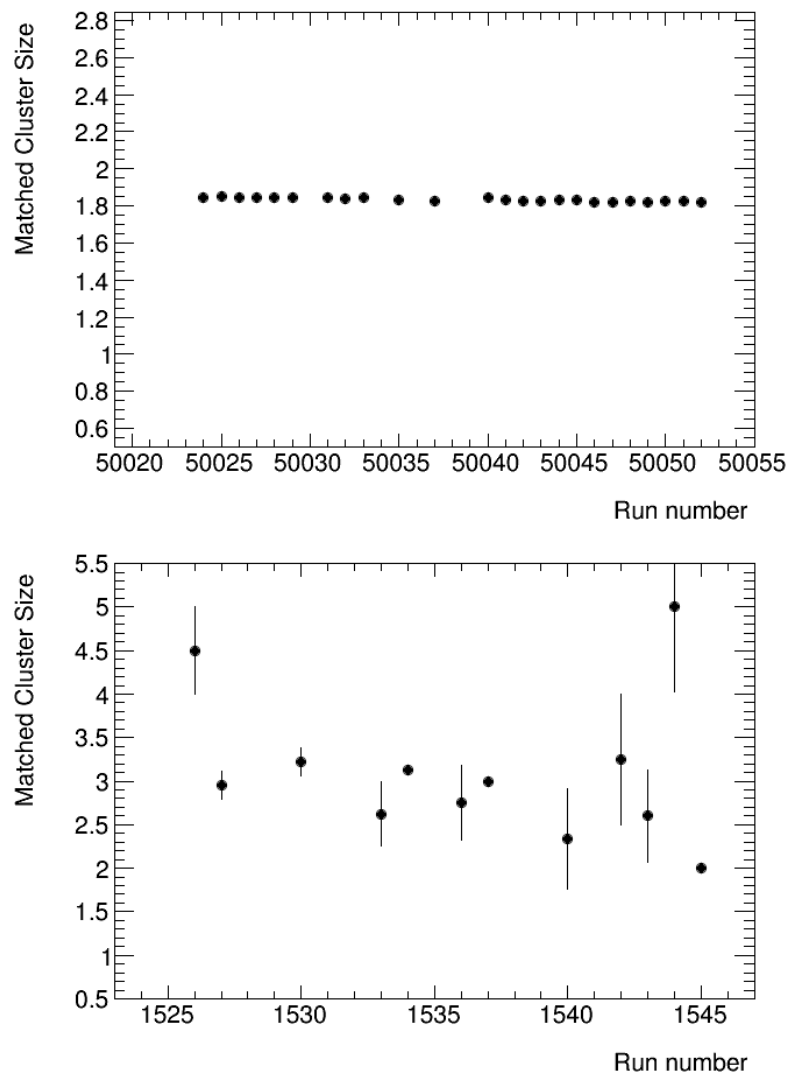


Figure 7.14: An example of the output from the `clustersvsrun` analysis class written for TBMon, showing the total matched cluster size for a sensor as a function of time (per run). The top is an example of a good set of runs while the bottom is an example of a set of runs with lower statistics and poorer alignment.

- $\eta$ -correction [82]
- Digital head-tail (DHT)

An example of the output from these various algorithms for a cluster size of two and  $\sigma = 58.24 \mu\text{m}$  is in Fig. 7.15. The choice of which residual distribution to consult depends on the setup and type of sensors used. For example, for high angle tilts it might be better to look at the DHT residual which uses the entry and exit point of a cluster, instead of the max TOT which considers the distribution of amount of charge deposited.

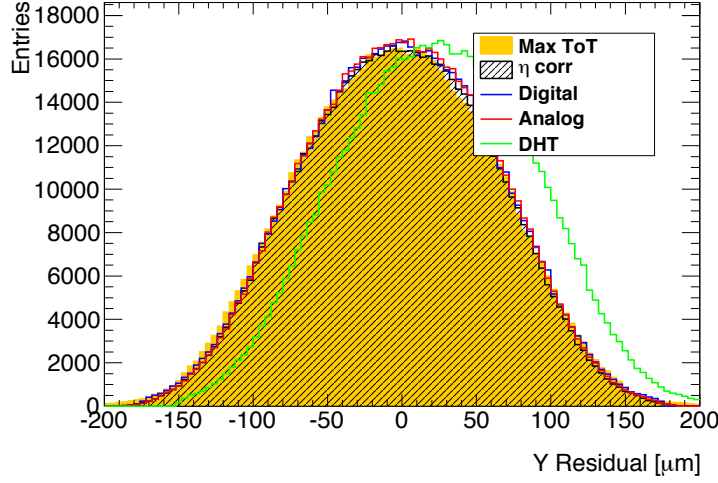


Figure 7.15: Residual for the y-direction for cluster size of two for various cluster algorithms with  $\sigma = 58.24 \mu\text{m}$ .

## 7.6 Results

The 3D devices tested in beams tests in 2011 and 2012 are listed in Table 7.1 in Section 7.3. Results from selected beam tests are presented below. Note that the data from CERN October 2012 was reconstructed by Matthias George and then subsequently analysed in TBMon by the author.

### 7.6.1 Tracking efficiency

The tracking efficiency for a pixel sensor is defined as the ratio of the number of measured hits close to a track, against the total hits predicted. These expected hits are determined using reconstructed tracks from a beam test. Figure 7.16 shows the sensor efficiency hit maps for the two FBK devices in the March 2012 beam test at DESY. The devices were FBK 11 (irradiated) and FBK 13 (non-irradiated) and were tilted to a  $\phi$  angle of  $15^\circ$ . The hitmaps on the left are for the lowest provided bias voltage and the right for the highest. Table 7.17 lists the voltages supplied for each set of runs and the corresponding efficiencies measured for each device for two threshold settings ( $1500 \text{ e}^-$  and  $1800 \text{ e}^-$ ). The values are presented in individual graphs in Fig. 7.17. FBK 11 is highly irradiated and required a significant mask to turn off noisy pixels, the effect of which can clearly be seen in the sensor hitmaps. At higher threshold the noise is significantly reduced until higher voltages. At this point, the emergence of an inefficient region (see Fig. 7.18) is probably due to shorting

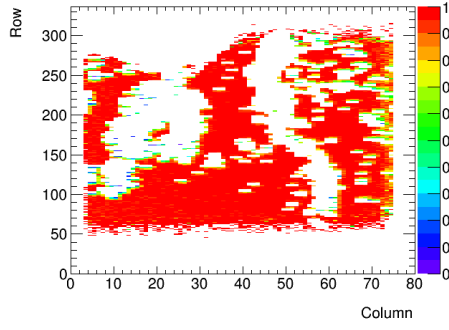
Table 7.3: Efficiency measured for bias voltage scans of FBK devices in Batch 2 of the IBL beam test at DESY, 2012.

FBK 11 (at threshold)			FBK 13 (at threshold)		
Bias Voltage	Efficiency		Bias Voltage	Efficiency	
	(1500 e <sup>-</sup> )	(1800 e <sup>-</sup> )		(1500 e <sup>-</sup> )	(1800 e <sup>-</sup> )
100 V	95.75	–	10V	99.10	–
110 V	95.74	–	15V	98.97	99.18
120 V	96.11	–	20V	99.01	98.79
130 V	96.04	–	25V	98.69	–
140 V	96.06	97.51	30V	99.23	98.48
150 V	96.12	94.70	–	–	–
160 V	96.08	93.30	–	–	–

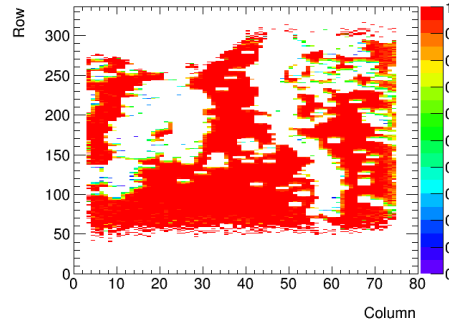
of the pixels and increased noise. The temperature in the beam test fluctuates depending on the quantity of dry ice, so this could also be related to the temperature of the device. However, temperature monitoring was not performed so this is inconclusive. Despite the issues, the remaining pixels for FBK 11 have an efficiency of  $\sim 96\%$  for a threshold of 1500 e<sup>-</sup> and between  $\sim 97$  and  $\sim 93\%$  for a threshold of 1800 e<sup>-</sup>. The non-irradiated device, FBK 13 has an overall efficiency of  $\sim 99\%$ . For FBK 13 the white area is a known bump-bonding issue.

A feature of 3D silicon sensors that is known, is that there is a loss of efficiency when a track passes perpendicularly through an electrode. This loss is recovered if the sensor is tilted as little as 10°. CNM sensors with the IBL design layout experience less of an efficiency loss through the electrodes due to their design. The electrodes of a CNM sensor stop  $\sim 20 \mu\text{m}$  before the wafer surface.

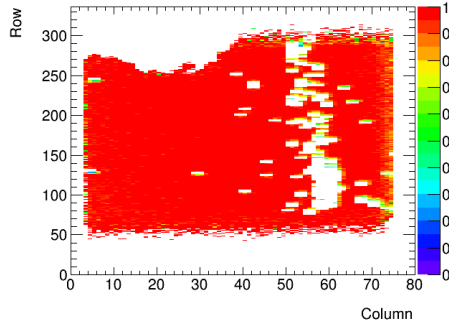
Tracks are extrapolated from the telescope hits. To reduce fake tracks, a matching hit in another DUT (usually the reference sensor) is required. The tracking efficiency can be studied within a pixel cell. Figure 7.19 shows the efficiency within the pixel cell of a non-irradiated FBK device on an FE-I4b readout card. Data is from the October IBL beam test at CERN in 2012. The device was tuned to a threshold of 2000 e<sup>-</sup>, with a TOT of 6 for 20 ke. It was biased to -25 V. To ensure high statistics, the results from all pixels have been combined. Because this data was taken at zero degrees incident angle, the inefficient area of the electrodes can be clearly seen in (b). When the sensor was tilted to 15°, as shown in (h), full efficiency is recovered. A focused study of the efficiency for the two electrode types was performed and can be seen in (d) for the readout electrodes and (f) for the bias electrodes. For each two dimensional hitmap, a one dimensional projection is shown below. The width of the lower efficiency region corresponds to the electrode diameter. The lower efficiency for the electrodes does not reach zero even though the electrodes in these FBK devices are



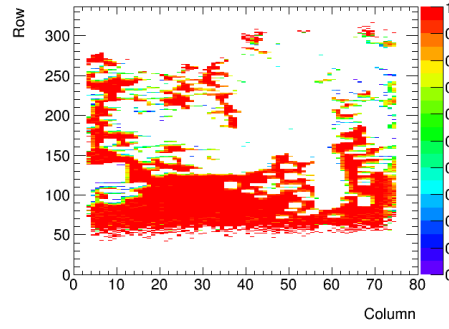
(a) FBK 11 at -100V. Threshold  $1500 \text{ e}^-$ .



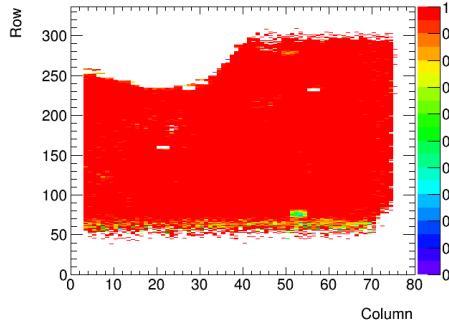
(b) FBK 11 at -160V. Threshold  $1500 \text{ e}^-$ .



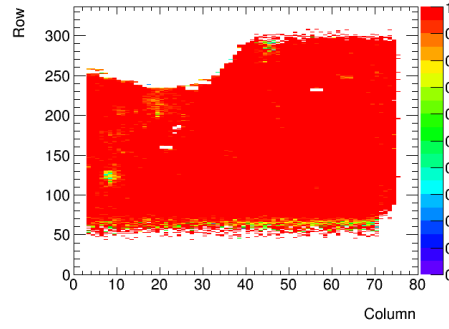
(c) FBK 11 at -140V. Threshold  $1800 \text{ e}^-$ .



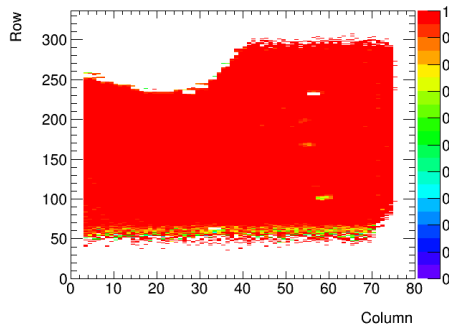
(d) FBK 11 at -160V. Threshold  $1800 \text{ e}^-$ .



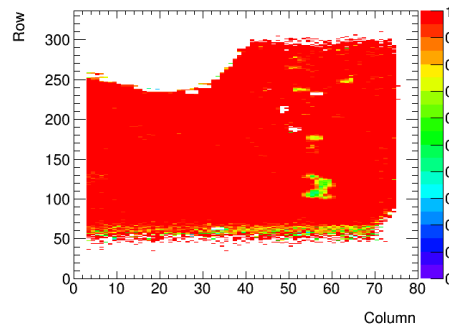
(e) FBK 13 at -10V. Threshold  $1500 \text{ e}^-$ .



(f) FBK 13 at -30V. Threshold  $1500 \text{ e}^-$ .



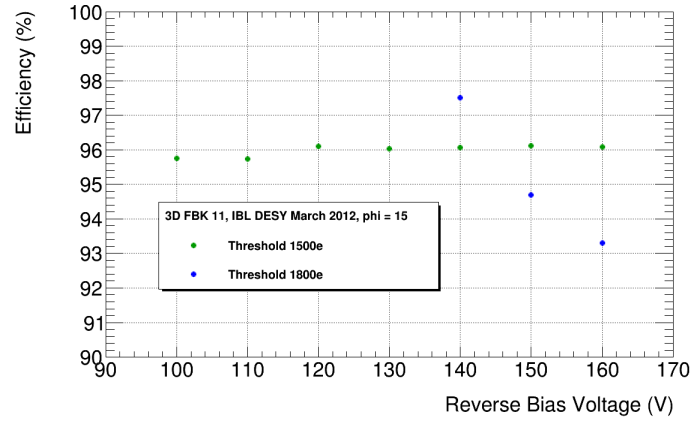
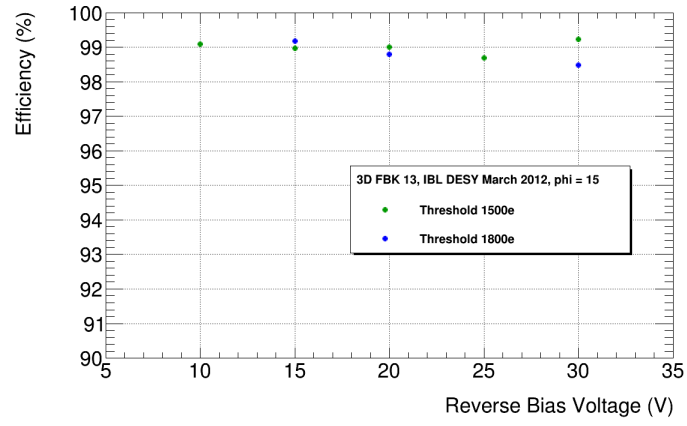
(g) FBK 13 at -10V. Threshold  $1500 \text{ e}^-$ .



(h) FBK 13 at -30V. Threshold  $1500 \text{ e}^-$ .

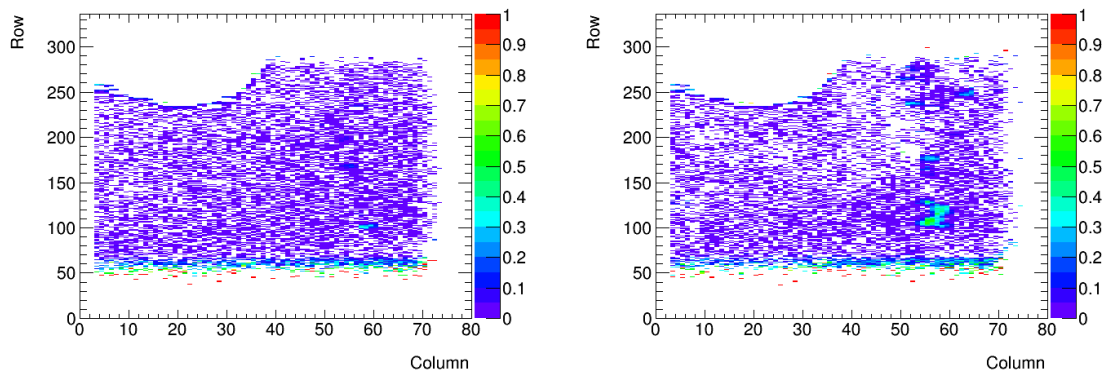
Figure 7.16: Sensor efficiency maps for (a – d) FBK 11 and (e – h) FBK 13 for the lowest (left) and highest (right) supplied bias voltages. Data from the DESY IBL beam test in March, 2012. The white areas for FBK 11 are due to masking of noisy pixels. For FBK 13 the white area is a known bump-bonding issue.



(a) FBK 11, irradiated to  $6 \times 10^{15} \text{ n(eq) cm}^{-2}$ .

(b) FBK 13, non irradiated.

Figure 7.17: Comparison of efficiency against reverse bias voltage for 3D silicon pixel detectors (a) FBK 11 and (b) FBK 13 in Batch 2 of the IBL beam test at DESY.

(a) FBK 13 at -15V. Threshold  $1800 \text{ e}^-$ .(b) FBK 13 at -30V. Threshold  $1800 \text{ e}^-$ .Figure 7.18: Comparison of inefficiency maps for non-irradiated 3D silicon pixel detector FBK 13 with a threshold of  $1800 \text{ e}^-$  in Batch 2 of the IBL beam test at DESY.

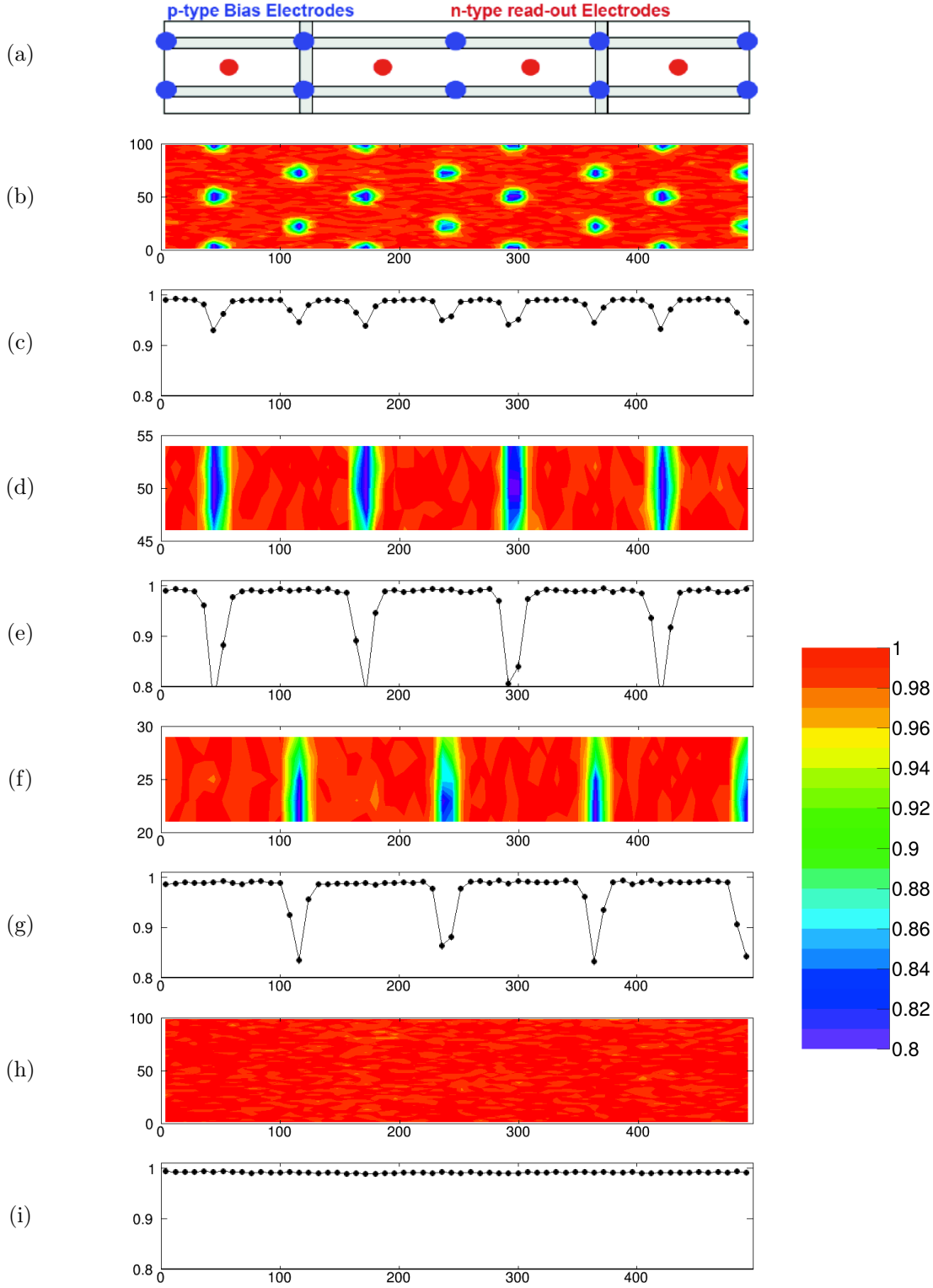
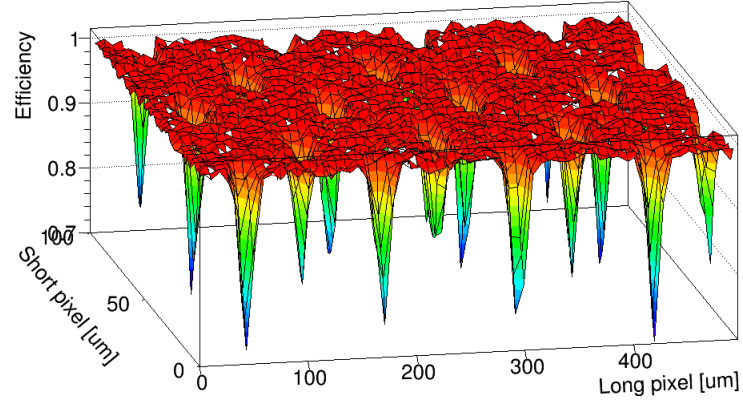
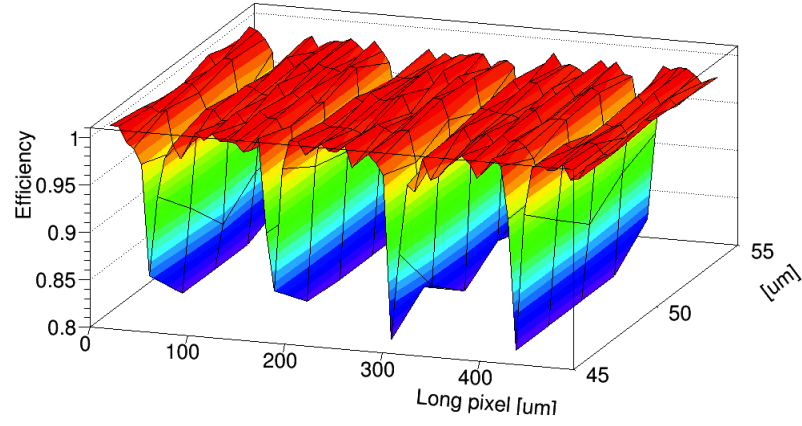


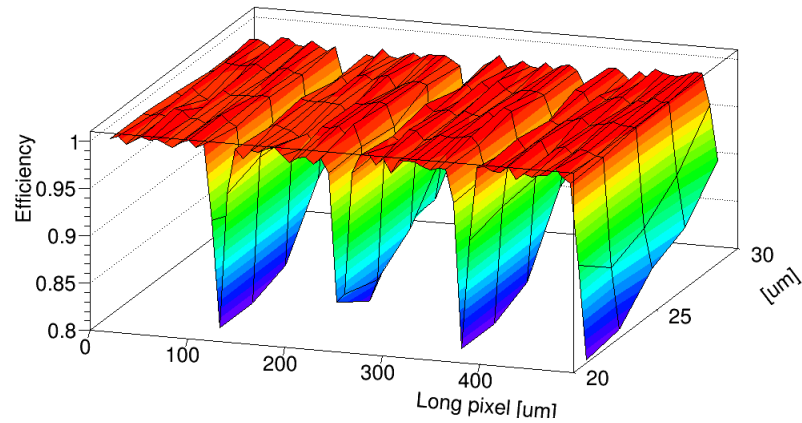
Figure 7.19: Two dimensional efficiency maps for an FBK non-irradiated IBL sensor. From the top: (a) mask detail centred on a single 3D cell and extended to half a cell in all directions. (b) 2D efficiency map for the FBK sensor at normal beam incidence, (c) 1D projection, (d) 2D efficiency map for the readout electrodes region, (e) 1D projection, (f) 2D efficiency map for the bias electrodes region, (g) 1D projection, (h) 2D efficiency map for the FBK sensors at  $15^\circ$  to the beam and (i) 1D projection.



(a) Three dimensional efficiency map for the pixel cell. The cell is centred, with half a pixel extended in each direction.



(b) Three dimensional efficiency map for the readout electrode region. The cell is centred, with half a pixel extended in the long pixel direction.



(c) Three dimensional efficiency map for the bias electrode region. The cell is centred, with half a pixel extended in the long pixel direction. The short pixel direction has been cut to 10  $\mu\text{m}$ .

Figure 7.20: Three dimension efficiency maps for non-irradiated FBK device in the IBL CERN beam test from October 2012. The device was at normal incidence to the beam.

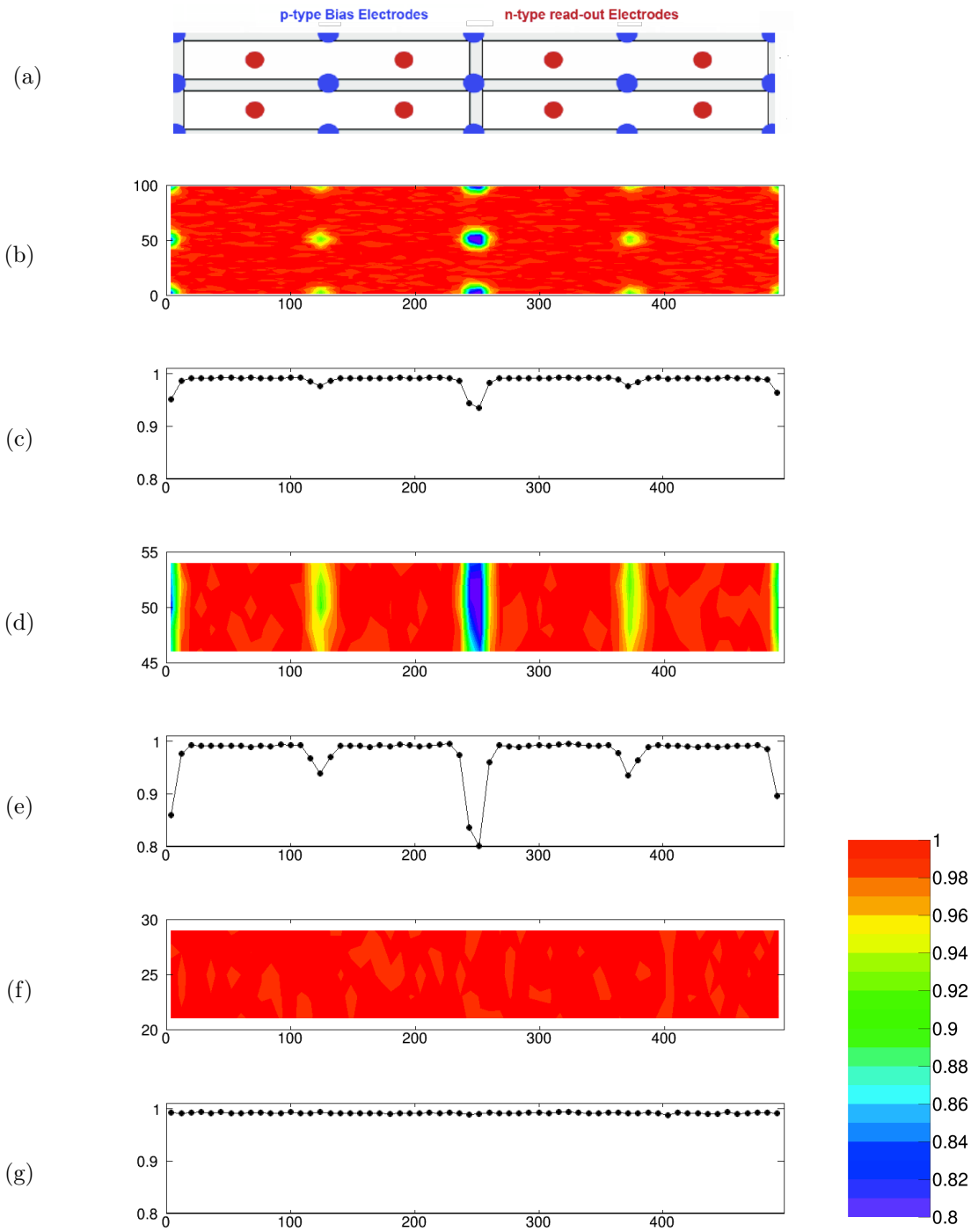


Figure 7.21: Two dimensional efficiency maps for a non-irradiated CNM IBL sensor. From the top: (a) mask detail arranged in a 2 x 2 matrix of pixel cells, (b) 2D efficiency map for four CNM pixels at normal incidence to the beam, (c) 1D projection, (d) 2D efficiency map for the bias electrodes region, (e) 1D projection, (f) 2D efficiency map for the readout electrodes region and (g) 1D projection.

empty. This is partly due to the resolution of the telescope and the fact that the beam incident angle will not be exactly perpendicular to the wafer surface (and therefore not parallel to the electrodes). Three dimensional efficiency maps for FBK can be found in Fig. 7.20.

For comparison, the pixel efficiency for the non-irradiated CNM 55 is shown in Fig. 7.21, with the bias and readout efficiency maps included. Note the change in pixel arrangement in the hitmaps. The pixels are now arranged in a 2 x 2 matrix. It is clear that there is no efficiency loss in the bias electrodes. The matched efficiency for this device at  $0^\circ$  is 98.71%.

The FBK sensor tested was from the same batch used to build the IBL. These efficiency plots show that the device is working as expected. The sensor efficiency at  $0^\circ$  is 97.93% and at  $15^\circ$  is 99.15%. The full efficiency recovery at  $15^\circ$  fulfils that requirement for IBL sensors. It is recommended that for studies at future beam tests, devices on FE-I4b readout cards should be irradiated to the fluence expected within the IBL lifetime. It is also recommended that further study of the inefficiency of the electrodes is performed, since this is still not fully understood.

### 7.6.2 Edge efficiency

The study of the edge efficiency was performed with two FE-I3 SINTEF active edge sensors, known as SINTEF 98 and SINTEF 115, in Batch 4 of the 3D beam at CERN in May, 2012. SINTEF 115 has been irradiated with protons to a fluence of  $3 \times 10^{15} \text{ n}_{eq}\text{cm}^{-2}$ . Recall that the pixel length is  $400 \mu\text{m}$  by  $50 \mu\text{m}$ , but that the edge pixels are extended in the long direction. For these devices the edge pixel was  $580 \mu\text{m}$  by  $50 \mu\text{m}$ .

Table 7.4: Breakdown of bias voltages for Batch 4 data from CERN beam test, May 2012. The reference sensor, CNM 55, was maintained at normal incidence to the beam at a bias voltage of -30 V.

GeoID	SINTEF 98 Bias Voltage	SINTEF 115	Initial Run No.	Final Run No.	Total Events
24	15 V	140 V	70441	70461	0.653 M
26	25 V	160 V	70471	70475	0.152 M
27	20 V	120 V	70477	70480	0.134 M
28	10 V	100 V	70484	70487	0.170 M
29	5 V	80 V	70491	70495	0.214 M

The reverse bias voltages applied to each DUT for a group of runs defined by a GeoID are displayed in Table 7.4. The first and last run number, along with the total number of events, are included to illustrate the size of each group and for future reference. A minimum of 100,000 total events are desired for good statistics, although the number of particles passing

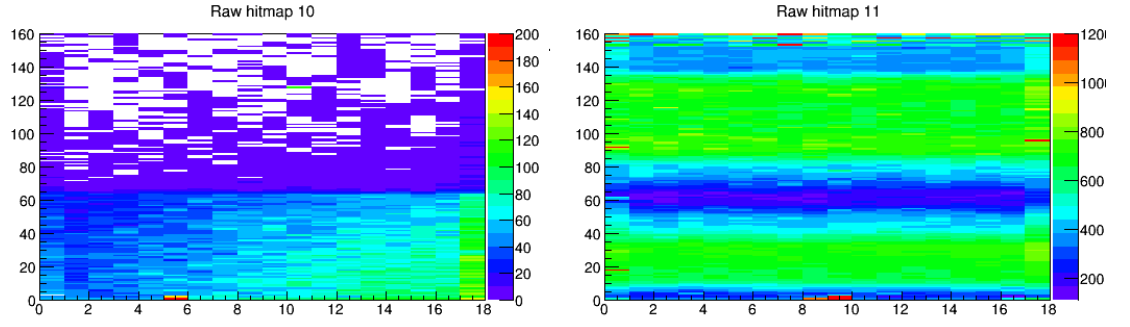
Table 7.5: Comparison of the efficient pixel width and total sensor efficiency for the 3D silicon pixel detectors SINTEF 98 and SINTEF 115, both on FE-I3 readout cards.

SINTEF 98			SINTEF 115		
Bias Voltage	Active width	Efficiency	Bias Voltage	Active width	Efficiency
5 V	$560.1 \pm 1.8$	0.9271	80 V	$343.3 \pm 1.7$	0.6141
10 V	$488.3 \pm 7.9$	0.9342	100 V	$392.2 \pm 85.6$	0.5650
15 V	$561.8 \pm 1.9$	0.9259	120 V	$357.5 \pm 0.2$	0.5969
20 V	$550.5 \pm 4.4$	0.9301	140 V	$327.9 \pm 6.6$	0.8079
25 V	$569.3 \pm 1.7$	0.9291	160 V	$341.0 \pm 4.4$	0.6100

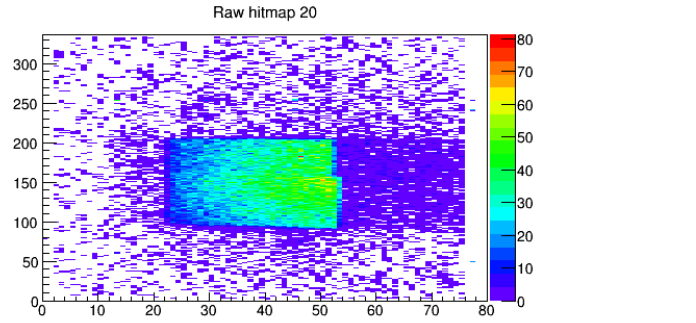
through each sensor will be determined by the sensor size, angle to the beam and percentage of masked pixels. The scintillator window is  $\sim 10$  mm x 10 mm, which is large enough to cover an FE-I3 sized detector, but not large enough for an FE-I4 device. Figure 7.22 shows the hitmaps for the three devices. Due to physical and time constraints only half of SINTEF 98 was aligned with the scintillator window, reducing the statistics for this device. As stated, the reference sensor surface is much larger than the scintillator window, which was centred in the device frame (see Fig. 7.22c). The dark strip in the centre of the hitmap for SINTEF 115 is due to damage from irradiation and not the size of the scintillator window.

The data were reconstructed in EUTelescope and analysed in TBMon. A particular focus on the analysis of the total sensor efficiency and of the efficiency of the edge pixels for each device. A study of the edge efficiency of the reference sensor, CNM 55, was not performed because it has been studied before (see Section 5.2.2). Figure 7.23 contains the hitmaps for all left edge pixels for SINTEF 98 at -15 V (a) and SINTEF 115 at -140 V (b). Note that the edge pixel is centred in the image, with half of the pixel height added above and below, and half the standard pixel width to either side. The results from all edge pixels are combined into a single pixel cell to increase statistics. The one-dimensional efficiency of the edge pixel for each reverse bias voltage supplied is shown in Fig. 7.24 for SINTEF 98 and Fig. 7.25 for SINTEF 115.

The efficient pixel width for each device as a function of bias voltage is listed in Table 7.5 and plotted in a graph in Fig. 7.26. The width at which the pixel is efficient to is fairly steady, except for the data set from GeoID 28, which corresponds to Fig. 7.24c (the data for SINTEF 98 taken at -10 V) and Fig. 7.25c (the data for SINTEF 115 at -140 V). These results are poorer than the other set of runs and this has resulted in lower statistics and consequently a poorer fit. It is expected that the efficiency for SINTEF 98 is lower than 100%. The device is at normal incidence to the beam and there is a greater density of electrodes compared to the now standard IBL 3D pixel design.

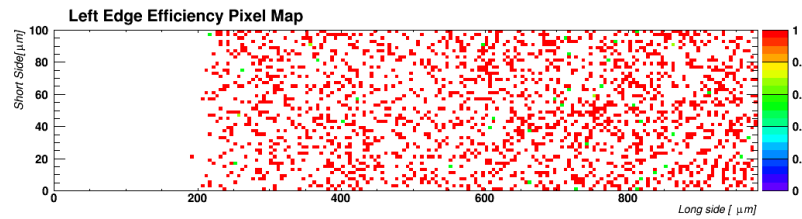


(a) Sensor hitmap for non-irradiated FE-I3 3D silicon device, SINTEF 98, biased at -15 V. (b) Sensor hitmap for irradiated FE-I3 3D silicon device, SINTEF 115, biased at -140 V.

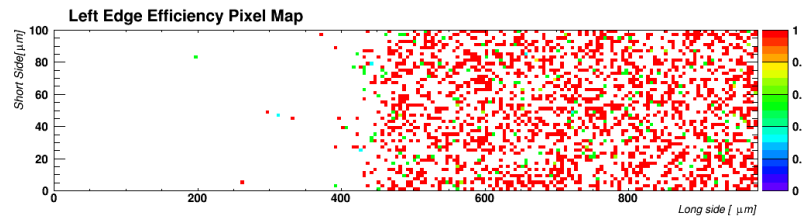


(c) Sensor hitmap for non-irradiated FE-I4 3D silicon device, CNM 55, biased at -30 V. CNM 55 was the reference sensor for the batch.

Figure 7.22: Comparison of the raw hitmaps for the three devices under test in Batch 4 of the CERN beam test, May 2012.



(a) SINTEF 98



(b) SINTEF 115

Figure 7.23: Comparison of combined efficiency pixel hitmaps for all the left edge pixels, folded into a single pixel cell.

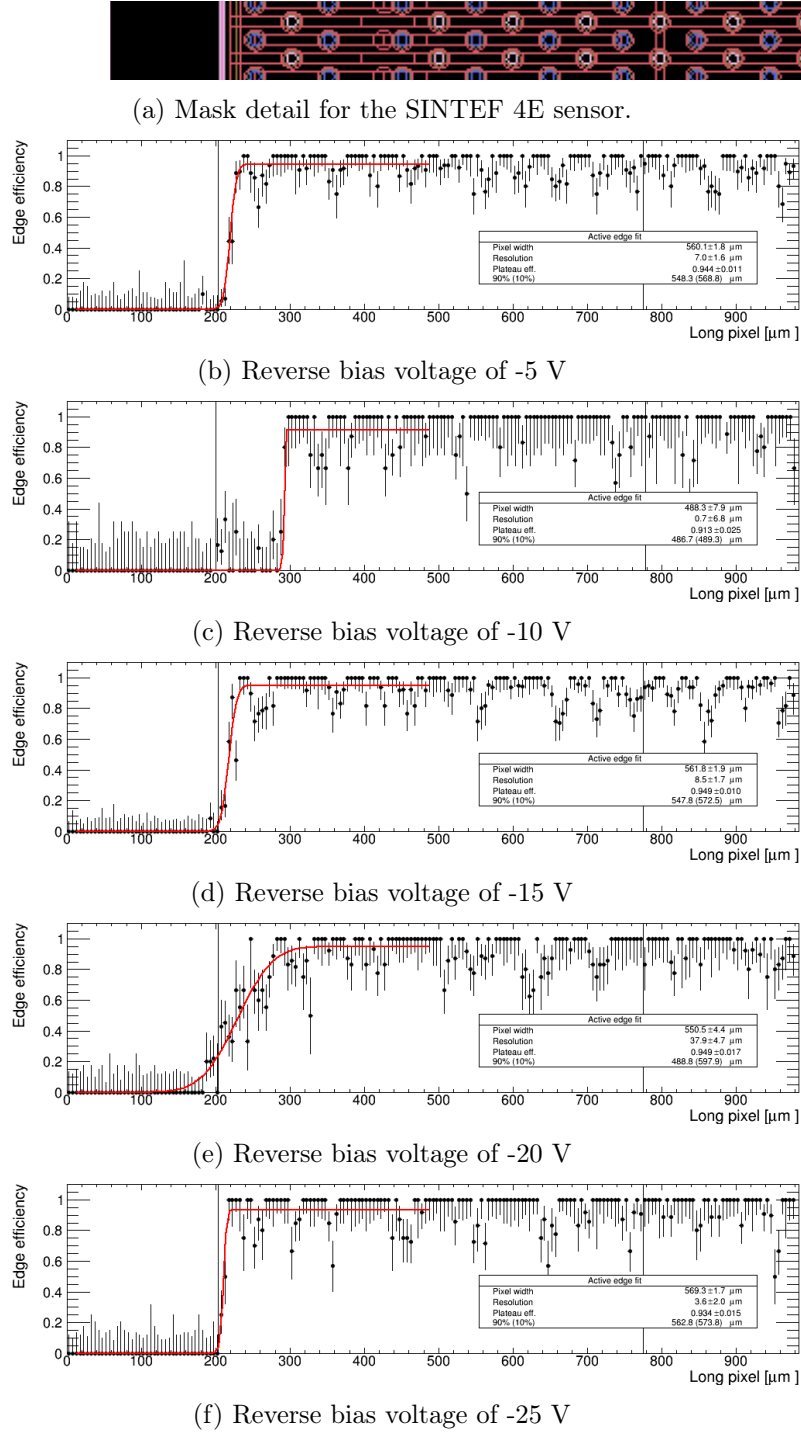
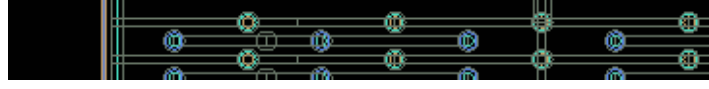
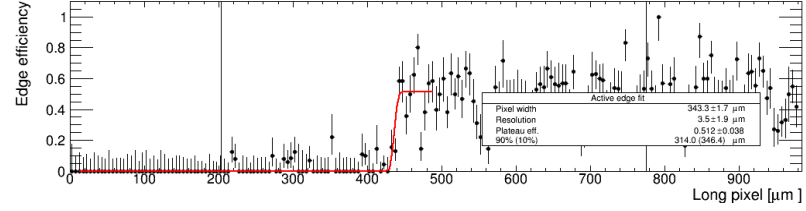


Figure 7.24: Edge efficiency pixels for SINTEF 98. The red line is a fit to the data. The black lines at 200  $\mu\text{m}$  and 780  $\mu\text{m}$  define the edges of the pixel.

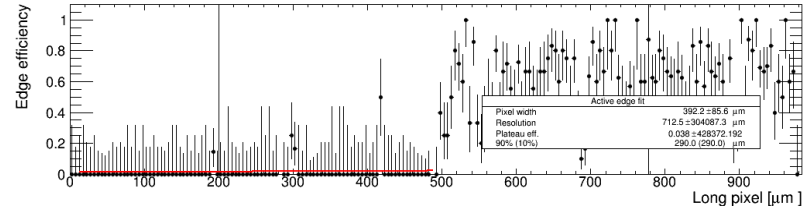




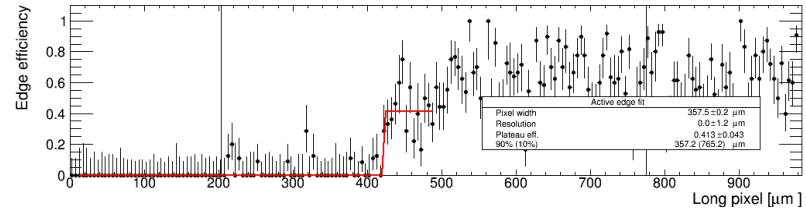
(a) Mask detail for the SINTEF 2E sensor.



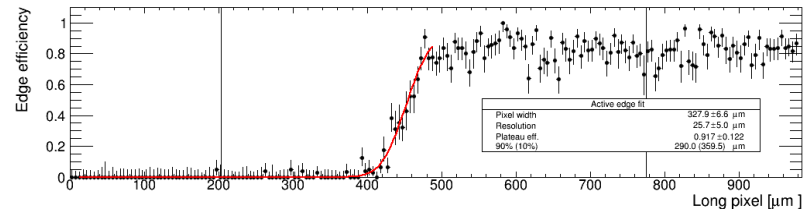
(b) Reverse bias voltage of -80 V



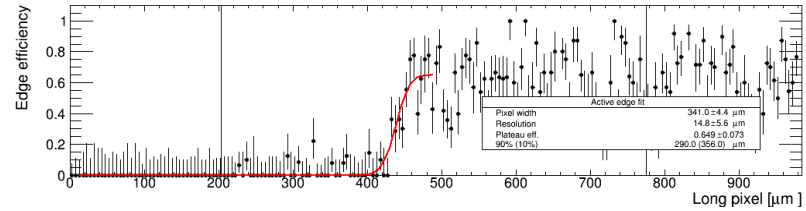
(c) Reverse bias voltage of -100 V



(d) Reverse bias voltage of -120 V

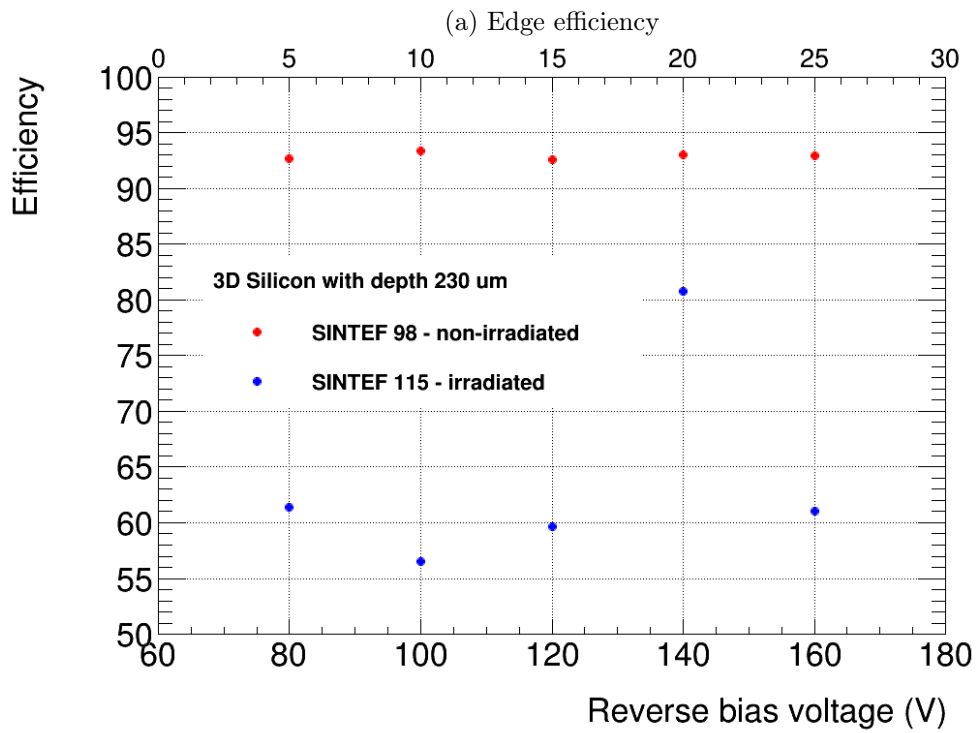
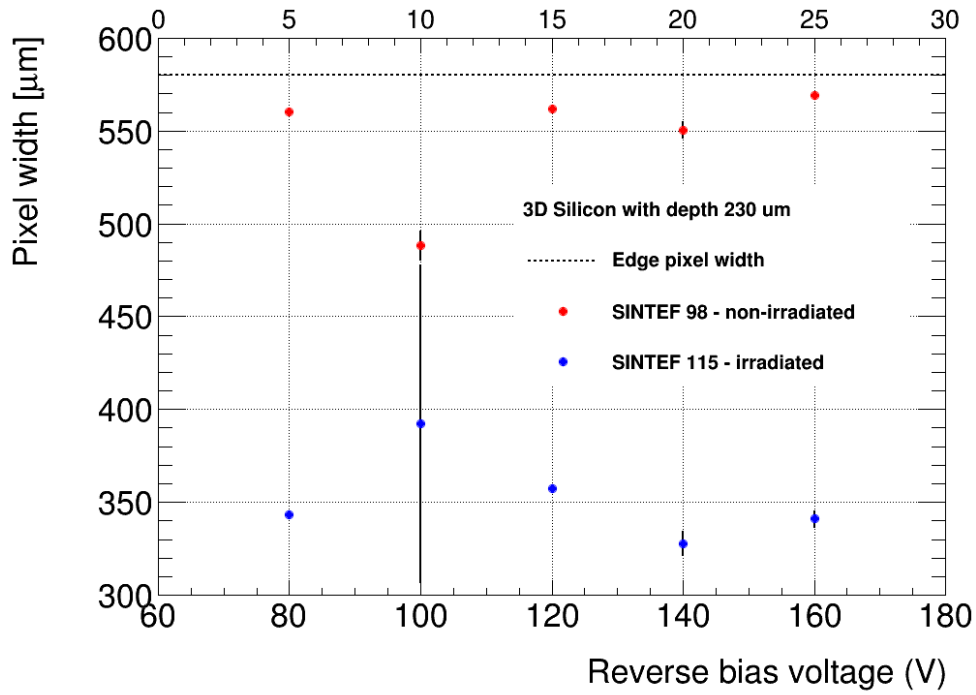


(e) Reverse bias voltage of -140 V



(f) Reverse bias voltage of -160 V

Figure 7.25: Edge efficiency pixels for SINTEF 115. The red line is a fit to the data. The black lines at  $200 \text{ } \mu\text{m}$  and  $780 \text{ } \mu\text{m}$  define the edges of the pixel.



(b) Total sensor efficiency

Figure 7.26: Efficiency for the edge pixels and whole sensor for SINTEF 98 and SINTEF 115. Note that the top x-axis refers to the bias voltages supplied to SINTEF 98 and the bottom y-axis the bias voltage supplied for SINTEF 115. The two results are plotted on the same graph for easy comparison of the trend.

### 7.6.3 Charge sharing

An important feature of sensor study is the total charge sharing between pixels. Total charge sharing is defined as the ratio of tracks resulting in two or more neighbouring hits over the total number of tracks through the sensor. However, as well as total charge sharing, we also want to study the sub-pixel regions where charge is shared such as at pixel borders. Charge sharing improves tracking resolution, but charge that is shared between two (or more) neighbouring pixels reduces the charge each pixels receives. This increases the likelihood that the charge per pixel is below threshold. Charge sharing will increase when the sensor is tilted, since particle tracks will pass through multiple pixels. Loss of charge may be an issue for irradiated sensors, which have a lower collected charge anyway. Figure 7.27, from reference [83] shows the charge sharing for the FBK device from the October IBL beam test at CERN in 2012 (described in Section 7.6.1) for  $0^\circ$  and  $15^\circ$ . Charge sharing increases when the sensor is tilted.

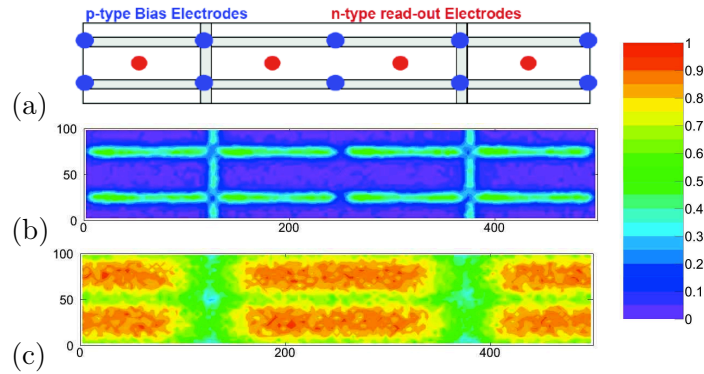


Figure 7.27: Two dimensional probability of charge sharing maps for an FBK non-irradiated IBL sensor. From the top: (a) mask detail centred on a single 3D cell and extended to half a cell in all directions. (b) 2D charge sharing map for the FBK sensor at normal incidence to the beam. (c) 2D charge sharing map for the FBK sensor at  $15^\circ$  to the beam. [83]

### 7.6.4 High eta studies

The location of 3D silicon detectors on the staves that make up the IBL was chosen as the very outer layers (see Section 4.1). This is the high-eta region and tracks will pass through the modules at  $\sim 5$  degrees to the beam pipe. Simulations of the result of installing 3D sensors at this position are in the process of being created and must be compared to real data.

The data set was taken in the June 2012 IBL beam test at CERN with a  $120 \text{ GeV}/c^2$  muon beam. The devices tested were FBK 13 and FBK 11 with CNM 55 as the reference sensor. All three devices were tuned to a threshold of  $1600 \text{ e}^-$  and a TOT of 8 for a deposited

Table 7.6: Information about the devices in Batch 1 of the IBL beam test at CERN in 2012.

	DUT 0	DUT 1	DUT 2
Sensor	FBK 13	FBK 11	CNM 55
Read Out Chip	FE-I4a	FE-I4a	FE-I4a
Fluence	0	$6 \times 10^{15} \text{ } n_{eq} \text{cm}^2$	0
Bias Voltage	- 20 V	- 160 V	- 30 V
Threshold	1600 $e^-$	1600 $e^-$	1600 $e^-$
TOT	8 TOT for 20 $ke^-$	8 TOT for 20 $ke^-$	8 TOT for 20 $ke^-$

Table 7.7: Breakdown of tilt angles for Batch 1a data from CERN IBL beam test, June 2012. Angles refer to the tilt of FBK 13 and FBK 11. The reference sensor, CNM 55, was maintained at normal incidence to the beam.

GeoID	Eta	Phi	Initial Run No.	Final Run No.	Total Events
75	0°	0°	1433	1468	2.65 M
78	60°	15°	1523	1569	3.16 M
79	70°	15°	1573	1612	3.06 M
80	80°	15°	1613	1655	3.12 M
82	85°	15°	1664	1710	3.31 M

charge of 20,000  $e^-$ . Table. 7.6 lists the important information for each sensor. The two FBK devices were mounted back-to-back in order to minimise the difference in incident angle, however for logistical reasons FBK 11 was mounted ‘upside-down’. Data for a set of runs were taken at normal beam incidence ( $\eta = \phi = 0^\circ$ ) and at  $\phi = 15^\circ$  with  $\eta = 60^\circ, 70^\circ, 80^\circ$  and  $85^\circ$ . Around three million events were recorded for each GeoID. This large data set was vital to ensure sufficient statistics for the subsequent reconstruction and analysis, since many tracks triggered by the scintillator would not pass through the highly tilted devices. This information is listed with the corresponding GeoIDs in Table. 7.7. The sensors were tilted with the wedge and rotation plate described in Section 7.2.3. A sketch of the setup can be found in Fig. 7.28.

The photographs in Fig. 7.29 show the setup of this batch with the lid of the cooling box removed for high eta angle of  $\sim 81^\circ$  and a  $\phi$  of  $\sim 15^\circ$  from above (a) and the side (b). The beam direction is from left to right.

### Masking of FBK 11

The module FBK 11 was irradiated to  $6 \times 10^{15} \text{ } n_{eq} \text{cm}^{-2}$  which resulted in a large number of noisy pixels. These pixels required a mask to reduce the amount of false read-out during data taking. Figure 7.30 shows the *enable* mask applied to the configuration file for FBK 11. This indicates which pixels were enabled (red in the image) and pixels that had been turned

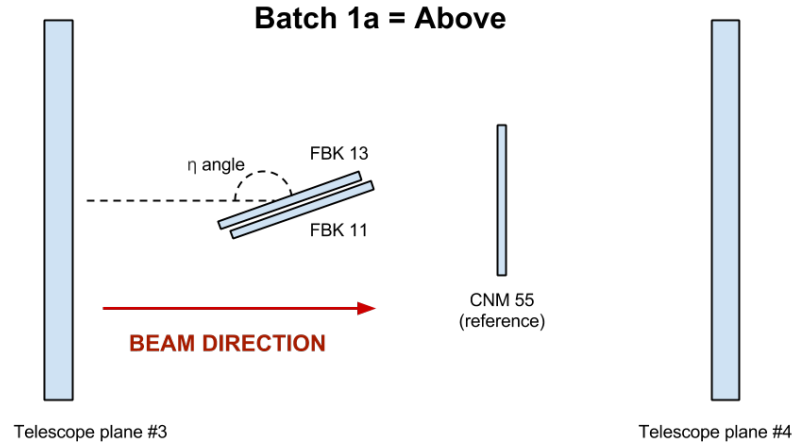


Figure 7.28: Sketch of the setup of Batch 1a of the June 2012 beam test at CERN. The devices under test are in the centre (labelled FBK 13 and FBK 11), with the reference device just to the right. The beam direction is from left to right.

off (black pixels). The large number of disabled pixels was an issue during the analysis for this sensor; tracks of six or seven pixels lengths were expected for high- $\eta$  angles. If a pixel was switched off in the middle of this track, two hits of cluster size three would have been recorded, skewing the cluster size distribution.

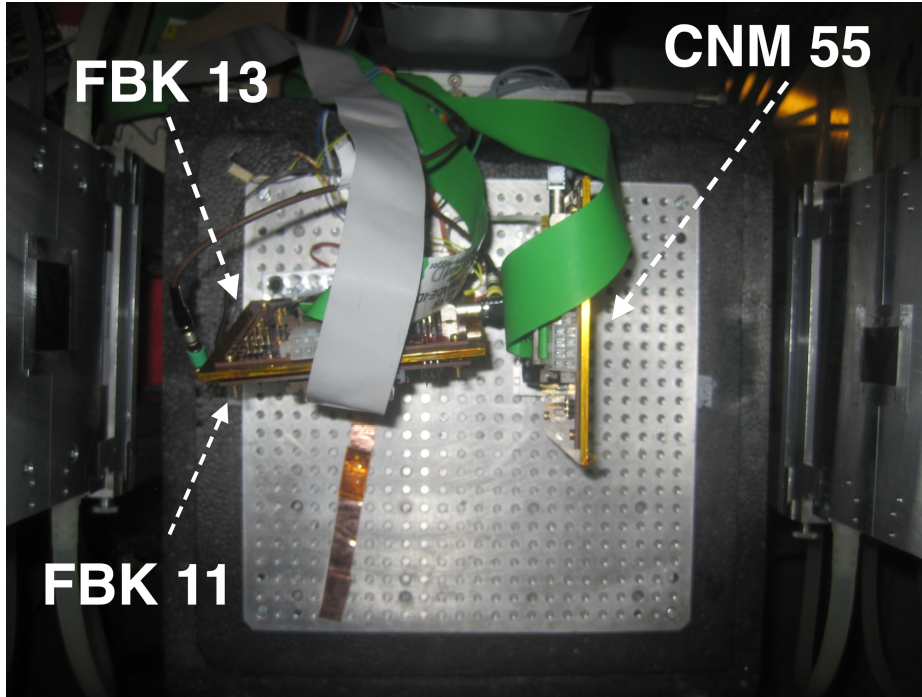
Because of the combination of the extreme complication of reconstructing the high eta angle data set and the masking of FBK 11, the final alignment of the devices has not been possible. The data below have been extracted during the reconstruction.

### Hitmaps

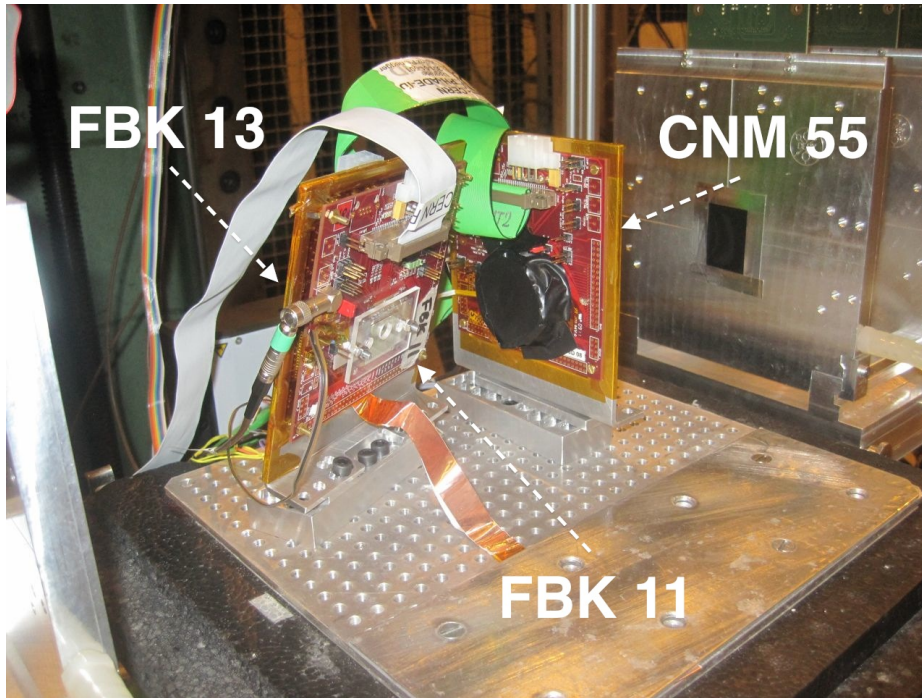
The hitmaps shown in Fig. 7.31 show the comparison between hits at normal beam incidence and at high eta angles. The latter show distinct long tracks. The masking of FBK 11 is clearly visible as white patches of zero hits. The red pixels are noisy and firing far more frequently than the other neighbouring pixels.

### Cluster size

Studying the cluster size as a function of the tilt angle of a module gives a clear indication of how well the sensor is performing. The cluster size in the x- or y-direction is determined by counting the total number of pixels in the cluster in the corresponding direction. Figure. 7.32 is a simulation of the expected track length of a particle through a tilted sensor of thickness  $230\text{ }\mu\text{m}$ . This simulation does not take into account threshold levels or defects due to irradiation damage, but is purely a mathematical calculation of the distance traversed.



(a) Above



(b) Side

Figure 7.29: Photograph of setup of Batch 1a, June beam test, CERN 2012 from above (a) and the side (b). In both photographs the beam direction is from left to right. FBK 13 and FBK 11, to the left, were mounted back-to-back. The GeoID was 80 which corresponds to a  $\phi$  of  $\sim 15^\circ$  and  $\eta$  of  $\sim 81^\circ$ .

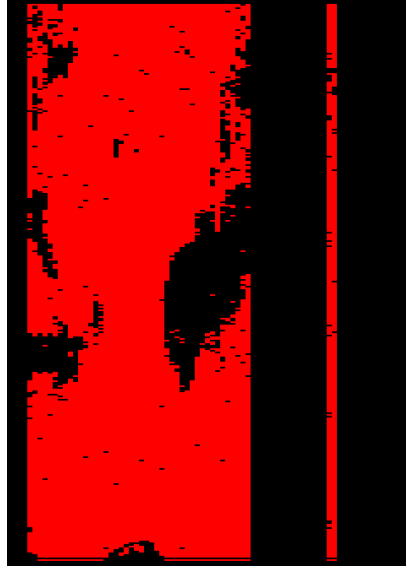


Figure 7.30: Enable mask for FBK 11, on an FE-I4 read out chip, irradiated to  $6 \times 10^{15} n_{eq}$ . The red sections indicate pixels which were enabled (set to 1) and the black sections are pixels which have been disabled (set to 0).

From this an estimate of the cluster size expected can be made. The actual cluster size is affected by charge sharing, charge reaching threshold, noisy pixels and further issues.

An indication of the noise recorded from the device can be obtained from looking at the lvl1 trigger distributions<sup>3</sup>. The data collection is synchronised and they all should arrive within a small window timeframe. This results in a peak in the lvl1 distribution. Due to a known feature with the FE-I4 readout card, some of the distributions exhibit a double peak structure. The lvl1 distribution for FBK 13 can be seen in Fig. 7.33a. For FBK 11, the lvl1 distribution is shown in Fig. 7.33b. The peaks of the top of the distribution can be seen, but there is a flat distribution of hits, known as a *plateau*, that were recorded at other times during the trigger window. These are most likely noisy hits.

The normalised cluster distributions presented in Fig. 7.34 show the cluster sizes (in number of pixels) for the reference sensor, CNM55, for normal beam incidence ( $0^\circ$ ) and for the other modules at  $\phi = 15^\circ$  with  $\eta = 60^\circ, 70^\circ, 80^\circ$  and  $85^\circ$ . Since the reference sensor was fixed throughout the data taking, it is expected that the cluster size will remain constant for each GeoID: this is observed.

Figures 7.35 and 7.36 display for the two devices under test, FBK13 and FBK11 respectively, the normalised cluster distributions for normal beam incidence ( $0^\circ$ ) and for  $\phi = 15^\circ$  with

<sup>3</sup>The lvl1 is the 16 frame trigger window described in Section 7.4.2.



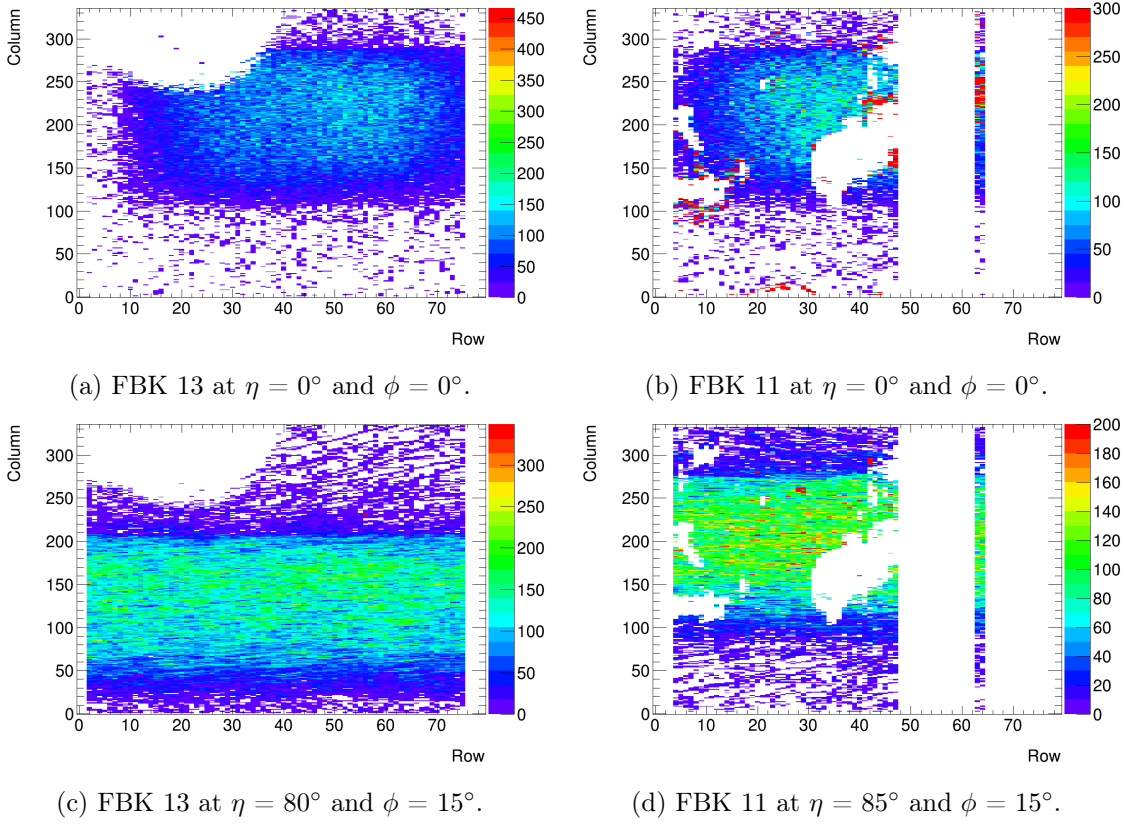


Figure 7.31: Comparison of two dimensional hitmaps for non-irradiated FBK 13 (left) and irradiated FBK 11 (right). Figures are for normal incidence angle (top) and high-eta angles (bottom). Data are for one run each. Note the respective colour scales.

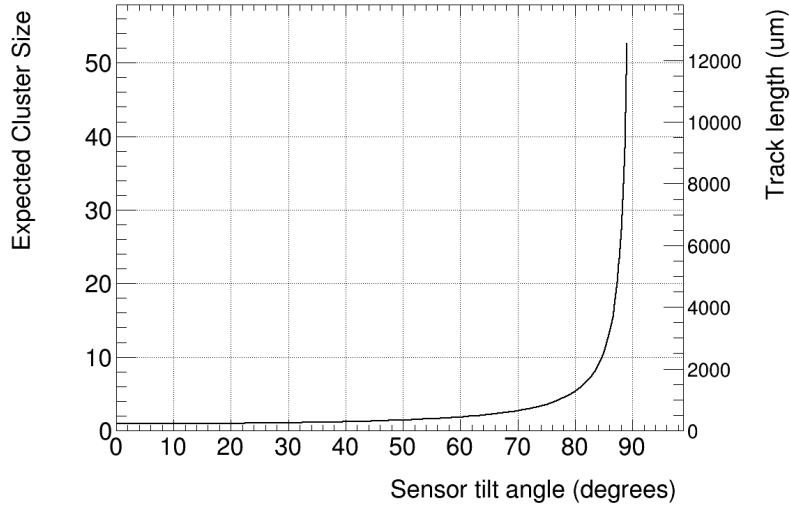


Figure 7.32: Simulated cluster size for a tilted sensor, taking only the geometric values into consideration.



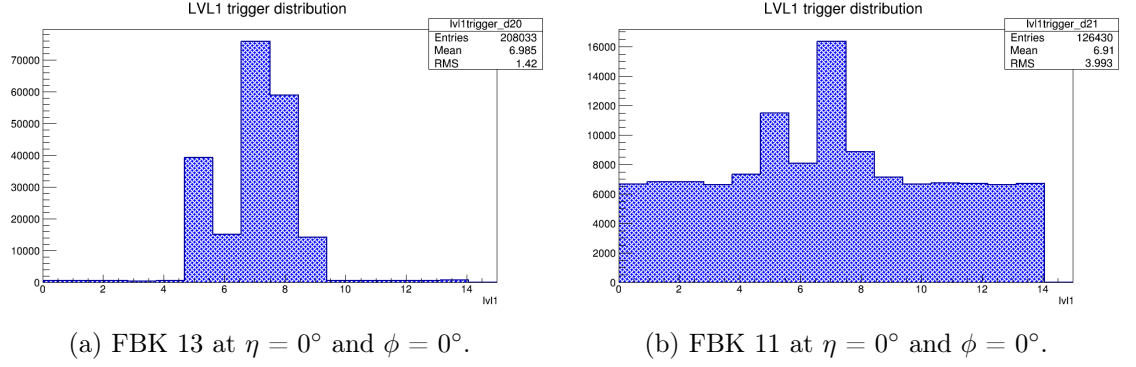


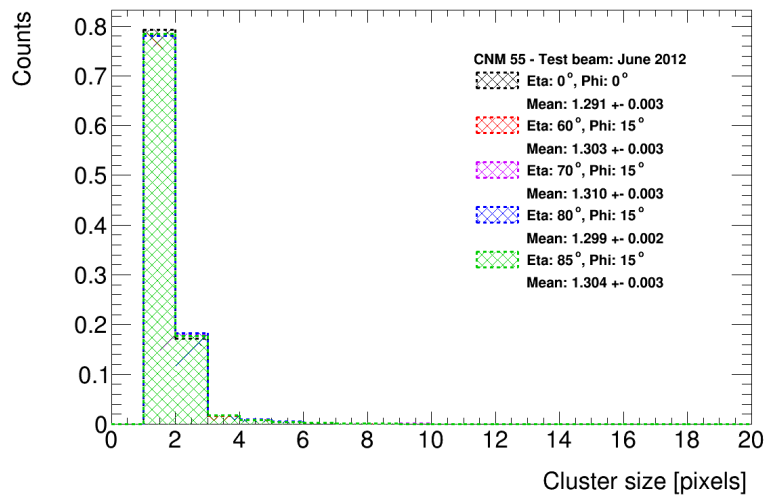
Figure 7.33: Comparison of the lvl1 distributions for FBK 13 and FBK 11. The double peak structure is a known issue. The flat distribution in (b) is due to out-of-time hits and can be attributed to a greater number of noisy pixels.

Table 7.8: Comparison of the mean cluster size in the x-direction at different angles for the 3D silicon pixel detectors, FBK 11 and FBK 13, in the June IBL beam test, 2012, biased to -160 V and -20 V respectively. Both detectors were tuned to a threshold of 1600  $e^-$ .

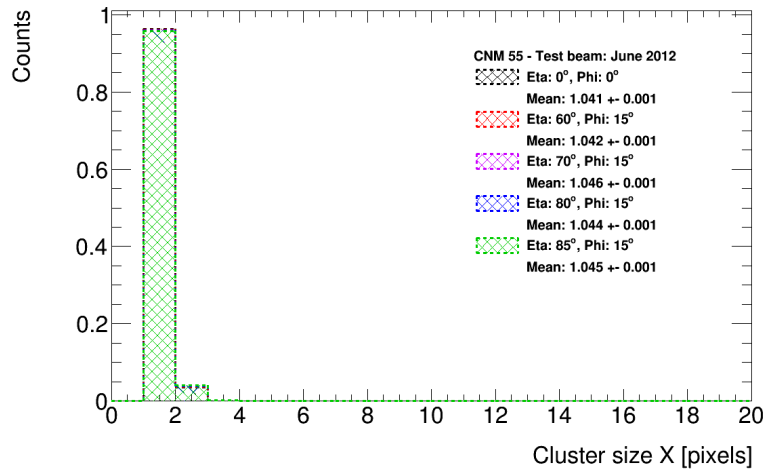
		FBK 13 (non-irradiated)		FBK 11 ( $6 \times 10^{15} n_{eq} cm^2$ )	
Eta	Phi	Cluster size X	Error (stat)	Cluster size X	Error (stat)
0°	0°	1.060	0.001	1.046	0.000
60°	15°	2.221	0.003	1.338	0.001
70°	15°	3.084	0.003	2.974	0.005
80°	15°	6.129	0.005	5.834	0.022
85°	15°	9.968	0.191	9.095	0.026

$\eta = 60^\circ, 70^\circ, 80^\circ$  and  $85^\circ$ . In each case, the top figure shows the combined cluster size (in pixels), the middle figure the cluster size in X and the lower figure the cluster size in Y. The errors in the cluster size are statistical only and give an indication of the likelihood of reproducing the results with the same setup. The systematic errors are not determined. The smaller cluster sizes for the irradiated FBK 11 sample can be accounted for due to the excessive noise from some pixels in this device, skewing the results to smaller values. An attempt was made to take this into account with cuts for eta angles  $80^\circ$  and  $85^\circ$  as can be seen in Fig. 7.37, however this is not possible for  $60^\circ$  because of the overlapping distributions. Furthermore, due to the large number of masked pixels, many long tracks will have been cut short, resulting in lower cluster sizes than expected.

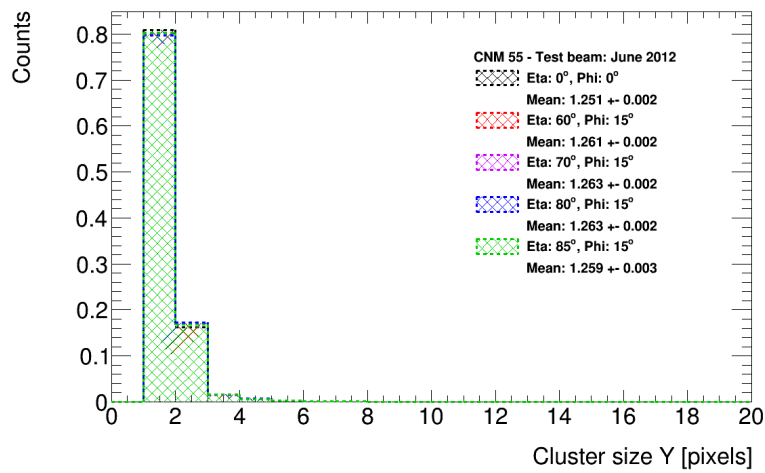
The mean value for each tilt angle is collected in Table 7.8 and plotted in Fig. 7.38 to compare to the expected cluster size. The results match the trend as expected. When simulated data becomes available, these results can be compared to further the understanding of the performance of 3D silicon devices in the high-eta regions of the IBL



(a) Total cluster size.

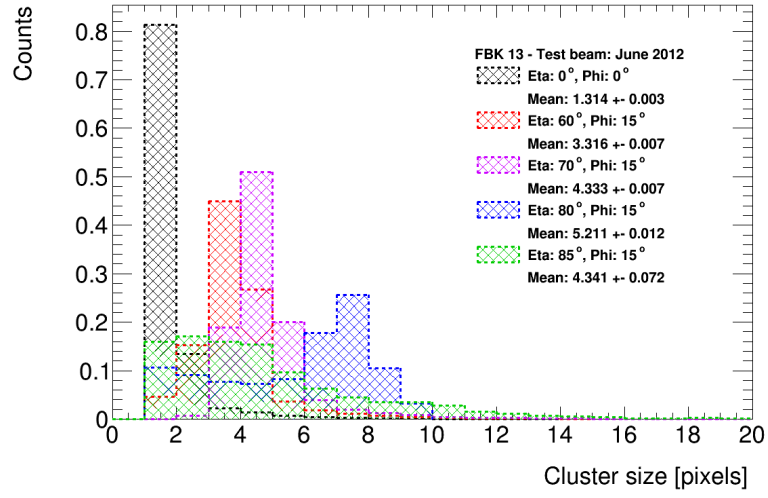


(b) Cluster size in the long pixel direction.

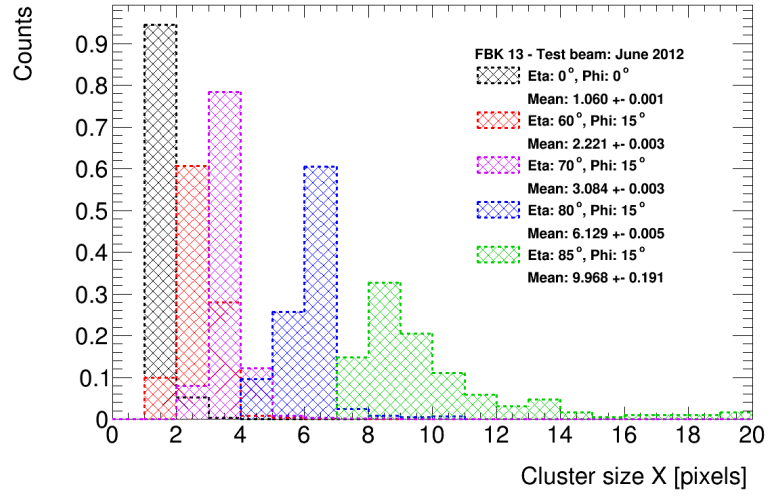


(c) Cluster size in the short pixel direction.

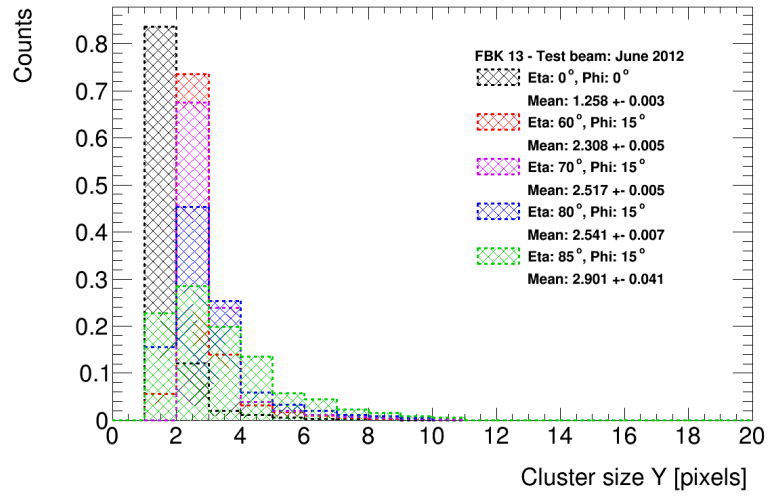
Figure 7.34: Comparison of cluster size distributions for CNM 55 for each set of tilt angles in the setup. Note that the angles shown in the legend are *not* the angle this device was tilted at. As the reference sensor, CNM 55 was maintained at an angle of 0° for all runs. The legend is for comparison with the other figures.



(a) Total cluster size.

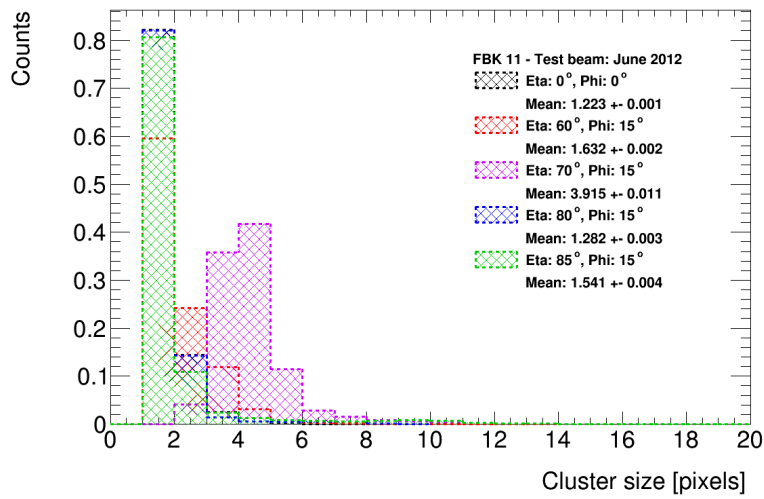


(b) Cluster size in the long pixel direction.

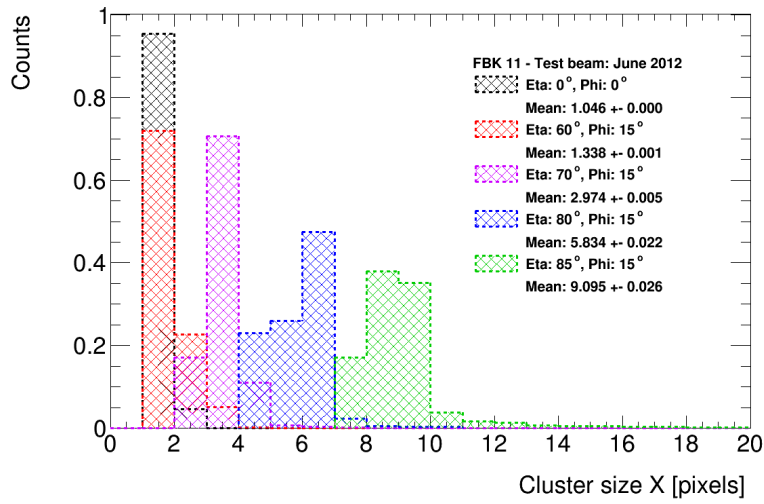


(c) Cluster size in the short pixel direction.

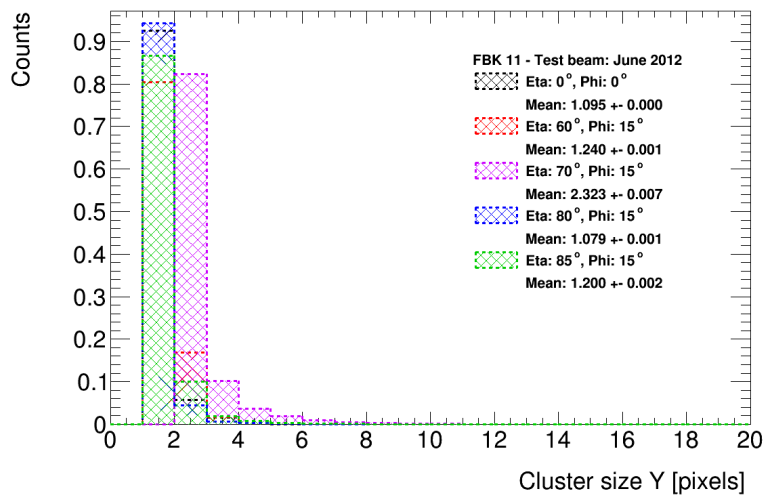
Figure 7.35: Comparison of the cluster size distributions at different angles for FBK 13 in the June IBL beam test, 2012.



(a) Total cluster size.

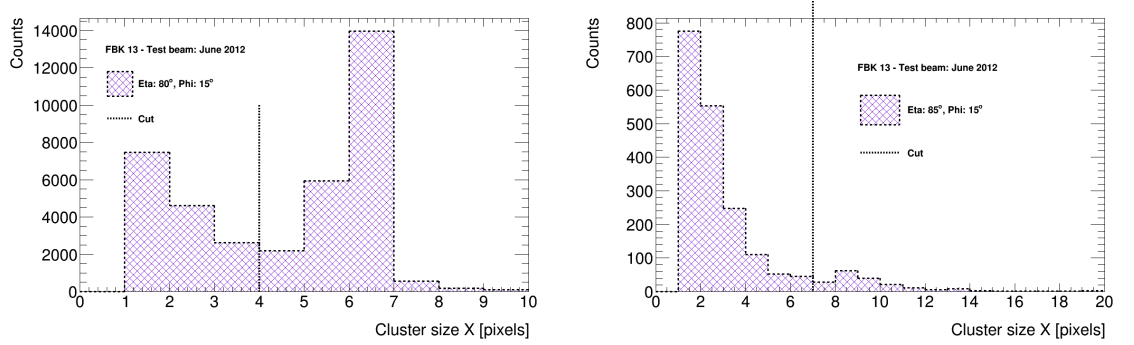


(b) Cluster size in the long pixel direction.



(c) Cluster size in the short pixel direction.

Figure 7.36: Comparison of the cluster size distributions at different angles for FBK 11 in the June IBL beam test, 2012.



(a) Cluster size distribution for FBK 13 at  $\eta = 80^\circ$  and  $\phi = 15^\circ$ .

(b) Cluster size distribution for FBK 13 at  $\eta = 85^\circ$  and  $\phi = 15^\circ$ .

Figure 7.37: Cluster size distributions for  $\phi = 15^\circ$  and  $\eta$  angles of (a)  $80^\circ$  and (b)  $85^\circ$  before applied cuts. The dashed line indicates the cut made for each angle.

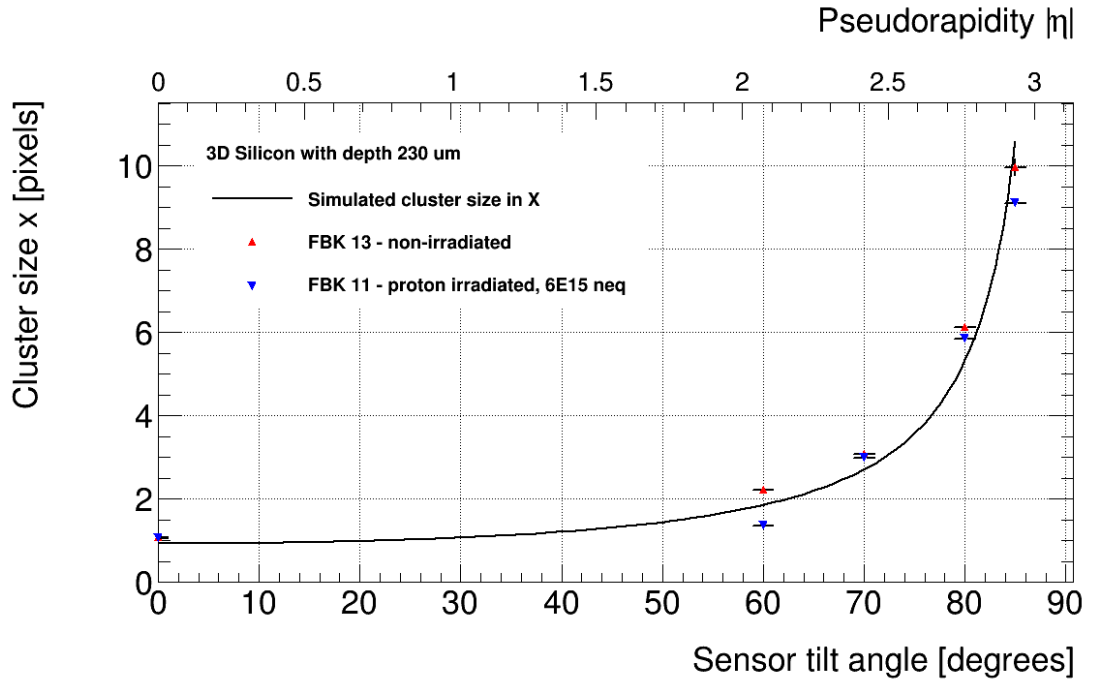


Figure 7.38: Mean cluster size recorded for 3D silicon pixel detectors, FBK 13 (non-irradiated) shown in red, and FBK 11 (proton irradiated to  $6 \times 10^{15} \text{ n}_{eq} \text{ cm}^{-2}$ ) shown in blue. The errors on the y-axis are the statistical errors, while the errors on the x-axis are an uncertainty of the tilt angle of  $\pm 1$  degree.



## 8 | Antiproton Beam Test

The Antihydrogen Experiment: Gravity, Interferometry, Spectroscopy, known as AEGIS [84, 85], is an experiment planned for the Antiproton Decelerator (AD) [86] at CERN, Geneva. Proposed in 2007, AEGIS aims to study the strength of the gravitational force between antihydrogen and matter, using the classical experiment of the Moire deflectometer [87]. This is a process involving two gratings to create a fringe pattern on the position-sensitive detector, as illustrated in Fig. 8.1.

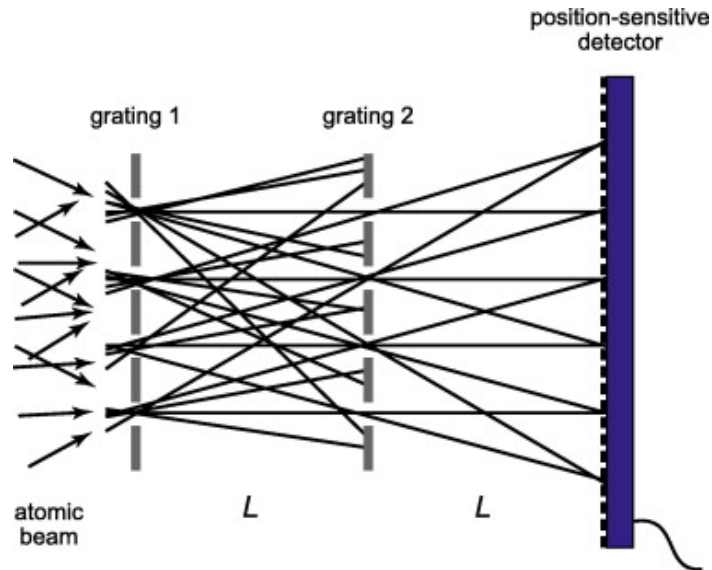


Figure 8.1: Sketch of the Moire deflectometer illustrating the use of two gratings to produce a fringe pattern on the position sensitive detector [85].

Research into the detectors required for this experiment is ongoing. A 3D silicon detector and a MIMOTERA detector [88] were selected for beam test experiments in December 2012 to compare pixel detectors to the performance of the silicon strip detector foreseen to be used. A simulation of the 3D silicon module was created to analyse the performance of the 3D silicon detector in a beam of antiprotons. This simulation, with comparison to selected experimental results, is presented here. The results for the MIMOTERA detector are in

reference [89].

## 8.1 Theoretical background

Antiparticles (specifically the antielectron or *positron*) were predicted by Paul Dirac in 1931 to solve the problem of negative energy states predicted by the Dirac equation and known as Hole Theory. They have equal mass to their matter counter-parts, but with opposite lepton and baryon numbers and an opposite charge. The positron, the first antiparticle to be discovered, was detected in 1933 by Carl Anderson in cosmic ray experiments in a cloud chamber [90]. Positron tracks in the chamber had the same curve radius as the electron tracks, but were bent in the opposite direction due to their positive charge.

Many neutral particles, such as photons and gluons, have identical antiparticles, or to put it another way, they are their own antiparticles. However, some neutral particles, such as the neutron do not due to their composite structure. The quarks within the neutron (one up-quark and two down-quarks) have charge, and hence have corresponding antiparticle partners. Consequently, the antineutron is composed of an antiup and two antidowns.

When particle and antiparticle pairs come into contact they annihilate, creating new particles such as pairs of photons. This process is allowed since charge, momentum and energy are all conserved. If the annihilation occurs with a particle from the nucleus of an atom, the newly created particles, such as pions, proton or neutrons, could cause the atomic nucleus to fragment. The secondary particles will interact with the surrounding matter via the processes described in Section 2.2.

## 8.2 Experimental setup

The Antiproton Decelerator (AD), illustrated in Fig. 8.2, is a storage ring that provides antiprotons to each of the fixed-target experiments, of which AEGIS is one. A schematic of the experimental setup for AEGIS is shown in Fig. 8.3.

The 3D silicon pixel detector chosen for the experiment is known as CNM 55. This is a non-irradiated IBL prototype manufactured at CNM, Spain and bonded to an FE-I4a readout card. CNM 55 is used as the reference sensor in many IBL beam tests. See Section 7.3 for more information on this sensor.

For the antiproton beam test, the 3D silicon device was mounted onto a custom support which was then placed onto a flange and secured in the six-cross vacuum chamber, as shown



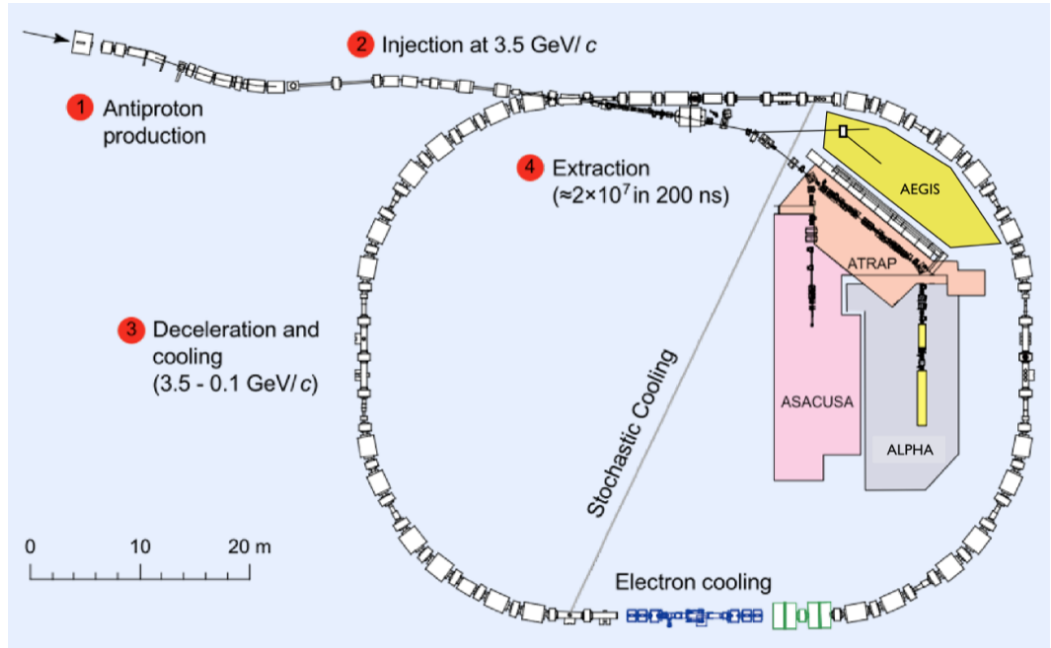


Figure 8.2: A schematic of the Antiproton Decelerator (AD) at CERN. The AD provides antiprotons to the four fixed-target experiments.

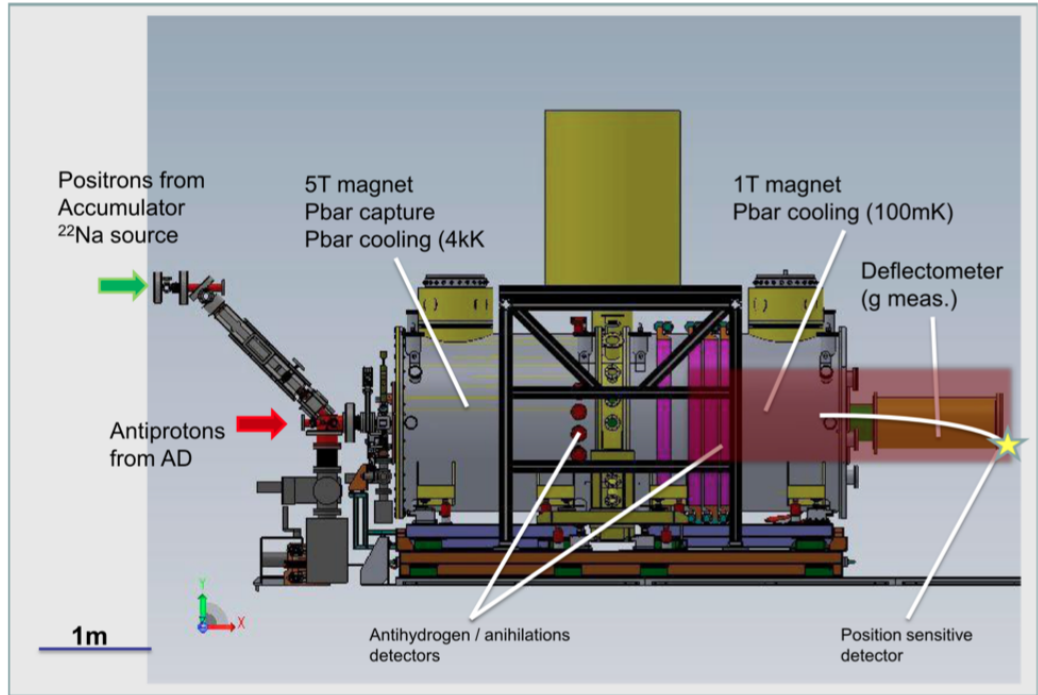


Figure 8.3: A schematic of the AEGIS experimental setup at CERN.

in the photographs in Fig. 8.4a and b respectively. This setup was sealed and a pump creates a vacuum inside. A bias voltage of -30 V was applied to the detector. Figure 8.5 shows a

wider view of the sealed experimental area. The AD delivers a beam of antiprotons every 100 s with an energy of  $\sim 100$  KeV. Figure 8.6 shows the simulated kinetic energy distribution of antiprotons within the beam pipe (after passing through aluminium degraders, but before they reach the 3D silicon detector) for beam tests in December 2012 [91]. Annihilation occurs within the initial layers of the sensor and secondary particles are produced into a  $4\pi$  solid angle. Data for secondary neutral particles and for all particles that escape the sensor are lost. Tracks are left for charged particles that travel through the sensor if the charge collected is above threshold. The 3D silicon pixel sensor is both the active target and the detector.

The trigger was provided by the beam and an appropriate delay was introduced to the source scan so that the trigger timeframe known as the *lwl1 window* coincided with the spill of antiprotons. The initial spill contained  $\sim 3 \times 10^7$  antiprotons, however this was greatly reduced after passing through two aluminium degraders, a silicon beam counter, another aluminium degrader and finally a titanium foil to separate vacuum regions in the setup. Within the chamber, a magnetic field separated the beam of antiprotons and consequently only a small fraction will have been incident on the sensitive part of the detector from each spill.

### 8.3 Initial results

The raw two dimensional hitmaps shown in Fig. 8.7 were produced using the source scan data taking setting with an external trigger. The method of taking a source scan in a laboratory setting is described in Section 6.4.4. Each frame shows a single event during a scan. In this case, an event refers to a window of data taking and not a single antiproton annihilation. Features in the hitmaps can be seen which are indicative of an antiproton annihilation within silicon, such as long tracks from light secondary particles which are produced almost parallel to the wafer surface. There are also areas of localised charge which could be due to the Bragg peak of a nuclear fragment. To study the process of antiproton annihilations within a 3D silicon pixel sensor, a simulation of the experimental setup was created.

### 8.4 Simulation

To understand the particle physics processes occurring within the detector during the beam test and the response of the detector, it is useful to simulate the experiment. By utilising existing packages for the prediction of particle behaviour, a simulation of the experiment in Geant4 [92, 93] was created.

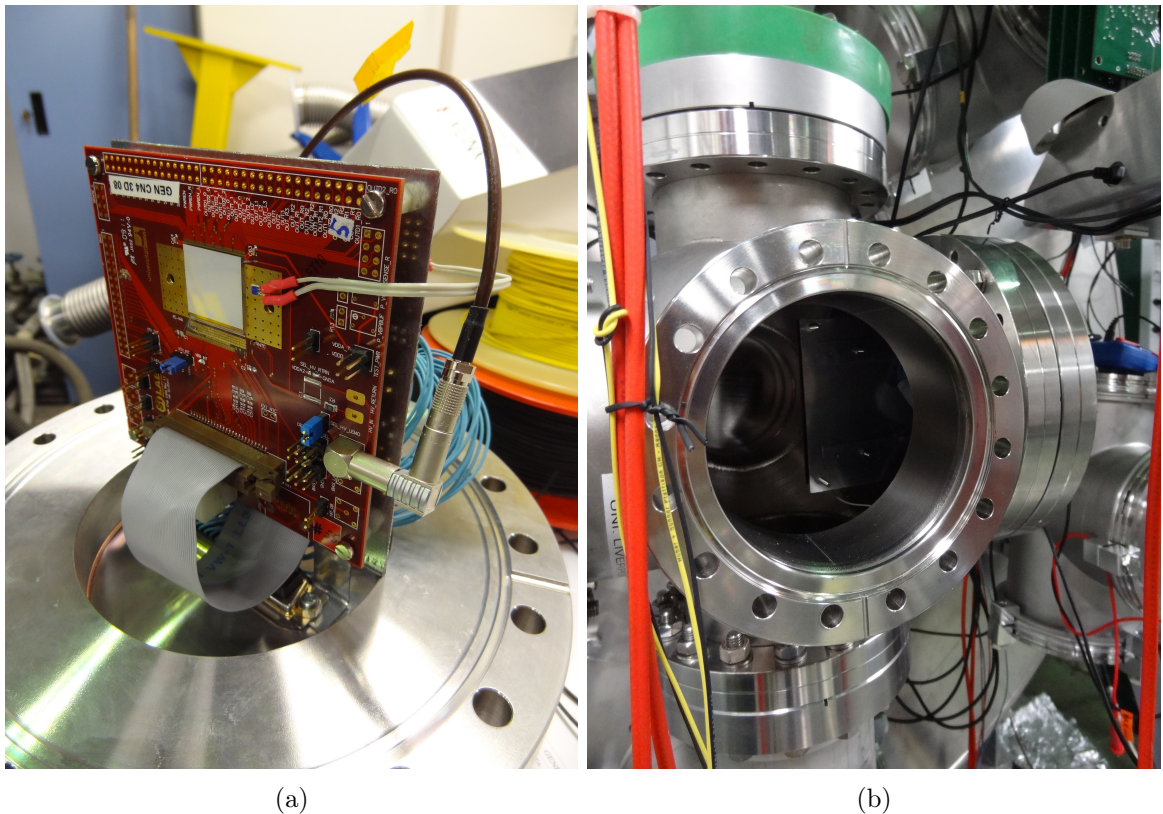


Figure 8.4: Photographs from the antiproton beam test setup. The 3D silicon CNM 55 detector is shown on (a) the custom support mount, which was mounted into (b) the six-cross vacuum chamber setup.

#### 8.4.1 Geant4 framework

Written in C++ [79], Geant4 (GEometry ANd Tracking) is an object-oriented Monte-Carlo framework that provides all the tools required for detector simulation and a variety of physics processes, depending on the needs of the user. It is used to study the interaction of particles with matter in high energy physics and accelerator physics, but also has applications in nuclear, medical and space physics<sup>1</sup>.

#### 8.4.2 Simulation setup

Separate classes handle specific functions within the simulation. A basic simulation requires a description of the geometry of the laboratory environment and the detector, a list of physics processes to be considered (including types of interactions and decay methods) and a class to direct the processes during each event throughout a run.

<sup>1</sup>See <http://geant4.web.cern.ch> for more information.



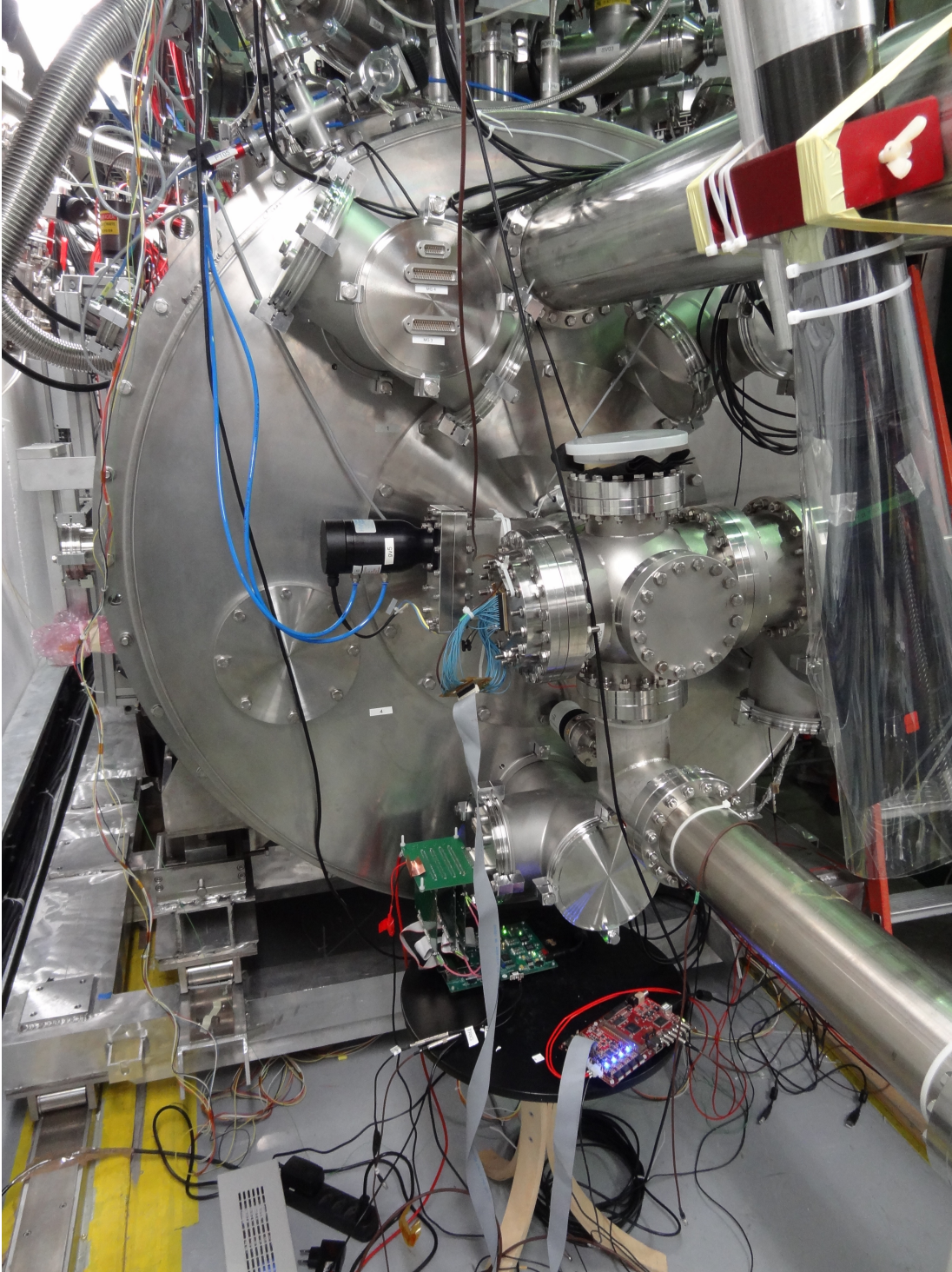


Figure 8.5: Photograph from the antiproton beam test setup. The six-cross vacuum chamber at the end of the beam line is shown. The USBPix board is located at lower centre.

### Physics list

Within the Physics List, the user must add all known physics processes that will occur during the simulation, it also allows the user to add new physics as required. If the user does

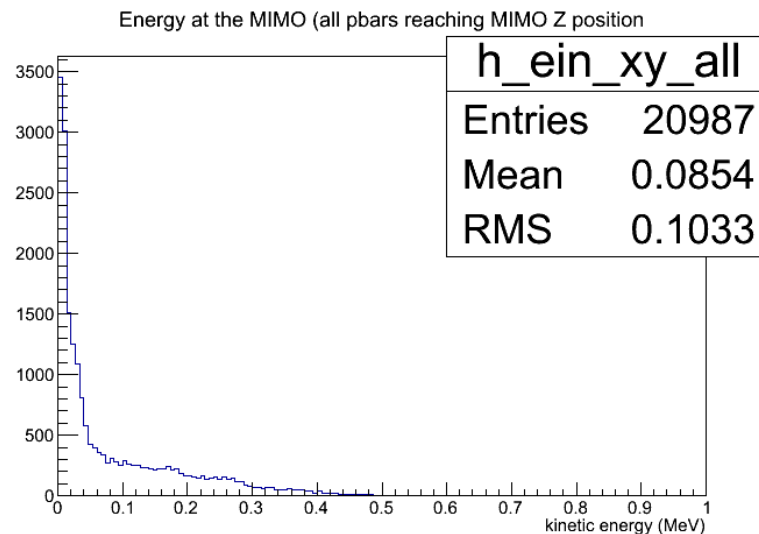


Figure 8.6: Simulated antiproton initial kinetic energy distribution for beam tests in December 2012 [91]. The simulation estimated the kinetic energy of the antiprotons after they had passed through aluminium degraders further up the beam pipe.

not wish to write their own physics lists, predefined lists are available depending on the application required, for which there are many for high energy physics [94]. The user chooses which list to use depending upon which physics processes are required and to what level of detail. Ideally, the answers would be ‘all processes’ and ‘highest level of detail’ respectively, however this would require much greater processing power and may not yield significantly finer details, so a compromise must be made. A way to control the detail of the simulation is through a threshold cut, which selects the point at which a process is deemed to have occurred. If the value of the cut is greater than the distance travelled by the particle, secondary particles will not be generated, the particle will not be tracked further in the sensitive material and it will be assumed to have deposited all of its remaining energy. It is therefore important to consider the cut threshold to use for electromagnetic processes, for example, to prevent tracking of infrared divergence in cases such as the emission of Bremsstrahlung radiation at lower and lower energies.

The physics list applied for this simulation is the Chiral Invariant Phase Space (CHIPS) model [95]. This model was specifically designed to study nucleon-antinucleon interactions at low energies. However, due to an inbuilt Geant4 cut on all charged particles with a kinetic energy below 1 eV, an additional patch to this physics list was required to prevent low energy anti-protons from being stopped (*killed* in the technical language) either before they reach the detector or when they are close to rest [96]. The patch defines a new lower energy limit of  $10^{-6}$  eV for anti-protons. This was also implemented into the simulation.

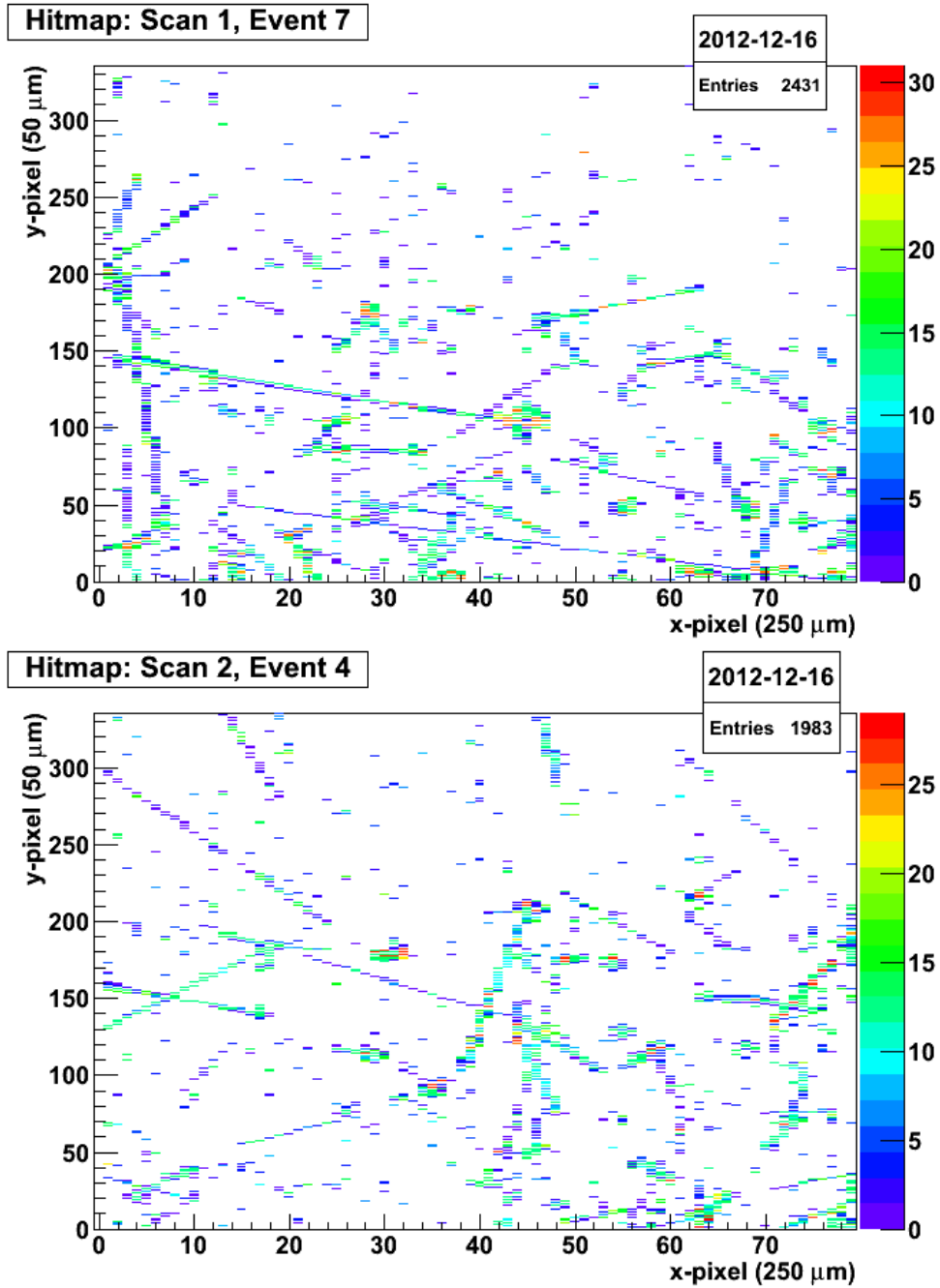


Figure 8.7: Raw 2D hitmaps for two events using the 3D silicon detector, CNM 55, from the antiproton beam test at CERN in December 2012. The pixel columns are on the x-axis and the number of rows on the y-axis. Here, an event refers to a window of data-taking during a scan. The colour scale shown is the time over threshold (TOT) per pixel.

### Detector geometry

The first object defined within the geometry must be the laboratory setting known as the *world*. This is the environment within which the entire simulation will take place. Each

subsequent object is defined as being part of the world. There are three steps to creating an object:

1. The volume of the solid must be declared, this describes the size and shape of the volume.
2. The material of the object is declared as a logical volume. All materials required must have been defined or called from a list of predefined materials earlier in the class.
3. Finally, the physical volume is declared, which describes the translational position from the centre of the world and includes any rotations.

These steps must be repeated for every object.

To create the 3D silicon detector for this simulation, the total wafer of silicon was initially defined. Afterwards, the wafer was split into 26,880 replicated and initial cells of pitch  $250\text{ }\mu\text{m}$  by  $50\text{ }\mu\text{m}$ , the pixel dimensions of the IBL design 3D sensor. Three layers on top of the silicon were added:  $1.5\text{ }\mu\text{m}$  of aluminium,  $0.8\text{ }\mu\text{m}$  of doped polysilicon and  $1.150\text{ }\mu\text{m}$  of thermal oxide [97]. The oxide layer ( $\text{SiO}_2$ ) isolates neighbouring readout electrodes. The layout is illustrated in Fig. 8.8. These additional layers between the beam and the silicon are important since they are a barrier to the antiprotons before they reach the sensitive silicon wafer. From the orientation of the sketch, in the simulation the antiprotons would enter the detector from the top downwards.



Figure 8.8: Sketch of the layout of the layers on the backside of the simulated 3D silicon detector [97] (not to scale). Antiproton direction is from the top, downwards.

### Primary generator action

The Primary Generator Action class controls the generation of particles for the simulation. The user can choose to generate particles from a stationary source, or as a beam. To match



the experiment, a beam was chosen. The particle type, energy and momentum must also be defined. A random number generator was used to provide a wide beam of antiprotons over the entire area of the detector, perpendicular to the wafer surface. The spread of initial antiproton position is illustrated in the hitmap in Fig. 8.9. Another random number generator took the chosen average particle momentum,  $p$ , and created antiprotons with a spectrum of kinetic energy,  $E_k$  using the following two formulae:

$$E = p^2 + m_0^2 \quad (8.1)$$

$$E_k = E - m_0 \quad (8.2)$$

where  $E$  is the total energy and  $m_0$  is the rest mass of the particle. In the case of the antiproton, this is  $938 \text{ MeV}/c^2$ . The energy spectrum used for the results in Section 8.5 is shown in Fig. 8.10. Some results were produced with a specific initial kinetic energy of the antiproton instead of this spectrum, these are clearly labelled.

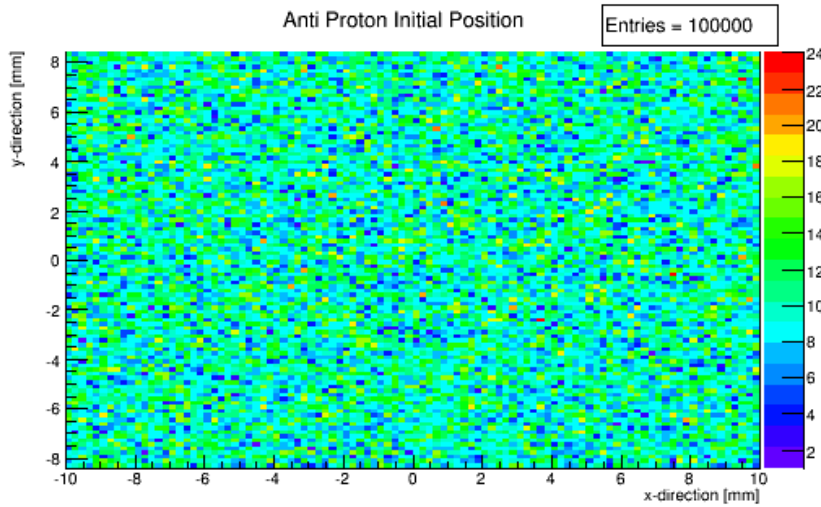


Figure 8.9: Two dimensional hitmap of the distribution of the initial antiproton position in the x-y plane. The centre of the hitmap (0, 0) corresponds to the centre of the detector.

### Digitisation

Digitisation is the process where the energy deposited within the sensitive detector is converted into charge collected. This mimics the real process of signal formation within the detector by using algorithms defining the physical processes involved. The creation of a digitisation of a 3D silicon sensor contributed to the PhD thesis of M. Borri [98] using simulations of the electric field within the pixels by C-H. Lai [99]. The electric field within



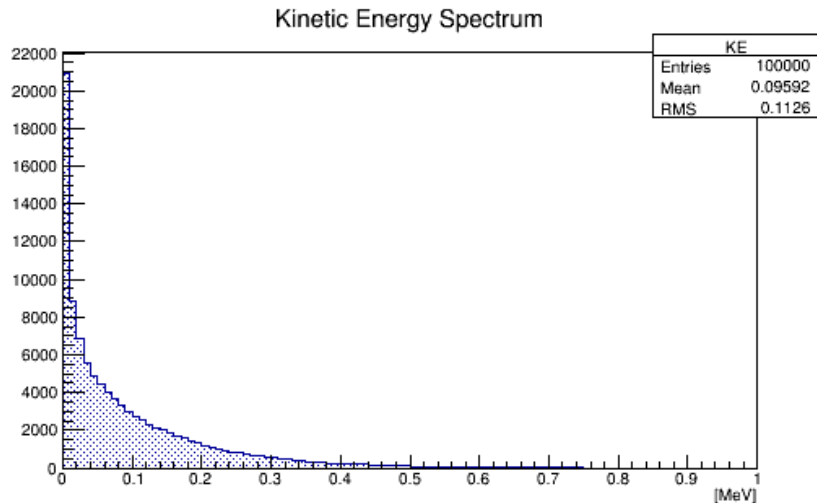


Figure 8.10: Simulated initial kinetic energy spectrum for antiprotons.

an unirradiated 3D silicon sensor biased at -30 V was generated by a simulation program called *Kurata*, named after the method developed by Kurata and the result fed into the digitiser [98]. Figure 8.11 shows the two dimensional hitmap of the Kurata simulated electric field [99]. In the hitmap, the inefficient regions of the electrodes can clearly be seen.

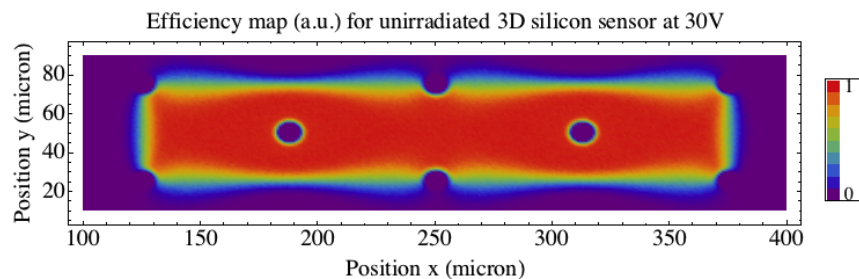


Figure 8.11: Simulated two dimensional efficiency map for a single 3D silicon non-irradiated pixel cell biased to -30 V [99].

The threshold cut set within the digitiser for the simulation was 1500 electrons. Figure 8.12 was produced from within the digitiser from hits from the simulated experiment. The data are collected from all pixels in the sensor and combined into one cell. The dimensions are correct and the electrodes are clearly visible, as expected, validating the digitiser within the simulation. There is lower charge collection at the edge of the pixel, due to charge sharing with neighbouring pixels. It should be noted that, as mentioned in Section 5.3, CNM differs from FBK in that the electrodes stop  $\sim 20 \mu\text{m}$  from the wafer surface and the efficiency within the electrodes would be expected to be higher than zero. Therefore, since the electric field map is 2D only, the digitiser is for FBK sensors, and for CNM it is only an approximation.

A 3D simulated electric field map is planned for the future allowing a full simulation of a CNM sensor with this electrode configuration, but not in time for this study.

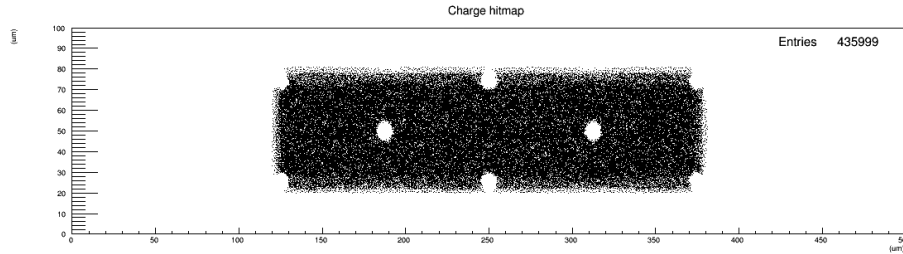
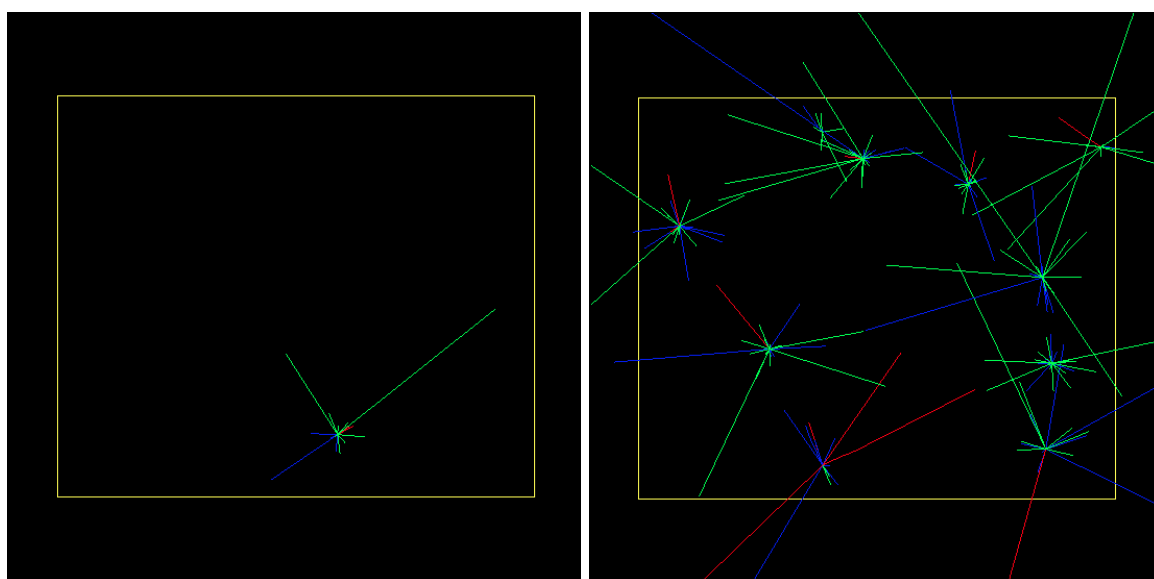


Figure 8.12: Simulated charge collection position for hits originating within a pixel using the digitiser. Data from all pixels are folded into a single cell. No charge is collected within the electrodes as expected. The lower charge collection at the edges is due to charge sharing with neighbouring pixels.

## Visualisation

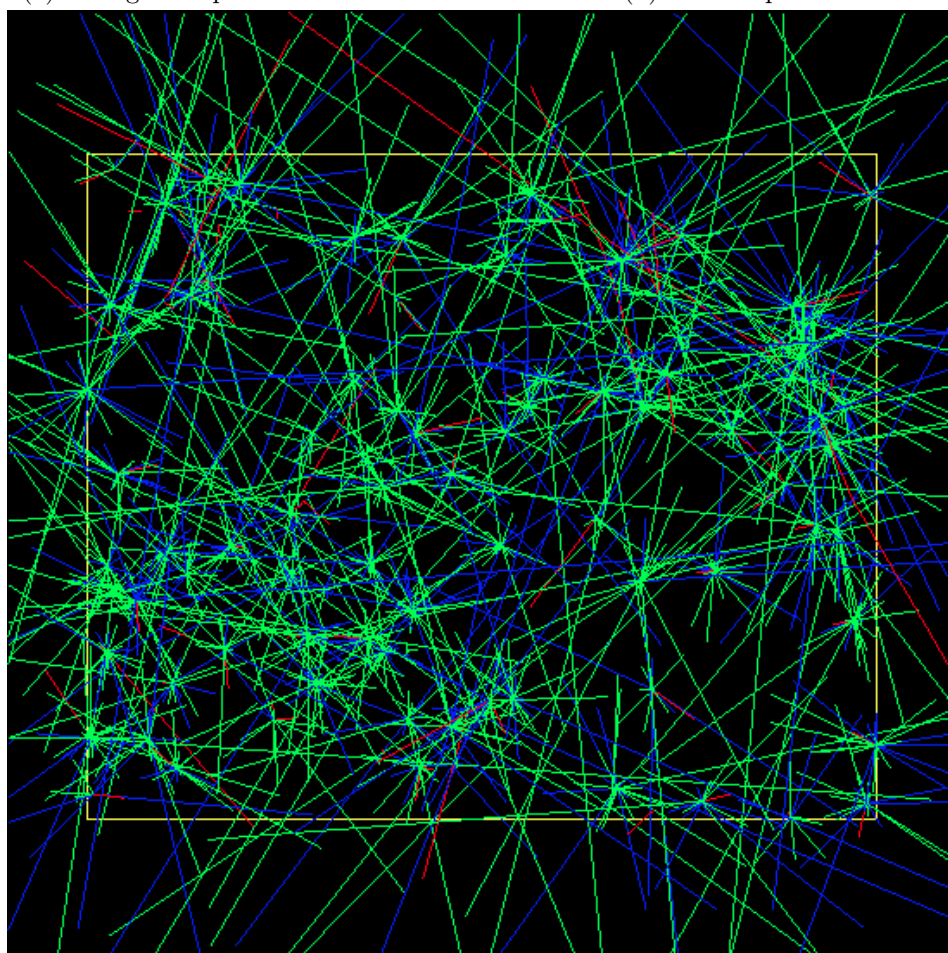
The three dimensional visualisation of the simulation is produced with the graphical application, OpenGL viewer. Default settings are selected in the file “vis.mac” which is called by the Geant4 User Interface manager in the main source code. Examples of the output from this viewer can be seen in Fig. 8.13 for (a) one event, (b) ten events and (c) 100 event. It becomes increasingly difficult to determine the centre of the annihilation with more events in one window. The particle tracks are colour coded by charge: red tracks are from negative particles, blue from positive particles and green tracks are particles with neutral charge. The yellow rectangle shows the outline of the 3D silicon detector device with the antiproton beam into the page. The layer on top of the device in this viewpoint is the aluminium layer. Tracks from particles with no charge will not be detected within the device, but may produce further secondary particles that are later detected.

Numerical information from each event can also be output to the screen. For example, Fig. 8.14 shows a screenshot of the information available about the initial antiproton track and the secondary particles produced from it. The position at each step, along with energy and step length data is displayed. It is also possible to see which volume this step occurred in and what process happened. In this example the process that killed the antiproton was an annihilation (*CHIPSNuclearCaptureAtRest*) at 117  $\mu\text{m}$  before the centre of the silicon wafer, which is in the doped silicon layer. The antiproton produced 21 secondary particles. Having this information available visually provides the user with a check that the simulation is running as expected, however for multiple events it is not convenient to process all output in this way.



(a) A single antiproton event

(b) Ten antiproton events



(c) One hundred antiproton events

Figure 8.13: Visual representations of antiproton annihilations within the 3D silicon sensor for (a) one event, (b) ten events and (c) one hundred events. The red lines show tracks from negatively charged particles, the blue lines are tracks from positive particles and the green lines are tracks from neutral particles (the latter are not measured within the sensor). The yellow box is the outline of the device, aluminium layer first.

```

*****
* G4Track Information: Particle = anti_proton, Track ID = 1, Parent ID = 0
*****

Step#    X          Y          Z          KineE      dEStep    StepLeng  TrakLeng  Volume    Process
0      -575 um    -4.53 mm    -7.48 mm    72.3 keV      0 eV      0 fm      0 fm      World     initStep
1      -118 um    -4.53 mm    -7.48 mm    72.3 keV9.15e-18 eV  457 um    457 um      World     Transportation
2      -117 um    -4.53 mm    -7.48 mm    7.22 keV 65.1 keV  1.86 um    459 um      Al     Transportation
3      -117 um    -4.53 mm    -7.48 mm    3.14 keV 4.07 keV  260 nm     459 um    DopedSilicon  msc
4      -117 um    -4.53 mm    -7.48 mm    3.14 keV 1.25 eV   141 nm     459 um    DopedSilicon  msc
5      -117 um    -4.53 mm    -7.48 mm    2.92 keV 229 eV   141 nm     459 um    DopedSilicon  msc
6      -117 um    -4.53 mm    -7.48 mm    2.56 keV 357 eV   136 nm     459 um    DopedSilicon  msc
7      -117 um    -4.53 mm    -7.48 mm    2.5 keV 60.9 eV  127 nm     460 um    DopedSilicon  msc
8      -117 um    -4.53 mm    -7.48 mm    2.43 keV 63.7 eV  126 nm     460 um    DopedSilicon  msc
9      -117 um    -4.53 mm    -7.48 mm    2.39 keV 43.2 eV  124 nm     460 um    DopedSilicon  msc
10     -117 um    -4.53 mm    -7.48 mm    1.92 keV 472 eV   123 nm     460 um    DopedSilicon  msc
11     -117 um    -4.53 mm    -7.48 mm    1.76 keV 155 eV   110 nm     460 um    DopedSilicon  msc
12     -117 um    -4.53 mm    -7.48 mm    1.13 keV 637 eV   106 nm     460 um    DopedSilicon  msc
13     -117 um    -4.53 mm    -7.48 mm    1.13 keV1.66e-07 eV  84.5 nm    460 um    DopedSilicon  msc
14     -117 um    -4.53 mm    -7.48 mm    276 eV  849 eV   84.5 nm    460 um    DopedSilicon  msc
15     -117 um    -4.53 mm    -7.48 mm    20.7 eV  255 eV   41.8 nm    460 um    DopedSilicon  msc
16     -117 um    -4.53 mm    -7.48 mm    0 eV  20.7 eV  57.3 nm    460 um    DopedSilicon  hIoni
17     -117 um    -4.53 mm    -7.48 mm    0 eV  0 eV      0 fm      460 um    DopedSilicon  CHIPSNuclearCaptureAtRest

:----- List of 2ndaries - #SpawnInStep= 21(Rest=21,Along= 0,Post= 0), #SpawnTotal= 21 -----
:   -117 um    -4.53 mm    -7.48 mm    300 MeV    pi0
:   -117 um    -4.53 mm    -7.48 mm    62.4 MeV    kaon+
:   -117 um    -4.53 mm    -7.48 mm    140 MeV    pi-
:   -117 um    -4.53 mm    -7.48 mm    15.9 MeV    neutron
:   -117 um    -4.53 mm    -7.48 mm    6.22 MeV    proton
:   -117 um    -4.53 mm    -7.48 mm    20 MeV     neutron
:   -117 um    -4.53 mm    -7.48 mm    4.9 MeV     neutron
:   -117 um    -4.53 mm    -7.48 mm    16.3 MeV    neutron
:   -117 um    -4.53 mm    -7.48 mm    35 MeV     proton
:   -117 um    -4.53 mm    -7.48 mm    6.95 MeV    proton
:   -117 um    -4.53 mm    -7.48 mm    74.7 MeV    proton
:   -117 um    -4.53 mm    -7.48 mm    6.7 MeV     alpha
:   -117 um    -4.53 mm    -7.48 mm    16.1 MeV    neutron
:   -117 um    -4.53 mm    -7.48 mm    30.6 MeV    proton
:   -117 um    -4.53 mm    -7.48 mm    20 MeV     proton
:   -117 um    -4.53 mm    -7.48 mm    24.6 MeV    neutron
:   -117 um    -4.53 mm    -7.48 mm    9.04 MeV    proton
:   -117 um    -4.53 mm    -7.48 mm    24.1 MeV    alpha
:   -117 um    -4.53 mm    -7.48 mm    38.6 MeV    neutron
:   -117 um    -4.53 mm    -7.48 mm    98.3 MeV    neutron
:   -117 um    -4.53 mm    -7.48 mm    5.97 MeV    alpha
:----- EndOf2ndaries Info -----

```

Figure 8.14: An extract of information displayed after a single antiproton annihilation event. Information about each step of the antiproton in the simulation is presented, along with a list of secondary particles produced. Note that in this list,  $x$  is the depth.

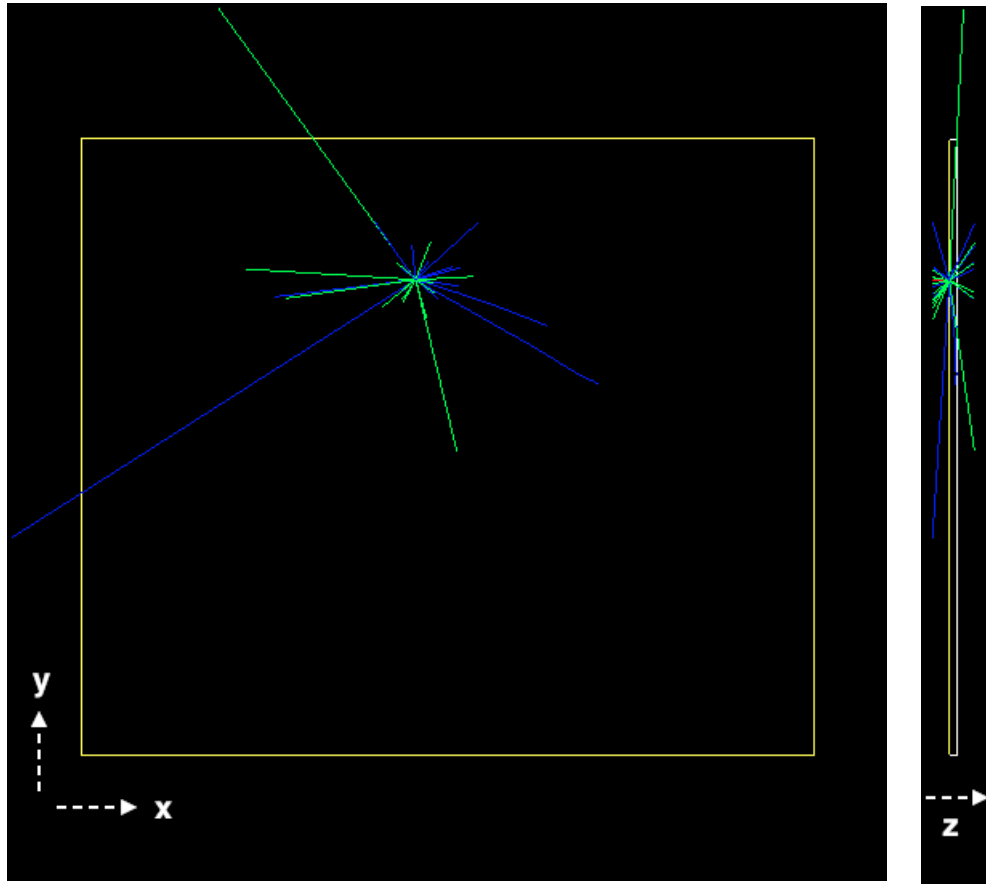
## 8.5 Simulation results

The simulation was run multiple times with various parameters to produce the following results. Where it is not clearly stated otherwise, it can be assumed that the simulation was run with the layout described in Section 8.4.2 with antiprotons and for 100,000 events.

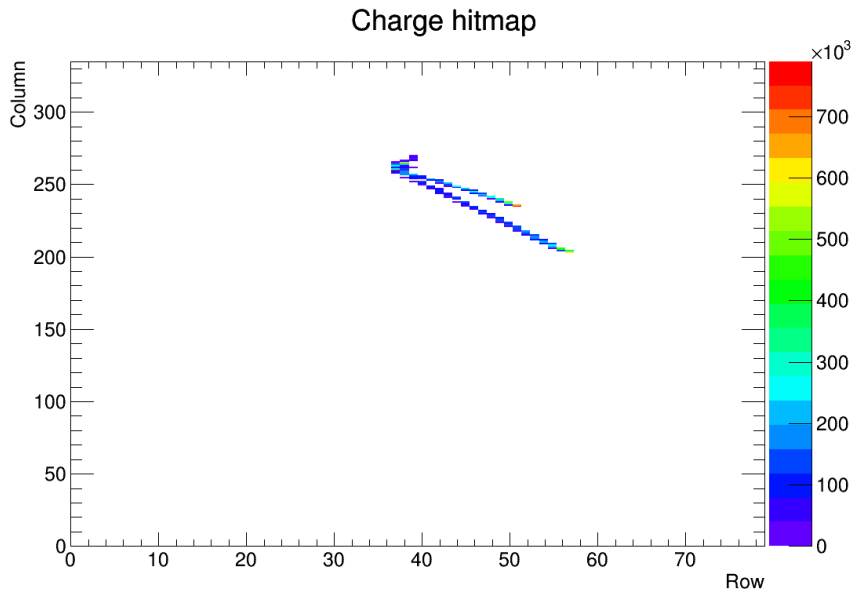
### 8.5.1 Two dimensional hitmaps

Row and column information from a single simulated event was plotted as a two dimensional hitmap. This is to provide a direct comparison to the data from the beam test. The benefit of a Monte Carlo simulation is that all of the information about an event is known. This can aid in the analysis and understanding of the data collected from the experiment. Figure 8.15 is an example of a single event which resulted in nuclear fragmentation. The annihilation of the antiproton produced 28 secondary particles; a  $\pi^+$  and  $\pi^-$  pair, 15 neutrons, 10 protons and a deuteron. It is important to note here that not all secondary particles are created from the energy of the annihilation, some will have been knocked out of the nucleus of the atom. As can be seen in Fig. 8.15b, many of these secondary particles travel in the negative  $z$  direction and therefore never enter the sensitive region of the detector. The two longest tracks in the detector are a result of the paths of two protons, which travel through the sensitive layer. At the end of their paths, they deposit a large fraction of their initial energy. This point could be mistaken for a deposit from a nuclear fragment and could confuse an annihilation position-finding algorithm. The neutrons do not deposit charge in the sensitive layer and are not directly detected. The existence of the neutrons can be inferred from the conservation of momentum, although the exact number and type are not known.

The hitmap in Fig. 8.16 shows the output from twenty events. Features such as long tracks and areas of localised charge are similar to those seen in the data from the beam test in Fig. 8.7. The pixel in which each annihilation occurred has been marked in Fig. 8.16b as a red bar. The clusters of charge formed by each event are asymmetrical and a well trained algorithm to distinguish between two events, and between an event and noise, is required. One possible cause of external noise would be from antiprotons annihilating elsewhere in the experimental setup and producing pions. When these pions reach the detector, they will deposit charge and cause a cluster. Figure 8.17 has two examples of a simulated run with pions as the initial particle. The events in this case are more localised with no, or very short, tracks. Figure 8.18 compares the output from annihilations which occurred in the aluminium layer or the silicon wafer. Visually there is very little to discriminate them.

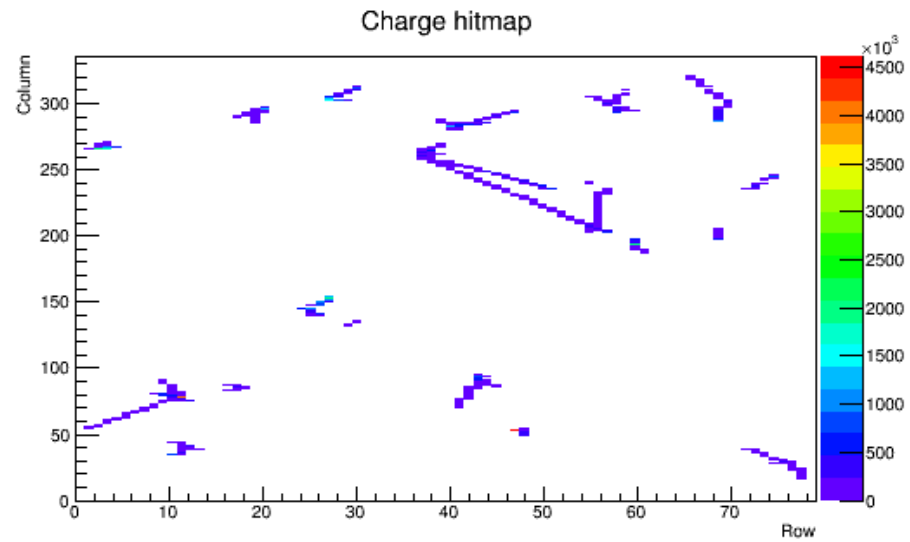


(a) Example of a single antiproton annihilation event. Antiproton beam direction is into the page. (b) Side.

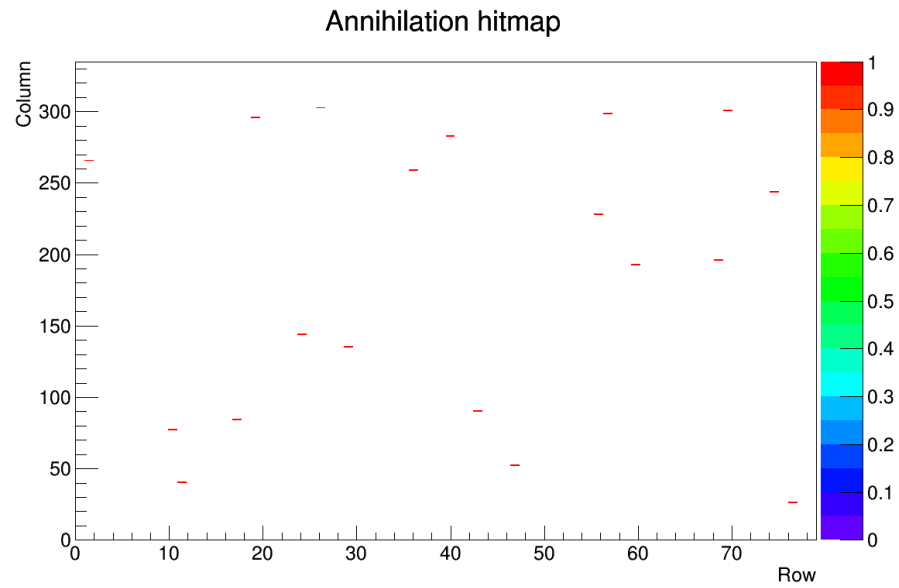


(c) Charge hitmap for the single antiproton event displayed in (a).

Figure 8.15: Comparison of the visual output from a single antiproton annihilation event from (a) the front and (b) the side, with (c) the simulated charge hitmap. The visual output shows positive (blue), negative (red) and neutral (green) secondary particles produced, although only charged particles passing through the detector will result in a track in (c).

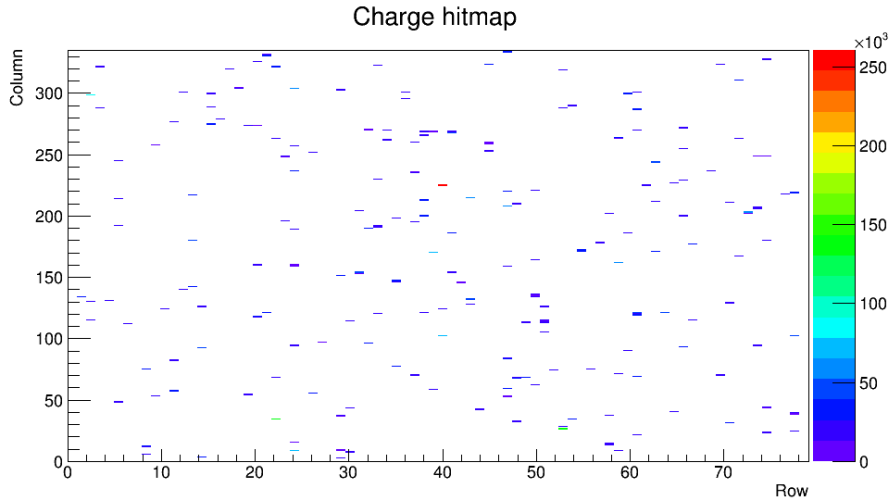


(a) Simulated charge collected for twenty antiproton events

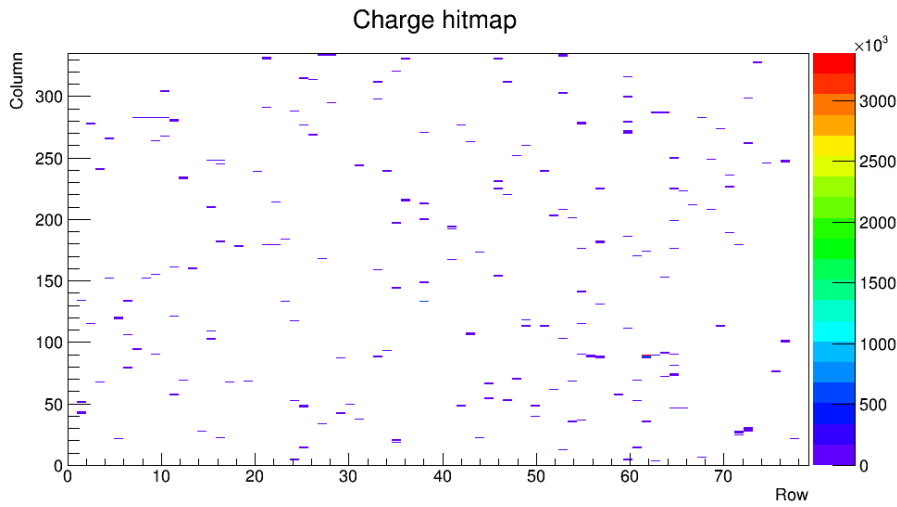


(b) Location of antiproton annihilations

Figure 8.16: (a) Two dimensional charge hitmap from 20 simulated antiproton events. Similar features to data such as long tracks and concentrated charge can be seen. The location for each simulated annihilation event is displayed in the hitmap in (b).



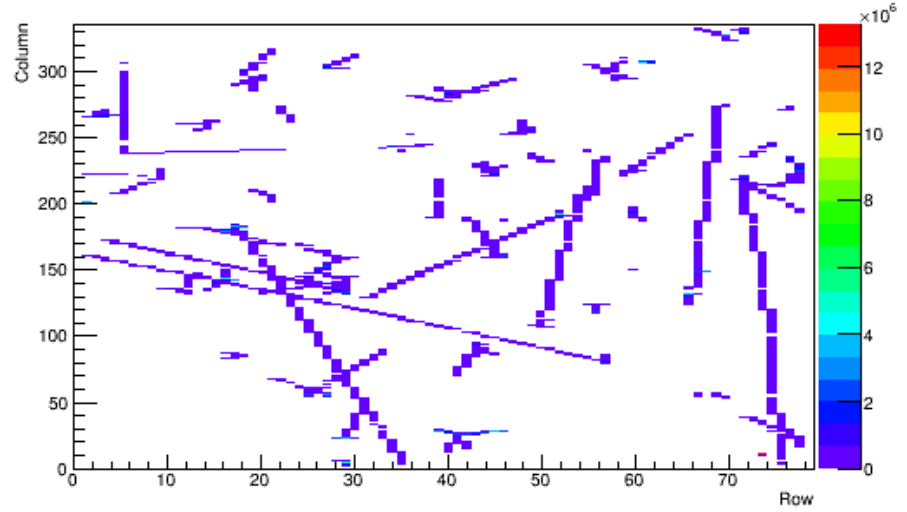
(a) Two dimensional charge hitmap from 200 simulated  $\pi^+$  events.



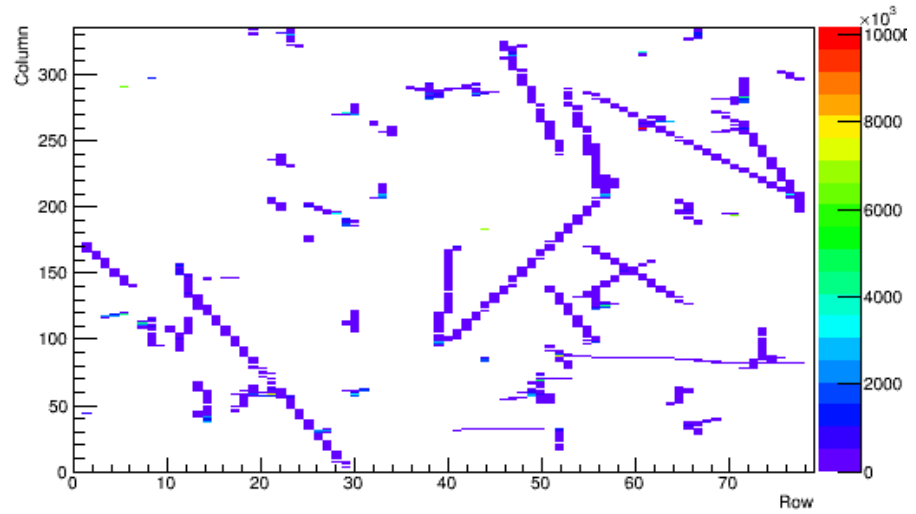
(b) Two dimensional charge hitmap from 200 simulated  $\pi^-$  events.

Figure 8.17: Comparison of two dimensional charge hitmaps from 200 simulated (a)  $\pi^+$  and (b)  $\pi^-$  events on the 3D silicon pixel detector with initial kinetic energies between 0–400 MeV.





(a) Simulated charge collected for 55 events where the annihilation of the antiproton occurred in the aluminium layer.



(b) Simulated charge collected for 51 events where the annihilation of the antiproton occurred in the silicon layer.

Figure 8.18: Comparison of the charge collected for  $\sim 50$  events where the antiproton annihilated in the (a) aluminium and (b) silicon layer.

### 8.5.2 Annihilation depth

The distance into the detector at which the annihilation of the antiproton occurs, known as the annihilation depth, is a very important value to study with simulated data. The experiment would be essentially useless if the antiprotons traversed the whole device without detection, consequently losing any positional information. The pie chart in Fig. 8.19 presents the proportion of antiprotons that annihilate in each layer of the detector for the given initial energy spectrum. As expected for antiprotons with a low kinetic energy, a large portion of the annihilations occurred in the non-sensitive layers, however 14.7 % annihilate within the silicon wafer. To study the distribution of the annihilation depth further, a one dimensional histogram of the final antiproton position in the simulated device is shown in Fig. 8.20 for the whole kinetic energy spectrum. This same data is displayed in Fig. 8.21 as a two dimensional hitmap of the annihilation depth as a function of the initial kinetic energy.

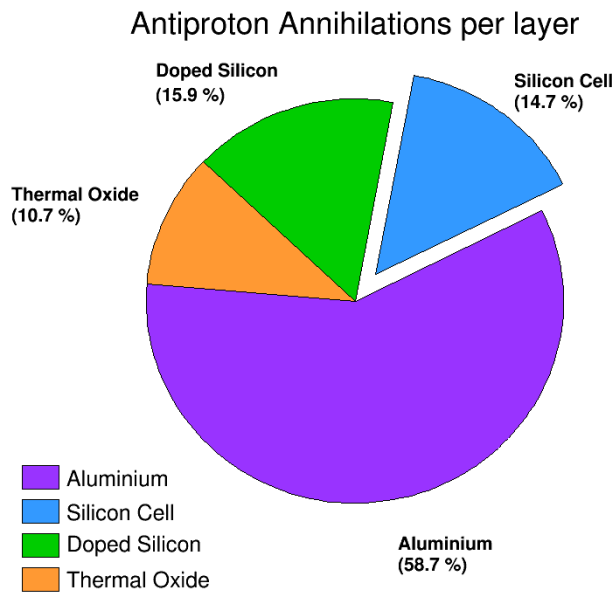


Figure 8.19: A pie chart to illustrate the percentage of annihilations that occur in each layer of the simulated detector for the spectrum of initial kinetic energy. Numbers were obtained from 100,000 simulated events.

The peaks in the number of annihilations as a function of the depth in the device shown in Fig. 8.20 and the corresponding smears<sup>2</sup> at the same depth in Fig. 8.21 are due to an increase of annihilations occurring at the border between two materials. However, there is no change in the material type at  $\sim 2 \mu\text{m}$  to explain the dip in the proportion of annihilations occurring

<sup>2</sup>The horizontal sections of the two dimensional distribution.

at this location. In the two dimensional plot, there is a concentration of annihilations at this same depth. The dip was unexpected and not readily explainable. This was investigated by a further study with antiprotons at a set initial kinetic energy. The energy points chosen were 0.05 MeV, 0.20 MeV, 0.35 MeV, 0.5 MeV, 0.65 MeV and 0.8 MeV, to give a full coverage over the depth in question. The distribution of annihilation depth for the different initial kinetic energies is shown in the lower section of Fig. 8.22, while the upper section is a graph of the mean depth and the initial kinetic energy. The first two distributions exhibit concentrated peaks due to proximity to the boundaries, however the subsequent four are similar in shape and no dip is seen.

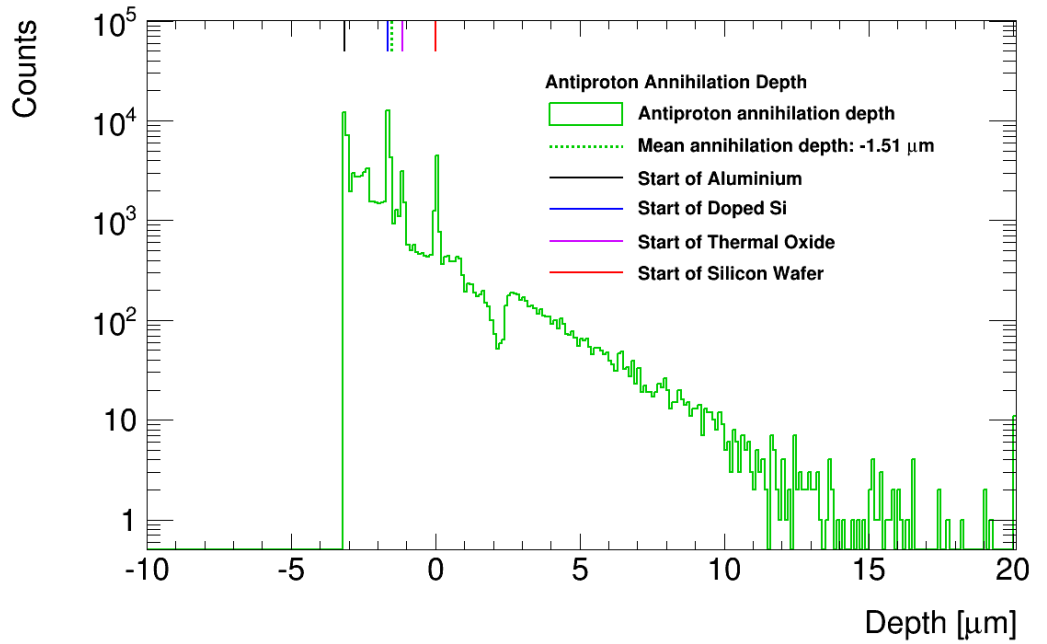


Figure 8.20: Simulated distribution of the annihilation depth. The peaks are boundaries between material types and the dip is under investigation.

The next investigation was with a uniform distribution of initial kinetic energy over 2 MeV. The layers on top of the sensor wafer were changed to vacuum in the simulation and runs of 100,000 events were taken for a silicon, copper and lead wafer respectively to investigate the dependence of the location of the dip with the atomic number,  $Z$ . The three cases were subsequently repeated for protons. A comparison of the annihilation depth within the three different materials can be seen in Fig. 8.23a and the depth at which the proton is stopped for the same materials in Fig. 8.23b. For antiprotons, the dip can clearly be seen for all three materials and there is a shift to increasing depth as the  $Z$  of the material increases. For protons, there are very small dips for silicon and copper at low depth, but a pronounced dip at  $\sim 5 \mu\text{m}$  for lead. The two dimensional hitmaps for the six setups can be found in Fig. 8.24. In these plots, the dip is now a discontinuity of the distribution at a certain energy range.

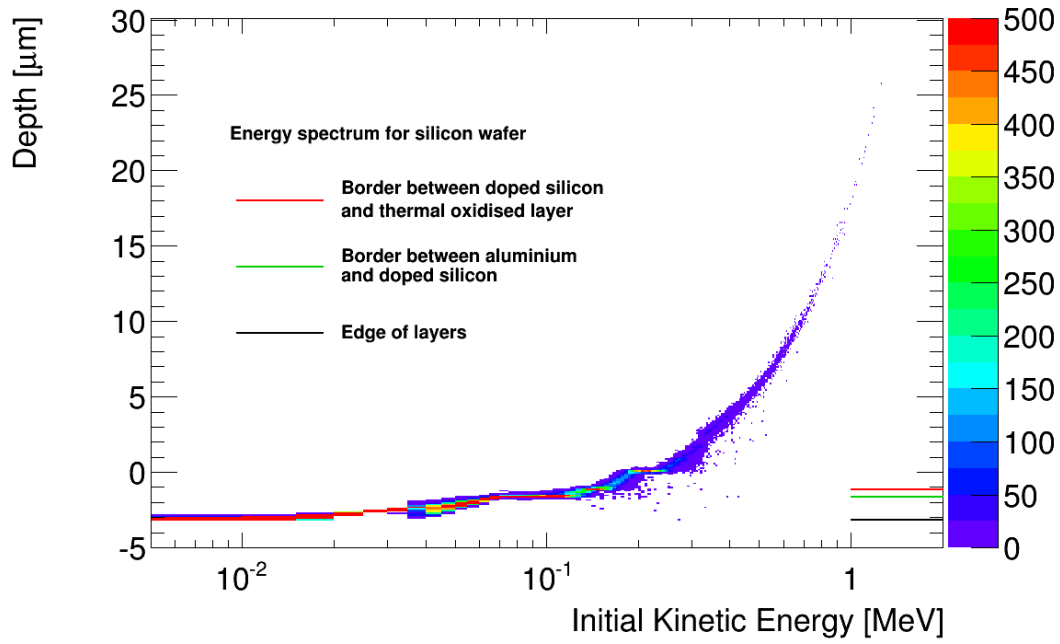


Figure 8.21: Annihilation depth of the simulated antiproton as a function of the initial kinetic energy.

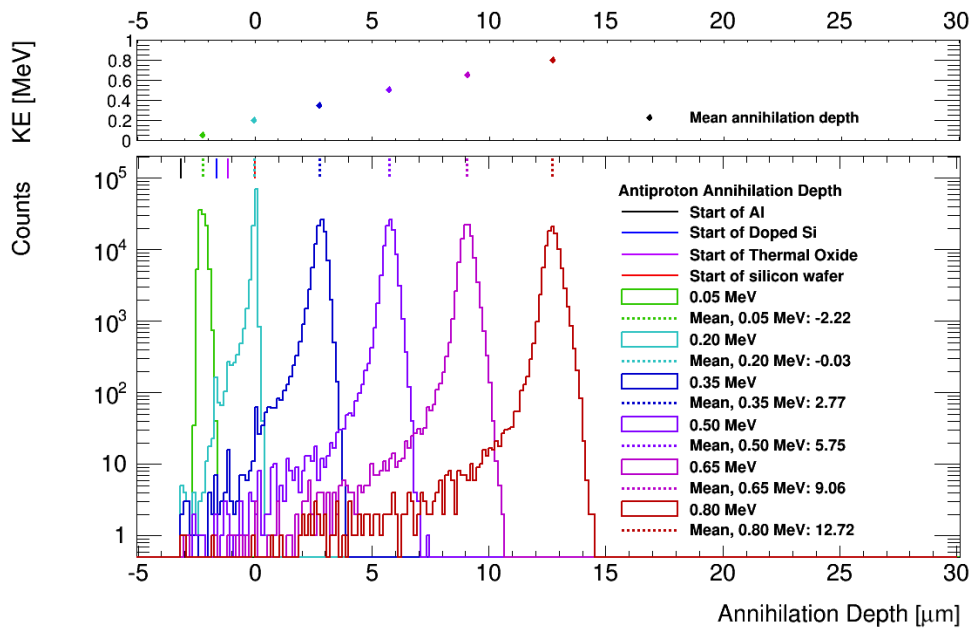
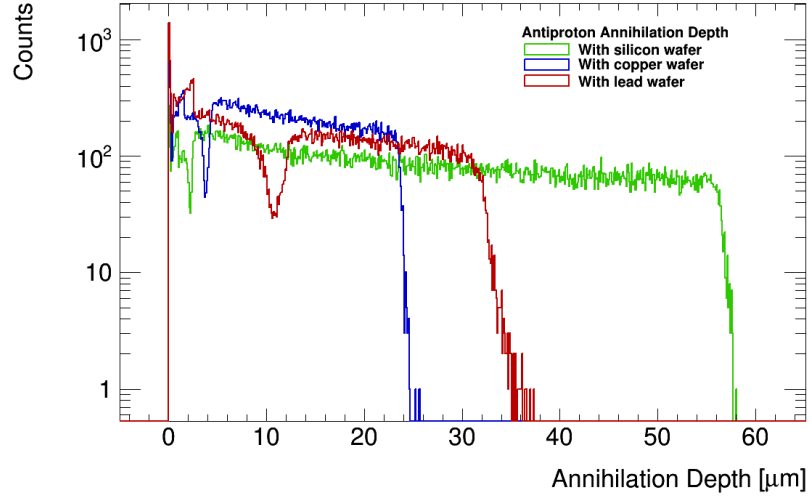
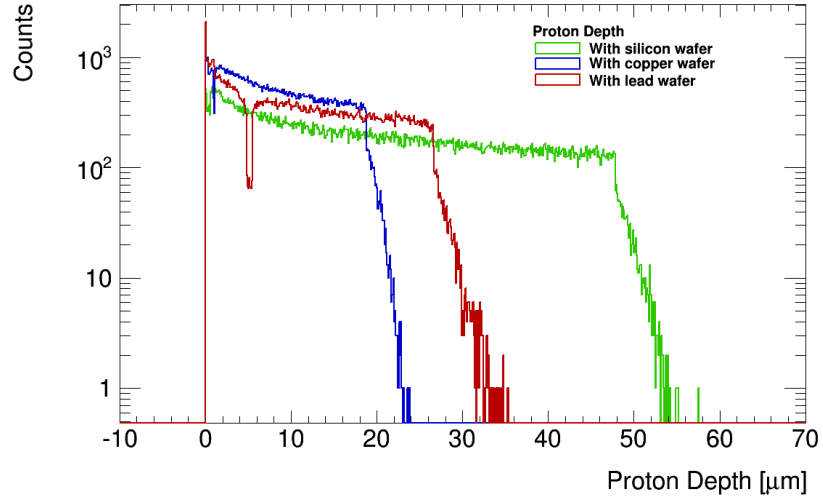


Figure 8.22: Simulated distribution of the antiproton annihilation depth for a fixed initial kinetic energy of 0.05 MeV (green), 0.20 MeV (cyan), 0.35 MeV (blue), 0.50 MeV (violet), 0.65 MeV (magenta), 0.80 MeV (red). Above is the mean annihilation depth for each initial kinetic energy.

This is most pronounced for antiprotons in lead in Fig. 8.24c. The most probable explanation of this feature is a corresponding known discontinuity in the list of cross-sections for physics processes within Geant4.



(a) Simulated data for antiprotons.



(b) Simulated data for protons.

Figure 8.23: Comparison of final depth of antiprotons (top) or protons (bottom) in a  $230\ \mu\text{m}$  thick wafer of silicon (green), copper (blue) or lead (red) for initial kinetic energies between 0 and 2 MeV.

The secondary particles produced before and after the discontinuity in the distribution in Fig. 8.24c are shown in Fig. 8.25. The energies chosen were 0.05 MeV, 0.20 MeV and 0.60 MeV. This was to investigate if the discontinuity was due to a new physics process becoming available after a specific energy. As can be seen in the figure, the secondary particles are produced at the same rates for all three energies.

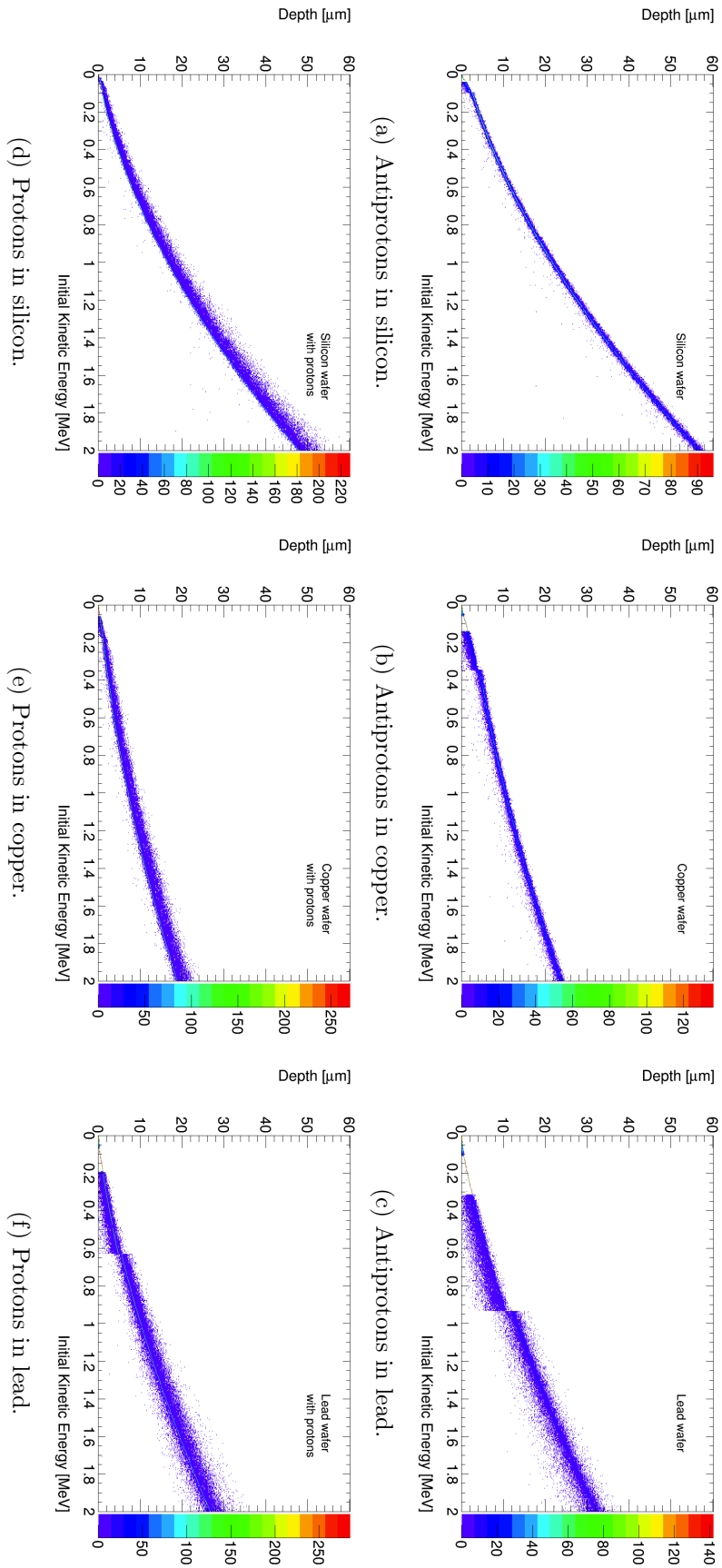


Figure 8.24: Comparison of final depth of antiprotons (top) or protons (bottom) in a 230  $\mu\text{m}$  thick wafer of silicon (left), copper (centre) or lead (right) for initial kinetic energies between 0 and 2 MeV.

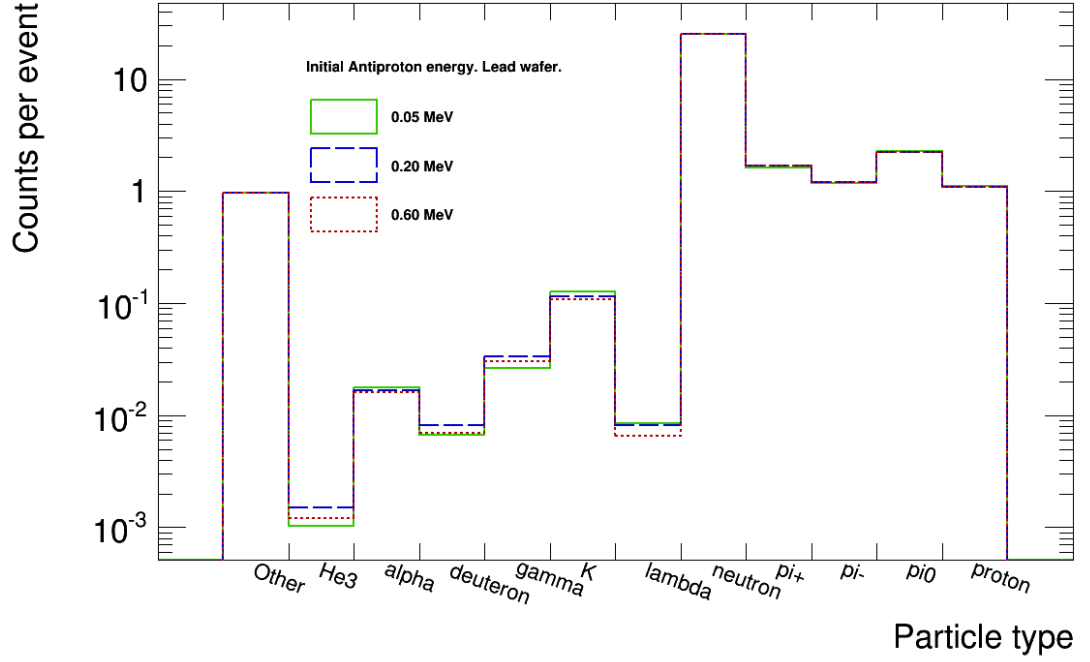


Figure 8.25: Comparison of secondary particles produced for three initial kinetic energies 0.05 MeV (green), 0.20 MeV (blue) and 0.60 MeV (red).

As mentioned in the section containing the description of the simulation, it is important to consider the threshold cuts applied to the physics lists. At the suggestion of a Geant4 expert [100], a study was performed to vary the threshold cuts applied. The default cut on the simulation had previously been 1 mm, with a separate cut of 0.001 mm for antiprotons. The study used antiprotons in a lead block with an initial kinetic energy between 0–2 MeV for 10,000 events. The threshold cut was varied from  $10^2$  mm to  $10^{-6}$  mm. As can be seen in Fig. 8.26, the dip is visible for threshold cuts from  $10^2$  mm to  $10^{-3}$  mm. For values lower than  $10^{-3}$  mm, the dip is gone and there is a constant number of annihilations with an increase in the depth, as would be expected. As a result, the final annihilation depth is reduced. The two dimensional hitmap of annihilation depth as a function of kinetic energy for  $10^{-6}$  mm is shown in Fig. 8.27 for comparison with Fig. 8.24c. The discontinuity at  $\sim 0.9$  MeV is no longer there. The consequence of this change is that the running time for 100,000 simulated events has increased from 45 minutes to nine hours due to the extra computation required.

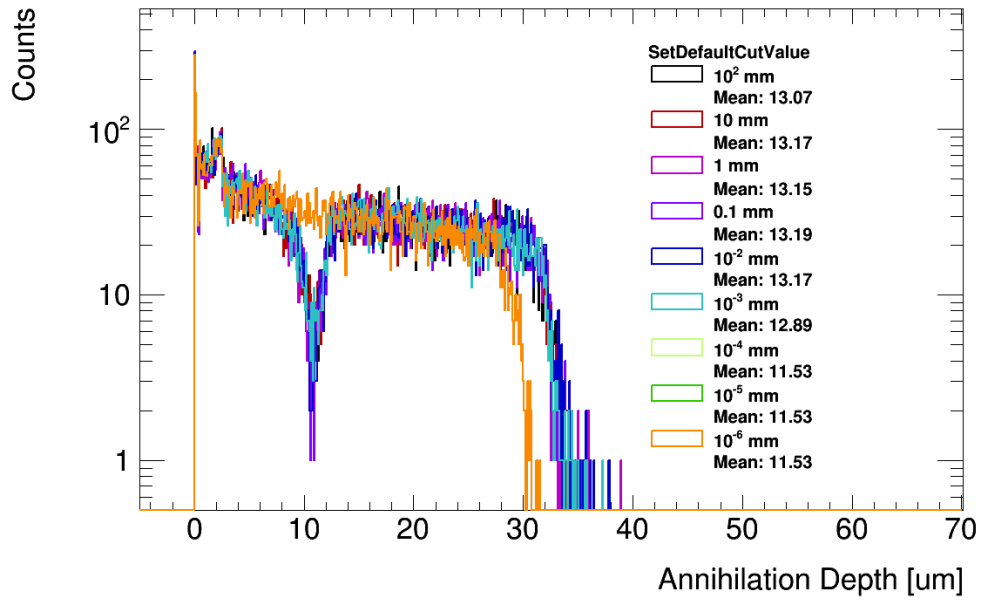


Figure 8.26: Distribution of the simulated antiproton annihilation depth in lead for changes in the SetDefaultCut parameter for Geant4.

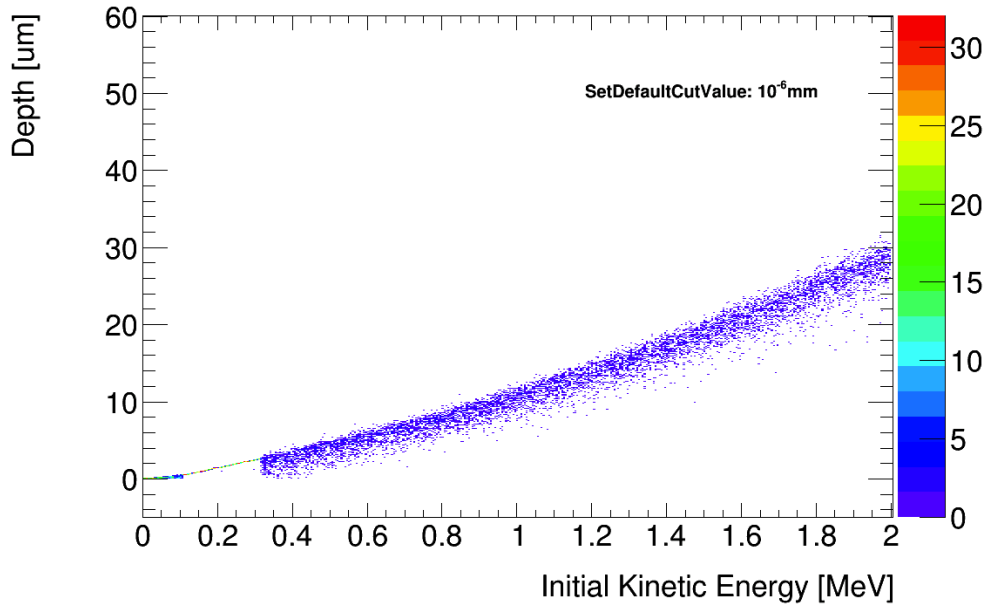


Figure 8.27: Annihilation depth of simulated antiprotons in a lead wafer as a function of the initial kinetic energy after a SetDefaultCut of  $10^{-6}$  has been applied.



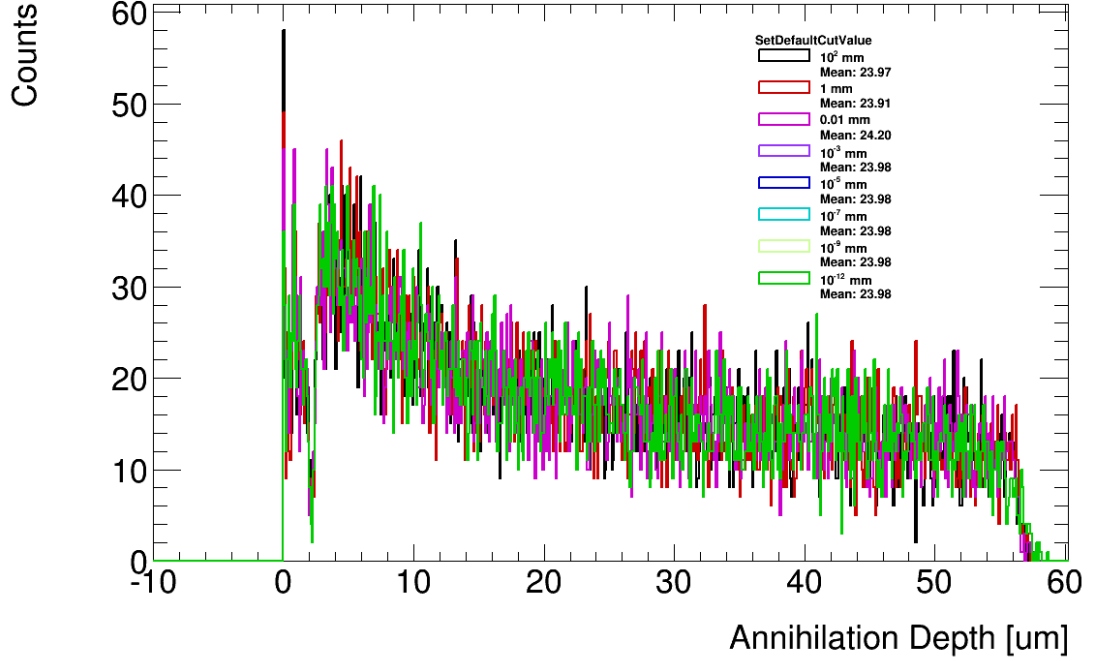


Figure 8.28: Distribution of the simulated antiproton annihilation depth in silicon for changes in the SetDefaultCut parameter for Geant4.

Unfortunately, when the material was changed back to silicon, the dip was still present. Even when the SetDefaultCutValue parameter was reduced to  $10^{-12}$  mm, as shown in Fig. 8.28, the distribution did not change. This suggests there is a feature in Geant4 that handles the physics processes that is not optimised for annihilations of antiprotons at such low kinetic energies. This issue is currently unresolved.

### 8.5.3 Secondaries produced

The multiplicity of the major annihilation products from the annihilation of an antiproton within silicon for the energy spectrum chosen are presented in Table 8.1, and shown in Fig. 8.29. These production rates are consistent with the rates simulated for the MIMOTERA detector in reference [89]. The MIMOTERA detector simulation also uses Geant4 with the CHIPS physics list and the patch described before. The result in the paper is compared to another Geant4 physics list called FRITIOF Precompound (FTFP) [101] and a discrepancy between the production of particles in the two lists is observed.

Table 8.1: Multiplicity of annihilation products for each simulated antiproton annihilation.

Particle Name	Multiplicity
proton	4.7208
pi0	2.20123
pi-	0.836186
pi+	1.76725
neutron	7.99366
lambda	0.0086867
K	0.104251
gamma	0.0311542
deuteron	0.259346
alpha	2.20935
He3	0.0222959
Other	0.263657

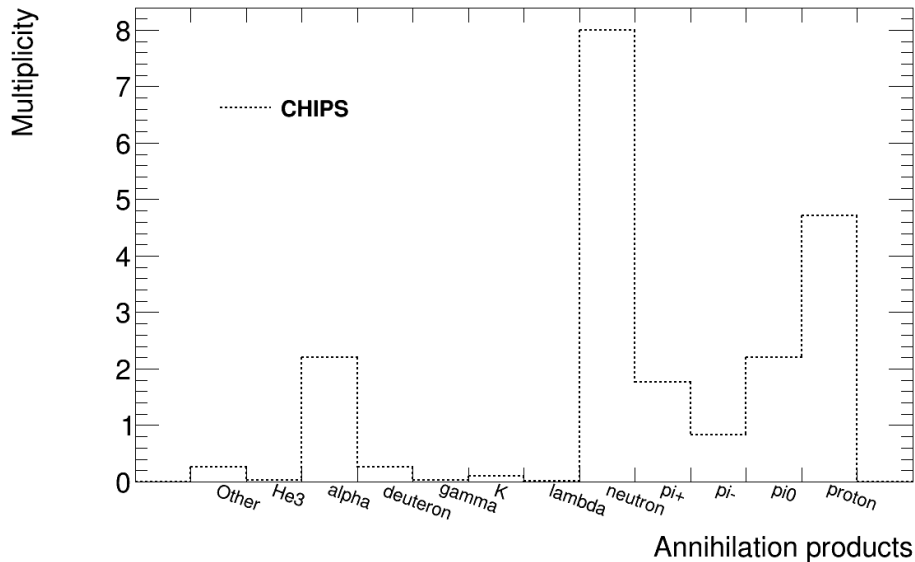


Figure 8.29: Multiplicity of annihilation products for each simulated antiproton annihilation.

## Pions

Pi mesons, also known as pions and written as  $\pi$ , are three particles composed of an up and a down quark-antiquark pair. Charged pions have a rest-mass of  $140 \text{ MeV}/c^2$  and a lifetime of  $2.6 \times 10^{-8} \text{ s}$ , which is a typical lifetime for weak interactions. Produced in pairs when the antiproton annihilates with a proton [102], the charged pions,  $\pi^+$  and  $\pi^-$ , will deposit charge as they travel through the detector. The resulting tracks are an indication of the position at which the annihilation occurred. The pions can also knock protons, neutrons and other nuclear fragments out of the nucleus of the atom at the location of the antiproton

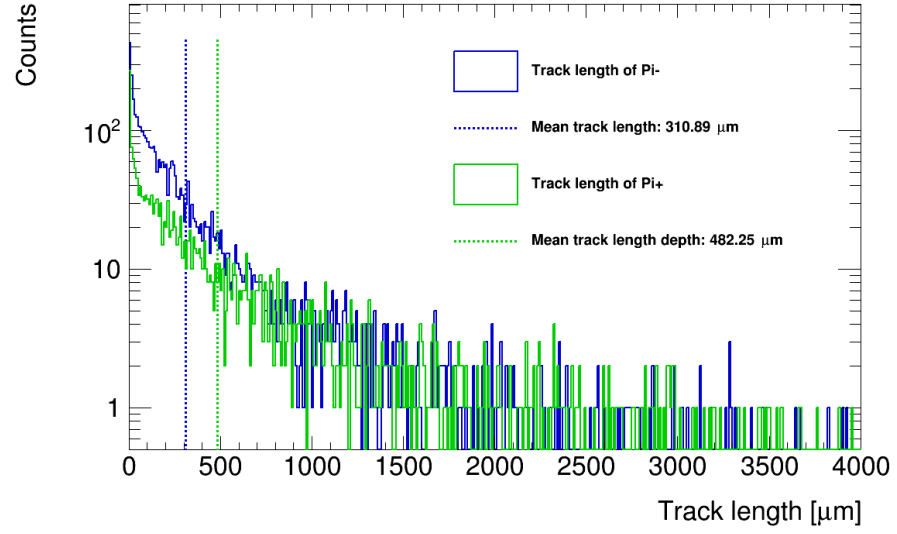


Figure 8.30: Simulated track length in the sensitive region of a 3D silicon pixel detector for charged pions created as a result of an antiproton annihilation.

annihilation. When an antiproton interacts with a neutron<sup>3</sup>, there is a greater ratio of  $\pi^-$  produced than  $\pi^+$ .

Within the simulation, the track length of charged pions was studied. Figure 8.30 shows the track length for  $\pi^+$  and  $\pi^-$  as a distance from the annihilation of the antiproton. Particles were selected to only be those produced directly as a result of an annihilation (using the `GetParentID()` selection on the track) and tracks were only measured either when the pion had deposited all of its energy, or when it crossed the boundary out of the detector. The thickness of the sensitive wafer is  $230\ \mu\text{m}$ . Therefore for a track length of  $1030\ \mu\text{m}$ , a minimum of three pixels will be traversed. Although it should be noted that track length does not necessarily scale with the number of pixels recording a hit. Many of the tracks will have travelled perpendicularly to the wafer surface and so fewer pixels would have a charge deposit within. Furthermore, even if the pion track is entirely parallel to the wafer surface, the charge deposited within each pixel might be below threshold and hence the track will no longer be detected.

The initial kinetic energy of the produced pions was also studied. Figure. 8.31 shows the distribution of the initial kinetic energy of charged pions.

<sup>3</sup>An antiproton is composed of two up-antiquarks and a down-antiquark, which is written in short-hand as  $\bar{u}\bar{u}\bar{d}$ . A neutron is composed of an up- and two down-quarks, written as  $udd$ . A quark-antiquark pair of up- or down-quarks will annihilate during an interaction between an antiproton and a neutron, with the remaining quarks combining to form charged or neutral pions.

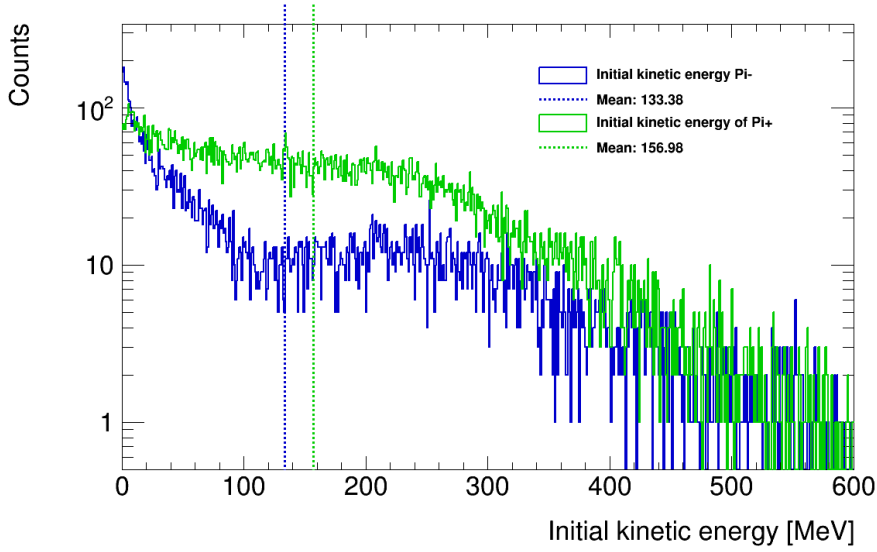


Figure 8.31: Simulated initial kinetic energy deposited in the sensitive region of a 3D silicon pixel detector for charged pions created as a result of an antiproton annihilation.

#### 8.5.4 Energy deposit

The total energy deposited in the silicon wafer per simulated event for 100,000 events is shown in Fig. 8.32. The distribution has a broad spread between 0 and 140 MeV with an average energy deposit per event of 22.58 MeV. To understand the distribution of this energy within the sensor, the fraction of total energy ( $E_{Total}$ ) deposited within the highest energy pixel (E1) was determined per event. This result is in Fig. 8.33. The histogram shows a wide spread in fraction of total energy within the highest energy pixel, with a mean at 34 %. The two dimensional version of Fig. 8.33 as a function of the initial kinetic energy of the antiproton can be found in Fig. 8.34. The fraction of  $E1 / E_{Total}$  has little dependence on the initial kinetic energy.

A comparison of the total energy deposited within the sensor depending on if the antiproton annihilated within the aluminium layer or within the sensitive bulk is shown in Fig. 8.35. The energy distributions are normalised to one for a simpler comparison. This is because the number of annihilations within aluminium is greater than the number within the silicon wafer for this initial energy spectrum. The total energy deposit per event for annihilations within silicon is slightly higher than for aluminium. This is to be expected since a greater amount of the total event will be measured for annihilations that occur within the silicon wafer. However, the difference is not enough to be able to discriminate between them with a cut on the pion energy.

The type of particles produced in an antiproton annihilation determine the signature of

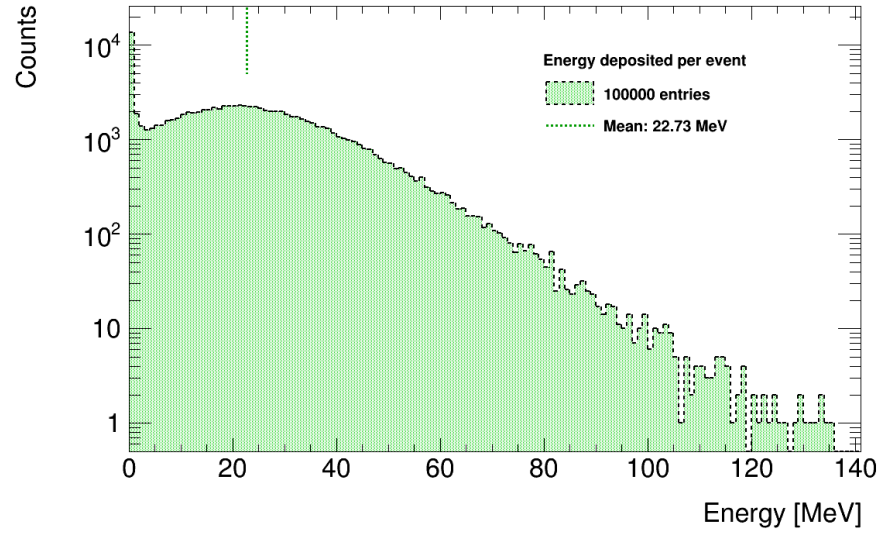


Figure 8.32: Distribution of the total energy deposited in the sensitive silicon wafer per simulated antiproton annihilation.

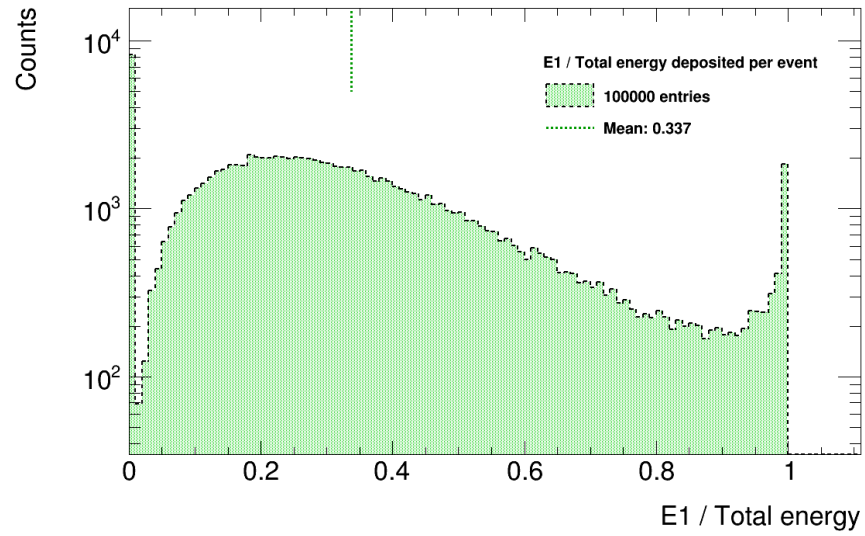


Figure 8.33: Distribution of the fraction of total energy deposited within the pixel cell with the greatest energy deposit (E1) per simulated antiproton annihilation.

the event. To assist in the identification of an annihilation it is important to study these secondary particles. The energy deposit contributed by different annihilation products per event is shown in Fig. 8.36. The red line for *heavy nuclei* includes the energy deposits of helium-3, deuteron and tritium. For the magenta line, designated *other*, the energy deposits of any remaining annihilation products are presented. The structure of this distribution, including the chosen particles, was to allow direct comparison with the corresponding figure

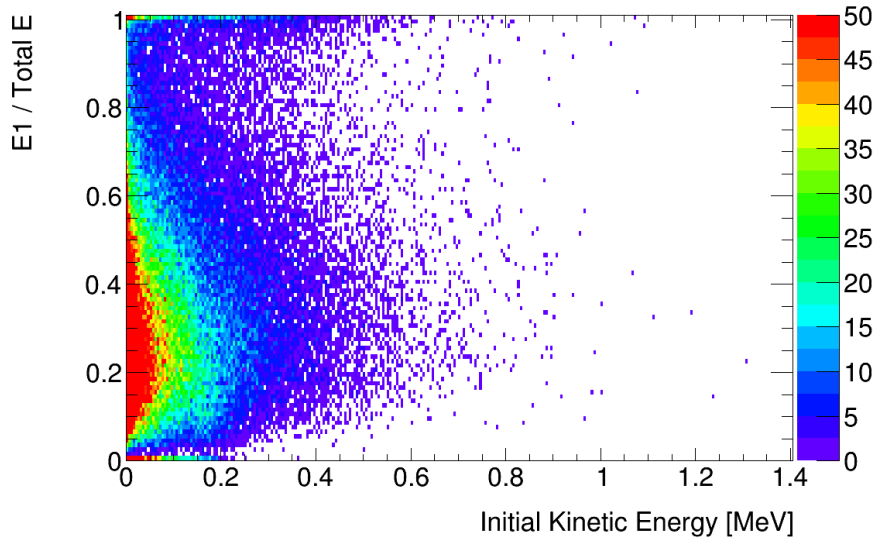


Figure 8.34: Distribution of the fraction of total energy deposited within the pixel cell with the greatest energy deposit (E1) per simulated antiproton annihilation as a function of the initial kinetic energy of the antiproton.

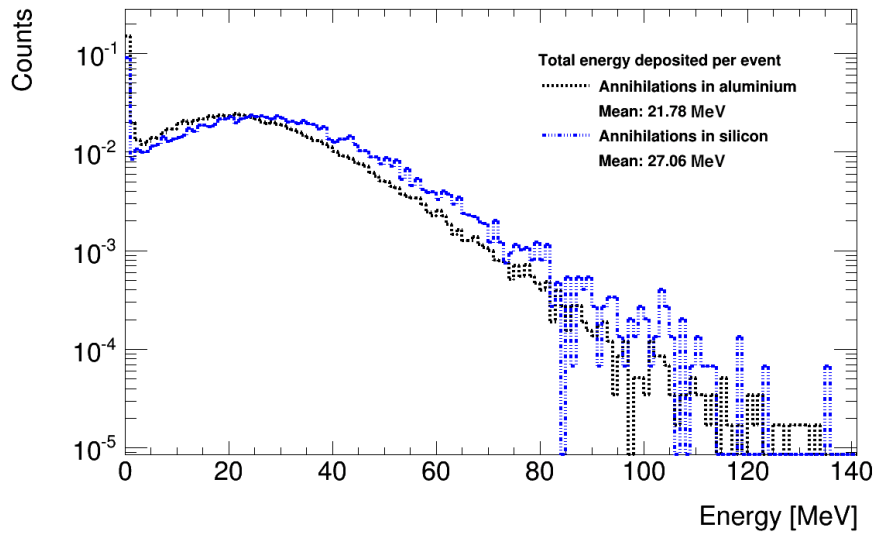


Figure 8.35: Comparison of the total energy deposited in the sensitive silicon wafer for simulated antiprotons in the aluminium layer (black) or the silicon bulk (blue).

from the MIMOTERA paper, in Fig. 8.37. The total energy deposit per particle type within the detector for the 3D silicon simulation is roughly four times greater than for the MIMOTERA detector. Since the MIMOTERA detector is much thinner than the 3D detector ( $\sim 14 \mu\text{m}$  compared to  $\sim 230 \mu\text{m}$ ), this is to be expected.

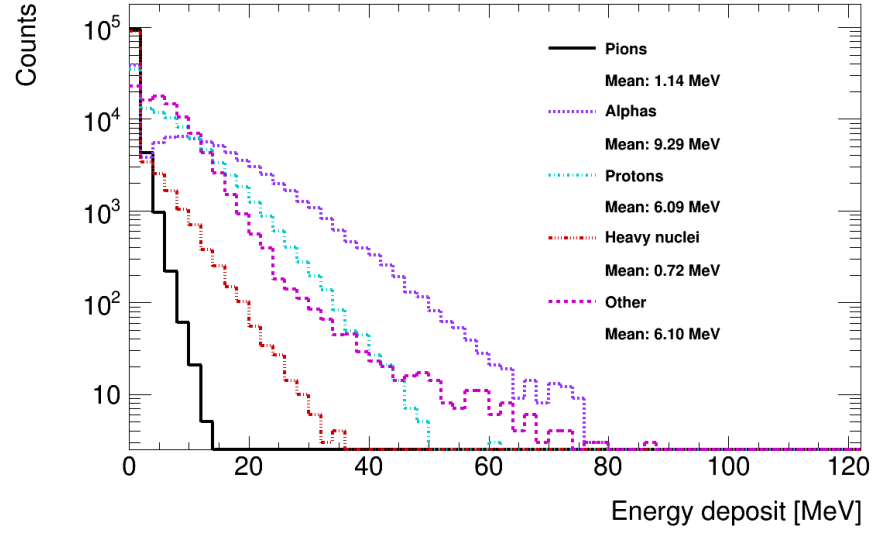


Figure 8.36: Distribution of the total energy deposited by selected annihilation products for a simulated antiproton annihilation in a 3D silicon pixel detector. Heavy nuclei are selected as: helium-3, deuteron and tritium. Other encompasses all further annihilation products produced.

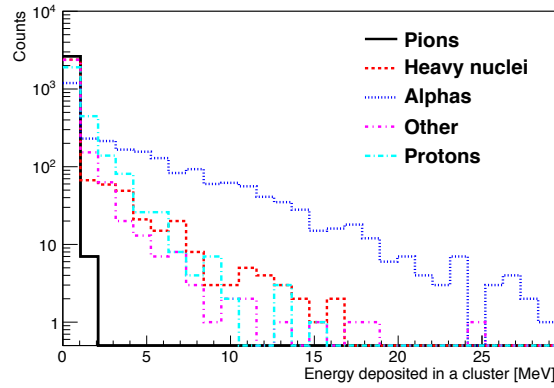


Figure 8.37: Fraction of total cluster energy for selected annihilation products from reference [89].

### 8.5.5 Charge collected

Similar to the figures shown in the previous section for energy (Section 8.5.4), the charge collected per simulated event was studied as calculated by the digitiser. Figure 8.38 shows the total charge collected per event. The two dimensional version as a function of the initial kinetic energy is in Fig. 8.39. The total charge collected has a landau distribution. The high number of counts at the very low charge region is most likely from events where most of the secondary particles that were created left the sensitive wafer after a short distance. The

comparison of the percentage of charge in the pixel with the most collect charge is in Fig. 8.40.

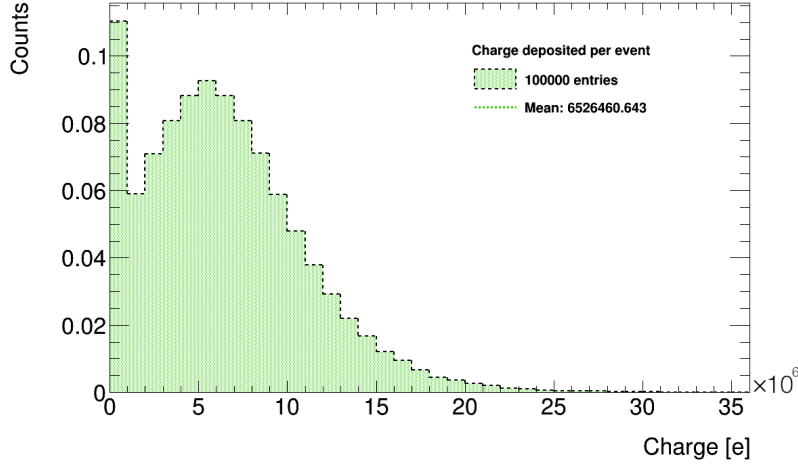


Figure 8.38: Distribution of the total charge deposited in the sensitive silicon wafer per simulated antiproton annihilation.

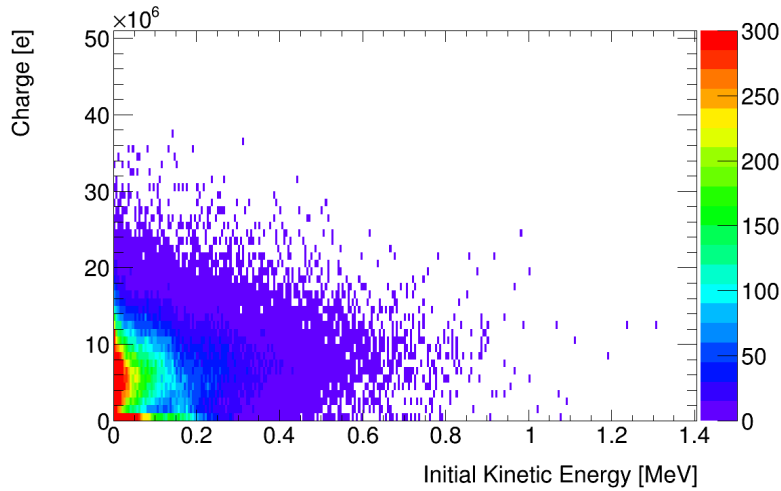


Figure 8.39: Distribution of the total charge deposited in the sensitive silicon wafer per simulated antiproton annihilation as a function of the initial kinetic energy of the antiproton.

The total charge collected per event for annihilations occurring in the aluminium layer, compared to the total charge from an annihilation in the silicon wafer, is shown in Fig. 8.41. As expected, there is a slight shift towards more charge collected within the silicon wafer, but not enough to discriminate between the two. This is similar to the same histogram produced for energy deposited within the sensor. Both curves have the same shape as the distribution for all annihilations shown in Fig. 8.38.



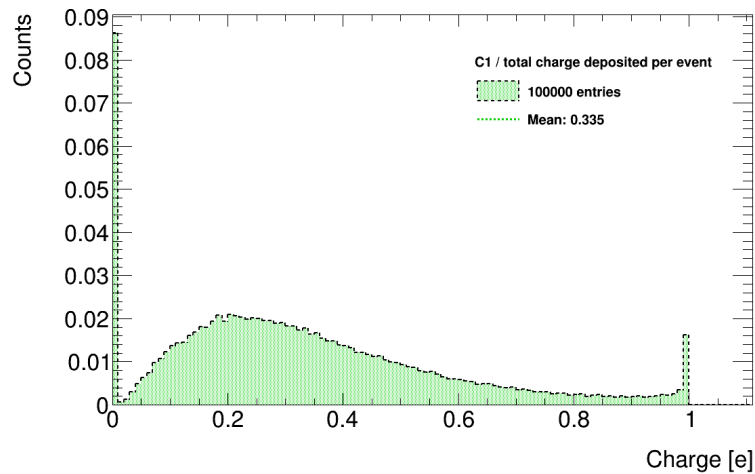


Figure 8.40: Distribution of the fraction of total charge deposited within the pixel cell with the greatest charge deposit (C1) per simulated antiproton annihilation.

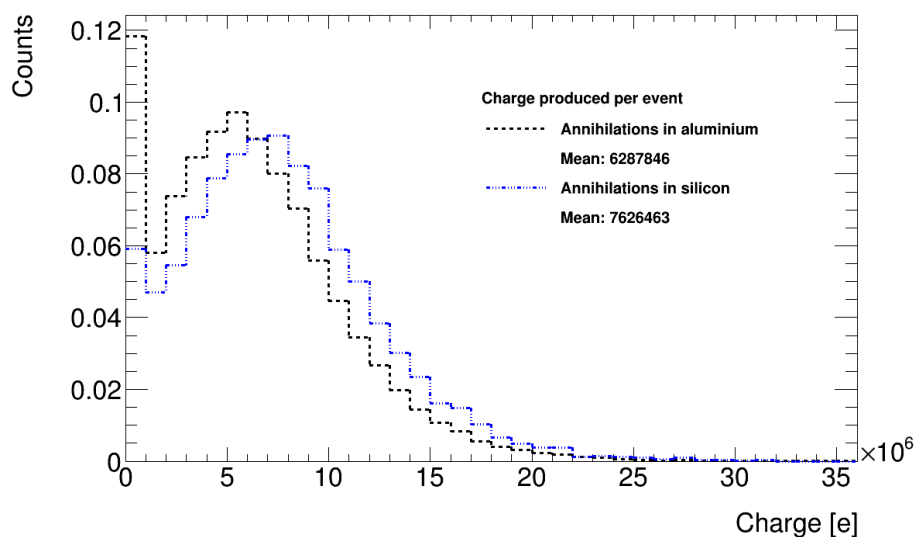
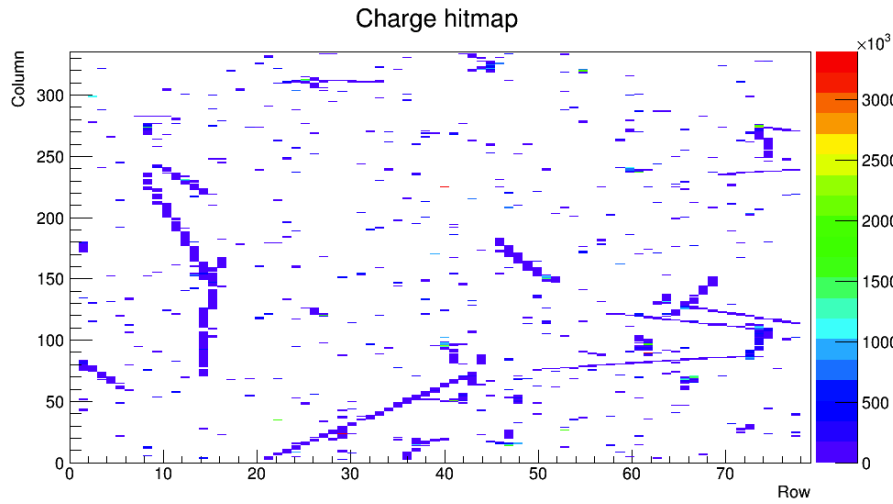


Figure 8.41: Comparison of the total charge deposited in the sensitive silicon wafer for simulated antiprotons in the aluminium layer (black) or the silicon bulk (blue).

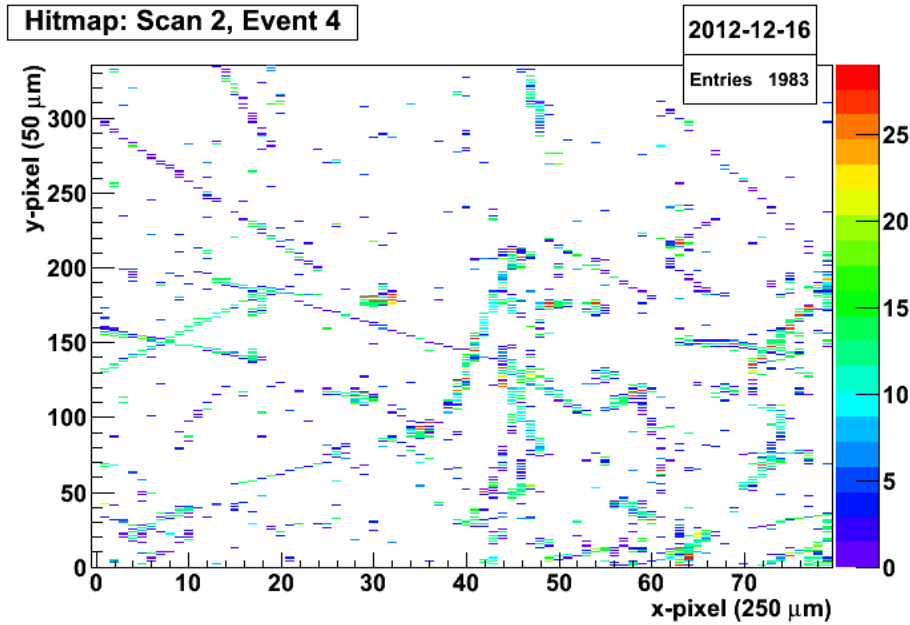
## 8.6 Summary

When an annihilation occurs within the detector chosen for the AEGIS experiment, it is extremely important that both the annihilation is identified, and the location is accurately recorded. To improve the algorithms written for the identification of an antiproton and where the annihilation position was located, good simulation data are required. The work on the algorithms is in the preliminary stages and results from this are not presented in this thesis.

Figure 8.42 allows a side-by-side visual comparison of a simulated charge hitmap for (a) antiproton annihilations and background pions and (b) the data from the beam test. The Geant4 simulation output shows many similar features to the actual events from data. This is encouraging and consequently the simulation will be a vital tool to create suitable algorithms to analyse the experimental data.



(a) Two dimensional hitmap from a simulated 3D silicon pixel detector combining 30 antiproton annihilations with 400 background charged pions.



(b) Raw two dimensional hitmap from the CNM 55 3D silicon pixel detector in an antiproton beam test at CERN in December 2012.

Figure 8.42: Comparison of simulated and experiment output of a 3D silicon pixel detector in an antiproton beam test.

## 9 | Summary and Conclusions

Prototypes from multiple manufacturing facilities of 3D silicon sensors on FE-I3 and FE-I4a readout cards have been studied in an intensive programme of beam tests to undergo qualification for the ATLAS IBL upgrade project. The author was present at every beam test between 2010 and 2012 to contribute to the collection and analysis of vital data for this qualification process. The qualification process was successful and 3D silicon modules will make up 25% of this new layer in the high eta region. Selected results are presented in this thesis. Results of a study into the efficiency of edge pixels from SINTEF with active edges was performed and found the non-irradiated device to be active to  $\sim 20 \mu\text{m}$  from the sensor edge.

IBL non-irradiated prototype sensors bonded to the FE-I4b readout cards have been tested in a beam test in October, 2012 and have been found to be working as expected [83]. Further beam tests of irradiated modules is required to study the response of the sensor and readout card after irradiation levels expected for the lifetime of the IBL.

3D silicon modules were used for the first time in an experiment outside of research and development at an antiproton beam test for the AEGIS experiment at CERN. A simulation was developed in Geant4 to facilitate the analysis of the results of this beam test. Output from the simulation is presented in this thesis with comparison to experimental data and a previous simulation with a MIMOTERA detector. The simulation is visually similar to data and will be vital to the development of algorithms to analyse experimental data.

Due to the work done during the course of this PhD, the writer of this thesis is a named author on the following peer-reviewed papers:

### Journal Articles:

- C. Nellist, et al., “*Beam Test Results of 3D Silicon Pixel Sensors for Future ATLAS Upgrades*”, Nucl. Instrum. Methods Phys. Res., A., 732 no. 0, (2013) 141-145.,  
<http://dx.doi.org/10.1016/j.nima.2013.07.002>.  
(<http://www.sciencedirect.com/science/article/pii/S0168900213009789>)

- R. Nagai, et al., “*Evaluation of novel KEK/HPK n-in-p pixel sensors for ATLAS upgrade with testbeam*”, Nucl. Instrum. Methods Phys. Res., A 699 (2013) 78-83
- ATLAS IBL Collaboration, “*Prototype ATLAS IBL Modules using the FE-I4A Front-End Readout Chip*”, J. Instrum. 7 (2012) P11010
- P. Grenier, et al., “*Test beam results of 3D silicon pixel sensors for the ATLAS upgrade.*”, Nucl. Instrum. Methods Phys. Res., A 638 (2011) 33-40
- P. Hansson, et al., “*3D silicon pixel sensors: Recent test beam results.*”, Nucl. Instrum. Methods Phys. Res., A 628 (2011) 216-220
- A. Micelli, et al., “*3D-FBK pixel sensors: Recent beam tests results with irradiated devices*”, Nucl. Instrum. Methods Phys. Res., A 650 (2011) 150-157

**Journal Articles in Preparation:**

- “*Annihilation of low energy antiprotons in silicon (working title)*”

Work has also been presented in the form of talks and posters at the following conferences and international meetings:

- **Talk:** “*Beam Test Results of 3D Silicon Pixel Sensors for Future ATLAS Upgrades*”. Vienna Conference on Instrumentation, Vienna, 12th February 2013.
- **Poster:** “*Analysis of 3D Silicon Pixel Detectors for ATLAS Upgrades*” ATLAS UK, Lancaster, 8th January 2013.
- **Talk:** “*Recent 3D Silicon Test Beam Results*” ATLAS Upgrade Week, CERN, 18th November 2012.
- **Talk:** “*Summary of IBL Test Beams in 2012*” IBL General Meeting, CERN, 10th October 2012.
- **Talk:** “*Characterisation and Test Beam Analysis of 3D Silicon Sensors for the ATLAS Upgrade*” IOP HEPP & APP Meeting, Queen Mary, University of London, London, 3rd April 2012.
- **Poster:** “*Characterisation and Data Analysis of 3D Silicon Pixel Detectors for the ATLAS Upgrade*” ATLAS UK, Glasgow, 5th January 2012.
- **Poster:** “*Characterisation and Data Analysis of 3D Silicon Pixel Detectors for the ATLAS Upgrade*” RAL Summer School, Oxford, September 2010.

# References

- [1] G. Aad et al., *Observation of a new particle in the search for the Standard Model Higgs boson with the ATLAS detector at the LHC*, Physics Letters B **716** no. 1, (2012) 1 – 29.  
<http://www.sciencedirect.com/science/article/pii/S037026931200857X>.
- [2] B. Martin and G. Shaw, *Particle Physics*. Wiley, second ed., 1997.
- [3] S. M. Sze, *Physics of Semiconductor Devices*, vol. Chapters 2-4. Wiley, 2nd ed., 202.
- [4] C. Kittel, *Introduction to solid state physics*. Wiley New York, 4th ed., 1971.
- [5] G. F. Knoll, *Radiation Detection and Measurement*, vol. Chapter 11. Wiley, 4th ed., 2010.
- [6] J. Beringer et al. (Particle Data Group), “Particle data booklet.” Phys. rev. d 86, 010001, 2012.
- [7] H. Young and R. Freeman, *University Physics*. 11th ed.
- [8] G. F. Knoll, *Radiation Detection and Measurement*, vol. Chapter 2. Wiley, 4th ed., 2010.
- [9] M. Moll, *Radiation tolerant semiconductor sensors for tracking detectors*, Nucl. Instrum. Meth. A **565** no. 1, (2006) 202 – 211.  
<http://www.sciencedirect.com/science/article/pii/S0168900206007571>.  
PIXEL 2005.
- [10] G. Lindström, *Radiation damage in silicon detectors*, Nucl. Instrum. Meth. A **512** no. 1–2, (2003) 30 – 43.  
<http://www.sciencedirect.com/science/article/pii/S0168900203018746>.
- [11] M. Moll, *Radiation damage in silicon particle detectors: microscopic defects and macroscopic properties*. *oai:cds.cern.ch:425274*. PhD thesis, Hamburg University, 1999.
- [12] M. Povoli, *Development of enhanced double-sided 3D radiation sensors for pixel detector upgrades at HL-LHC*. PhD thesis, DISI - University of Trento, 2013.
- [13] E. Fretwurst et al., *Reverse annealing of the effective impurity concentration and long term operational scenario for silicon detectors in future collider experiments*, Nucl. Instrum. Meth. A **342** no. 1, (1994) 119–125.  
<http://www.sciencedirect.com/science/article/pii/0168900294914176>.

- [14] W. Adam et al., *Radiation hard diamond sensors for future tracking applications*, Nucl. Instrum. Meth. A **565** no. 1, (2006) 278 – 283.  
<http://www.sciencedirect.com/science/article/pii/S0168900206007777>.  
PIXEL 2005.
- [15] G. Aad et al., *ATLAS pixel detector electronics and sensors*, JINST **3** no. 07, (2008) P07007.
- [16] <http://home.web.cern.ch/about>, 2013. <http://home.web.cern.ch/about>.
- [17] L. Evans and P. Bryant, *LHC Machine*, JINST **3** no. 08, (2008) S08001.
- [18] C. Lefèvre, *The CERN accelerator complex. Complexe des accélérateurs du CERN*, Dec, 2008.
- [19] F. R. Elder, R. V. Langmuir, and H. C. Pollock, *Radiation from Electrons Accelerated in a Synchrotron*, Phys. Rev. **74** (1948) 52–56.  
<http://link.aps.org/doi/10.1103/PhysRev.74.52>.
- [20] E. Wilson, *An Introduction to Particle Accelerators*. Oxford University Press, 2001.
- [21] O. S. Brüning, P. Collier, P. Lebrun, S. Myers, R. Ostojic, J. Poole, and P. Proudlock, *LHC Design Report*, vol. 1 chapter 2. CERN, Geneva, 2004.
- [22] ATLAS Collaboration, *The ATLAS Experiment at the CERN Large Hadron Collider*, JINST **3** no. 08, (2008) S08003.
- [23] The ALICE Collaboration, *The ALICE experiment at the CERN LHC*, JINST **3** no. 08, (2008) S08002.
- [24] The CMS Collaboration, *The CMS experiment at the CERN LHC*, JINST **3** no. 08, (2008) S08004.
- [25] The LHCb Collaboration, *The LHCb Detector at the LHC*, JINST **3** no. 08, (2008) S08005.
- [26] “Tyrannosaurus.” Wikipedia. [http://en.wikipedia.org/wiki/T\\_rex](http://en.wikipedia.org/wiki/T_rex).
- [27] ATLAS Collaboration, *ATLAS detector and physics performance: Technical Design Report, 1*. No. ATLAS-TDR-14 ; CERN-LHCC-99-014 in Technical Design Report ATLAS. CERN, Geneva, 1999.
- [28] ATLAS Collaboration, *ATLAS inner detector: Technical Design Report, 1*. No. ATLAS-TDR-4 ; CERN-LHCC-97-016 in Technical Design Report ATLAS. CERN, 1997.
- [29] ATLAS Collaboration, *ATLAS inner detector: Technical Design Report, 2*. Technical Design Report ATLAS. CERN, Geneva, 1997.
- [30] R. Beccherle et al., *MCC: the Module Controller Chip for the ATLAS Pixel Detector*, Nucl. Instrum. Meth. A **492** no. 1–2, (2002) 117–133.  
<http://www.sciencedirect.com/science/article/pii/S0168900202012792>.

- 
- [31] T. Akesson et al., *Electron identification with a prototype of the Transition Radiation Tracker for the ATLAS experiment: ATLAS TRT collaboration*, Nucl. Instrum. Meth. A **412** no. 2–3, (1998) 200–215.  
<http://www.sciencedirect.com/science/article/pii/S0168900298004574>.
- [32] ATLAS Collaboration, *ATLAS calorimeter performance: Technical Design Report*, vol. ATLAS-TDR-1 ; CERN-LHCC-96-040 of *Technical Design Report ATLAS*. CERN, Geneva, 1996.
- [33] ATLAS Collaboration, *ATLAS muon spectrometer : Technical Design Report*. No. ATLAS-TDR-10 ; CERN-LHCC-97-022 in *Technical Design Report ATLAS*. CERN, 1997.
- [34] P. Vankov. ITk subcommittee meeting, 2011.
- [35] M. Capeans et al., *ATLAS Insertable B-Layer Technical Design Report*, Tech. Rep. CERN-LHCC-2010-013. ATLAS-TDR-19, CERN, Geneva, Sep, 2010.
- [36] H. Kagan, M. Mikuž, and W. Trischuk, “ATLAS diamond beam monitor (DBM).” <https://edms.cern.ch/document/1211792/1>, 2012. ATL-IP-ES-0187.
- [37] C. ATLAS, *ATLAS Insertable B-Layer Technical Design Report Addendum*, Tech. Rep. CERN-LHCC-2012-009. ATLAS-TDR-19-ADD-1, CERN, Geneva, May, 2012. Addendum to CERN-LHCC-2010-013, ATLAS-TDR-019.
- [38] M. Barbero et al., *Submission of the first full scale prototype chip for upgraded ATLAS pixel detector at LHC, FE-I4A*, Nucl. Instrum. Meth. A **650** no. 1, (2011) 111–114.  
<http://www.sciencedirect.com/science/article/pii/S0168900210026781>.
- [39] The ATLAS IBL collaboration, *Prototype ATLAS IBL modules using the FE-I4A front-end readout chip*, JINST **7** no. 11, (2012) P11010.  
<http://stacks.iop.org/1748-0221/7/i=11/a=P11010>.
- [40] F. Hirsch, “Results from the commissioning of the ATLAS pixel detector with (and without) cosmics data.” ICALEPCS 2009, Kobe.
- [41] M. G. Albrow et. al., *The FP420 R&D Project: Higgs and New Physics with forward protons at the LHC*, JINST **4** (2009).
- [42] S. Grinstein et al., *Beam Test Studies of 3D Pixel Sensors Irradiated Non-Uniformly for the ATLAS Forward Physics Detector*, [arXiv:1302.5292](https://arxiv.org/abs/1302.5292) [physics.ins-det].
- [43] S. Parker, C. Kenney, and J. Segal, *3D - A proposed new architecture for solid-state radiation detectors*, Nucl. Instrum. Meth. A **395** (1997) 328–343.
- [44] C. Da Viá, *Silicon sensors go 3D*, Cern Courier (2012).
- [45] A. A. Ayón, R. L. Bayt, and K. S. Breuer, *Deep reactive ion etching: a promising technology for micro- and nanosatellites*, Smart Materials and Structures **10** no. 6, (2001) 1135. <http://stacks.iop.org/0964-1726/10/i=6/a=302>.

- [46] “SINTEF homepage.” Online, 2013. <http://www.sintef.no/home/>.
- [47] C. Kenney, S. Parker, J. Segal, and C. Storment, *Silicon detectors with 3-D electrode arrays: Fabrication and initial test results*, IEEE Transactions on Nuclear Science **46** no. 4 PART 3, (1999) 1224–1236. <http://www.scopus.com/inward/record.url?eid=2-s2.0-0033311423&partnerID=40&md5=7806e2f694a025679d5c6eaa56c01e8f>. cited By (since 1996)81.
- [48] T.-E. Hansen et al., *First fabrication of full 3D-detectors at SINTEF*, JINST **4** no. 03, (2009) P03010. <http://stacks.iop.org/1748-0221/4/i=03/a=P03010>.
- [49] *3D Active Edge Silicon Sensors Test Results*. September, 2006.
- [50] C. Da Viá et al., *Radiation hardness properties of full-3D active edge silicon sensors*, Nucl. Instrum. Meth. A **587** (2008) 243–249.
- [51] G.-F. Dalla Betta et. al, “Characterization of 3D-DDTC detectors on p-type substrates.” Arxiv:0911.4864v1, 2009.
- [52] C. Da Viá et al., *3D silicon sensors: Design, large area production and quality assurance for the ATLAS IBL pixel detector upgrade*, Nucl. Instrum. Meth. A **694** no. 0, (2012) 321–330. <http://www.sciencedirect.com/science/article/pii/S0168900212008509>.
- [53] C. Da Viá et al., *3D active edge silicon sensors with different electrode configurations: Radiation hardness and noise performance*, Nucl. Instrum. Meth. A **604** no. 3, (2009) 505 – 511. <http://www.sciencedirect.com/science/article/pii/S0168900209004227>.
- [54] M. Mathes et al., *Test beam characterization of 3-D silicon pixel detectors*, IEEE Transactions on Nuclear Science **55** no. 6, (2008) 3731–3735. <http://www.scopus.com/inward/record.url?eid=2-s2.0-58849092737&partnerID=40&md5=c7fbf2cbe8cbd5dc37de2a4697bbc814>. cited By (since 1996)10.
- [55] M. Da Rold et al., *Study of breakdown effects in silicon multiguard structures*, Nuclear Science, IEEE Transactions on **46** no. 4, (1999) 1215–1223.
- [56] C. Kenney, S. Parker, and E. Walckiers, *Results from 3-D silicon sensors with wall electrodes: near-cell-edge sensitivity measurements as a preview of active-edge sensors*, Nuclear Science, IEEE Transactions on **48** no. 6, (2001) 2405–2410.
- [57] I. Rubinskiy, *Irradiation and beam tests qualification for ATLAS IBL Pixel Modules*, Nucl. Instrum. Meth. A **699** no. 0, (2013) 67 – 71. <http://www.sciencedirect.com/science/article/pii/S0168900212004573>. Academia Sinica, Taipei, Taiwan, December 5 – 8, 2011.
- [58] M. Povoli et al., *Slim edges in double-sided silicon 3D detectors*, JINST **7** no. 01, (2012) C01015. <http://stacks.iop.org/1748-0221/7/i=01/a=C01015>.



- 
- [59] ATLAS 3D Collaboration Collaboration, P. Grenier et al., *Test Beam Results of 3D Silicon Pixel Sensors for the ATLAS upgrade*, Nucl. Instrum. Meth. A **638** (2011) 33–40, [arXiv:1101.4203 \[physics.ins-det\]](#).
- [60] P. Hansson et al., *3D silicon pixel sensors: Recent test beam results*, Nucl. Instrum. Meth. A **628** no. 1, (2011) 216 – 220.  
<http://www.sciencedirect.com/science/article/pii/S0168900210015111>.  
Proceedings of the 12th International Vienna Conference on Instrumentation.
- [61] M. Backhaus et al., *Development of a versatile and modular test system for ATLAS hybrid pixel detectors*, Nucl. Instrum. Meth. A **650** no. 1, (2011) 37 – 40.
- [62] University of Bonn, “USBpix - USB based readout system for ATLAS FE-I3 and FE-I4.” <http://icwiki.physik.uni-bonn.de/twiki/bin/view/Systems/UsbPix>.
- [63] B. LBNL ATLAS Group, “Turbodaq.”  
<http://pixdata.lbl.gov/html/TurboDAQ.html>.
- [64] *STcontrol User Guide*, 2013. <http://icwiki.physik.uni-bonn.de/twiki/bin/view/Systems/STcontrolUserGuide>.
- [65] D. Autiero, Y. Caffari, L. S. Esposito, A. Marotta, J. Marteau, and P. Migliozi, *Characterization of the T24 electron beam line available at DESY*, OPERA Note (2004).
- [66] G. Thayer, et al., “Construction of high speed, massively parallel, atca based data acquisition systems using modular components.” Tipp, 2011.
- [67] S. Tsiskaridze, *Beam Test Performance of 3D Pixel Detectors for the IBL Upgrade*, Master’s thesis, Universitat Autònoma de Barcelona, 2012.
- [68] J. Baudot et al., *First Test Results Of MIMOSA-26, A Fast CMOS Sensor With Integrated Zero Suppression And Digitized Output*, 2009 IEEE NSS Conference Record (2009) 1169.
- [69] G. Troska, *PhD thesis: Qualification studies of ATLAS Pixel Sensors for usage in IBL- and SLHC-Experiments with the EUDET Testbeam-Telescope*. PhD thesis, Technische Universität Dortmund - Experimentelle Physik IV, 2011.
- [70] R. Radebaugh, N. Frederick, and J. Siegwarth, *Flexible laminates for thermally grounded terminal strips and shielded electrical leads at low temperatures*, Cryogenics **13** no. 1, (1973) 41 – 43.  
<http://www.sciencedirect.com/science/article/pii/0011227573902646>.
- [71] E. Corrin, *EUDAQ Software User Manual*, 2010.
- [72] A. Bulgheroni, For the EUDET-JRA1 Consortium, *Results from the EUDET telescope with high resolution planes*, Nucl. Instrum. Meth. A **623** (2010) 399.
- [73] I. Rubinsky, *EUTelescope offline track reconstruction and DUT analysis software*, EUDET-Memo-2010-12. Retrieved on Sep 8 (2011).

- [74] “MillepedeII.” Online - [https://www.wiki.terascale.de/index.php/millepede\\_ii](https://www.wiki.terascale.de/index.php/millepede_ii).
- [75] R. Mankel, *A concurrent track evolution algorithm for pattern recognition in the HERA-B main tracking system*, Nucl. Instrum. Meth. A **395** no. 2, (1997) 169 – 184. <http://www.sciencedirect.com/science/article/pii/S0168900297007055>.
- [76] A. Bulgheroni, T. Klimovich, P. Roloff, and A. Zarnecki, *EUTelescope: tracking software*, EUDET-Memo-2007-20 **144** (2007).
- [77] H. Hölbe, *C Event Display (CED)*. Deutsches Elektronen-Synchrotron, 2011.
- [78] K. N. Sjøbæk, *Full simulation of a testbeam experiment including modeling of the Bonn ATLAS Telescope and ATLAS 3D pixel silicon sensors*, Master’s thesis, Department of Physics, University of Oslo, Oslo, Norway, 2010.
- [79] “Cplusplus.com.” Online, 2013. <http://www.cplusplus.com/>.
- [80] R. Brun and F. Rademakers, *ROOT — An object oriented data analysis framework*, Nucl. Instrum. Meth. A **389** no. 1–2, (1997) 81 – 86. <http://www.sciencedirect.com/science/article/pii/S016890029700048X>. New Computing Techniques in Physics Research V.
- [81] R. Barlow, *Statistics: A Guide to the Use of Statistical Methods in the Physical Sciences*. The Manchester Physics Series. Wiley, 1999.
- [82] R. Turchetta, *Spatial resolution of silicon microstrip detectors*, Nucl. Instrum. Meth. A **335** (1993) 44–58.
- [83] C. Nellist et al., *Beam test results of 3D silicon pixel sensors for future upgrades*, Nucl. Instrum. Meth. A **732** no. 0, (2013) 141 – 145. <http://www.sciencedirect.com/science/article/pii/S0168900213009789>. Vienna Conference on Instrumentation 2013.
- [84] L. Jørgensen, *The AEGIS antihydrogen gravity experiment*, Hyperfine Interactions **212** no. 1-3, (2012) 41–49. <http://dx.doi.org/10.1007/s10751-011-0382-9>.
- [85] A. Kellerbauer et al., *Proposed antimatter gravity measurement with an antihydrogen beam*, Nucl. Instrum. Meth. B **266** no. 3, (2008) 351 – 356. <http://www.sciencedirect.com/science/article/pii/S0168583X07017740>. XIV International Workshop on Low Energy Positron and Positronium Physics.
- [86] S. Baird et al., *The Antiproton Decelerator: AD*, Nucl. Instrum. Meth. A **391** no. 1, (1997) 210 – 215. <http://www.sciencedirect.com/science/article/pii/S0168900297003598>.
- [87] O. Kafri and I. Glatt, *Moire Deflectometry: A Ray Deflection Approach To Optical Testing*, Optical Engineering **24** no. 6, (1985) 246944–246944–. [+http://dx.doi.org/10.1117/12.7973607](http://dx.doi.org/10.1117/12.7973607).
- [88] L. Badano et al., *A real-time beam monitor for hadrontherapy applications based on thin foil secondary electron emission and a back-thinned monolithic pixel sensor*, in *Proceedings of DIPAC, Venice, Italy*. 2007.

- 
- [89] S. Aghion et al., *Annihilation of low energy antiprotons in silicon*, arXiv:1311.4982 [physics.ins-det] (2013).
- [90] C. D. Anderson, *Cosmic-Ray Positive and Negative Electrons*, Phys. Rev. **44** (1933) 406–416. <http://link.aps.org/doi/10.1103/PhysRev.44.406>.
- [91] *Private communication with G. Bonomi and A. Gligorova*, 2nd september, 2013.
- [92] J. Allison et al., *Geant4 developments and applications*, Nuclear Science, IEEE Transactions on **53** no. 1, (2006) 270–278.
- [93] S. Agostinelli et al., *Geant4—a simulation toolkit*, Nucl. Instrum. Meth. A **506** no. 3, (2003) 250 – 303.  
<http://www.sciencedirect.com/science/article/pii/S0168900203013688>.
- [94] J. Apostolakis et al., *GEANT4 Physics Lists for HEP*, pp. , 833–836. 2008.
- [95] P. Degtyarenko, M. Kossov, and H.-P. Wellisch, *Chiral invariant phase space event generator*, Eur. Phys. J. A **8** (2000) 217–222.
- [96] G. Bonomi, A. Magnani, and C. Riccardi, “Simulation of antiproton-nucleus annihilation at rest.”.
- [97] *Private communication with S. Grinstein and O. Rohne*, 25th june, 2013.
- [98] M. Borri, *Characterization of 3D Silicon Assemblies for ATLAS Pixel Upgrade*. PhD thesis, School of Physics and Astronomy, University of Manchester, 2013.
- [99] C.-H. Lai, *Simulation of 3D sensors*. PhD thesis, School of Physics and Astronomy, University of Manchester, 2013.
- [100] *Private communication with A. Ribon and N. Pacifico*, 2nd september, 2013.
- [101] A. Galoyan and V. Uzhinsky, *Simulation of Light Antinucleus-Nucleus Interactions*, arXiv:1208.3614 [nucl-th] (2012).
- [102] G. Bendiscioli and D. Kharzeev, *Antinucleon-nucleon and antinucleon-nucleus interaction. A review of experimental data*, La Rivista Del Nuovo Cimento Series 3 **17** no. 6, (1994) 1–142. <http://dx.doi.org/10.1007/BF02724447>.